REFRACTIVE EFFECTS IN PHASE OBJECTS AND ASSOCIATED PHENOMENA

by

RICARDO BUCCELLATO

Submitted in partial fulfillment of
the requirements for the degree of
Doctor of Philosophy
in the
Department of Physics,
University of Natal.

Durban 1994

To my parents and family
and to those who matter.

Preface

The work described in this thesis was carried out in the Laser Group of the Plasma Physics Research Institute at the University of Natal, Durban, between March 1990 and March 1994, under the supervision of Prof. M.M. Michaelis and Dr P.F. Cunningham.

These studies represent original work performed by the author and have not been submitted in any form to another university. Where use was made of the work of others, it has been duly acknowledged in the text.

R. BUCCELLATO

Acknowledgements

I would like to thank the following people for their help:

Prof. M.M. Michaelis, my supervisor, whose advice and persuasive powers made this work a reality and whose enthusiasm was contagious.

Dr. P.C. Cunningham, for his supervision of the first experimental investigation.

Prof. M.A. Hellberg, for his help in smoothing out the financial and administrative difficulties encountered throughout the duration of this work.

Dr. J.A.R. Waltham, who showed me the ropes in the Laser Laboratory and for coming up with the idea for the first investigation.

Nicola Lisi, for his help with the experimental investigation of the Colliding Shock Lens.

Dr. G.R.L. Mace, for his help in the general realm of physics and numerical methods.

M. Kuppen, for his help and encouragement.

The staff of the Mechanical and Electronic Physics Workshop, headed by **W. de Beer**, without their excellent workmanship and readiness to help, this work would not have been possible. Thank You!

The **Foundation for Research and Developement** for their financial

assistance.

Finally, my parents, my family and friends for their patience, encouragement and support.

Abstract

The effect of the refraction of a laser beam propagating through three different phase objects, i.e. a laser produced plasma and two different gas media, is investigated in this thesis. It is shown that these effects have useful applications. As an introduction to the work performed, a basic discussion of the theory of light is given.

In the first experimental study, the accuracy of using the Refractive Fringe Diagnostic, as a tool to determine the electron density profiles of laser produced plasmas, is investigated [Buccellato *et al.* (1992)]. A comparative study is performed between an established method of determining the electron density profiles of laser produced plasmas, i.e. Nomarski interferometry, and the Refractive Fringe Diagnostic, by comparing experimental data obtained from the same laser shot. For the electron density profiles investigated, it is shown that the Refractive Fringe Diagnostic over-estimates the electron density by an order of magnitude. It is suggested that the electron density errors are due to the inherent assumptions of the Refractive Fringe Diagnostic. To verify this, a numerical simulation into the accuracy of the RFD is performed on a mathematically modelled plasma. The discrepancy in the numerical results are consistent with those of the experimental results and these can be attributed to the assumptions made by the Refractive Fringe Diagnostic.

Laser light refracted by a gas medium, with a specific density profile, may produce a near diffraction limited focal spot. The remaining two experimental investigations deal with two novel gas lenses: the Pulsed Gas Lens and the Colliding Shock Lens.

A radially expanding cylinder of gas produces a suitable density structure to focus laser light. A design of a gas lens, the Pulsed Gas Lens, using this principle is proposed as a final focusing lens for a laser fusion power station [Buccellato *et al.* (1993a)]. To establish the feasibility of such a lens a proof-of-principle design for the lens is given. A numerical simulation of this lens is performed by modelling the gas flow from the lens and raytracing through the determined density profiles inside the lens. It is found that this lens can be used as a focusing element. To establish certain practical aspects of the proof-of-principle design, a beam deflection device was constructed and tested. This beam deflection device models the lensing principle of the proposed lens. The laser beam deflection observed did not match the computed deflection. The opening mechanism for the proof-of-principle design did not produce an instantaneous opening of the chamber as was assumed in the simulation. The opening mechanism must be modified to decrease the opening time.

Diverging spherical shock waves, produced by pairs of opposing electrodes evenly spaced on a circumference, produce a converging cylindrically symmetric shock wave. After convergence a suitable density structure exists for near diffraction limited focusing to occur. It is found that the Colliding Shock Lens is a varifocal lens: the focal length and lens diameter increase with time [Buccellato *et al.* (1993b)]. A numerical simulation is performed to model the operation of the Colliding Shock Lens. The numerical results compare favourably with the experimental results. From the simulation it is established that the lens diameter can be scaled up by increasing the physical size of the lens and the input energy to the lens. Potential applications of the colliding shock lens are discussed.

To conclude this thesis, the results of the separate investigations are summarised.

Contents

List of Figures

Chapter 1

Introduction

Light is the essence of life and not surprisingly, a great deal of attention has been given to unravelling the mysteries of light. The ancient Greek philosophers believed that light and vision were one and the same and it was not until approximately 1000 A.D. that Alhazen, an Arab scholar, distinguished the difference between light and vision. The question "What is the nature of light?", has attracted a great deal of attention since the 17^{th} Century. A brief review of the historical development of the perception of light and the evolution of the laser will be given and the concept of refraction will be introduced. The work performed in this thesis will be outlined at the end of the chapter.

1.1 The Evolution of the Perception of Light

The start of modern optics can be traced back to the empirical discovery of the law of refraction by Willebrord Snell in 1621. René Descartes, in 1637, explained this law by modelling light as a pressure transmitted by an elastic medium. Robert Hooke, in 1665, proposed that light consisted of vibrations of an aether and explained refraction as the deflection of a wavefront. This hypothesis was rejected by Isaac Newton in 1671 since it did not explain the rectilinear propagation of light. Newton, studying the dispersion of light by a prism, concluded that white light was made up of different colours and he initially proposed various models for light. In 1675, Newton proposed that light consisted of particles but in certain instances these particles generated wave motions in the aether. He substantiated his argument by explaining diffraction, the colour of thin films and Newton rings. He modified his theory in 1704 and explained light as a stream of particles which suffer periodic fits. He later added that these particles have sides in order to explain double refraction.

Christiaan Huygens, in 1678, proposed a wave theory of light, consistent with the rectilinear propagation of light, to explain reflection, refraction and double refraction. He proposed that each point of a wavefront is the source of a secondary wavelet. It was not until the early 19^{th} Century that the wave theory of light was generally accepted. Thomas Young, in 1801, introduced the principle of interference between light waves and used this to explain Newton rings. Augustin Fresnel incorporated Huygen's wave description and the principle of interference to explain the propagation of a light wave. These waves were presumed to be longitudinal. In 1816, he used the wave theory to calculate experimentally observed diffraction patterns. Young, in 1817, suggested that light consisted of vibrations transverse to the direction of propagation in order to explain polarization. However, he did not account

for the light medium needed to sustain this wave.

The concept of the nature of light took a dramatic turn near the end of the 19^{th} Century. James Maxwell, in 1864, proposed that light was an electromagnetic wave supported by some medium. This theory was boosted by the experimental discovery of electromagnetic radiation by Heinrich Hertz in 1887 and the discovery that electromagnetic waves do not need a medium to propagate by Albert Einstein in 1905. The concept of the quantum nature of light evolved in 1900 when Max Planck, in order to explain black body radiation, assumed that electromagnetic radiation was produced in discreet units which had an energy, E, related to a frequency, f, by $E = hf$, where h is a constant. In 1905, Einstein proposed a theory that light consisted of particles of specific energy, E, and he used this to derive the equation governing the photoelectric effect. In 1909, Einstein proposed the co-existence of particles and waves in a radiation field. The quantum hypothesis of light began to gain general acceptance when Arthur Compton, in 1923, explained his x-ray scattering results in terms of scattering of quanta of radiation by free electrons. The quantum of radiation was named the photon by G. N. Lewis in 1926. Through the work of Bohr, Born, Heisenberg, Schrödinger, De Broglie, Pauli and Dirac, the theory of light was refined to what we know today.

1.2 What is Light?

Light corresponds to the electromagnetic radiation in the range from approximately 384 THz to approximately 769 THz. Light can be viewed submicroscopically as a stream of photons where each photon has a specific energy given by $E = hf$, momentum given by $p = \frac{h}{\lambda}$ and a constant speed in vacuum

given by $c = f\lambda$. Macroscopically, this stream of photons exhibits both wave and particle like behaviour. To explain certain optical phenomena either the wave nature of light or the particle nature of light is used. On the question "What is a photon?", Einstein said " I spent my life to find out what a photon is and I still don't know it."

The most common mechanism responsible for the emission of light is the excitation of an atom from its ground state to an excited state by the collision of the atom with either an atom, an electron or a photon. This excited state lasts for a time period of the order of 10^{-9} s and on relaxation to the ground state, a photon is released. The energy of the photon is equal to the quantized energy change of the atom from the excited state to the ground state.

There are a wide variety of different light sources, e.g. the incandescent light bulb, the gas discharge tube and the laser. It is the laser that is used in this investigation.

1.3 The Laser

The idea behind the stimulated emission of radiation was proposed by Einstein [Einstein (1917)], but it was only experimentally realised in 1955. Gordon *et al.* [Gordon *et al.* (1955)] used the stimulated emission between the lowest two levels of the ammonia molecule to amplify microwave radiation of wavelength 12.6 mm. Their device was named a maser, an acronym for microwave amplification by the stimulated emission of radiation. Schawlow and Townes [Schawlow and Townes (1958)] proposed the extension of the maser to amplify shorter wavelengths. The first light amplification by the stimulated emission of radiation, i.e. laser, was demonstrated by Maiman *et*

al. [Maiman *et al.* (1961)]. The two levels in the ruby crystal were used to produce pulsed red light of wavelength 694.3 nm. The first continuous wave laser was demonstrated by Javan *et al.* [Javan *et al.* (1961)] using a gas medium consisting of a mixture of Helium and Neon. To date, lasers with frequencies ranging from microwaves to x-rays have been developed.

Laser light has the unique feature of high intensity, directionality, coherence, and narrow spectral width. These features have given lasers a wide range of applications, some of which are considered in this thesis.

1.4 Refraction

Refraction is the main topic under investigation in this thesis, thus a basic understanding of this phenomena is needed.

The speed of light in vacuum is given by:

$$c = \frac{1}{\sqrt{\epsilon_0 \mu_0}}, \tag{1.1}$$

where ϵ_0 is the permittivity of free space and μ_0 is the permeability of free space.

The phase velocity of light in a homogeneous isotropic dielectric is given by:

$$v_p = \frac{1}{\sqrt{\epsilon \mu}}, \tag{1.2}$$

where ϵ is the permittivity of the dielectric and μ is the permeability of the dielectric.

Light propagating into a dielectric from vacuum will experience a change in speed and this speed change will result in the light experiencing refraction or "bending". This speed change and its dependence on the frequency of the light can be understood by studying the interaction of the incident electromagnetic wave with the arrays of atoms making up the dielectric. Refraction can be visualised by considering a plane light wavefront incident on a dielectric, as shown in figure 1.1.

The section of the wavefront interacting with the dielectric slows down relative to the remaining section which is still propagating in vacuum. With continued interaction, the direction of propagation of the plane wavefront in the dielectric differs from that in vacuum. This change in direction is given by:

$$\frac{\sin\theta_i}{\sin\theta_r} = \frac{n_2}{n_1} \tag{1.3}$$

where n_1 is the refractive index of the medium that the light was travelling in and n_2 is the refractive index of the medium that the light travelled into. The refractive index of a medium is defined as the ratio of the speed of light in vacuum to the speed of light in the medium, i.e.

$$\begin{aligned} n &\equiv \frac{c}{v_p} \\ &= \sqrt{\frac{\epsilon\mu}{\epsilon_0\mu_0}}. \end{aligned} \tag{1.4}$$

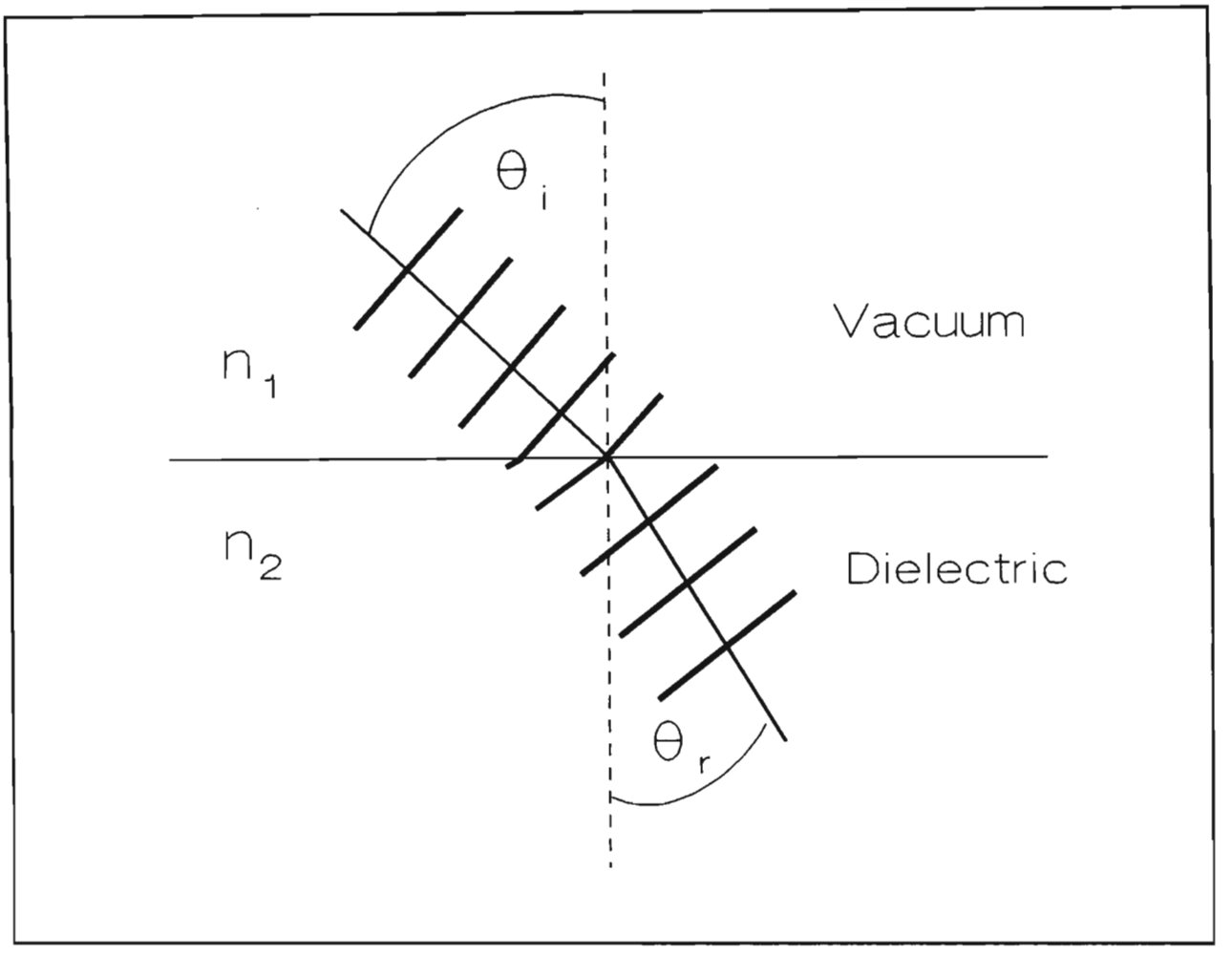

Figure 1.1: Refraction of a plane wavefront.

1.5 Thesis Outline

In this thesis, the effect of the refraction of laser light through three different phase objects is investigated. The first investigation deals with the accuracy of using the Refractive Fringe Diagnostic in determining the electron density profiles of laser produced plasmas. The following investigations deal with the development of two novel pulsed gas lenses: the Pulsed Gas Lens and the Colliding Shock Lens. Each investigation has been dealt with separately and only pertinent theory, relevant to the understanding of each investigation, has been included in each chapter. For a fuller theoretical picture the reader is referred to standard literature in the text.

Chapter 2

Comparative Electron Density Measurements for the Refractive Fringe Diagnostic and Nomarski Interferometry

2.1 Introduction

"A plasma is a quasi-neutral gas of charged and neutral particles which exhibits collective behaviour" [Chen (1974)]. Irradiation of a gas [Maker *et al.* (1963), Meyerand and Haught (1963)] or a solid [Verber and Adelman (1963), Honig and Woolston (1963), Linlor (1963)], with high intensity laser light, will produce a plasma. Laser produced plasmas (LPP) have a wide range of applications, e.g. laser fusion; x-ray sources; x-ray lasers; sources of energetic particles and beat wave accelerators [Key (1986)]. For these

applications, a knowledge of the electron density profile of LPP is required. Electron density profiles of LPP can be determined by optical probing. Interferometric, schlieren and shadowgraphic techniques are commonly used in the optical probing of LPP and a review of these techniques is given by Hall [Hall (1986)] and by Basov *et al.* [Basov *et al.* (1986)].

Interferometers are the most widely used optical probes for LPP and numerous studies have been performed [Attwood *et al.* (1978), Raven and Willi (1979), Fedosejevs *et al.* (1979)]. The refraction of a probe beam through a phase object can also be used to study the phase object concerned [Evtushenko *et al.* (1971), Keilmann (1972), Schreiber *et al.* (1973), Kogelschatz and Schneider (1972), Benattar and Popovics (1983)]. The first quantitative refractive fringe diagnostic, to evaluate the electron density profiles of LPP, was proposed by Michaelis and Willi [Michaelis and Willi (1981)] and was later revised by Cunningham *et al.* [Cunningham *et al.* (1986a)]. This diagnostic has been applied to the study of flames [Michaelis *et al.* (1985)] and shocks in air [Waltham *et al.* (1987), Bacon *et al.* (1989), Buccellato *et al.* (1993b)].

The Refractive Fringe Diagnostic (RFD) is a simple method of diagnosing the electron density profiles of LPP. However, the accuracy of this method has not been thoroughly determined. In this chapter, a comparative study is performed, between a Nomarski interferometer and the RFD, in determining the electron density profiles of LPP [Buccellato *et al.* (1992)]. This comparison is based on experimental data obtained from the same laser shot. A numerical simulation of the comparison is performed to access the effect of the assumptions of the RFD on the accuracy of the diagnostic and to verify the experimental results.

2.2 Theory

The topic of interest in this investigation is the optical diagnosis of LPP. The mechanism responsible for LPP formation is of secondary importance and thus it is not discussed here. A comprehensive review of LPP is given by Hughes [Hughes (1975)].

An electromagnetic wave propagating through a plasma will experience refraction. The refractive index (n), for a homogeneous plasma, is given by the ratio of the speed of light in vacuum (c) to the phase velocity (v_p) of the electromagnetic wave in the plasma:

$$\begin{aligned} n &\equiv \frac{c}{v_p} \\ &= \frac{ck}{w}, \end{aligned} \tag{2.1}$$

where k is the propagation vector and w the angular frequency of the wave. For a fully ionised cold plasma (no collisions and no drift velocity) with no static magnetic field, equation 2.1 can be expressed as [Hughes (1975)]:

$$n \simeq \sqrt{1 - \frac{w_{pe}^2}{w^2}}, \tag{2.2}$$

where w_{pe} is the electron plasma frequency. The electron plasma frequency is the natural frequency of the electrostatic oscillations of the electrons due to disturbances of the charge neutrality of the plasma and is it given by:

$$w_{pe}^2 = \frac{N_e e^2}{m_e \epsilon_0}, \tag{2.3}$$

where N_e is the electron density, e is the charge of an electron, m_e is the mass of an electron and ϵ_0 is the permittivity of free space. Incorporating equation 2.3 into equation 2.2, the refractive index of a homogeneous plasma can be expressed as:

$$n \simeq \sqrt{1 - \frac{N_e}{N_c}}, \tag{2.4}$$

where N_c is the critical electron density for a laser probe beam with vacuum wavelength, λ, which is given by:

$$N_c = \frac{4\pi^2 m_e \epsilon_0 c^2}{\lambda^2 e^2}. \tag{2.5}$$

The critical electron density is the maximum electron density a laser probe beam can penetrate before it is reflected. If the wavelength of the laser probe beam is chosen such that $N_c \gg N_e$, equation 2.4 can be approximated by:

$$n \simeq 1 - \frac{N_e}{2N_c}. \tag{2.6}$$

A LPP, which is generated in vacuum by the irradiation of a solid target with high intensity laser light, is inhomogeneous and is often spherically symmetric. A slice through this plasma, perpendicular to the incident LPP generating laser beam, will have circular symmetry and the refractive index (equation 2.6) can be expressed as:

$$n(r) \simeq 1 - \frac{N_e(r)}{2N_c}, \tag{2.7}$$

where r is the radial distance.

A laser probe beam propagating through a LPP is going to be refracted and it will experience a change in optical path length (OPL) and phase due to the plasma. A light ray, traversing an optically thin (i.e. no absorption) plasma slice, is shown in figure 2.1.

A light ray entering the LPP with a height, p, is refracted as it traverses the plasma and exits the plasma with an angle α. If one traces the light ray back into the plasma, the apparent source of the light ray is given by:

$$y = \frac{p}{\cos \alpha} + d \ \tan \alpha, \tag{2.8}$$

where d is the distance between the axis of symmetry and the object plane. If one assumes that one has negligible refraction, i.e. $\alpha \ll 1°$, then equation 2.8 can be simplified to:

$$y \simeq p. \tag{2.9}$$

Equation 2.9 implies that the path of the light ray traversing the plasma is a straight line. The OPL of the light ray traversing the plasma is then given by:

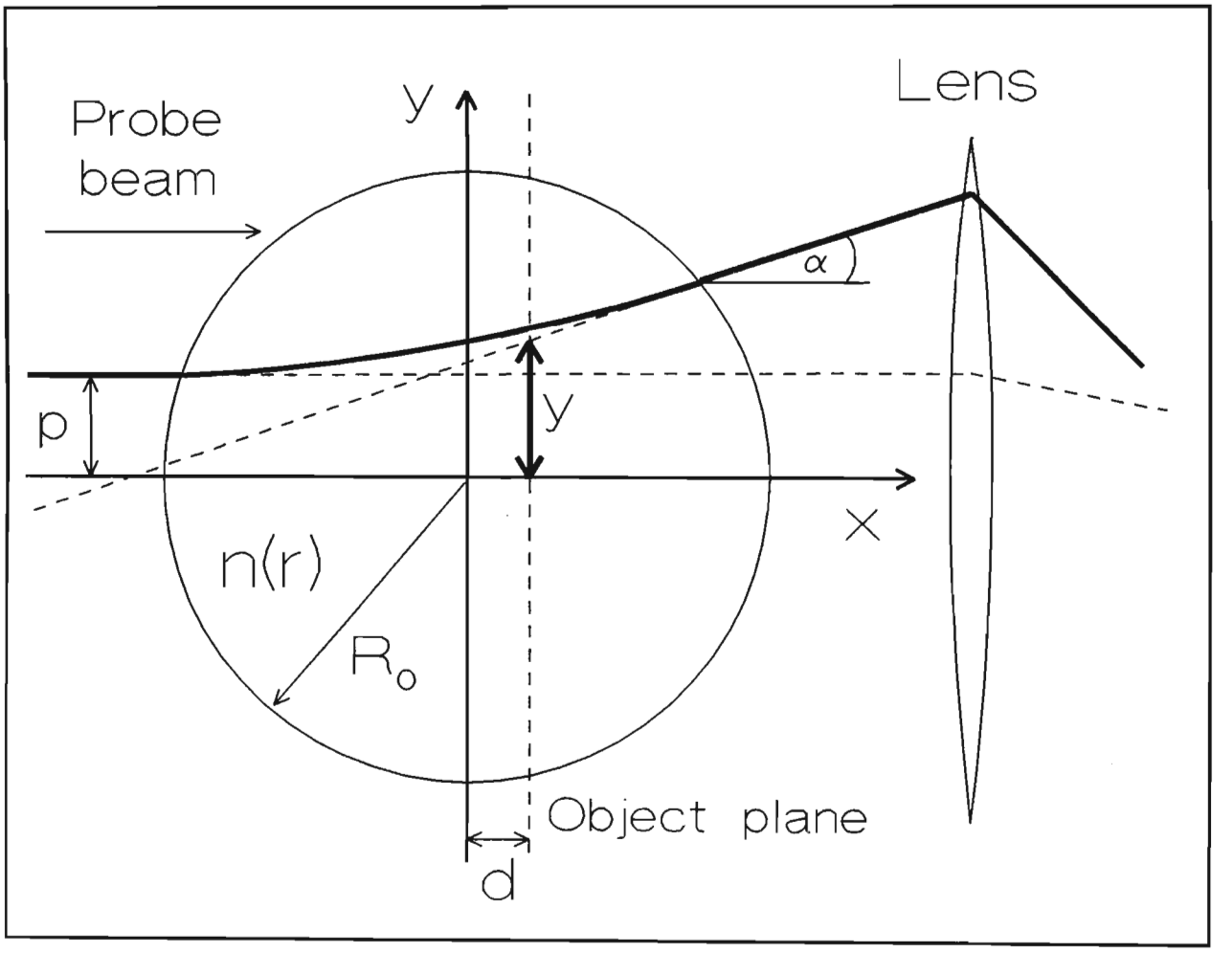

Figure 2.1: A light ray traversing a plasma slice.

$$\phi(y) = 2\int_{y}^{R_0} \frac{n(r)r}{\sqrt{r^2 - y^2}}\, dr, \tag{2.10}$$

which is in the form of an Abel integral. To evaluate the refractive index one has to Abel invert equation 2.10:

$$n(r) = -\frac{1}{\pi}\int_{r}^{R_0} \frac{\phi'(y)}{\sqrt{y^2 - r^2}}\, dy. \tag{2.11}$$

By knowing the change in OPL of the laser probe beam due to the LPP, the refractive index of the LPP can be calculated by equation 2.11. In turn, the electron density can be calculated by equation 2.7. The change in OPL of the probe beam can be measured by an interferometer.

An alternative method is to calculate the angle of refraction (α) and geometrically deduce the refractive index and thus the electron density of the LPP. This is the essence of the RFD.

The advantages of optical probing of LPP, with laser light, is the high spatial (order of μm) and temporal (order of ps) resolution obtainable. However, a disadvantage is that the maximum electron density that can be probed is dependent on the wavelength of the probing laser. For lasers with ultraviolet wavelengths, the maximum electron density that can be probed is of the order of $10^{22} cm^{-3}$ (equation 2.5).

2.2.1 Interferometry

Conventional interferometers divide a laser probe beam into two equal parts and direct only one part through the phase object to be investigated. When these two parts are recombined, an interference pattern is formed due to the relative phase shift between the two laser beams.

The fringes on the interferogram represent iso-phase contours, i.e. the change in the OPL between the light traversing the plasma and that not traversing the plasma, which can be given by geometrical arguments from figure 2.1 (assuming negligible refraction):

$$\phi(y) - 2\sqrt{R_0^2 - y^2} \equiv \psi(y), \tag{2.12}$$

form visible fringes when $\psi(y)$ is an integral number of wavelengths:

$$\psi(y) = F\lambda, \tag{2.13}$$

where $F = 0, 1, 2 \cdots, n$.

If one performs the integration implied in equation 2.11 on the experimental data $\psi(y)$:

$$-\frac{1}{\pi}\int_r^{R_0} \frac{\psi'(y)}{\sqrt{y^2 - r^2}}\, dy \quad = \quad -\frac{1}{\pi}\int_r^{R_0} \frac{\phi'(y)}{\sqrt{y^2 - r^2}}\, dy$$

$$
\begin{aligned}
&+ \quad \frac{1}{\pi}\int_r^{R_0} \frac{2y}{\sqrt{(R_0^2-y^2)(y^2-r^2)}}\,dy, \\
&= \quad n(r)-1, \qquad (2.14)\\
&\equiv \quad \Delta n(r). \qquad (2.15)
\end{aligned}
$$

In obtaining equation 2.14 one has noted that:

$$\frac{1}{\pi}\int_r^{R_0} \frac{2y}{\sqrt{(R_0^2-y^2)(y^2-r^2)}}\,dy = -1. \qquad (2.16)$$

By differentiating equation 2.7:

$$\Delta n(r) \simeq -\frac{\Delta N_e(r)}{2N_c}, \qquad (2.17)$$

but:

$$\Delta N_e = N_{e,plasma} - N_{e,vacuum} = N_e - 0 = N_e, \qquad (2.18)$$

thus:

$$\Delta n(r) \simeq -\frac{N_e(r)}{2N_c}. \qquad (2.19)$$

Equating equations 2.15 and 2.19 one gets:

$$N_e(r) = \frac{2N_c}{\pi} \int_r^{R_0} \frac{\psi'(y)}{\sqrt{y^2 - r^2}}\, dy. \tag{2.20}$$

Alternatively, one could obtain a more accurate value for N_e by employing equation 2.4 in the form:

$$N_e(r) = N_c(1 - n^2(r)), \tag{2.21}$$

with $n(r)$ determined by equation 2.14, but for our purposes equation 2.20 will suffice.

Deutsch and Beniaminy [Deutsch and Beniaminy (1982)] have shown that one can reduce the errors due to the differentiation of noisy interferometric data ($\psi'(y)$), by an order of magnitude, by manipulating equation 2.20 to remove the differentiation of $\psi(y)$. Integrating equation 2.20 by parts results in [Deutsch and Beniaminy (1982)]:

$$N_e(r) = \frac{2N_c}{\pi} \left(\frac{\psi(R_0) - \psi(r)}{\sqrt{{R_0}^2 - r^2}} + \int_r^{R_0} \frac{[\psi(y) - \psi(r)]y}{(y^2 - r^2)^{3/2}}\, dy \right). \tag{2.22}$$

In obtaining equation 2.22, one assumed cylindrical symmetry about the axis of the heating laser beam and no refraction of the laser probe beam in the LPP. Deviations from these assumptions will result in errors in the calculated electron densities. Vest [Vest (1975)] showed that the Abel inversion of the change in OPL interferometric data, in the presence of strong refraction, yields accurate results if the interferogram is formed with appropriate imaging, i.e. imaging on the axis of symmetry of the LPP. This corresponds to $d = 0$ in figure 2.1. Sweeney *et al.* [Sweeney *et al.* (1976)] showed that these

errors can be reduced if the probe beam has a probing wavelength four times smaller than the heating laser pulse. Pawlowicz [Pawlowicz (1991a,b)], using an interferometric data analysis technique which takes into account strong refraction of the laser probe beam in the LPP, confirmed Vests conclusion, i.e. Abel inversion of the change in OPL interferometric data, in the presence of strong refraction, yields accurate results if the interferogram is formed with appropriate imaging.

The Nomarski interferometer is a commonly used interferometer for LPP diagnosis. This interferometer was first proposed by Nomarski [Nomarski (1955)] for the use in microscopy and was adapted for LPP by Benattar *et al.* [Benattar *et al.* (1979)].

2.2.2 Nomarski Interferometer

The Nomarski interferometer is a polarization type interferometer. A schematic representation of the interferometer is given in figure 2.2 [Benattar *et al.* (1979)]. The interferometer consists of two 45° polarizers, an imaging lens and a Wollaston prism.

A Wollaston prism is made up of two quartz prisms placed together to make a parallel plate. The prisms are cut so that the optical axes are orthogonal to each other and to the direction of the probe beam. A probe beam, which is linearly polarized at 45° to the optical axis of the first prism by polarizer P_1, is divided into an ordinary and extraordinary ray by the first prism. These two components are equal in intensity, orthogonally polarized with respect to each other and travel at different speeds in the prism. At the junction of the prisms the two components of the laser beam see a difference in the refractive index. The ordinary ray of the laser beam in the first prism

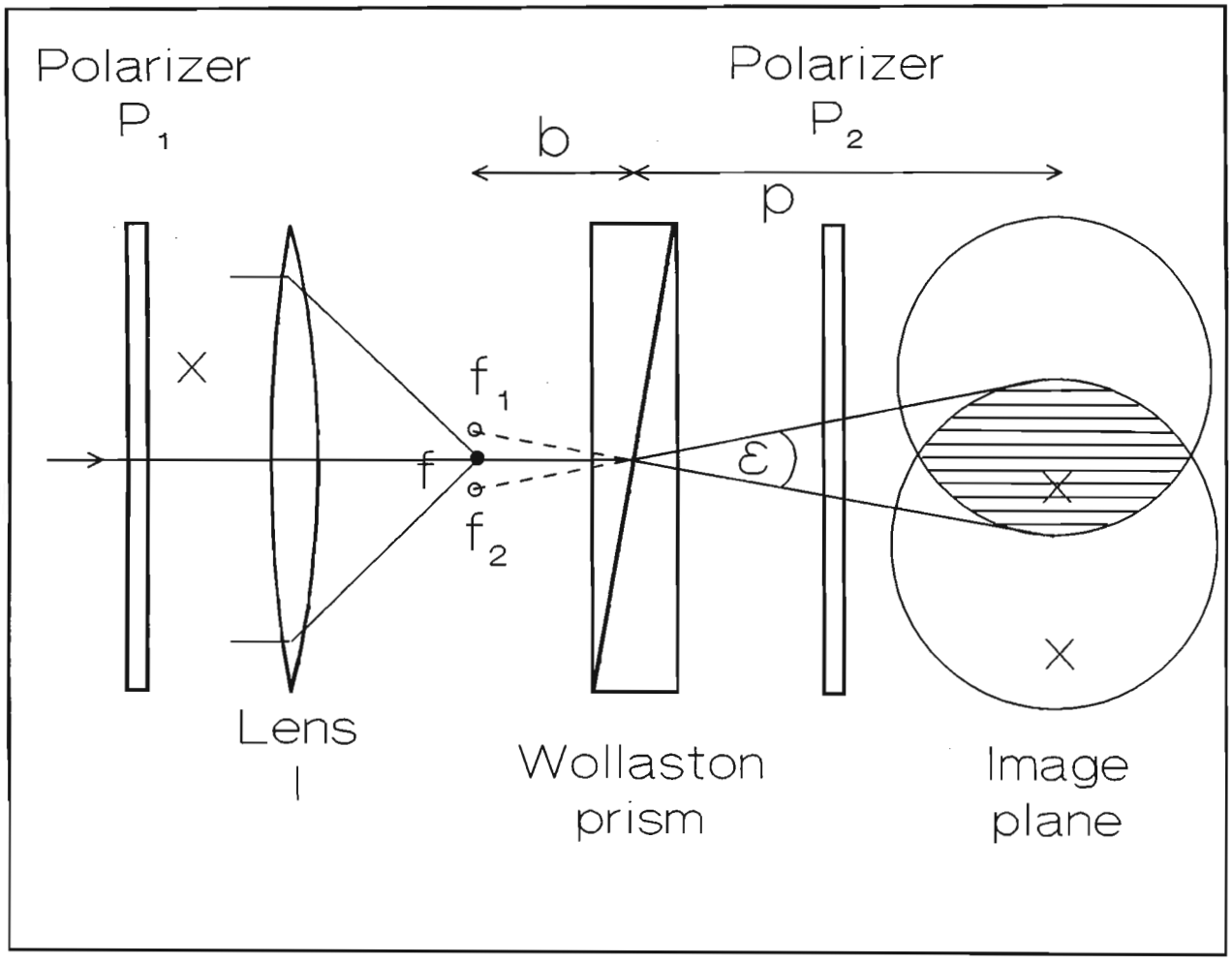

Figure 2.2: A schematic representation of a Nomarski interferometer.

becomes the extraordinary ray in the second prism, and vice versa. The two beams thus emerge from the Wollaston prism with an angular separation, ϵ.

An object, illuminated by the probe beam, is imaged onto the image plane by the lens l. Two images of the object are produced on the image plane by the Wollaston prism. The two images can be thought of as originating from two virtual foci, f_1 and f_2. The two beams, emerging from the Wollaston prism, are orthogonally polarized with respect to each other and thus no interference occurs on the image plane. A further 45° polarizer, P_2, is needed to produce interference fringes. The two polarizers can be either crossed or uncrossed. The fringe separation is given by:

$$i = \frac{\lambda p}{\epsilon b}, \tag{2.23}$$

where p, b, and ϵ are given in figure 2.2 The fringe spacings can be varied by changing the position of the Wollaston prism and the fringe orientation can be changed by rotating the Wollaston prism.

The Nomarski interferometer can act as a normal or differential interferometer, depending on the values of ϵ and b chosen. A differential interferometer measures the gradient of the change in OPL due to the plasma while a normal interferometer measures the change in OPL due the plasma. A normal interferometer was used in this investigation. The diameter of the laser beam, ϵ and b were chosen so that the image of the plasma overlapped with an undisturbed region of the probe beam.

The advantages of using a Nomarski interferometer are given by Benattar *et al.* [Benattar *et al.* (1979)] and are summarised below:

- alignment and stability problems are reduced
- a wide range of wavelengths can be used without modifications needed
- the equal optical path length, between the virtual foci (f_1 and f_2) and the central interference fringe (located on the axis of the interferometer) enables *ps* laser pulses to be used which have inherently low temporal coherence
- the spatial resolution is determined by the quality of the lens
- the optical components are commonly available.

2.2.3 Refractive Fringe Diagnostic

The visualisation of the formation of refractive fringes from a spherical or cylindrical plasma, which has a monotonically decreasing electron density profile tending to zero at R_0, is shown in figure 2.3. R_0 is termed the effective plasma radius. The probe beam, refracted by the plasma, interferes with the probe beam not traversing the plasma, forming visible refractive fringes at a distance L behind the plasma. From the spacings of these refractive fringes, the refractive index profile of the LPP can be calculated.

Light rays traversing a spherically symmetric phase object obey Bouger's formula [Born and Wolf (1965)]:

$$p_i = r_i n(r_i) \sin\theta, \tag{2.24}$$

where r_i is the distance from the centre of the phase object to the i^{th} light ray, $n(r_i)$ is the refractive index at r_i, θ is the angle between the i^{th} ray and

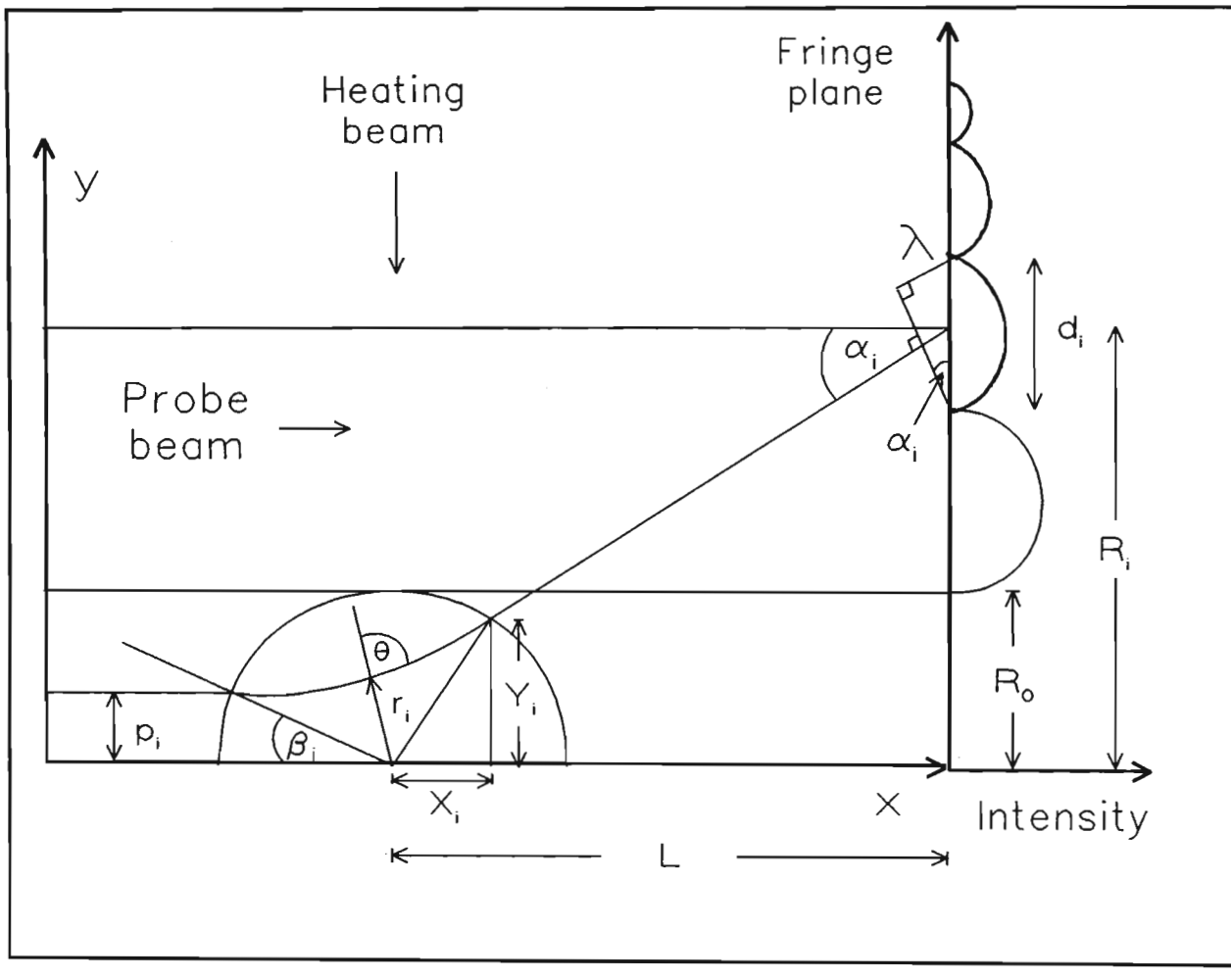

Figure 2.3: The geometry of the RFD.

a line joining the i^{th} ray to the origin, and p_i is the impact parameter of the i^{th} ray.

If one assumes that the path of the light ray in the plasma is parabolic (figure 2.4), the refractive index at point (h) is given by equation 2.24:

$$\begin{aligned} n(r_i) &= \frac{p_i}{r_i \sin\theta} \\ &= \frac{p_i}{r_i \sin\frac{\pi}{2}} \\ &= \frac{p_i}{r_i}, \end{aligned} \tag{2.25}$$

where p_i and r_i are geometrically deducible from figure 2.4.

At the ray entrance point (j), equation 2.24 can be expressed as:

$$\begin{aligned} p_i &= R_0 n(R_0) \sin\beta_i \\ &= R_0 \sin\beta_i, \end{aligned} \tag{2.26}$$

since $n(R_0) \simeq 1$.

The geometry of the parabolic light ray path in the plasma is expanded for clarity in figure 2.5. The line segments ij and ik are tangents to the parabola at the points (j) and (k), respectively, and the line jk joins the tangent points (j) and (k). The ray path in the plasma is given by:

$$y'(x') = ax'^2, \tag{2.27}$$

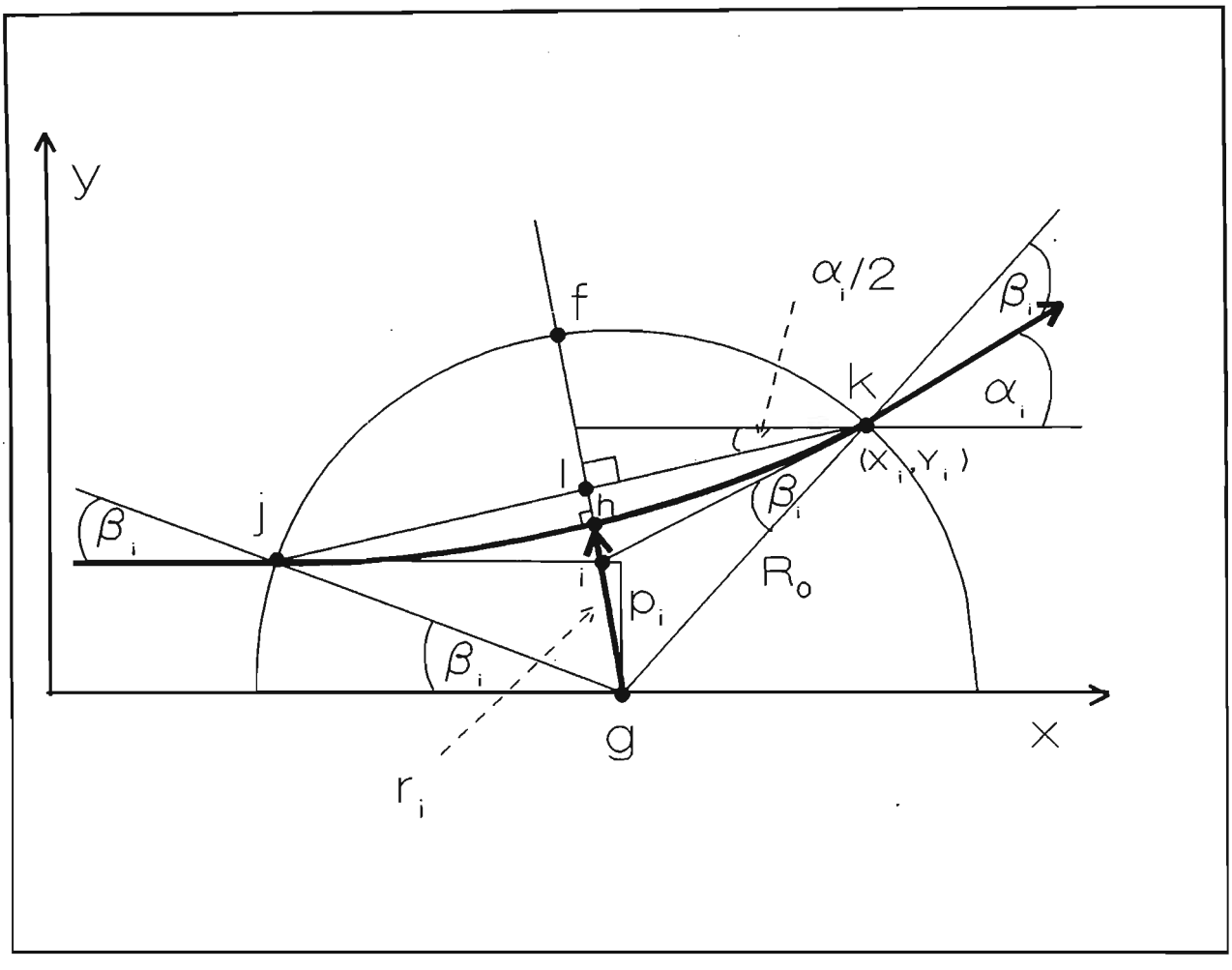

Figure 2.4: The RFD geometry of the ray path in the plasma.

and the gradient at any point on the ray path is given by:

$$\frac{dy'}{dx'} = 2ax'. \tag{2.28}$$

The line segment joining points (i) and (k) is given by:

$$y'_{ik}(x') = 2ax'^2 + i, \tag{2.29}$$

and at point (k), i.e. (x'_1, y'_1):

$$y'_{ik}(x'_1) = 2ax'^2_1 + i. \tag{2.30}$$

Rearranging equation 2.30 and incorporating equation 2.27:

$$\begin{aligned} i &= y'_{ik}(x'_1) - 2ax'^2_1 \\ &= y'_1 - 2y'_1 \\ &= -y'_1, \end{aligned} \tag{2.31}$$

i.e. the line segment $ih = hl$.

From figure 2.4, at point (h):

$$r_i = gh = gl - \frac{1}{2}il, \tag{2.32}$$

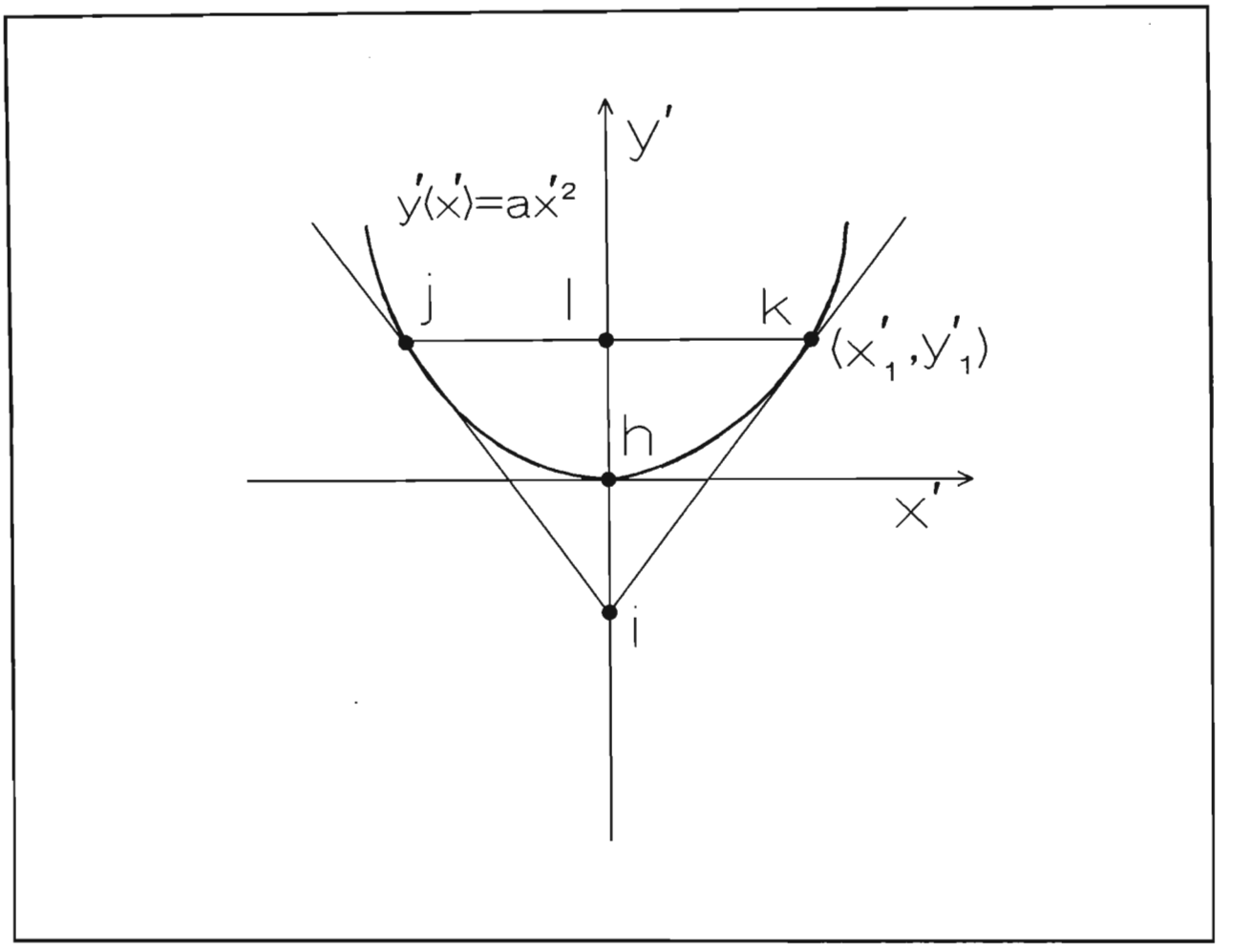

Figure 2.5: The geometry of a parabolic ray.

where:

$$gl = R_0 \sin(\frac{\alpha_i}{2} + \beta_i), \tag{2.33}$$

and:

$$il = R_0 \cos(\frac{\alpha_i}{2} + \beta_i) \tan \frac{\alpha_i}{2}, \tag{2.34}$$

thus:

$$r_i = R_0 \sin(\frac{\alpha_i}{2} + \beta_i) - \frac{1}{2} R_0 \cos(\frac{\alpha_i}{2} + \beta_i) \tan \frac{\alpha_i}{2}. \tag{2.35}$$

Substituting equation 2.35 and equation 2.26 into equation 2.25, with some trigonometric manipulation, the refractive index is given by:

$$n(r_i) = \frac{\cos \frac{1}{2}\alpha_i \sin \beta_i}{\sin \beta_i + \frac{1}{2} \sin \frac{\alpha_i}{2} \cos(\frac{1}{2}\alpha_i + \beta_i)}, \tag{2.36}$$

Note: The denominator of equation 2.36 in the paper of Cunningham *et al.* [Cunningham *et al.* (1986a)] is in error. The term $\frac{1}{2} \sin \frac{\alpha}{2}$ has been incorrectly typed as $\frac{1}{2} \sin \alpha$.

Equation 2.36 expresses the refractive index of the LPP on a radius, given by equation 2.35, as a function of two angles: α_i and β_i. These angles can be geometrically derived with reference to figure 2.3 and figure 2.4. If one

assumes that the wavefronts are planar at the fringe plane then the refraction angle of the i^{th} ray is given by:

$$\alpha_i = \sin^{-1} \frac{\lambda}{d_i}, \tag{2.37}$$

where d_i is the dark fringe separation enclosing the i^{th} bright fringe and λ is the wavelength of the laser probe beam.

The path of the light ray exterior to the LPP is given by:

$$y(x) = \tan \alpha_i \; x + constant, \tag{2.38}$$

but:

$$\begin{aligned} y(L) &= \tan \alpha_i \; L + constant \\ &= R_i, \end{aligned} \tag{2.39}$$

thus:

$$y(x) = \tan \alpha_i \; x + R_i - \tan \alpha_i \; L. \tag{2.40}$$

At the light ray exit point from the LPP, i.e.(X_i, Y_i), the light ray intersects the LPP boundary. The LPP boundary is given by:

$$y(x)^2 + x^2 = R_0^2. \tag{2.41}$$

To find the intersection point, equation 2.40 is substituted into equation 2.41:

$$(\tan\alpha_i(x - L) + R_i)^2 + x^2 = R_0^2, \tag{2.42}$$

and the relevant root of equation 2.42 is determined. The intersection point is [Campbell (1985)]:

$$X_i = L - \frac{R_i \tan\alpha_i + L}{1 + \tan^2\alpha_i} + \frac{\sqrt{R_i^2\tan^2\alpha_i - L^2\tan^2\alpha_i + 2LR_i\tan\alpha_i - (R_i^2 - R_0^2)(1 + \tan^2\alpha_i)}}{1 + \tan^2\alpha_i},$$

and:

$$Y_i = \sqrt{R_0^2 - X_i^2}. \tag{2.43}$$

The angle β_i can be expressed as:

$$\beta_i = \tan^{-1}\left(\frac{Y_i}{X_i}\right) - \alpha_i. \tag{2.44}$$

The electron density profile of the defocused shadowgraph can be evaluated from the fringe separations by using equations (2.7), (2.36), (2.35), (2.44) and (2.37).

A constraint in applying the RFD exists. The use of ray optic techniques is only justified if [Born and Wolf (1965)]:

$$\left|\frac{\delta N_e}{\delta y}\right| \ll 2\frac{N_c - N_e}{\lambda}. \tag{2.45}$$

It is important to note some of the assumptions that the RFD makes and these will be repeated here, i.e. *the light wavefronts are assumed to be locally planar at the fringe plane, there must be spherical or cylindrical plasma symmetry and parabolic light ray paths in the plasma.*

2.3 Experimental arrangement

The experimental arrangement is shown schematically in figure 2.6. A Q-switched ruby laser, with a 5 mm mode selecting aperture within the laser cavity, was focused onto massive carbon targets in a vacuum chamber evacuated to pressures less than 10^{-5} torr. A $f/1.5$ anti-reflection coated lens triplet (L_r) was used to focus the ruby beam onto the carbon targets with a focal spot diameter of 60 μm. With typical laser output energies of 400 mJ in 40 ns (FWHM), the irradiance on target was typically in the order of $10^{11}\,\mathrm{Wcm^{-2}}$.

The Foucault technique on a 30 μm diameter Nickel wire was used to determine the position of the focal plane of the lens, L_r. This position was recorded on a TV imaging system enabling the carbon targets to be placed in the focal plane of the lens with an accuracy of 60 μm. The Nickel wire at the focal plane of the lens, L_r, was imaged by a $f/5$ lens (L_n) onto the Nomarski interferometer TV camera. The position of the Refractive Fringe

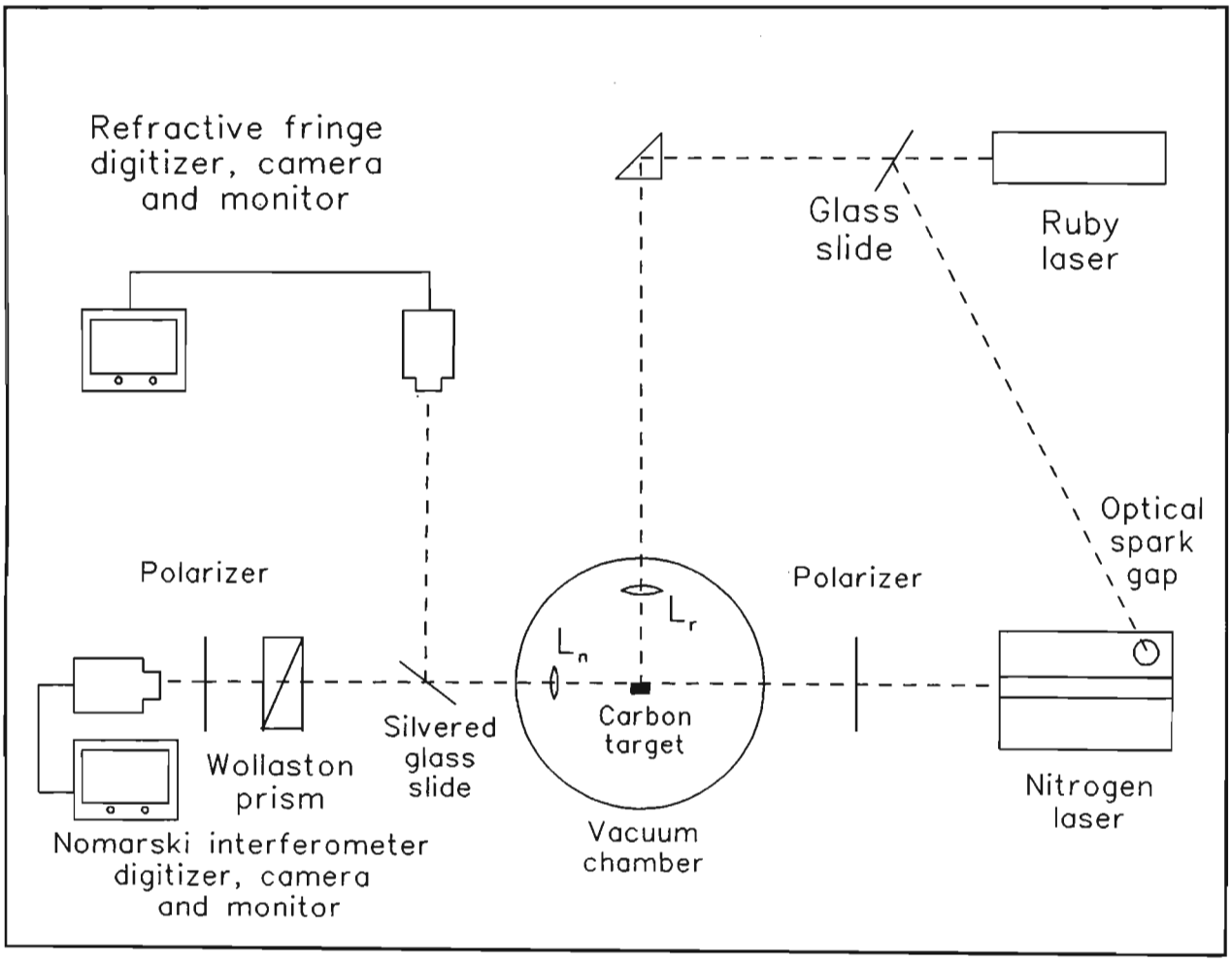

Figure 2.6: The experimental setup.

camera was adjusted to image a plane, on the camera side of the target, 10.4 mm from the target.

The LPP was probed with a Nitrogen laser of wavelength 337 nm and a pulse length of 1 ns (FWHM). The Nitrogen laser was synchronised with the Ruby laser by using an in-line laser-triggered spark gap [Cunningham *et al.* (1986b)], triggered by 8 % of the ruby laser beam (via a glass slide). The probe times of the plasma were varied by means of a dogleg (not shown in figure 2.6) which varied the distance the ruby light travelled between the ruby laser and the carbon target. The probe times were determined by two photodiodes connected to a Tektronix 485 oscilloscope. The photodiodes (not shown in figure 2.6) were arranged to detect the back reflections of the Ruby and Nitrogen lasers from the vacuum chamber windows.

The polarizers (Glan Taylor prisms), of the Nomarski interferometer, were crossed with respect to each other and together with the Wollaston prism were aligned to give interference fringes parallel to the carbon target. A partially silvered glass slide was used to direct a small percentage of the Nitrogen laser probe beam to the Refractive Fringe TV camera.

The recording and digitization (Oculus 200 real time frame grabber) of the resultant images on the TV cameras were synchronised with the firing of the ruby laser. The spatial resolution of the images is limited by the imaging system to approximately 3.5 μm.

2.4 Results

Two Nomarski interferograms and their corresponding RFD defocused shadowgraphs of the LPP, probed at 30 ± 10 ns after the start of the Ruby heating pulse, are shown in figure 2.7 and figure 2.8.

Three-dimensional representations of the electron density profiles of the LPP, evaluated from the Nomarski interferograms of figure 2.7(a) and figure 2.8(a), are shown in figure 2.9 and figure 2.10, respectively. The electron densities were evaluated at different inversion lines traversing the plasma and parallel to the target face.

A comparison between the electron densities, on the ruby laser axis, evaluated from the defocused shadowgraphs of the RFD and the corresponding electron densities evaluated from the Nomarski interferograms (from figure 2.9 and figure 2.10), are given in figure 2.11 and figure 2.12. An agreement of within an order of magnitude between the two diagnostics is obtained.

2.5 Discussion

From the Nomarski interferograms shown in figure 2.7(a) and figure 2.8(a), it is evident that the plasma is not spherically symmetric but symmetric about the axis of the ruby laser pulse. The electron densities were thus evaluated at different distances from the target along inversion lines perpendicular to the ruby laser axis.

The Nomarski interferometry errors shown in figure 2.11 and figure 2.12

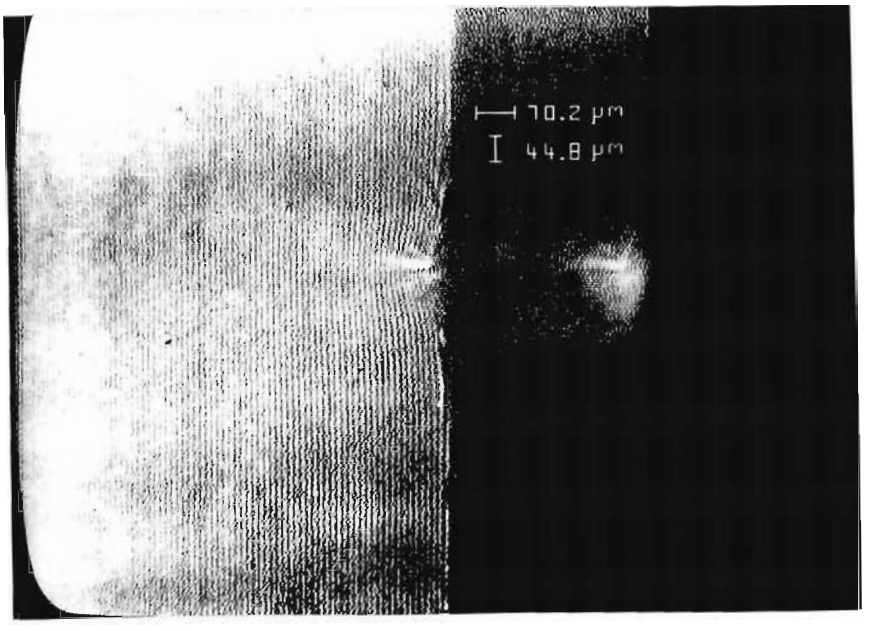

a)

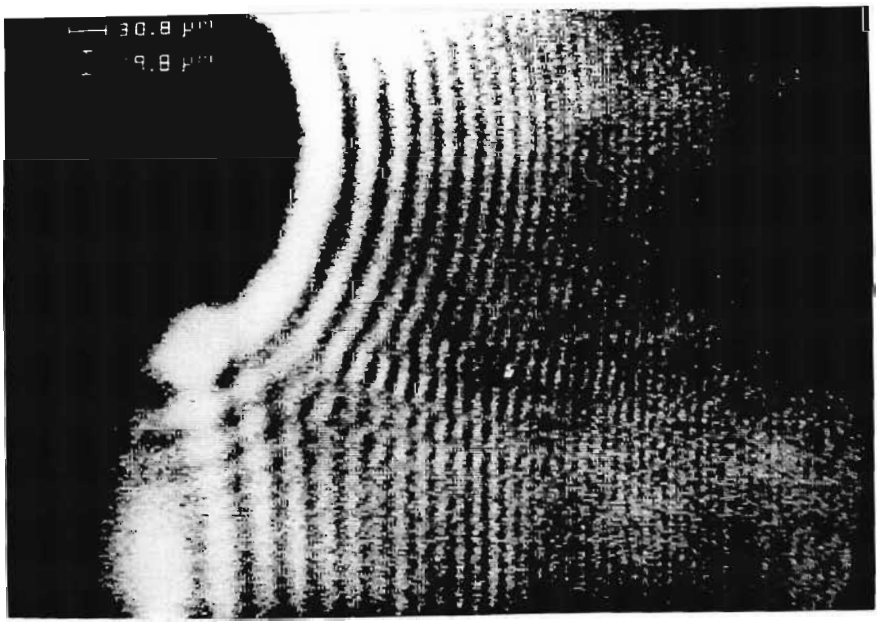

b)

Figure 2.7: (a) A Nomarski interferogram of a LPP at irradiance $3.5 \times 10^{11}\ Wcm^{-2}$. (b) Corresponding RFD defocused shadowgraph.

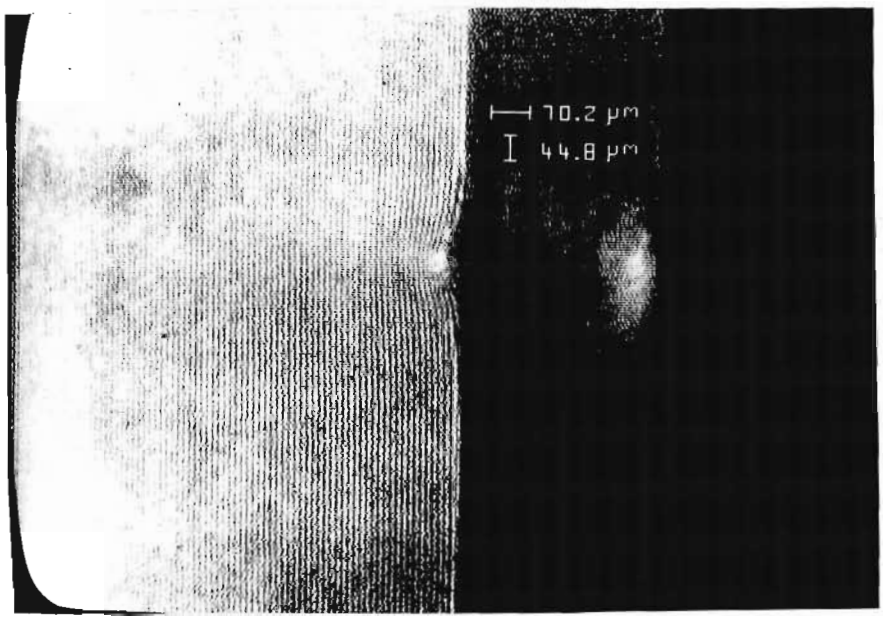

a)

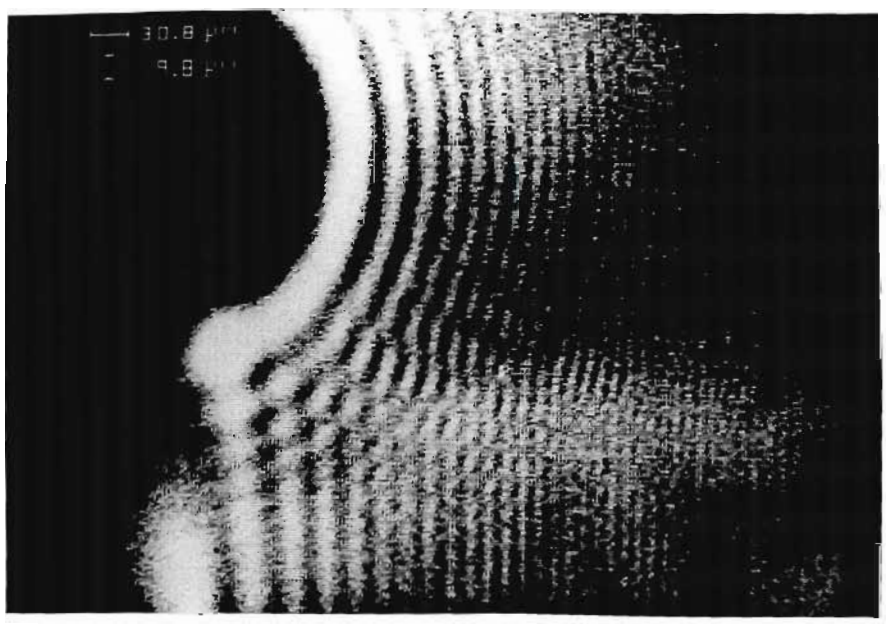

b)

Figure 2.8: (a) A Nomarski interferogram of a LPP at irradiance $4.8 \times 10^{11}\ Wcm^{-2}$. (b) Corresponding RFD defocused shadowgraph.

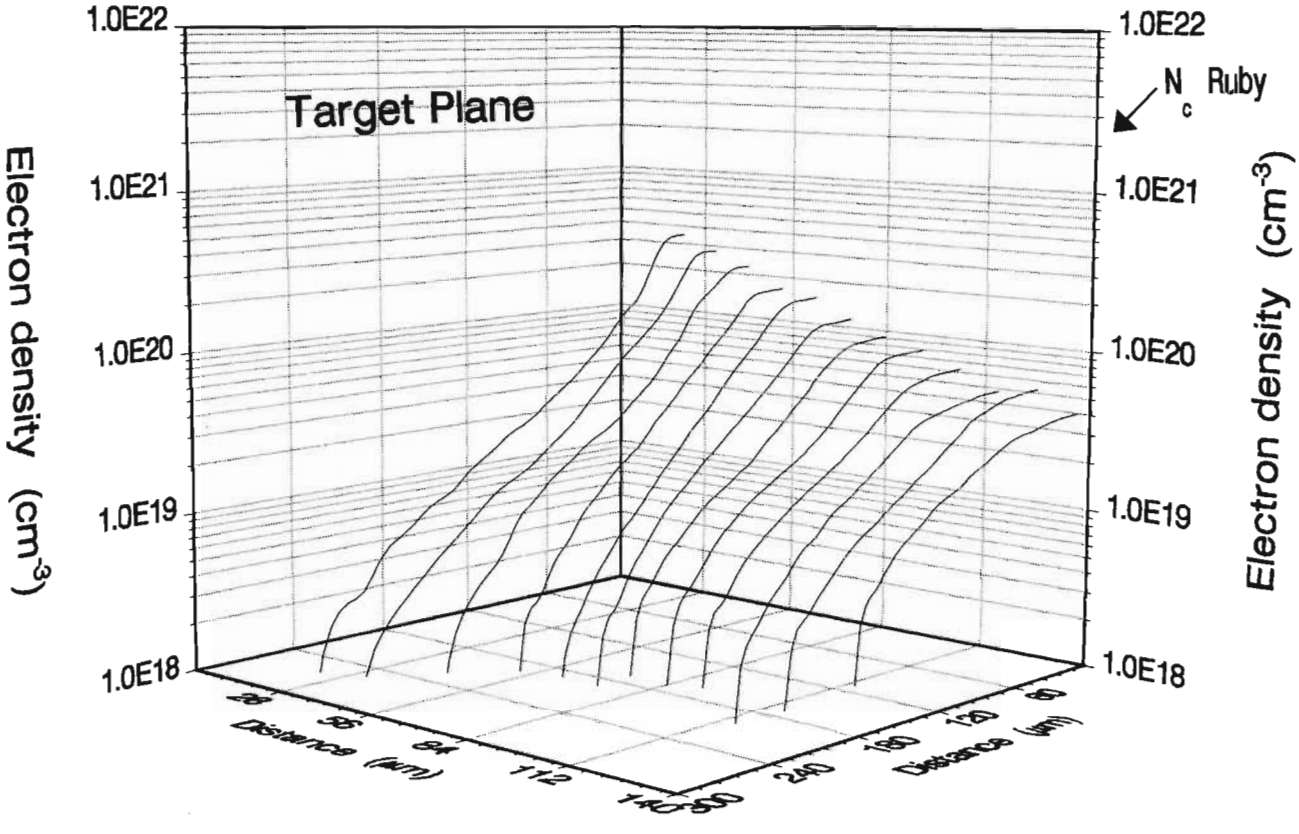

Figure 2.9: 3-D Electron density profile evaluated from the Nomarski interferogram of figure 2.7(a).

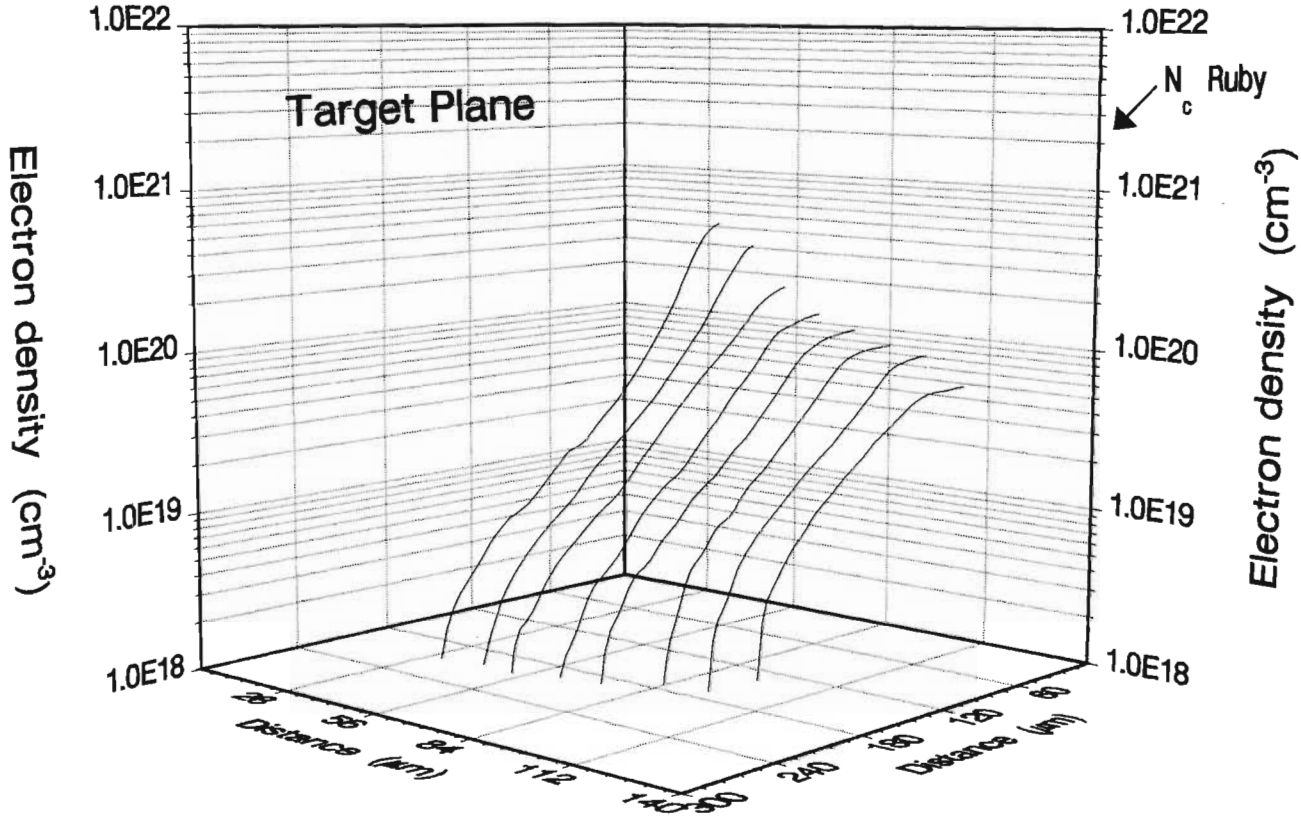

Figure 2.10: 3-D Electron density profile evaluated from the Nomarski interferogram of figure 2.8(a).

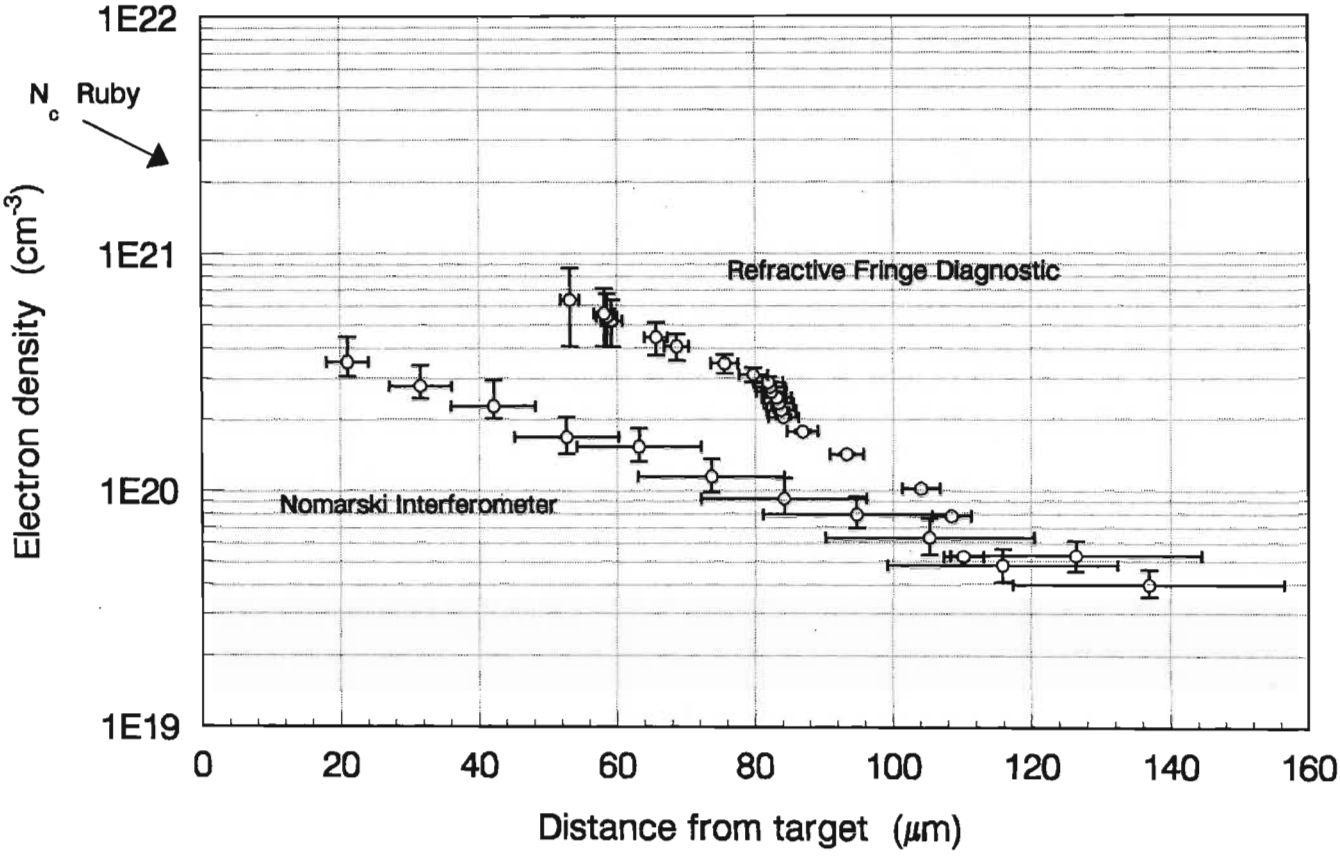

Figure 2.11: Comparison between the electron density profile, evaluated on the ruby laser axis, from the RFD defocused shadowgraph and the Nomarski interferogram of figure 2.7.

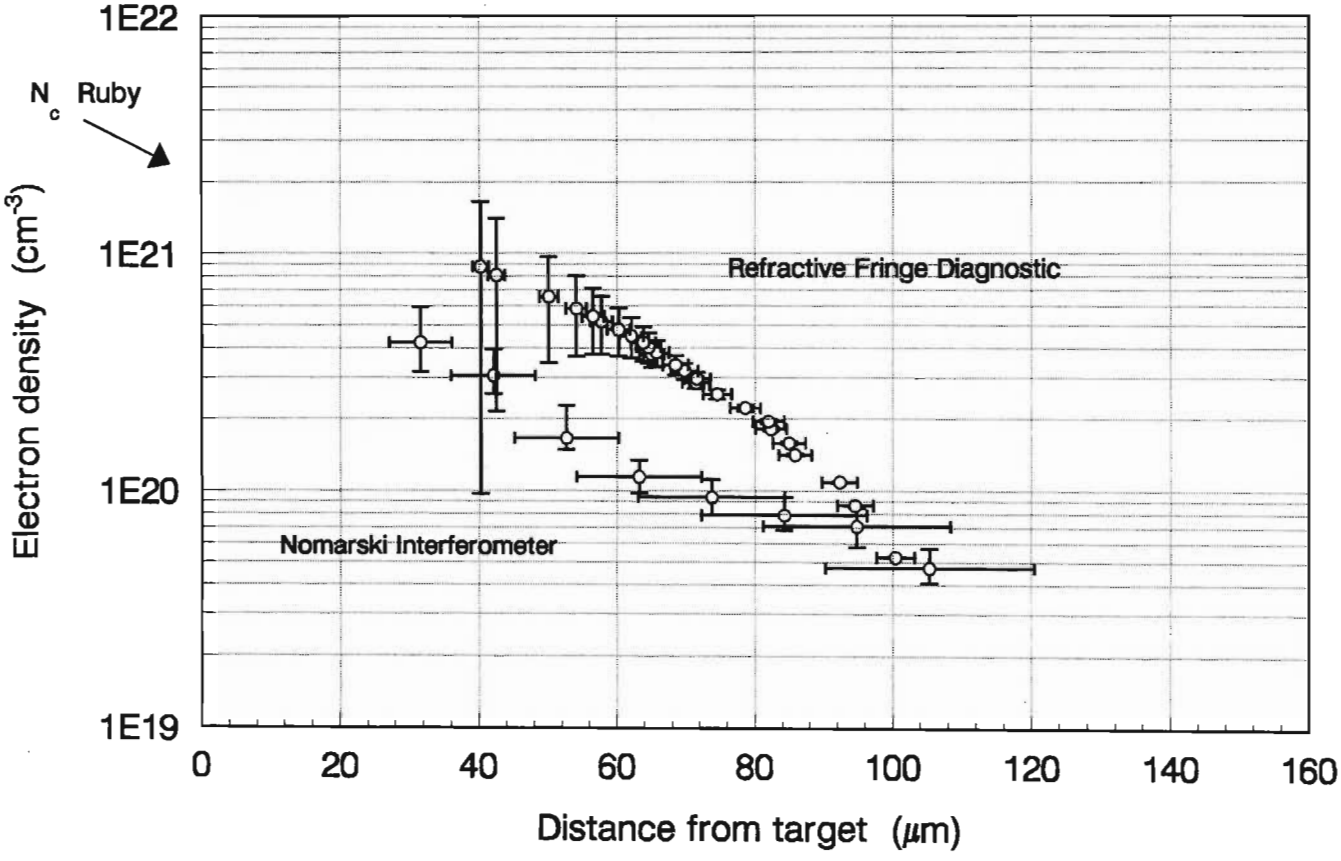

Figure 2.12: Comparison between the electron density profile, evaluated on the ruby laser axis, from the RFD defocused shadowgraph and the Nomarski interferogram of figure 2.8.

were due to the uncertainties in the change in OPL data extracted from the Nomarski interferograms. The uncertainties were due to the limited spatial resolution of the interferograms. The error region increases as one approaches the boundary of the plasma due to the increase in the error in measuring the fringe shifts from the interferograms. These errors do not take into account possible errors in the Abel inverted electron densities due to refraction of the laser probe beam in the plasma. Sweeney *et al.* [Sweeney *et al.* (1976)], using raytracing techniques on mathematically modelled LPP with similar density scale lengths as those found in figure 2.11 and figure 2.12, have shown that large errors exist in the Abel inverted electron densities in regions of high electron densities where considerable refraction of the probe beam occurs. In these regions, the Abel inverted electron densities are appreciably lower than the actual electron densities, especially if a frequency doubled probe beam is used rather than a shorter wavelength probe beam. The errors in the electron densities, for the Nomarski interferometer shown in figure 2.11 and figure 2.12, are thus possibly greater than shown for these regions.

In the RFD the electron densities close to the target are given by the fringes furthest from the caustic region (the black semi-circular region on the RFD defocused shadowgraphs). Due to the limited spatial resolution of the RFD defocused shadowgraphs, the errors in determining the fringe separations increase with decreasing fringe widths. The errors in the resultant electron density profiles thus increase as one approaches the target, as is evident from figure 2.11 and figure 2.12.

Bearing in mind that the Nomarski interferometry electron densities in figure 2.11 and figure 2.12 do not take into account the errors due to refraction of the probe beam in the plasma, an agreement between the two diagnostics of within an order of magnitude is obtained. The electron densities evaluated from the RFD are higher than those obtained by Nomarski interferometry.

Better agreement between the two diagnostics is obtained in the regions of lower electron density.

The discrepancy between these results can be attributed to non-parabolic paths of the probe beam in the LPP and the asymmetry of the LPP.

The path of two light rays propagating through a LPP, for different impact parameters, p_i, are shown in figure 2.13. The dashed line represents the assumed parabolic ray path in the plasma and the triangular region, enclosing this dashed line, is the probable ray path region. This region is smaller for rays with larger impact parameters than it is for rays with smaller impact parameters. One would then expect the errors, due to the parabolic path assumption, to be larger for smaller impact parameters than larger impact parameters. This is consistent with the experimental results in figure 2.11 and figure 2.12 where the electron density errors decrease with increasing distance from the target.

Benattar and Popovics [Benattar and Popovics (1983)] mathematically modelled a LPP by:

$$N_e = AN_c e^{-B\frac{r}{R_0}} \ cm^{-3}, \tag{2.46}$$

where $A = 0.0845$, $B = 5.45$ and $N_c = 9 \times 10^{21} \ cm^{-3}$ ($\lambda = 0.35 \ \mu m$), and found that the electron density errors, due the assumption of parabolic ray paths in the plasma increased, with increasing electron density. They concluded that the parabolic ray path assumption in the LPP was invalid. The results in figure 2.12 are normalised ($\frac{r}{R_0}$ where $R_0 = 200 \ \mu m$) and compared to the prediction of Benattar and Popovics in figure 2.14. The predicted and the experimental results compare favourably.

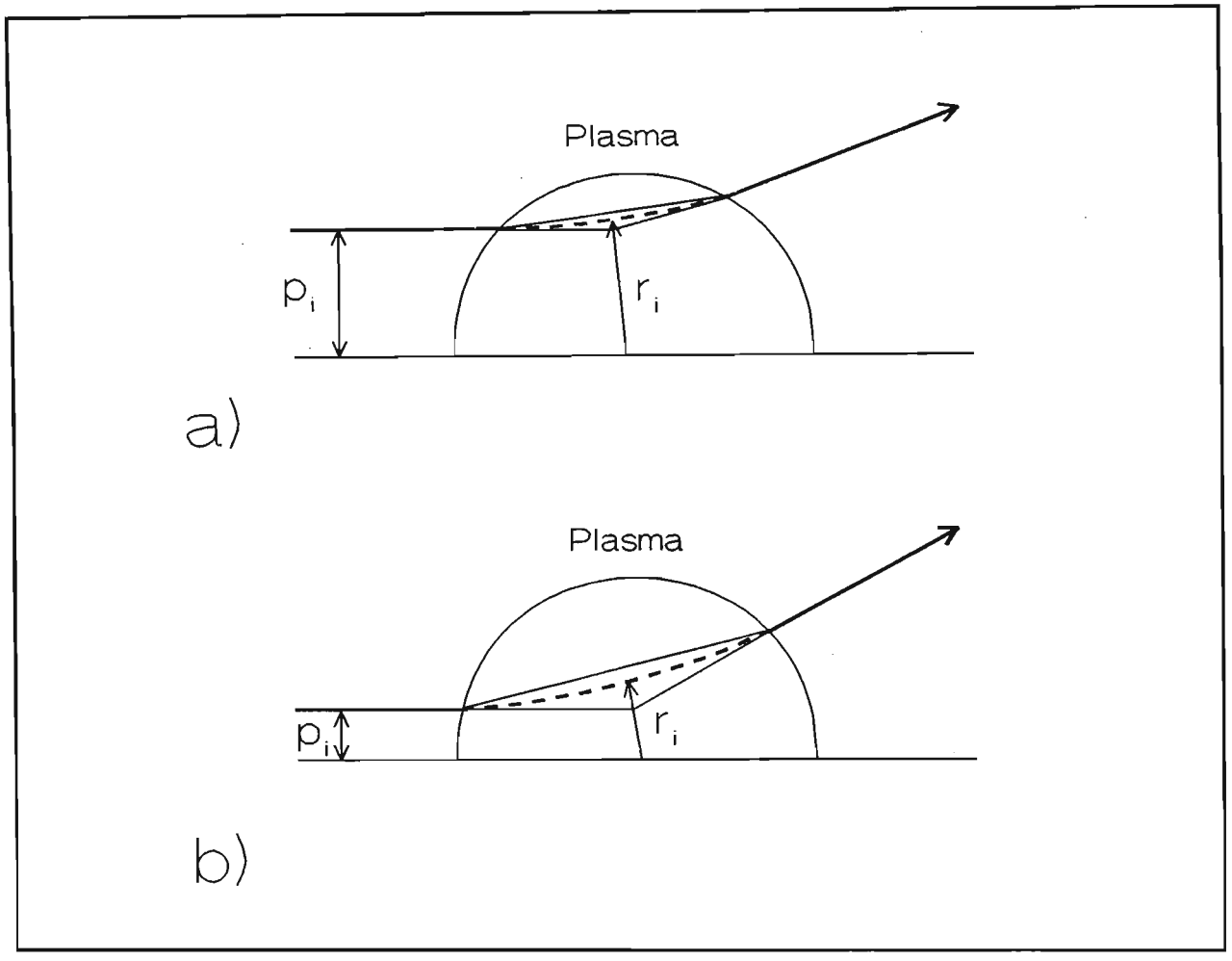

Figure 2.13: The path of two light rays propagating through a LPP for different impact parameters (p_i) a) large impact parameter b) small impact parameter.

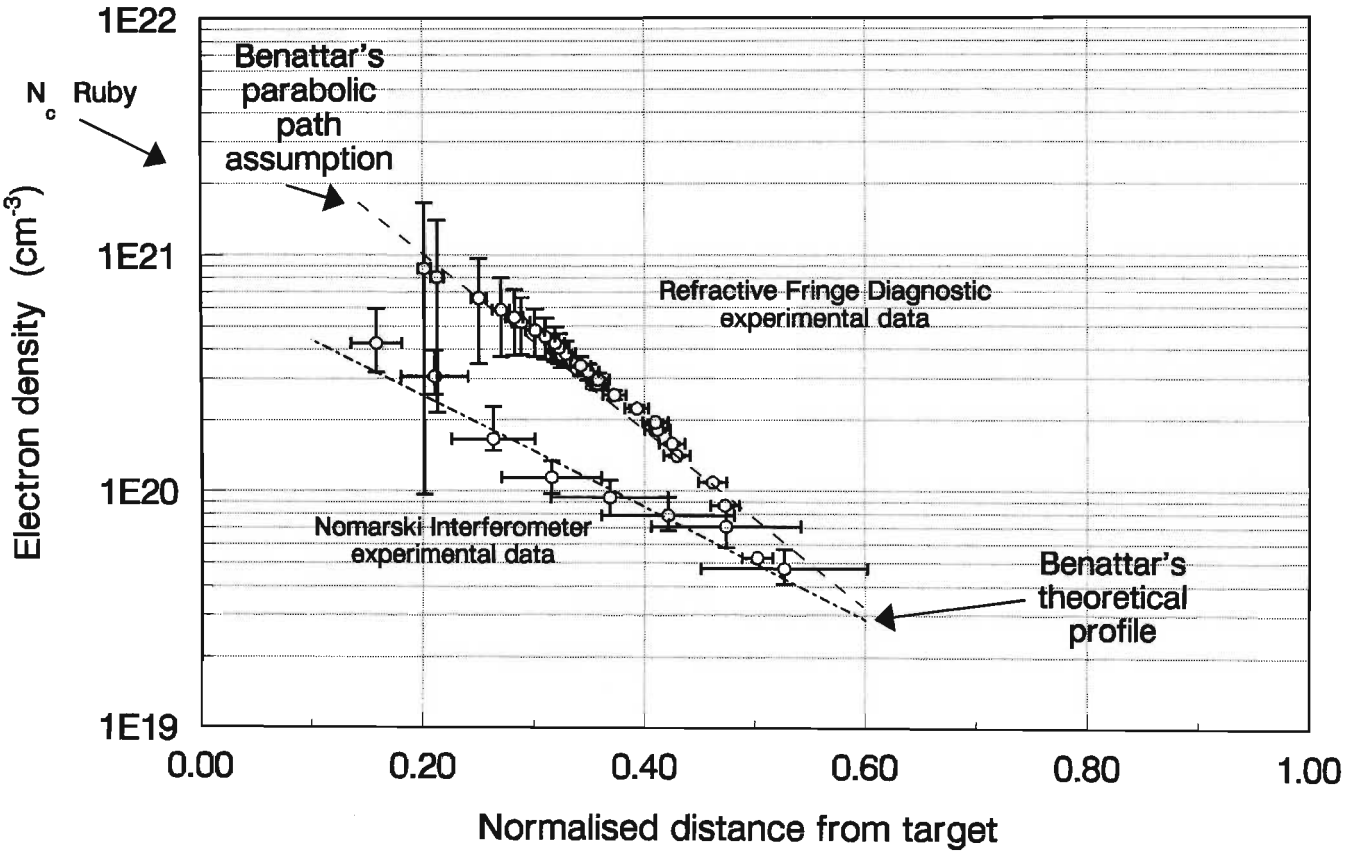

Figure 2.14: Comparison between the experimental data and the prediction of Benattar and Popovics.

The deviation from the assumed symmetry in the derivation of the formulae of the RFD, will result in errors in the RFD electron densities. From figure 2.7(b) and figure 2.8(b), it is clear that the caustic region (the black semi-circular region) is not perfectly circular. These errors are difficult to quantify.

From equation 2.5, the critical electron density for $\lambda = 337\ nm$ is $9.8 \times 10^{21}\ cm^{-3}$. This is considerably less than the maximum electron density probed, i.e. $N_e \simeq 1 \times 10^{21}\ cm^{-3}$. The use of equation 2.6 is thus valid.

From figure 2.11, the electron density gradient is approximately $10^{24}\ cm^{-4}$. From equation 2.45, for $N_c = 9.8 \times 10^{21}\ cm^{-3}$ and $N_e = 10^{21}\ cm^{-3}$, the measured gradient must be much less than $2.6 \times 10^{26}\ cm^{-4}$. Ray optical analysis was thus justified in this investigation.

2.6 Numerical Simulation

The experimental investigation has shown that there is a discrepancy between the electron densities determined by the Nomarski interferometer and those determined by RFD. It is suggested that the parabolic ray path assumption, in the LPP, was the main contributing factor for the discrepancy. In the comparison it was assumed that the Nomarski interferometer electron density measurements were accurate. To clarify the contributing factors for the discrepancy, a numerical raytrace through a mathematically modelled spherical LPP was performed and refractive fringes were generated for different object plane distances (L). From these theoretically generated fringes, the RFD was used to determine the electron density profile of the mathematically modelled LPP.

The numerical investigation, in this section, is the extension of the work of Campbell [Campbell (1985)]. Campbell numerically accessed the accuracy of the revised RFD. However, an important factor was overlooked in his investigation, i.e. the effect of the object plane distance on the accuracy of the RFD.

2.6.1 Numerical Raytrace

The LPP is assumed to be spherically symmetric and a slice through the LPP is shown in figure 2.15.

The optical path length of a light ray through a plasma slice is given by:

$$OPL = \int_A^B n(x,y)\, ds. \tag{2.47}$$

From figure 2.15, it is clear that:

$$ds^2 = dx^2 + dy^2. \tag{2.48}$$

Since:

$$y = f(x), \tag{2.49}$$

and:

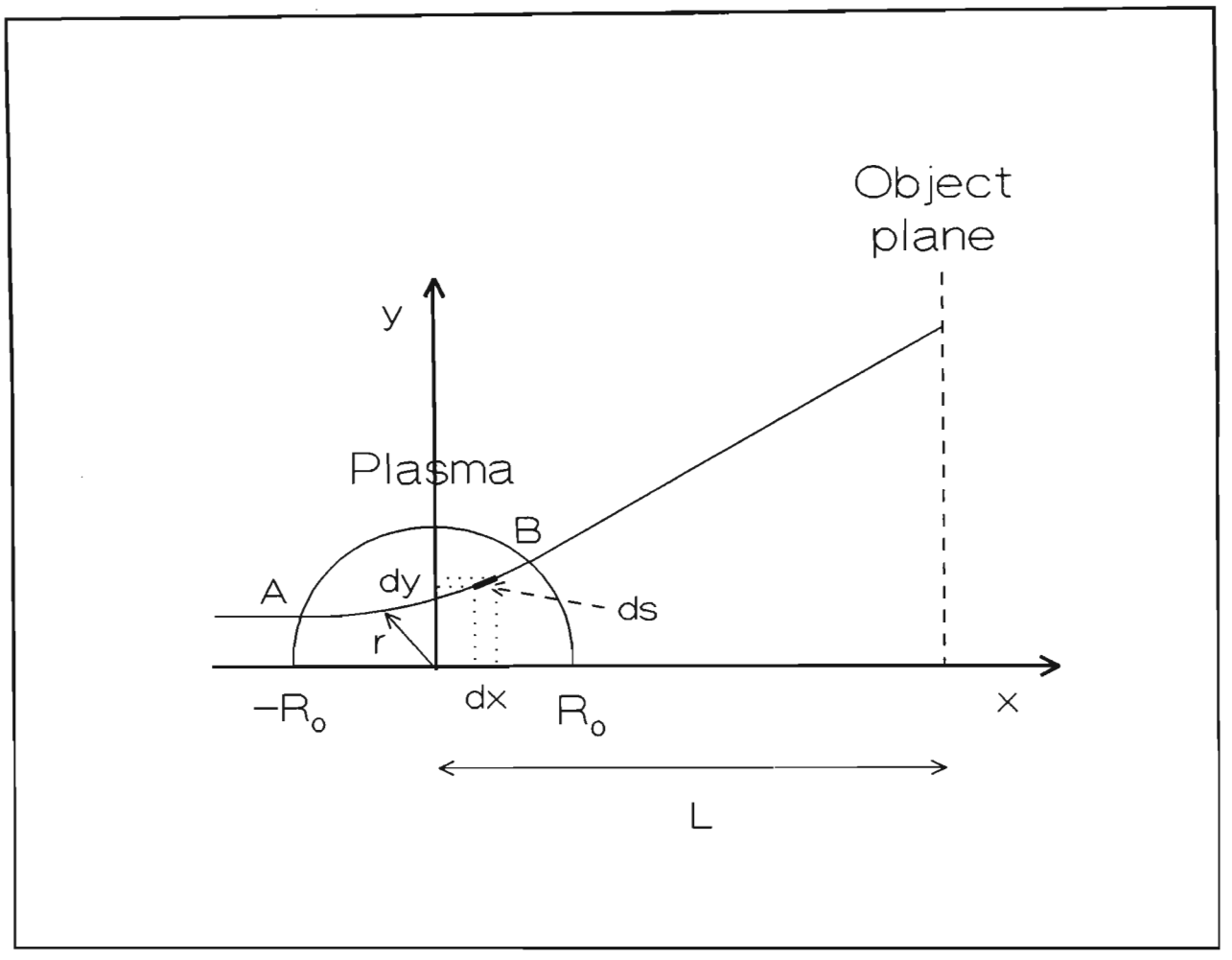

Figure 2.15: A light ray traversing a plasma slice.

$$\frac{dy}{dx} \equiv \dot{y}, \tag{2.50}$$

then:

$$dy = \dot{y}dx, \tag{2.51}$$

and thus equation 2.48 can be expressed as:

$$ds = \sqrt{1 + \dot{y}^2}dx. \tag{2.52}$$

Substituting equation 2.52 into equation 2.47, the OPL of the light ray through the LPP is given by:

$$OPL = \int_A^B n(x,y)\sqrt{1 + \dot{y}^2}\, dx, \tag{2.53}$$

where it is now understood that A and B denote the x values at points A and B.

Fermat's principle states that a light ray will traverse a phase object through the shortest possible route, i.e.:

$$\delta \int_A^B n(x,y)\sqrt{1 + \dot{y}^2}\, dx = 0. \tag{2.54}$$

Solving equation 2.54 by Euler's equation:

$$\frac{d}{dx}\frac{\delta l}{\delta \dot{y}} - \frac{\delta l}{\delta y} = 0, \tag{2.55}$$

where:

$$l = l(x, y, \dot{y}) = n(x, y)\sqrt{1 + \dot{y}^2}, \tag{2.56}$$

one finds that:

$$\ddot{y} + \dot{y}(1 + \dot{y}^2)\frac{1}{n(x, y)}\frac{\delta n(x, y)}{\delta x} - (1 + \dot{y}^2)\frac{1}{n(x, y)}\frac{\delta n(x, y)}{\delta y} = 0. \tag{2.57}$$

Performing order reduction on equation 2.57 by setting $y_1 = y$ and $y_2 = \dot{y_1}$:

$$\dot{y_2} = (1 + y_2^2)\frac{1}{n(x, y)}\frac{\delta n(x, y)}{\delta y} - y_2(1 + y_2^2)\frac{1}{n(x, y)}\frac{\delta n(x, y)}{\delta x}. \tag{2.58}$$

Modelling the refractive index field by:

$$n(x, y) = \sqrt{1 - ae^{\frac{-br}{R_0}}}, \tag{2.59}$$

where $a = 11.115$, $b = 13.816$ and $R_0 = 59\ \mu m$, equation 2.58 can be expressed as:

$$y_2 = \frac{abe^{\frac{-br}{R_0}}}{2n^2(x,y)R_0 r}(1+y_2^2)(y_1 - y_2 x). \tag{2.60}$$

Equation 2.60 governs the path of the light ray in the plasma and can be solved using the 4^{th} order Runge-Kutta numerical technique.

2.6.2 Results and Discussion

A numerical raytrace through the mathematically modelled plasma, for different impact parameters, p, is given in figure 2.16. A similar raytrace, covering a larger distance from the LPP, is given in figure 2.17. From these figures the formation of the caustic region is evident. The caustic region is the region, after the LPP, out of which all the rays have been refracted. This region is the dark semi-circular region in figure 2.7(b) and figure 2.8(b). With increasing distance from the plasma centre, L, the height of the caustic region approaches the effective plasma radius ($R_0 = 59\ \mu m$). This radius is reached at $L \simeq 30\ mm$. One would expect the error in R_0, due to the incorrect location of the object plane, to have an effect on the accuracy of the RFD. If the refractive fringe plane imaged is within the caustic region of the LPP, interference between refracted light rays will also affect the accuracy of the RFD.

From figure 2.16 and figure 2.17 it is clear that the light rays, with small impact parameters, are refracted the most. If these light rays are refracted outside the field of view of the imaging system of the RFD, information regarding the electron densities close to the target will be lost. For a finite aperture size, this loss increases with increasing object distance.

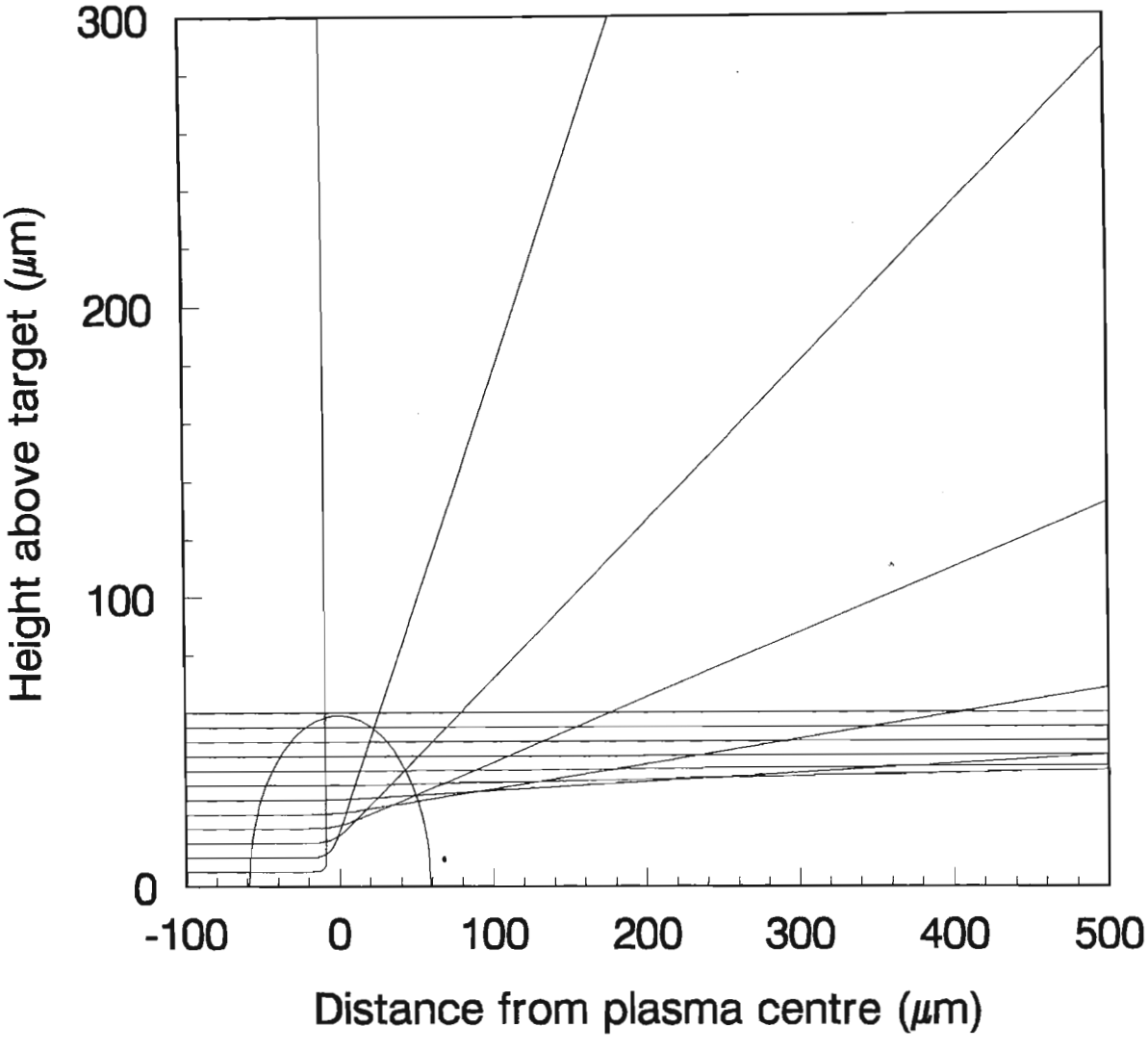

Figure 2.16: A numerical raytrace through the mathematically modelled LPP for a distance up to 500 μm from the LPP centre.

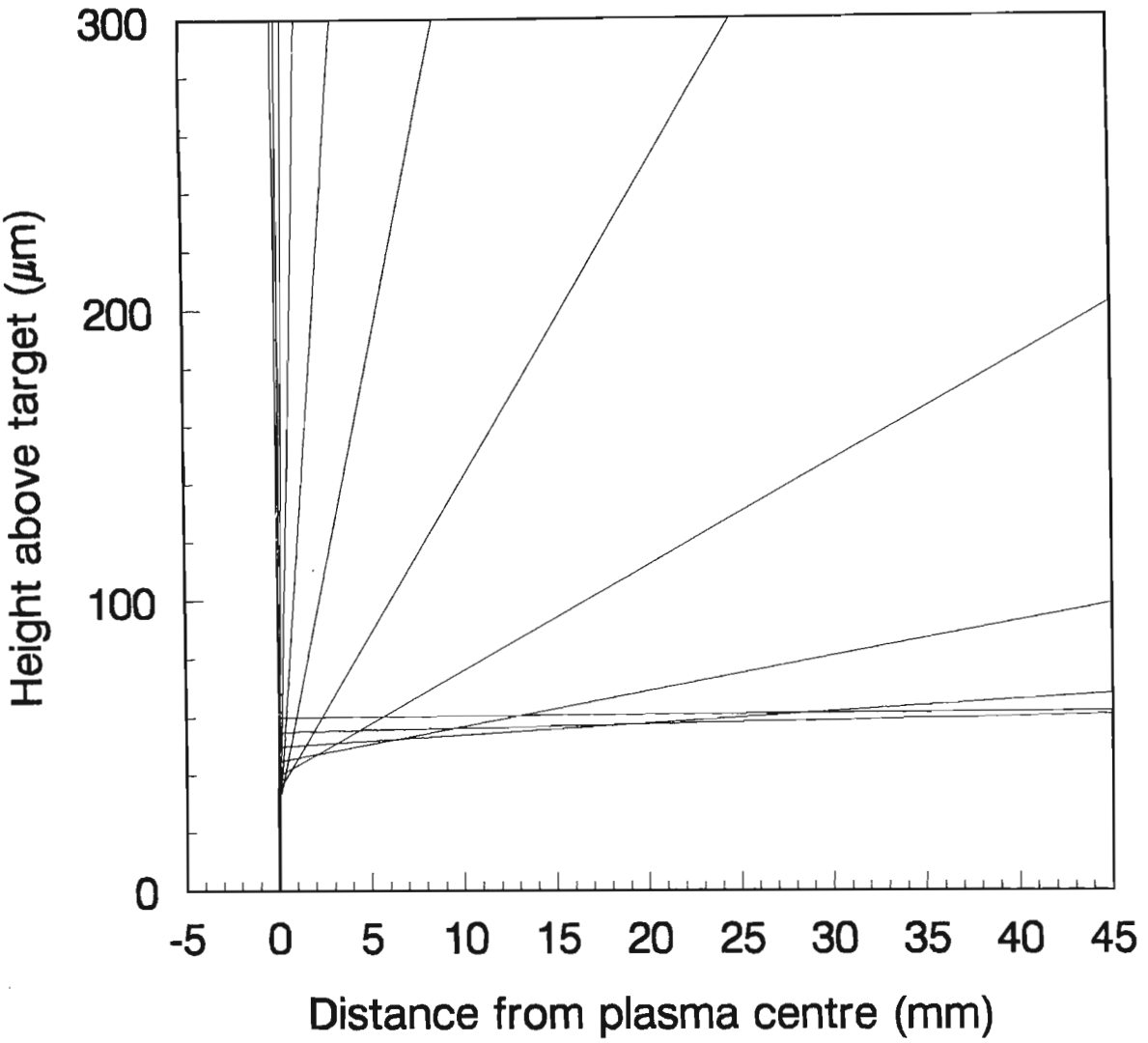

Figure 2.17: A numerical raytrace through the mathematically modelled LPP for a distance up to 45 *mm* from the LPP centre.

The RFD, in calculating the refraction angle, α, makes the assumption that the wavefront is planar at the object plane. To access the accuracy of this assumption, the shape of the wavefront was numerically determined for different object plane distances. The wavefronts, plotted relative to the object plane, are shown in figure 2.18. The curves in figure 2.18 represent the position of the wavefront when the OPL of the light rays are equal to the object plane distance. A magnified representation of the wavefront at $L = 30\ mm$ is given in figure 2.19. The refractive fringe positions at $L = 30\ mm$ are shown in figure 2.19. These fringes were numerically derived by successively raytracing through the LPP, incrementing p after each raytrace, to determine where constructive and destructive interference occurred on the object plane. Campbell adopted a different approach. The object plane was divided into a number of cells and complex amplitude addition was used to deduce the net relative intensity incident in each cell. The relative intensity distribution was used to deduce the resultant fringe positions. The fringe positions at $L = 500\ \mu m$ were found to be identical for both methods.

As expected, the separation between dark fringes in figure 2.19, is equal to the wavelength of the Nitrogen probe laser ($\lambda = 337\ nm$). However, the separation between the first dark fringe and the caustic region is only half a wavelength. This separation is considered in the RFD calculations that follow.

From figure 2.19, it is evident that the planar wavefront assumption is more accurate between dark fringes furthest from the caustic region. For a particular L, one would thus expect the error in the RFD refraction angle to decrease with increasing dark fringe separation number. From figure 2.18, it is not immediately clear what effect L will have on the refraction angle for a particular dark fringe separation number. One would expect the wavefront curvature, for a particular dark fringe separation, to decrease with increasing

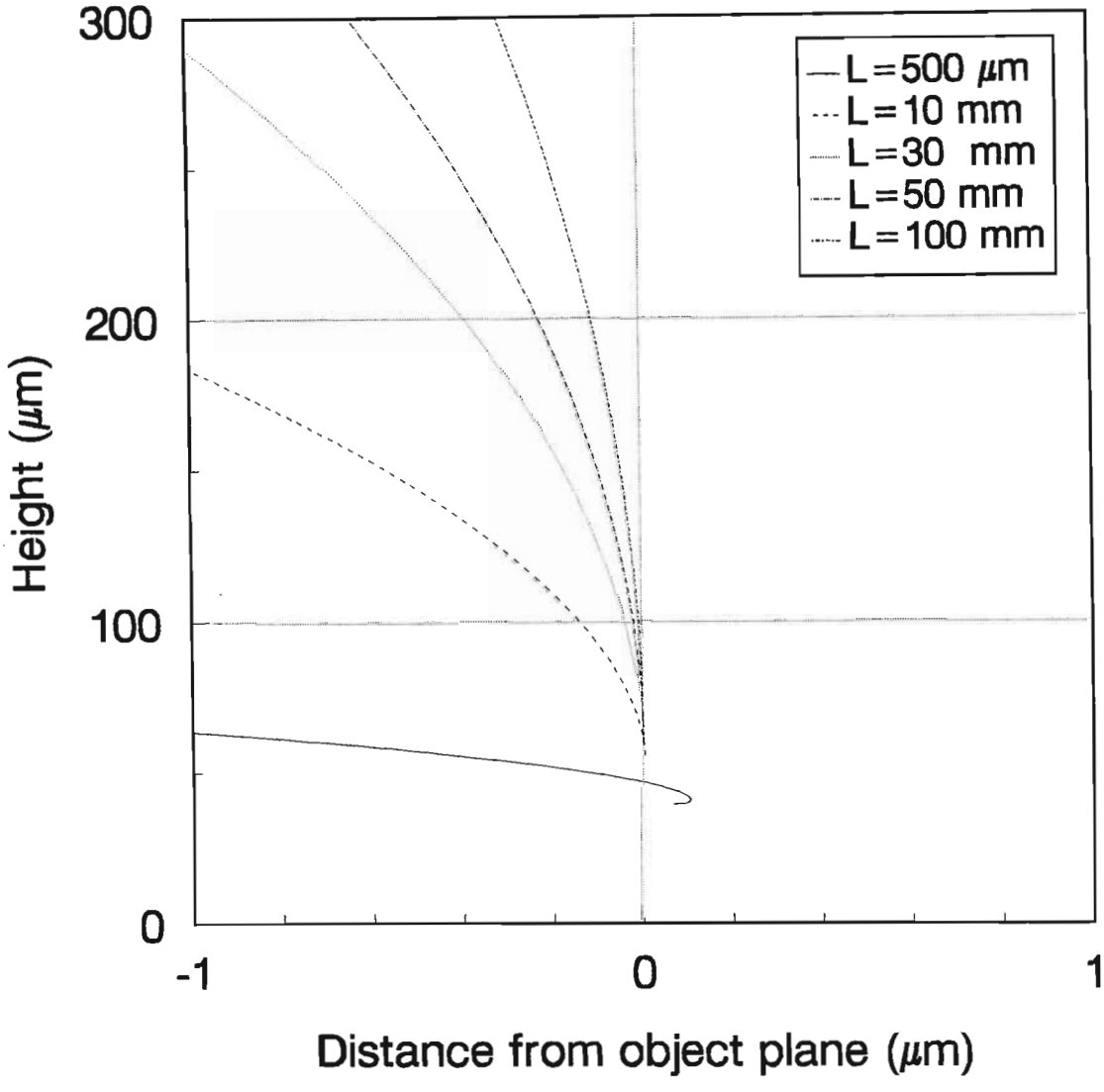

Figure 2.18: The light wavefront shape, relative to the object plane distances (L), for different object plane distances.

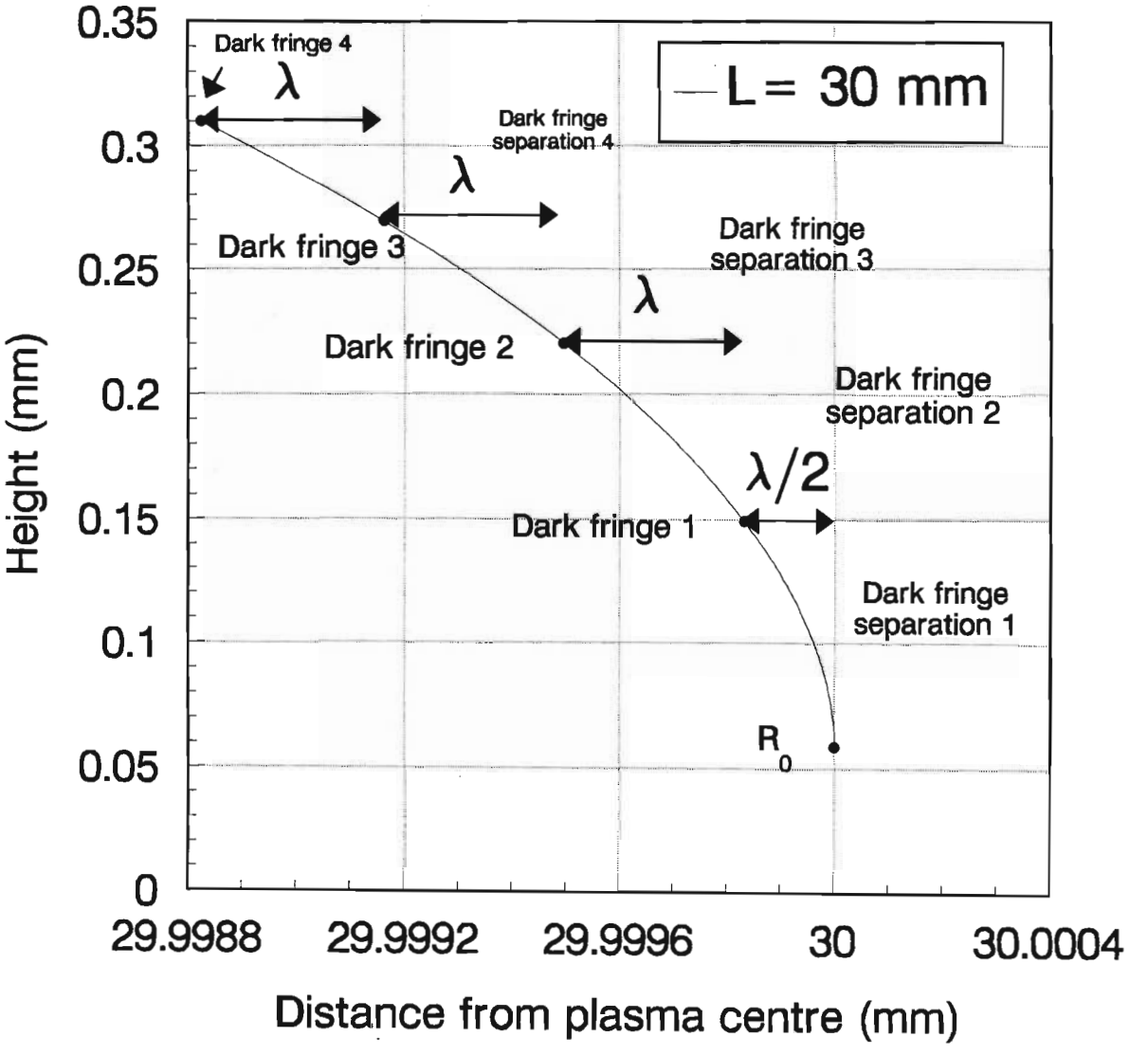

Figure 2.19: A magnified representation of the light wavefront shape at $L = 30\ mm$.

L. The error in the refraction angle, for a particular dark fringe separation, would thus decrease with increasing L. The positive distance values for the wavefronts, in figure 2.18, are due to the object plane being inside the limiting region of the caustic region.

From the numerically deduced refractive fringes for different L, the RFD refraction angles were calculated from equation 2.37. These angles are compared, in figure 2.20, to the numerically deduced refraction angles. As predicted, for a particular L, the errors decrease with increasing dark fringe separation number. For a particular dark fringe separation number, the errors decrease with increasing L, except for the first dark fringe separation. The error in the RFD refraction angle, for the first dark fringe separation, increases with increasing L. This can be attributed to the increase in the separation between the caustic region and the first dark fringe with L, and the subsequent deterioration of the planar wavefront approximation across this region.

The numerically deduced fringe positions were used by the RFD to determine the electron density profile of the mathematically modelled LPP. A comparison between the calculated electron density profile and the theoretical profile, using the numerically determined values of the refraction angle, for different L, is given in figure 2.21. A similar comparison, using the RFD calculated values of the refraction angle, is given in figure 2.22. The effect of the refraction angle error for $L = 30\ mm$, on the calculated electron density profile, is given in figure 2.23. Approximately 30 dark fringes were used in each comparison.

The effect of the object plane location on the accuracy of the RFD is evident in figure 2.21. For $L = 500\ \mu m$ the effective plasma radius is underestimated and the LPP is thought to be smaller than it actually is. The RFD thus

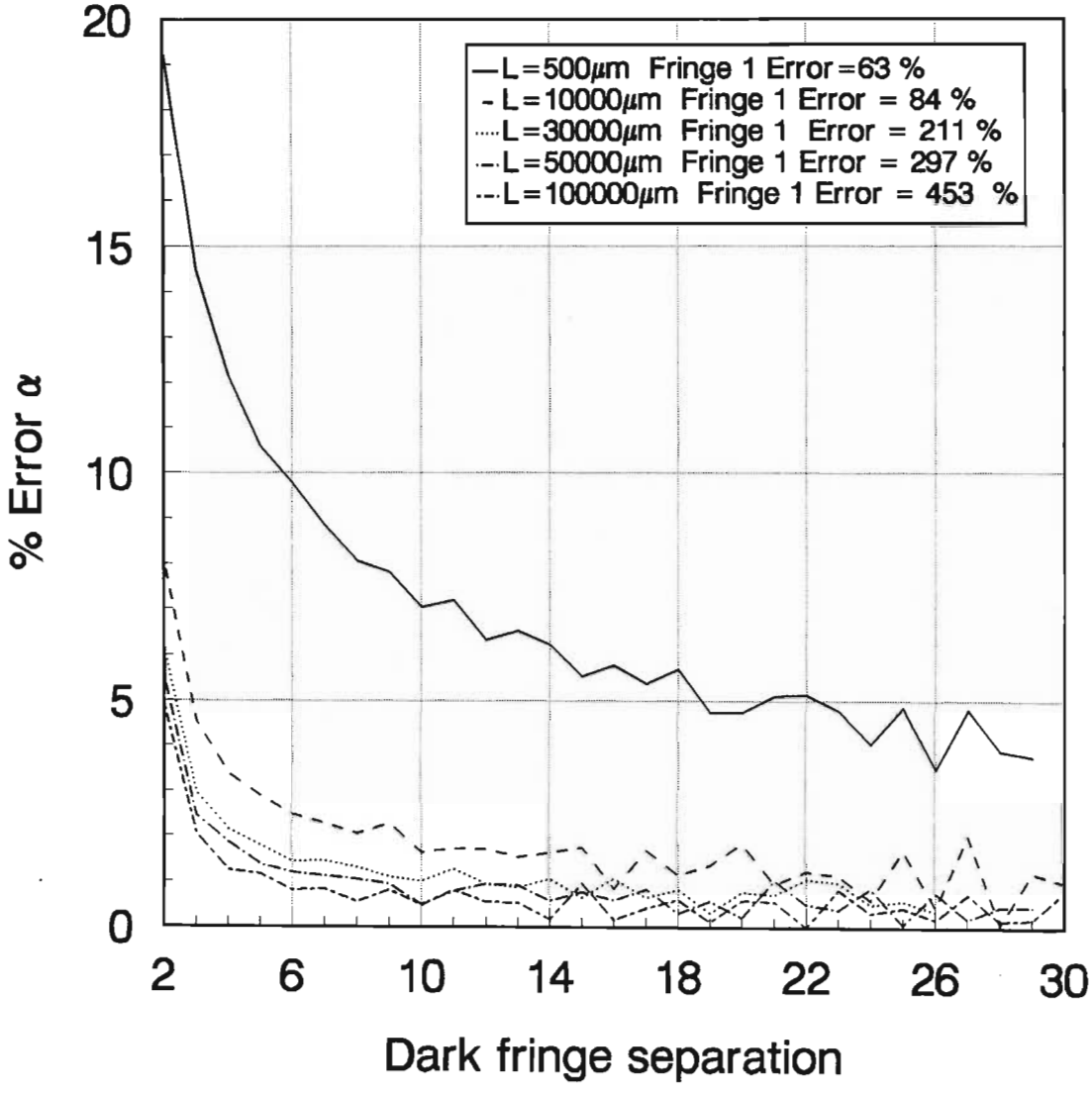

Figure 2.20: The percentage error of the calculated RFD refraction angles relative to the raytraced refraction angles.

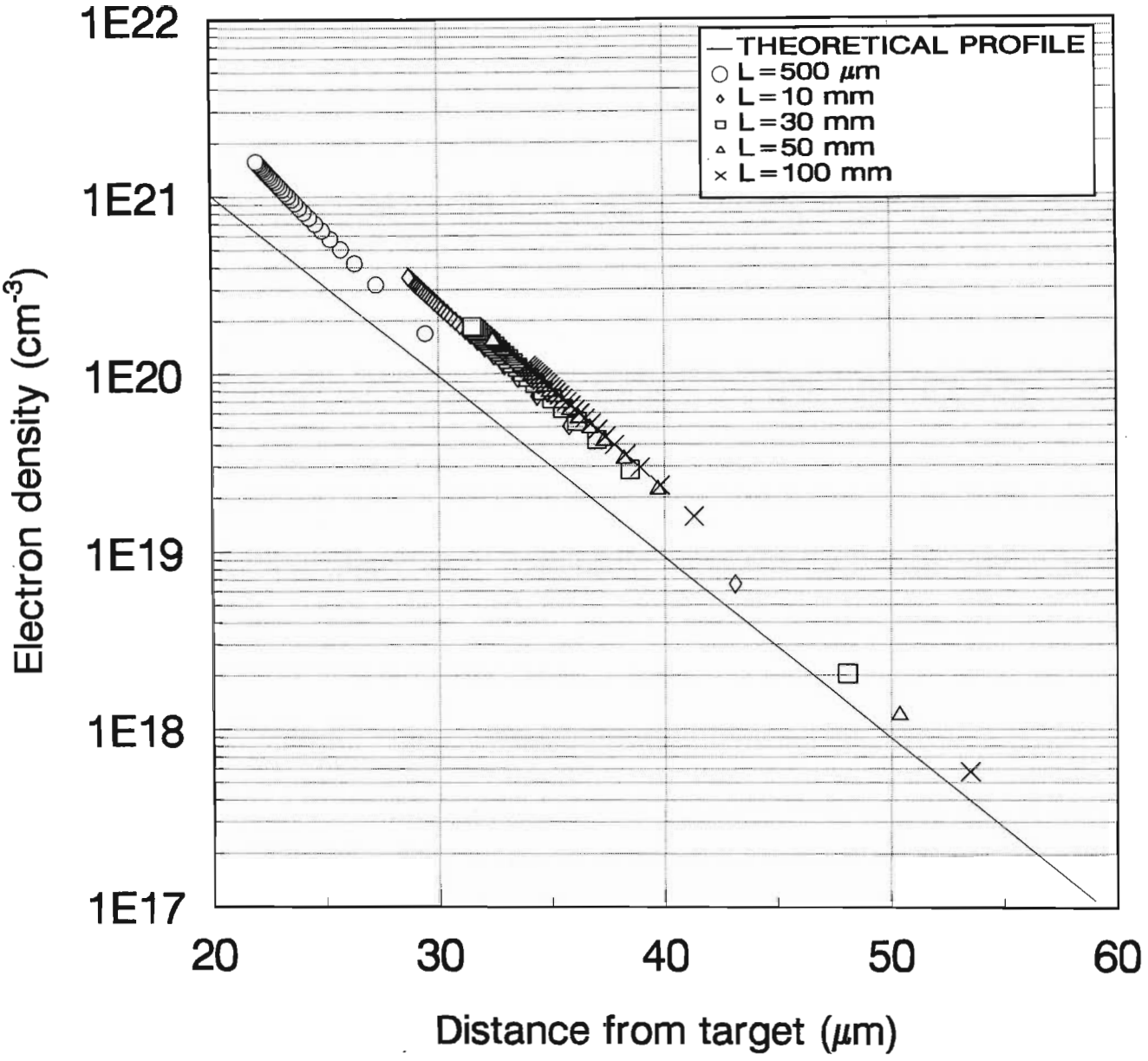

Figure 2.21: A comparison between the calculated electron density profile and the theoretical profile, using the numerically determined values of the refraction angle.

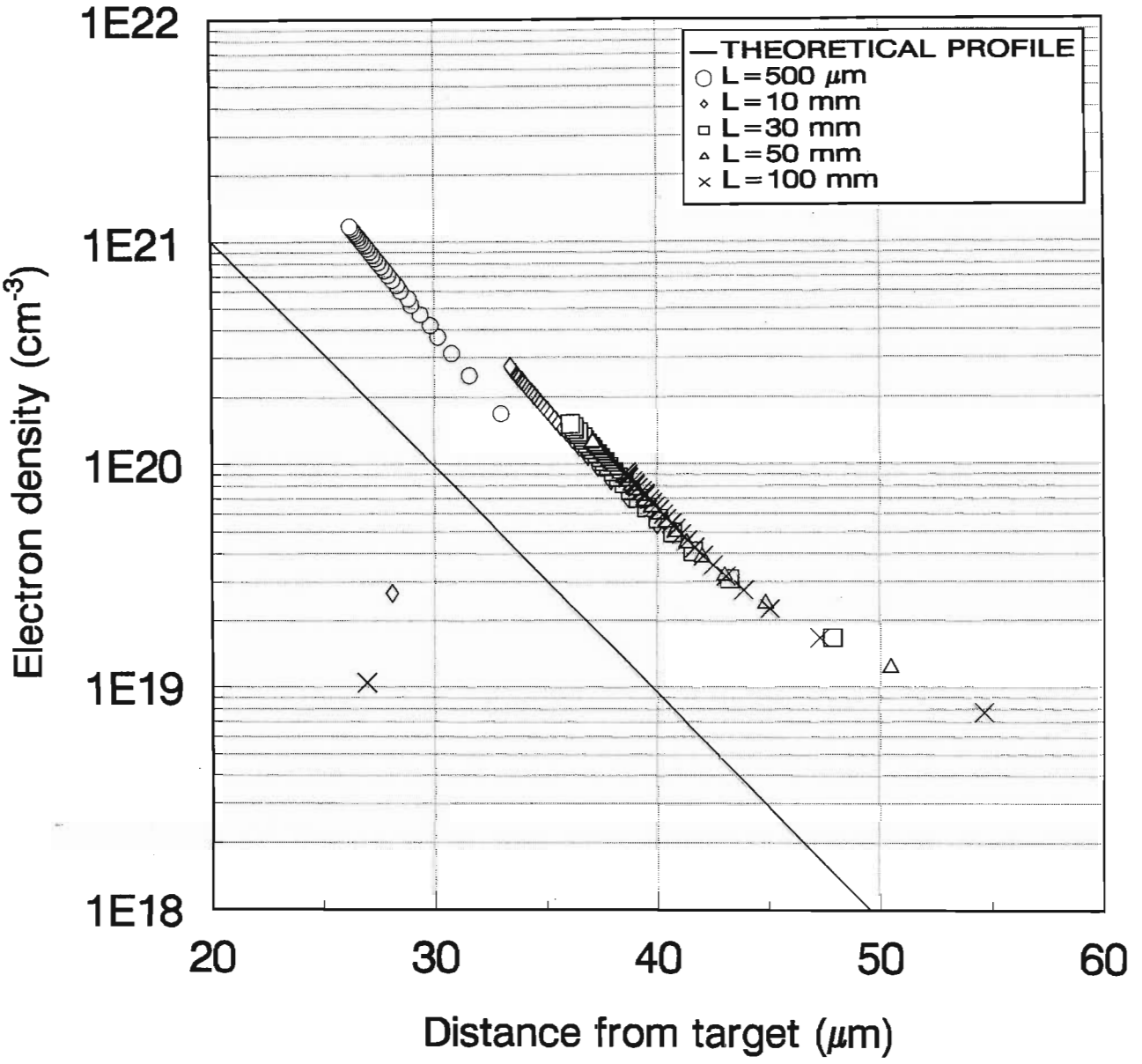

Figure 2.22: A comparison between the calculated electron density profile and the theoretical profile, using the RFD calculated values of the refraction angle.

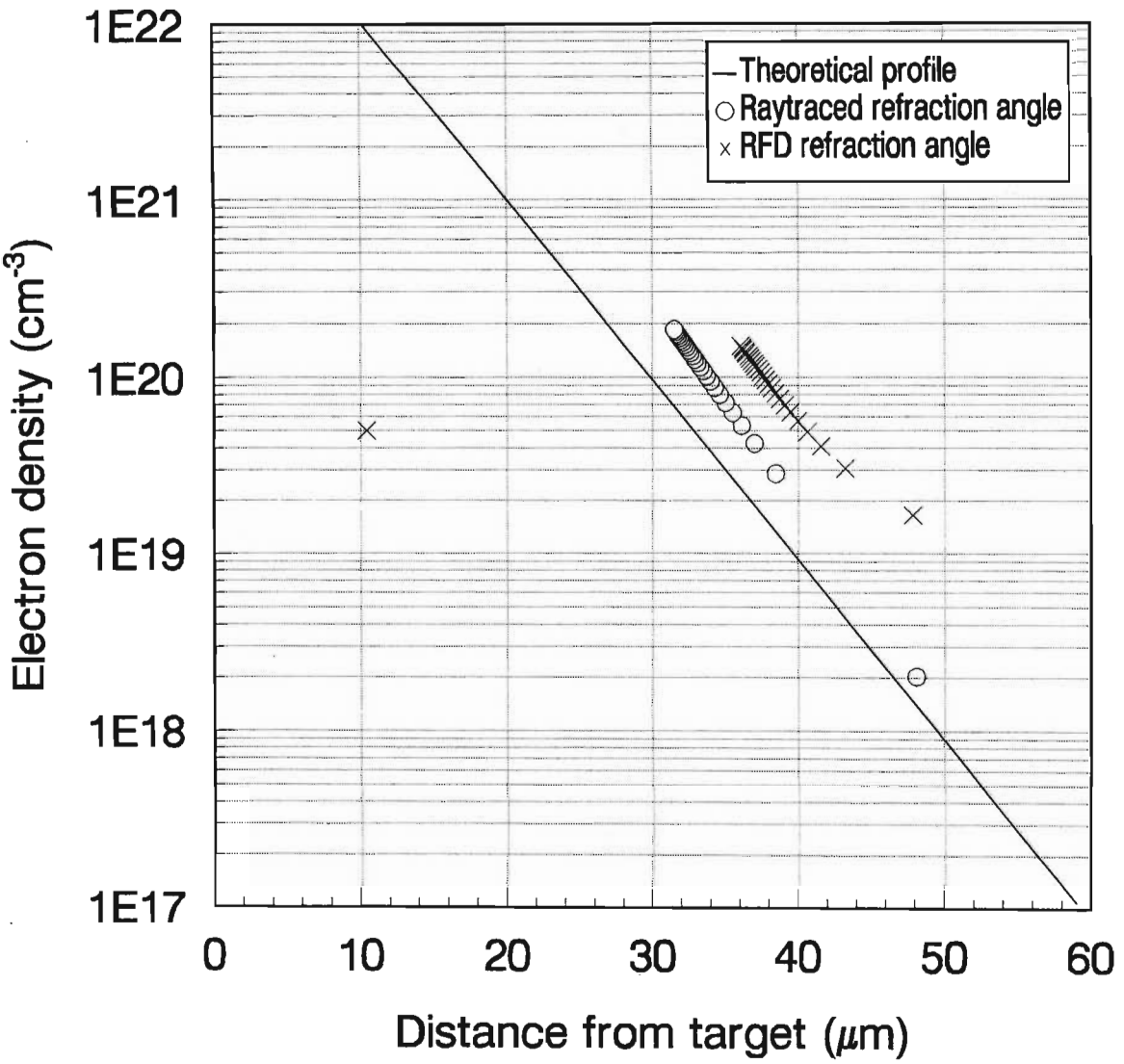

Figure 2.23: The effect of the refraction angle error on the calculated density profile for $L = 30\ mm$.

interprets the refractive fringes to have originated from a region close to the target plane. The increase in L from $L = 500\ \mu m$ to $L = 30\ mm$ has a dramatic effect on the calculated electron density region. With increasing L, the error in the effective plasma radius decreases and the calculated electron density regions span a wider region closer to the plasma boundary. The over-estimation of the effective plasma radius ($L > 30\ mm$) has a minor effect on the accuracy of the RFD. If one extends the electron density profile of $L = 30\ mm$, one finds that the calculated profile crosses the theoretical profile at a distance of 59 μm from the plasma centre, i.e. the effective plasma radius.

From figure 2.21, for $L = 30\ mm$, the effect of the parabolic path assumption of the light rays in the LPP is clearly visible. The error in the electron density increases with increasing distance from the plasma boundary. This implies, as previously mentioned, that the parabolic path assumption is only valid for rays with large impact parameters, i.e. light rays which experience slight refraction.

The addition of the planar wavefront approximation at the object plane, has a significant effect on the accuracy of the RFD. From figure 2.22 and figure 2.23 it is clear that the errors of the RFD electron densities increase, especially in the regions near the plasma boundary. This is due, as previously mentioned, to the increase in the calculated refraction angle error near the plasma boundary. The lone data points in figure 2.22 and figure 2.23 are due to the large errors in the calculated RFD refraction angle of the first dark fringe separation. The theoretical and RFD electron densities differ by approximately an order of magnitude.

Throughout the numerical investigation, the LPP was assumed to be spherically symmetric. The effect of non-spherical symmetry, on the accuracy of

the RFD, was not investigated.

Campbell, in his numerical investigation of the accuracy of the revised RFD, predicted that the location of the object plane would have an effect on R_0 and the calculated α. These, in turn, would affect the accuracy of the RFD. However, his comparison was performed for $L = 500\ \mu m$; a region where the errors in R_0 and α are large.

If one compares the experimental results of figure 2.11 and figure 2.12 with the numerical comparison of figure 2.22, it appears that the experimental results resemble the numerical results where the object plane is within the limiting region of the caustic region, i.e. $L = 500\ \mu m$. This is highlighted by the fact that the last fringe shift, in figure 2.8(a), is detectable 200 μm from the target implying $R_0 \simeq 200\ \mu m$. The effective plasma radius, from figure 2.8(b), is only 166 μm. The experimental comparison was thus performed in a region where the errors in R_0 and α are large and these errors greatly affect the accuracy of the RFD. However, following the trend shown in figure 2.22, the effect of the underestimation of the effective plasma radius would not significantly change the conclusion of the experimental investigation, i.e. the two diagnostics agree within an order of magnitude.

To determine the correct object plane distance, the technique suggested by Campbell must be used. The LPP must be simultaneously imaged, at different planes, to determine the limiting region of the caustic region. At this point the radius of the caustic region will be equal to the effective plasma radius.

A limitation on the applicability of the RFD exists. The RFD can only be used for LPP with monotonically decreasing electron densities. The RFD will not be able to accurately interpret the electron density profiles of LPP,

produced with target irradiances of the order of $10^{15}\ Wcm^{-2}$, where electron density profile steepening occurs due to radiation-pressure effects [Attwood *et al.* (1978)].

2.7 Conclusion

The RFD, in determining the electron density profiles of LPP, was found to over-estimate the electron densities by an order of magnitude. The position of the object plane was found to be vital in order to minimise the RFD errors. The assumptions made by the RFD, i.e. parabolic ray paths in the LPP and planar wavefronts at the object plane, were found to be responsible for the inaccuracies of the RFD electron densities. The effect of symmetry on the accuracy of the LPP was not investigated. However, bearing in mind the limitations of the RFD, the RFD is a useful diagnostic due to its simplicity, i.e. it requires essentially one lens and one camera and the deconvolution of electron densities is mathematically trivial.

Chapter 3

The Pulsed Gas Lens

3.1 Introduction

With the recent success of the JET experiment in producing over one megawatt of thermonuclear power [Jet Team (1992)], fusion has come a major step closer to being a realistic source of energy. The impressive results obtained by the magnetic fusion community will undoubtedly benefit all types of controlled fusion research. Just as there exist several types of fission power stations, from the less than man size power plants on board satellites to the gigawatt (GW) fast breeder reactors, so will there exist several types of fusion reactors. Whilst the tokamak is a sensible choice as the central power generator for a large industrial conglomeration, its minimum electrical output ($1\ GW$) makes it an inconvenient choice for less developed regions.

In the African context in particular, a laser fusion power station with its variable output ($100\ MW < P_e < 1\ GW$) is a more appealing concept. It

is not generally realised that laser-fusion break-even (thermonuclear power out = electrical power in) could occur before the turn of the century. The classified Halite-Centurion program has shown that a radiation drive in the region of 10 MJ, produces a large (but undisclosed) thermonuclear yield. On the basis of these and other results Lawrence Livermore National Laboratory hopes to be granted funds to build a Laser Microfusion Facility with a MJ Neodymium glass laser as its driver, before 1999. The Japan Osaka team are meanwhile confident that their 100 kJ "Gekko Upgrade" will approach break-even in the nearer future.

A somewhat neglected question is: "*Beyond break-even, beyond single pulse yield, what optics ?*"

All Inertial Confinement Fusion (ICF) reactor studies locate the optics many meters from the target. This is because neutron and α particle damage calculations show that no solid state optical component (lens, frequency doubler/tripler or $\lambda/10$ mirror surface) will resist the several shots per second loading required for reactor operation. In one Los Alamos National Laboratory conceptual design the first lens is 80 m from the target [Phipps (1989)]. Livermore Laboratories chose 10 m [Pitts (1985)] as do Basov *et al.* [Basov *et al.* (1988)] at the Lebedev. It has been proposed [Michaelis *et al.* (1991a)] that a pulsed gas lens (PGL) may help to overcome this problem, thereby considerably reducing the size of a future ICF reactor. An attractive feature of gas lenses is that they have a higher breakdown threshold than solid state lenses, enabling higher energy laser beams to be focused.

In this chapter the feasibility of using a PGL as a focusing lens is investigated. A proof-of-principle PGL design is presented and its performance and optical quality are numerically investigated. In view of constructing this device an experimental investigation into certain practical aspects of the PGL was

performed on a beam deflection device [Buccellato *et al.* (1993a)]. The results of this investigation are presented in this chapter. The experimental work presented here is the continuation of the work started by Clemens Dempers, a member of the Plasma Physics Research Institute of the University of Natal. He was responsible for designing and building the beam deflection device and for doing some preliminary tests on it before leaving the project.

3.2 Pulsed Gas Lens Application

The first application envisaged for the PGL (and the only one seriously considered in this chapter) is that of gas laser driven thermonuclear fusion. In particular we consider the Hydrogen Flouride (HF) laser proposed at Los Alamos Laboratory by Phipps [Phipps (1989)]. Whilst it is likely that ICF will be demonstrated with the Nova upgrade solid state laser, relatively few engineers envisage such a laser as a reactor driver. Nova can only fire a few shots per day. Even with specially designed flash lamp shields the Nova upgrade will only improve on this by an order of magnitude. Gas lasers can be far more economical and could be designed to fire at a high repetition rate.

A cursory examination of Phipps' proposed 170 MJ HF laser system (figure 3.1) shows it to consist of three main components: the laser head and amplifiers, the pressure gradient interface (PGI) and the target chamber.

The function of the PGI is simply to isolate the target from the laser in such a manner that the gas pressure is always below that at which plasma forms and laser light is absorbed. The PGI essentially consists of a large number of fast butterfly valves, opening onto a vacuum chamber so that the PGI pressure rises from high vacuum to $\frac{1}{3}$ bar over 80 m.

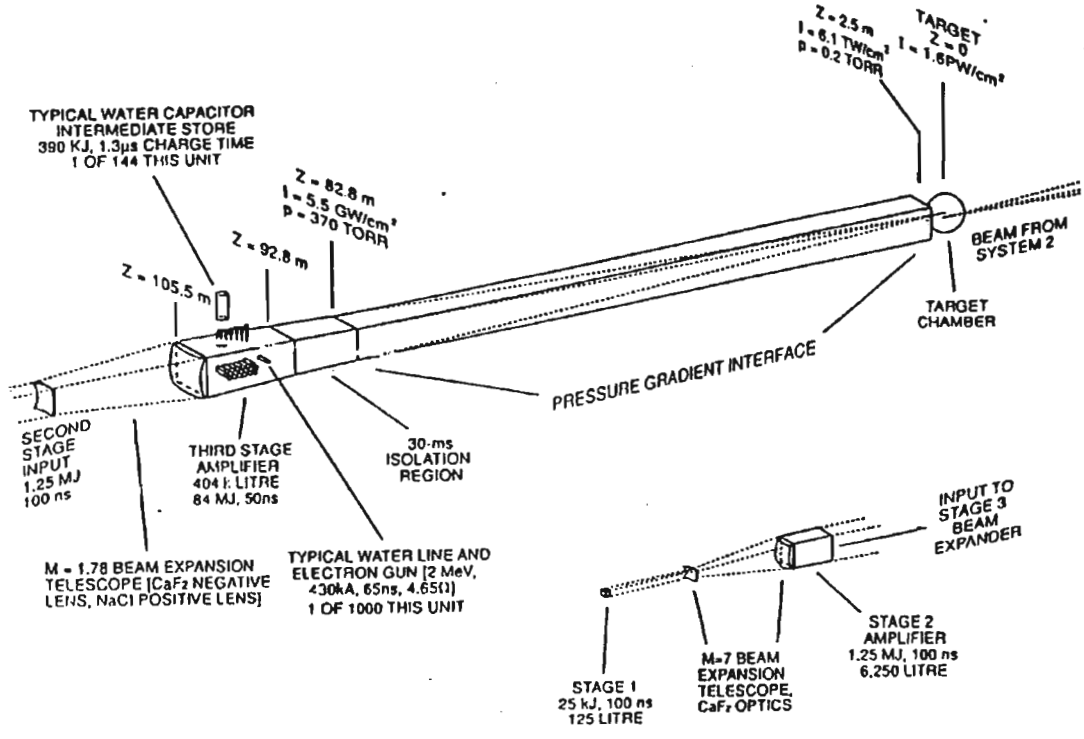

Figure 3.1: Phipps' proposed HF laser system [Phipps (1989)].

The Laser Group at the University of Natal has suggested to the Los Alamos group that the PGI could become a PGL [Michaelis *et al.* (1991a)]. The butterfly valves would have to open fast enough to create an appropriate density profile that would serve to focus the infra red light, without the 6 m x 6 m single crystal NaCl segmented lens placed before the final amplifier. This lens is one of the major capital items in the design.

There are other potential applications for the PGL and two possible applications are briefly mentioned. The first is for X-ray lasers: X-ray lasers require very high power optical lasers to drive them - just as some optical lasers require high power flash lamps. Most X-ray lasers require the laser driver to be line focused. As shorter X-ray wavelengths are realised, even higher laser driver powers are required (100 TW). Pulsed gas lenses might be able to line focus these ultra high powers without breakdown of the gas.

The second application is in satellite positioning and propulsion. NASA and Strategic Defense Initiative Organization have a strong laser propulsion program [Kare (1987)]. However, the demands on the optical train will be perhaps even more challenging than for laser driven fusion: 40 Hz x 500 kJ to launch a small satellite (20 kg). Thermal effects in the focusing optics could be minimised by using a PGL.

3.3 Pulsed Gas Lens Principle

Hecht [Hecht (1989)] broadly defines a lens as a "refracting device that is used to reshape (light) wavefronts in a controlled manner". This is conventionally done by passing the light wavefront through one or several interfaces, shaped in a particular manner, which separate two different homogeneous

media. A homogeneous medium is one where the refractive index is constant throughout the medium. The interaction of a plane light wavefront with a bi-convex lens is shown in figure 3.2. The plane wavefront on interaction with the spherical lens surface is refracted and converges to a point.

A further way of reshaping a light wavefront is by passing it through a cylindrically shaped inhomogeneous medium where the refractive index only varies radially, decreasing outwards in a prescribed fashion, from the optical axis. The planar front as it propagates through the medium will change shape as different portions of the wave will propagate at different speeds depending on the refractive index.

This type of lens is termed a gradient index lens or GRIN lens and the PGL is such a lens. In essence, a PGL is a type of Wood lens [Wood (1905)]. A Wood lens is a plane parallel disk with a refractive index profile which varies radially with the distance from the optical axis. Wood showed that a disk of this nature can act as a converging or diverging lens depending on the refractive index profile. If the refractive index profile is a decreasing function of the radial distance then the lens is a converging lens. If the refractive index profile is an increasing function of the radial distance then the lens is a diverging lens. His lens was manufactured out of gelatin. In a PGL; however, one has a cylindrical region of gas with a smoothly decreasing radial density profile as shown in figure 3.3. The density profile along the z-axis is constant.

The density of a neutral gas made up of species in constant ratio is related to its refractive index by the Gladstone-Dale law:

$$n = 1 + k\rho, \tag{3.1}$$

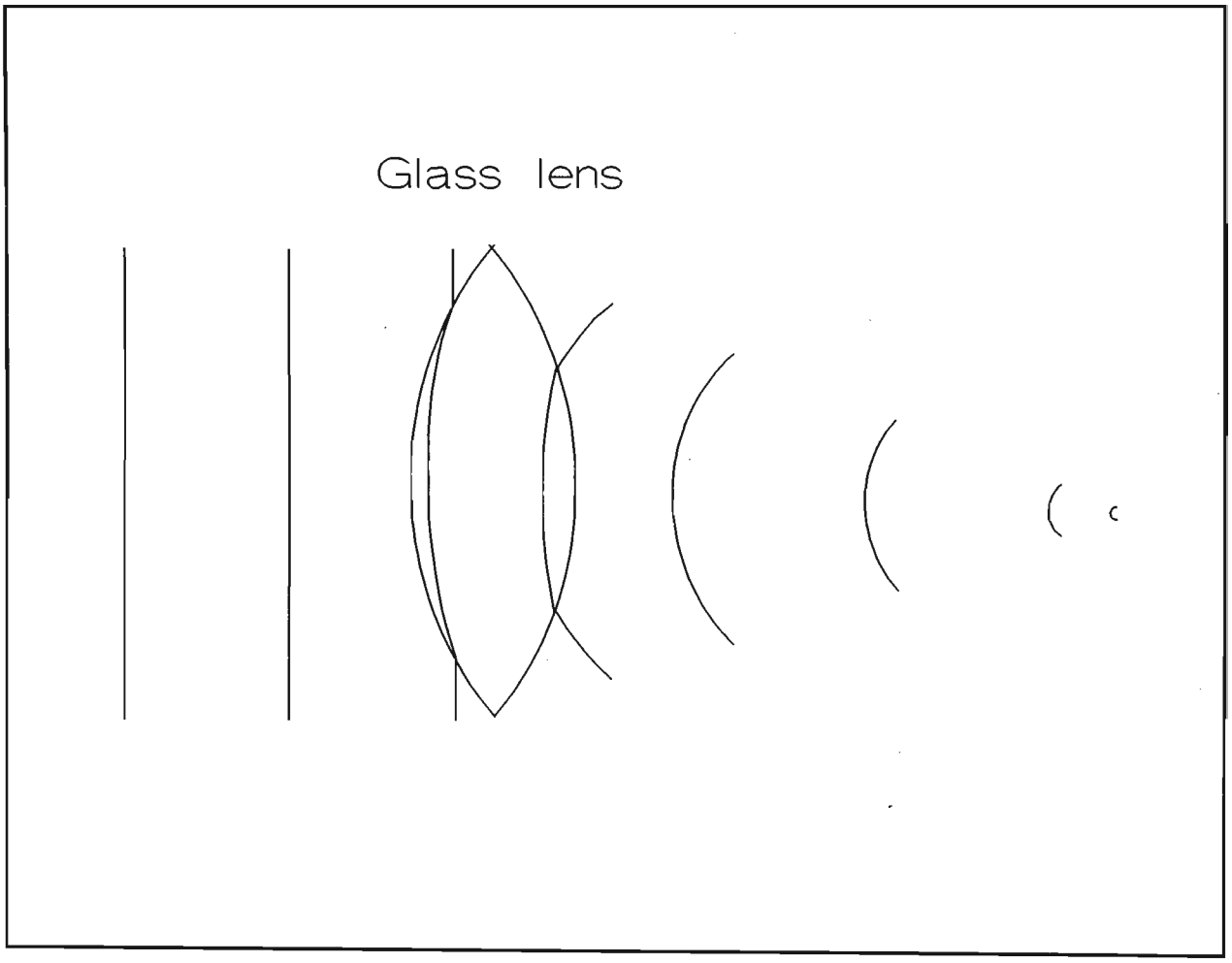

Figure 3.2: A plane light wavefront propagating through a bi-convex lens.

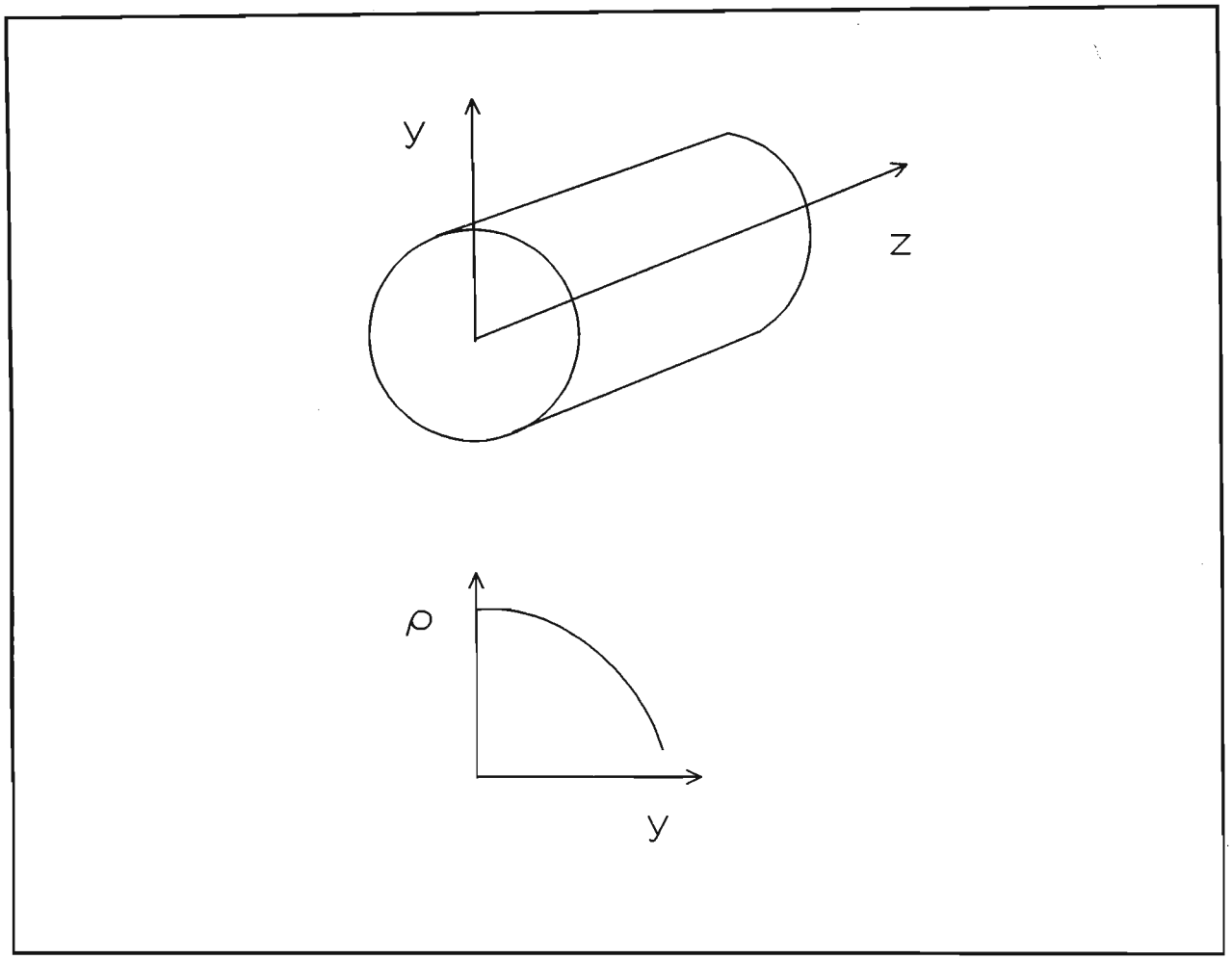

Figure 3.3: The density field of a PGL.

where ρ is the gas density and k is a constant characteristic of the gas concerned and of the wavelength of light interacting with the gas. Since the refractive index and the density of a gas are linearly related, the radial refractive index profile of the PGL is of the same shape as the density profile shown in figure 3.3.

The interaction of a plane light wavefront with a PGL is shown in figure 3.4. The wavefront propagates faster at the edges than in the centre of a PGL since the refractive index monotomically decreases from the centre. The wavefront thus converges to a point.

The obvious question that arises is: what is the optimum density profile for a point focus and how does one obtain a cylindrically symmetric region of gas with such a profile ?

Fletcher [Fletcher (1954)] showed that if a GRIN rod has a refractive index profile given by:

$$n = n_0 \, Sech(\alpha y), \tag{3.2}$$

where n_0 and α are constants and y is the radial distance from the optical axis, meridional light rays are sharply imaged.

Equation 3.2 can be expanded into the first two terms of a series of power y^2:

$$n = n_0(1 - \alpha^2 y^2)^{\frac{1}{2}}, \tag{3.3}$$

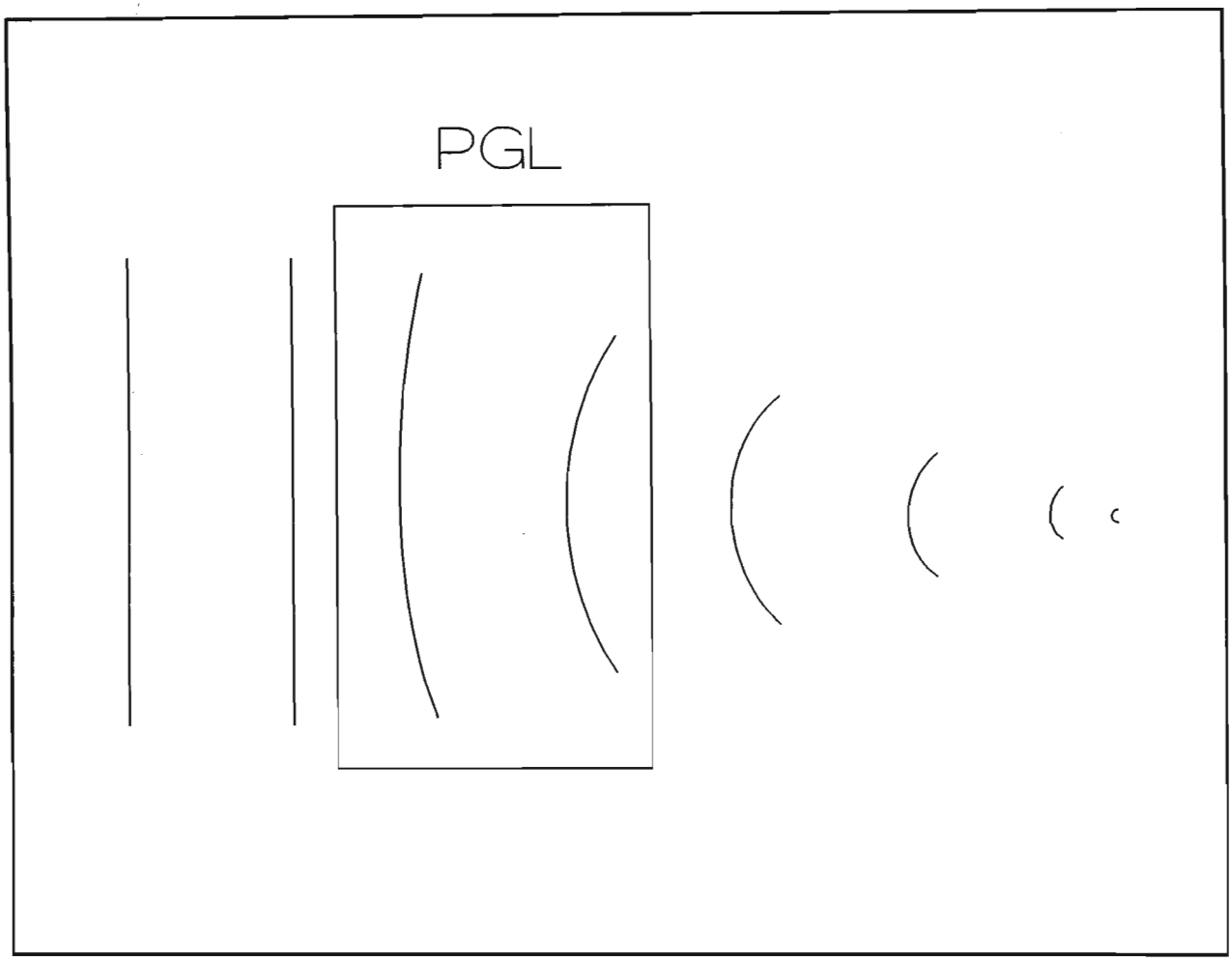

Figure 3.4: A plane light wavefront propagating through a PGL.

and approximated by:

$$n \simeq n_0(1 - \frac{1}{2}\alpha^2 y^2), \tag{3.4}$$

if $\alpha^2 y^2 \ll 1$.

It is possible to find an analytic solution for the light ray trajectories in a PGL for the radial refractive index field given by equation 3.4. Since the refractive index profile is radially symmetric about the optical axis of the PGL, a slice in the y-z plane of the cylindrical region given in figure 3.3 is only considered.

The ray path in a refractive index field, n, is given by the ray equation:

$$\frac{d}{ds}(n\frac{dr}{ds}) = \nabla n, \tag{3.5}$$

where s is the arc length measured along the ray from some arbitrary point on it and $r = r(s)$ is the vector function of the ray. If the ray trajectories are almost parallel to the z-axis (figure 3.3) then $ds \approx dz$ and equation 3.5 can be written as the paraxial ray equation:

$$\frac{d}{dz}(n\frac{dy}{dz}) = \frac{dn}{dy}, \tag{3.6}$$

where $y = y(z)$ and $n = n(y)$. Substituting equation 3.4 into equation 3.6:

$$\begin{aligned} \frac{d}{dz}(\frac{dy}{dz}) &= \frac{n_0}{n}(-\alpha^2 y) \\ &\simeq -\alpha^2 y, \end{aligned} \tag{3.7}$$

since $\frac{n_0}{n} \simeq 1$. Solving equation 3.7 for the ray trajectories inside the PGL , given the initial conditions that the rays are parallel to the PGL axis when they enter the PGL and that they enter with a height y_0 relative to the central axis, one gets a harmonic solution with a period $\frac{2\pi}{\alpha}$:

$$y(z) = y_0 \, Cos(\alpha z), \tag{3.8}$$

where z is the distance along the PGL axis. The light rays are thus focused to a point.

The desired refractive index profile can be obtained by suddenly allowing a cylinder of high pressure gas to expand radially, producing a smoothly decreasing radial density profile symmetric about the length of the cylinder. At some time after the initiation of the gas expansion, a refractive index profile suitable for focusing will be obtained.

3.4 Proposed Pulsed Gas Lens Design

The cylindrical PGL design that has been proposed to the Los Alamos group as a final optical element of a laser fusion system is shown in figure 3.5 [Michaelis *et al.* (1991a)].

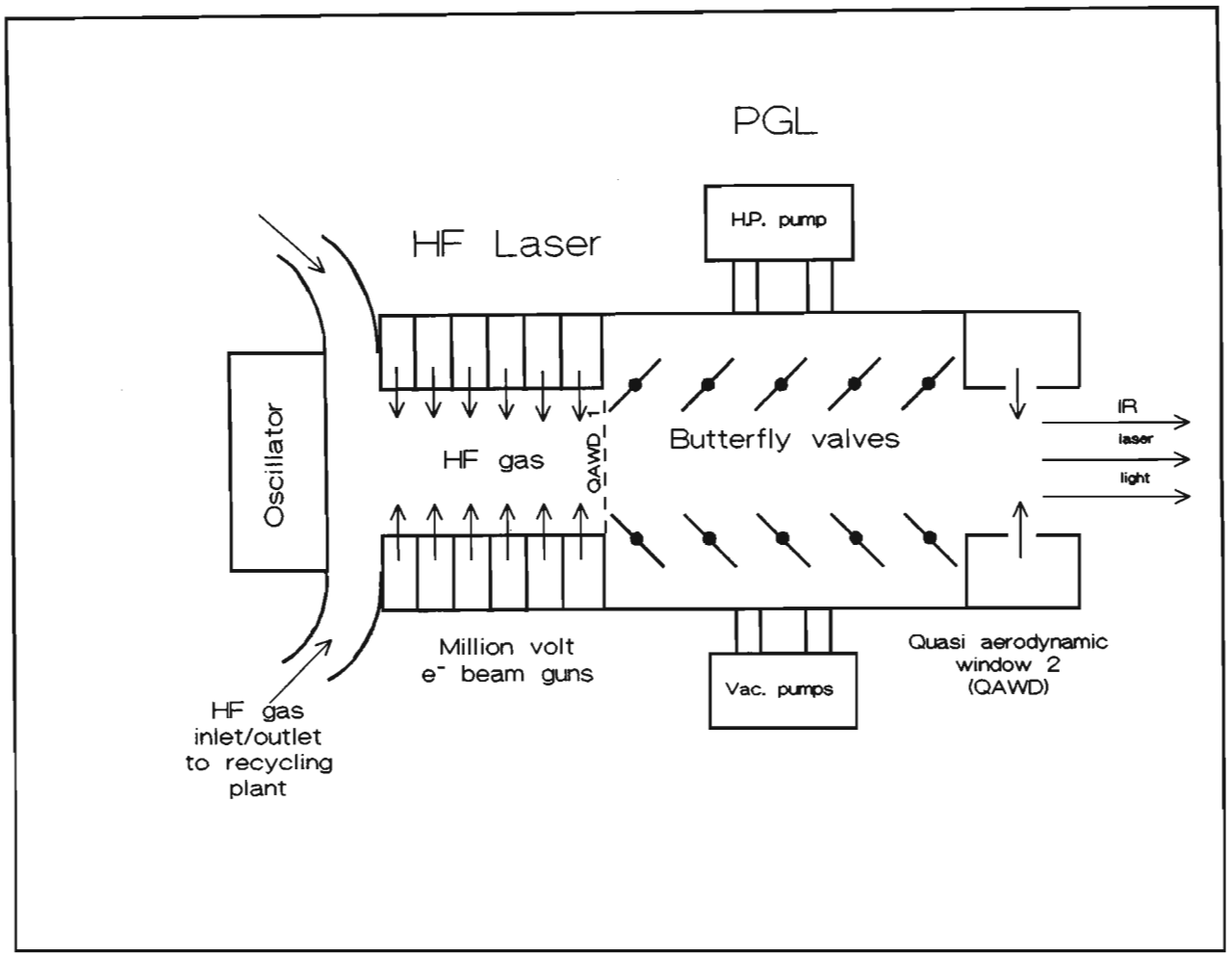

Figure 3.5: Proposed PGL design for Phipps' laser fusion system.

It consists of a HF laser and a PGL separated by quasi-aerodynamic windows (QAWD). A QAWD is a fast mechanical shutter. The PGL is pressurised by high pressure pumps and venting of the PGL is obtained by fast butterfly valves opening onto vacuum. The QAWD are needed to contain the gas. The PGL could be designed to serve a triple purpose: first as the final focusing lens; second as a nuclear and debris shield for the expensive oscillator optics up-beam; and thirdly as the exhaust gas extraction system for the gas laser.

To test the feasibility of a PGL as a focusing element the Laser Group at the University of Natal is planning in the near future to build and test a single-shot cylindrical PGL. The proposed design for a single shot cylindrical PGL is shown in figure 3.6.

It consists of a pipe, 3 m long and 0.6 m in diameter, which is closed at both ends by a glass window. The PGL is pressurised to 8 *bar* and venting the PGL is obtained by rupturing glass windows evenly spaced along the walls of the pipe by exploding wires fixed to the glass. The wires are exploded by discharging a capacitor bank through the wires to ground.

Such an opening of the PGL might degrade the focusing quality of the PGL since the gas is constrained to expand through the slots in the pipe. The radial symmetry of the refractive index profile required for focusing might be destroyed.

An alternate design for the cylindrical PGL is to make the cylinder out of thin mylar, closed at both ends by a glass window, with the same dimensions as figure 3.6. The thickness of the mylar must be chosen so that at the desired operating pressure the mylar is close to bursting. An even rupture of the mylar can be obtained by having an explosive wire wrapped around the mylar cylinder.

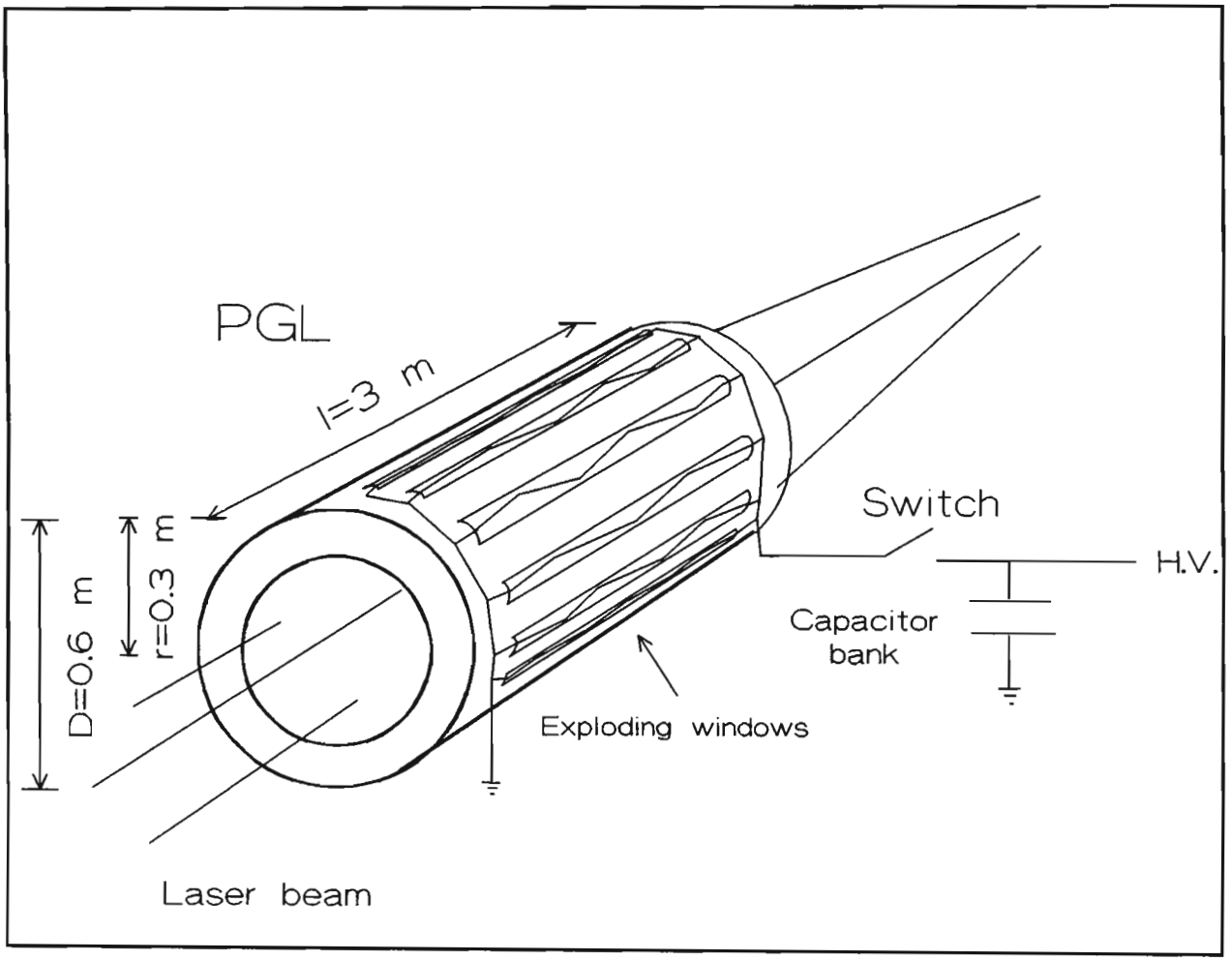

Figure 3.6: Proposed single-shot PGL design.

The choice of the gas used to pressurise the PGL is important. A gas with a low condensation and sublimation temperature and a low light absorbency at the wavelength of the laser light used, is needed. For the proof-of-principle design carbon dioxide gas is adequate.

The focal length of the proposed PGL can be estimated using the graded index formula. The graded index formula assumes the refractive index profile to be linear, decreasing radially from the centre of the PGL.

The lens aspect ratio is:

$$\frac{l}{r} = 10. \tag{3.9}$$

For CO_2 depressurised from 8 *bar* to atmospheric pressure the maximum change of the refractive index is:

$$\Delta n \simeq 2.9 \times 10^{-3}. \tag{3.10}$$

Using the graded index formula to approximate the deflection:

$$\theta = \frac{l}{r} \times \Delta n \simeq 2.9 \times 10^{-2}\ radians, \tag{3.11}$$

the focal length is thus:

$$f = \frac{r}{\theta} = \frac{0.3}{2.9 \times 10^{-2}} \simeq 10\ m. \tag{3.12}$$

This focal distance is inline with previously mentioned currently used focal distances in laser fusion experiments. The above method is an inaccurate method of determining the focal distance of the PGL. A more thorough method is needed.

3.5 Theoretical Simulation of the Proposed Pulsed Gas Lens

To simulate the operation of the proposed PGL to determine the time that focusing is achieved after the PGL is exploded, the associated focusing distance and the optical quality of the focus; one needs to numerically simulate the time evolution of the density structure inside the PGL and numerical raytrace through the resultant density profiles.

3.5.1 Numerical Methods in Fluid Dynamics

Richardson [Richardson (1910)] was one of the first persons to apply a numerical method to solve a physical problem characterised by partial differential equations. Using a human computer he determined the stresses in a masonry dam. Thom [Thom (1933)] presented one of the earliest numerical solutions for the partial differential equations governing viscous fluid dynamics. He modeled the flow past a circular cylinder at low speeds. With the advent of electronic computers numerous methods have been developed to solve fluid dynamic problems. Roache [Roache (1985)] gives a detailed account of the historical development and the different numerical methods in fluid dynamics.

Supersonic compressible flow is governed by a set of hyperbolic equations. Courant *et al.* [Courant *et al.* (1928)] published a paper on the numerical treatment of these equations using the method of characteristics. The basic theory and numerical procedures of this method are outlined by Shapiro [Shapiro (1954)]. These equations can also be solved by Lagrangian methods [Fromm (1961)] where the motion of individual particles is traced.

For problems in two dimensions Eulerian methods, where the fluid flows through a space-fixed reference mesh, are generally preferable. A problem associated with Eulerian methods arises with the treatment of shock waves. The mesh spacing must be smaller than the shock thickness or else oscillations develop which destroy the accuracy of the method. This problem also applies to Lagrangian meshes and was pointed out by Courant *et al.* [Courant *et al.* (1928)].

A common method employed to deal with this problem is to smear out the shock over several computational cells by introducing artificial dissipation. This may be done implicitly or explicitly. The solution away from the shock is not affected by this method. Von Neummann and Richtmyer [Von Neummann and Richtmyer (1950)] proposed an explicit artificial dissipation scheme where the viscosity coefficient is proportional to the square of the velocity gradient. Instead of using explicit viscosities, implicit dissipation terms inherent in conservative finite difference methods employed to solve the inviscid gas dynamic equations, may be sufficient to smear out the shocks.

Roache [Roache (1972)] pointed out that the Von Neumann and Richtmyer explicit artificial viscosity term was a second order truncation error similar to that obtained implicitly due to the truncation error of the finite difference equations employed. Certain methods require both implicit and explicit shock smearing dissipation terms to achieve stability for particular

conditions.

A method as an alternate to smearing the shock over several computational cells was proposed by Moretti and Abbett [Moretti and Abbett (1966)]. This shock fitting technique has only been useful in modeling simple transonic flows.

Courant and Friedrichs [Courant and Friedrichs (1948)] presented the inviscid compressible flow equations in conservation form and Lax [Lax (1954)] presented the first finite difference scheme to solve these equations. Further finite difference schemes have been developed to solve these equations and a comparison between these different methods on a one-dimensional shock tube problem was performed by Sod [Sod (1978)].

The numerical method employed to model the PGL operation is the Fluid in Cell (FLIC) method of Gentry *et al.* [Gentry *et al.* (1966)]. This is an Eulerian finite difference scheme which uses an explicit artificial viscosity term to enable the automatic treatment of shocks.

Fluid in Cell Differencing Scheme

The FLIC Scheme of Gentry *et al.* [Gentry *et al.* (1966)] is an Eulerian finite difference method which solves the time dependent equations of motion for unsteady compressible fluid flow problems. The fluid flow equations in conservation form (in cylindrical co-ordinates with radial symmetry for two space dimensions) for an inviscid gas where body forces are absent and heat transfer phenomena are neglected are:

conservation of mass:

$$\frac{\delta\rho}{\delta t} + \frac{1}{r}\frac{\delta}{\delta r}(r\ \rho v) + \frac{\delta}{\delta z}(\rho u) = 0, \tag{3.13}$$

conservation of momentum:

$$\frac{\delta(\rho u)}{\delta t} + \frac{1}{r}\frac{\delta}{\delta r}(\rho u\ vr) + \frac{\delta}{\delta z}(\rho u^2 + p) = 0 \tag{3.14}$$

$$\frac{\delta(\rho v)}{\delta t} + \frac{\delta}{\delta z}(\rho u\ v) + \frac{\rho v^2}{r} + \frac{\delta}{\delta r}(\rho v^2 + p) = 0, \tag{3.15}$$

conservation of energy:

$$\frac{\delta I}{\delta t} + v\frac{\delta I}{\delta r} + v\frac{\delta I}{\delta z} = -\frac{p}{\rho}(\frac{1}{r}\frac{\delta(vr)}{\delta r} + \frac{\delta u}{\delta z}). \tag{3.16}$$

The FLIC method is similar to the Particle in Cell (PIC) method of Evans and Harlow [Evans and Harlow (1957)]. The PIC method uses Lagrangian fluid particles to transport mass, momentum and energy through an Eulerian mesh of cells. The FLIC method uses similar difference equations as the PIC method but uses a different transport calculation not based on individual particles. The FLIC method uses an upwind differencing method. A detailed description of this method is given by Roache [Roache (1985)].

The FLIC method subdivides the flowfield into a mesh of cells. Each cell is given initial values of density, velocity and pressure. Specific internal energy for each cell is calculated using equation A.7 . New values for density, velocity, pressure and specific internal energy, for each cell, are calculated for a time increment δt. The acceleration caused by the pressure gradients

are used to calculate intermediate values of velocity and specific internal energy for each cell. Using these values mass flow across the cell boundaries in the time increment δt is calculated. Assuming that this mass flow carries momentum and energy corresponding to intermediate values of velocity and specific internal energy of the donor cell, the flow of momentum and energy is computed. Conservation of mass, momentum and energy are used to calculate the final values of velocity, density, pressure and specific internal energy in each cell, for the time increment δt. This process is repeated until one arrives at the desired time. A full description of the FLIC method, including the computational mesh, difference equations and boundary conditions are given in Appendix A.

The accuracy of the FLIC method has been determined by several workers. Butler [Butler (1966)] computed the interaction of plane shocks with rectangular objects and blunt bodies and found that the simulated results were consistent with experimental results. Meintjies [Meintjies (1975)] studied the flow dynamics inside an expansion tube. He found that the FLIC method accurately modeled the propagation of the rarefraction wave inside a shock tube. Further applications of the FLIC method are given by Harlow and Amsden [Harlow and Amsden (1970)].

3.5.2 Pulsed Gas Lens Simulation

The FLIC FORTRAN code of Meintjies [Meintjies (1975)], optimized for better efficiency and modified for the PGL geometry, was used to model the radial expansion of a cylinder of high pressure gas into a surrounding region at atmospheric pressure. The computational mesh is given in figure 3.7. Due to the radial symmetry about the optical axis (z axis), a slice in the y-z plane is only considered.

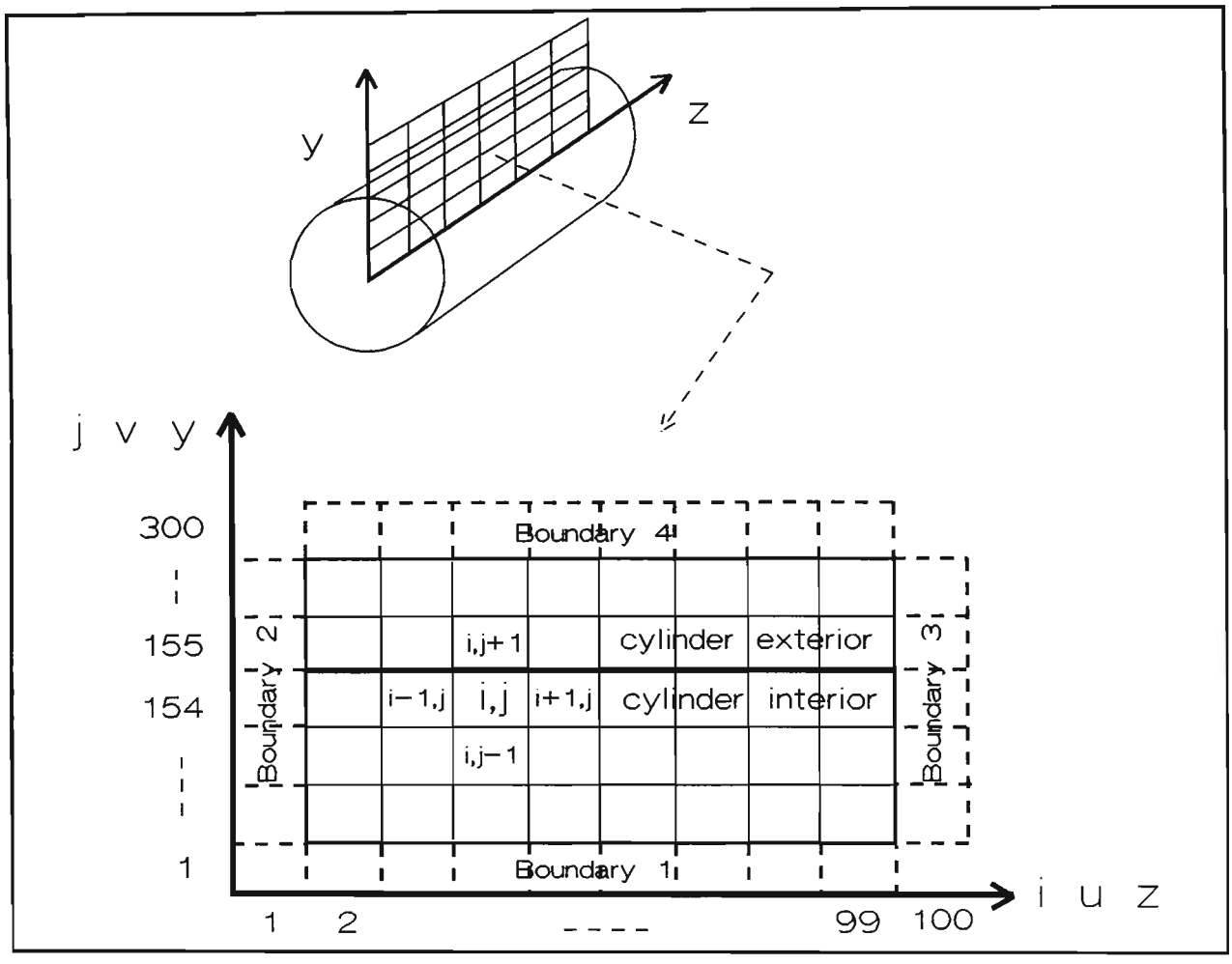

Figure 3.7: FLIC computational mesh for the PGL.

The computational mesh is a cylindrical co-ordinate system which consists of 100 $\times$ 300 cells. Each cell is in the shape of a rectangular torus with dimensions given by equations A.4 to A.6. The boundary conditions are set by fictitious cells which enclose the interior cells. Boundaries 1, 2 and 3 are closed allowing the gas only to expand out the computational mesh through the open boundary 4. Cells 2 to 154, in the radial direction, model the conditions inside the cylinder of gas while cells 155 to 299 model the conditions outside the cylinder of gas. The gas expansion outside the cylinder is constrained to expand only radially by boundaries 2 and 3. The flow variables will thus vary radially but will be constant along the length of the cylinder.

The cylinder of gas is pressurised with carbon dioxide gas and it is assumed that the gas expands into a region of carbon dioxide gas at atmospheric pressure. This problem is analogous to a one-dimensional shock tube problem. A one-dimensional shock tube showing the different features inside the tube, for an ideal gas, is shown in figure 3.8.

The high pressure region in the shock tube is separated from the low pressure region by a diaphragm. When the diaphragm is ruptured, a compression wave propagates into the low pressure gas (region 1). This compression wave quickly steepens to produce a shock front. As the gas expands into region 1 an emptying wave or rarefraction wave propagates into the high pressure gas (region 4) at the speed of sound in the high pressure gas. A contact surface between the high pressure gas and the low pressure gas is formed during the gas expansion (between regions 2 and 3) and this follows the shock front.

Computed radial density, pressure and temperature curves for different times after the start of gas expansion, for the proposed PGL initially pressurised to 8 bar and for a PGL initially pressurised to 3 bar, are shown in fig-

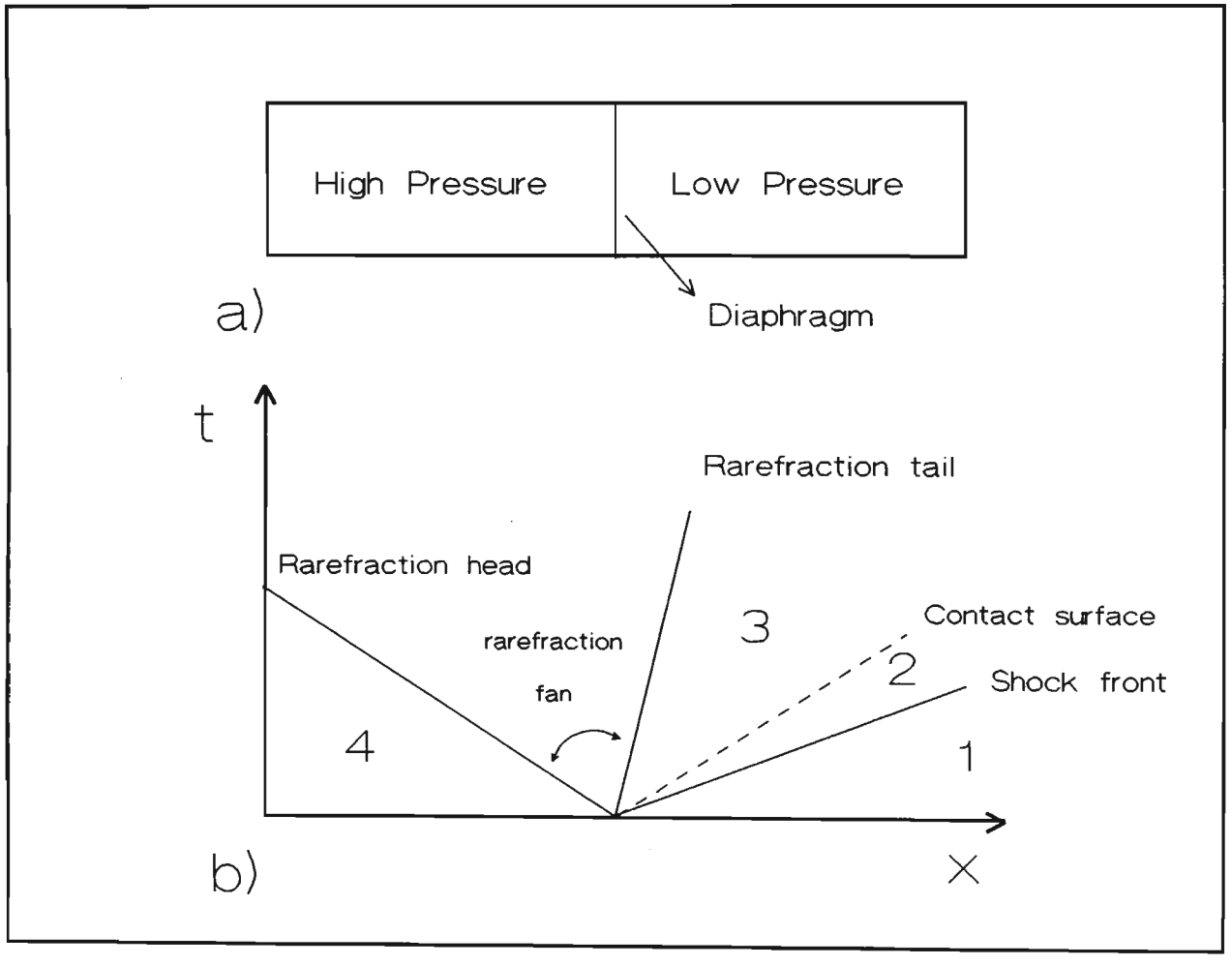

Figure 3.8: One-dimensional shock tube a) shock tube b) (x-t) diagram.

ures 3.9 to 3.14. These curves were computed for $\delta z = 3\ cm$, $\delta y = 2\ mm$ and $\delta t = 2.5\ \mu s$. Explicit artificial viscosity ($K = 0.5$ and $B = 0.5$) was used to stabilise the solution by smearing the shock front over several computational cells.

The shock front propagating into region 1 is characterised by a sharp increase in pressure, temperature and density. The shock front weakens as it propagates into region 1. The contact region between the high pressure and low pressure gas can be divided into two separate regions: the region between the contact surface and the shock front (region 2) and the region between the rarefraction tail and the contact surface (region 3). As the contact region propagates behind the shock front, this region increases in size and the flow variables, which are relatively constant in their respective regions, decrease in magnitude. The temperature in region 2 is higher than the temperature in region 1. This region has been heated by the propagating shock front. The temperature in region 3 is lower than the temperature in regions 1, 2 and 4. This low temperature is due to the adiabatic expansion that the gas in this region has experienced. The density in region 3 is higher than the density in region 2. This is due to the temperature in region 2 being greater than the temperature in region 3 while the pressure is relatively constant throughout the contact region. The rarefraction wave propagating into region 4 is characterised by an increase in the flow variables from regions 3 to 4.

The sharp increase in the flow variables near the exit of the flow field ($y = 0.6\ m$) at late times is due to reflections from the output boundary 4. These reflection do not affect the solution inside the cylinder which is the region of interest for focusing.

The overall stability and the performance of the numerical simulation is determined by the Courant number (C) [Courant *et al.* (1928)] which is given

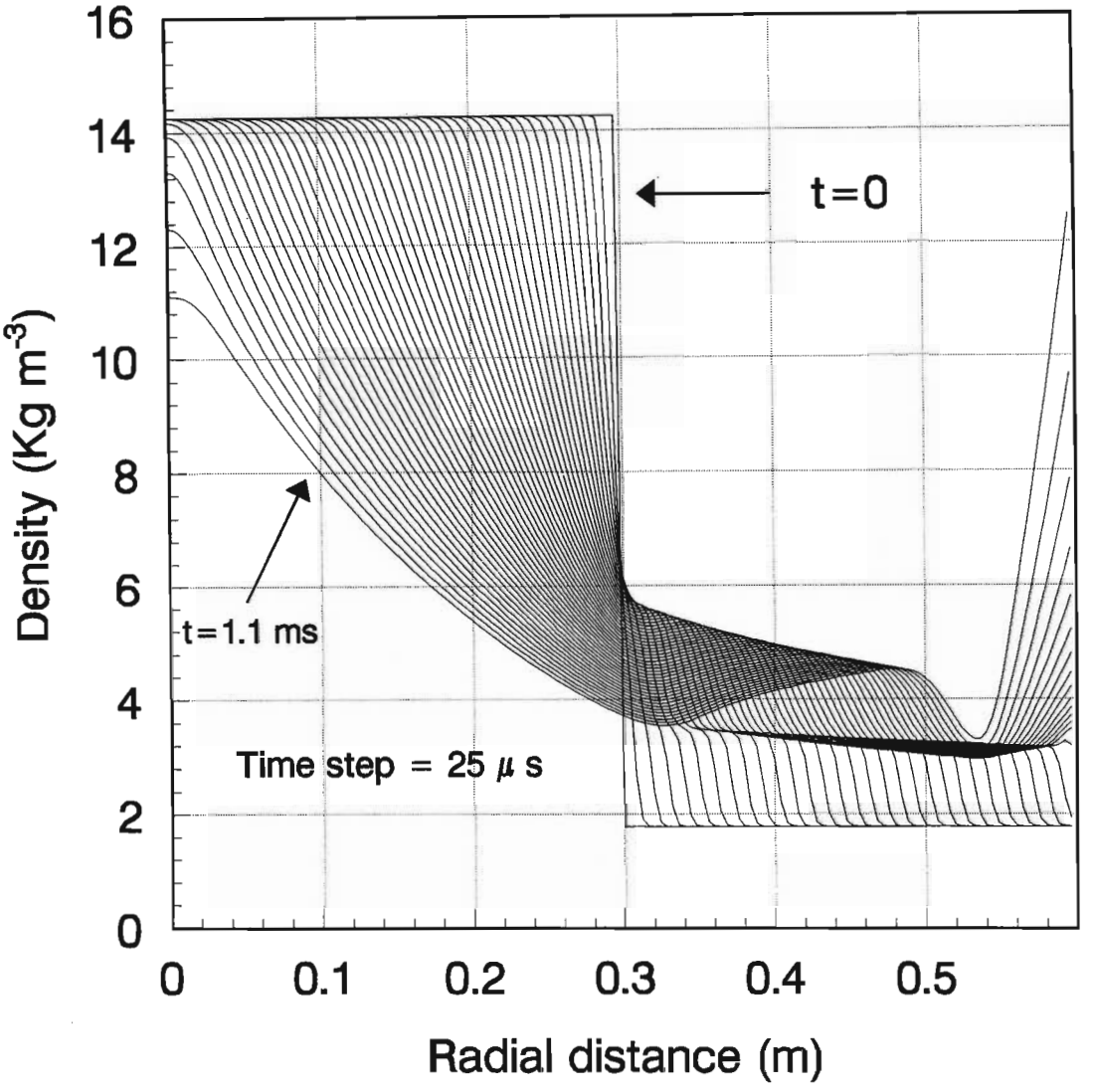

Figure 3.9: Time evolution of density profiles inside an expanding gas cylinder, 0.6 m in diameter and pressurised to 8 bar.

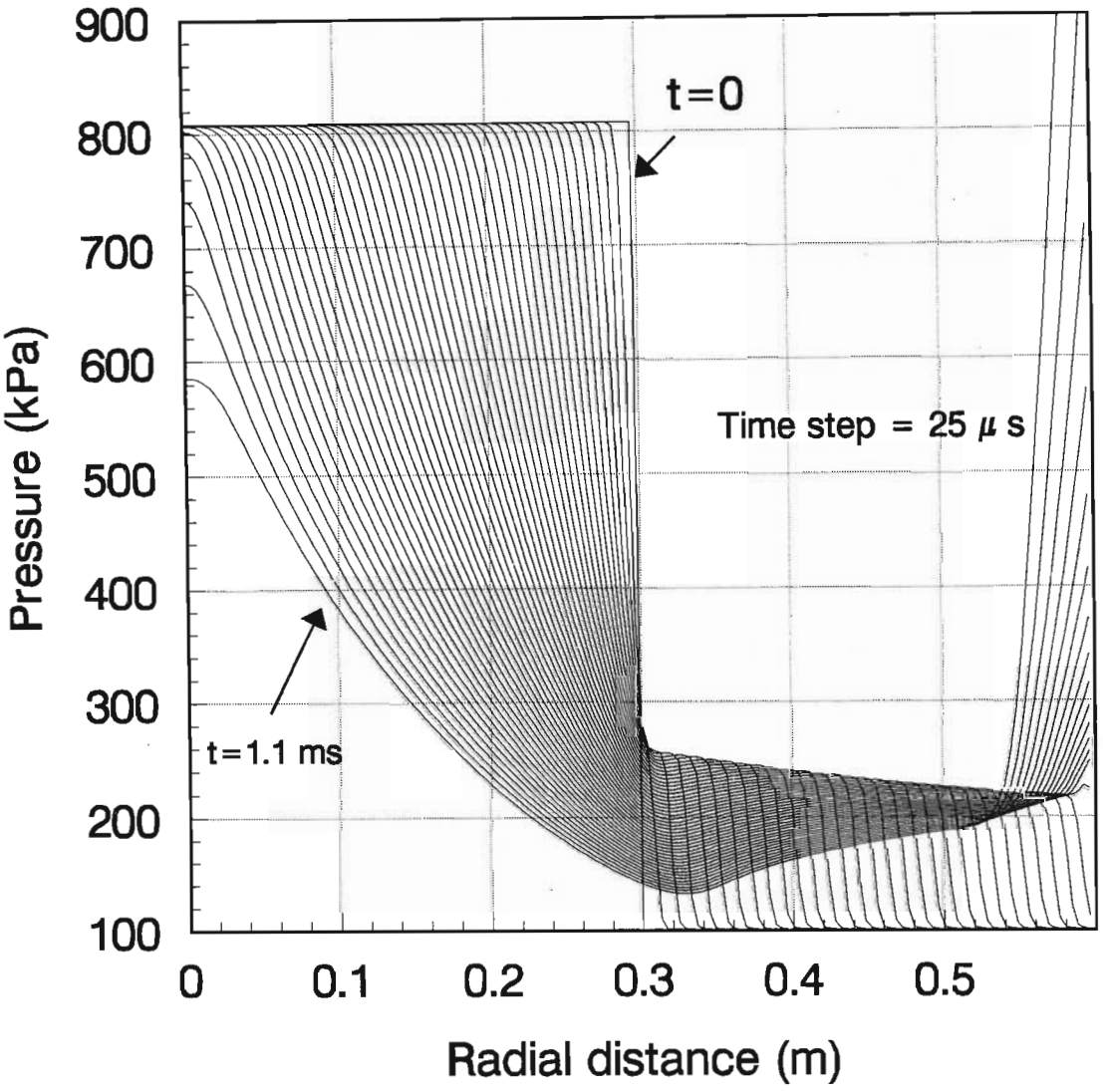

Figure 3.10: Time evolution of pressure profiles inside an expanding gas cylinder, 0.6 m in diameter and pressurised to 8 bar.

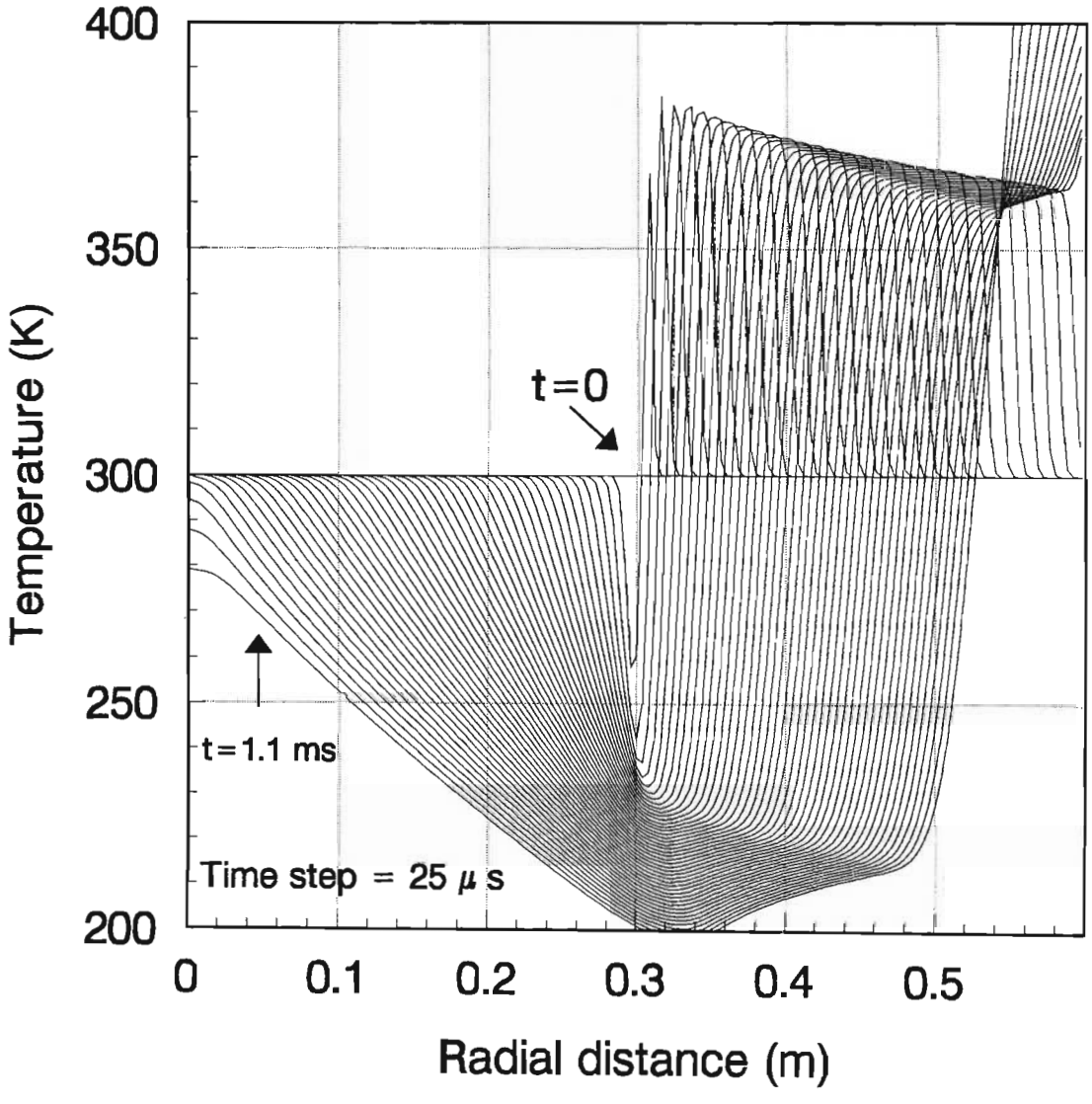

Figure 3.11: Time evolution of temperature profiles inside an expanding gas cylinder, 0.6 m in diameter and pressurised to 8 bar.

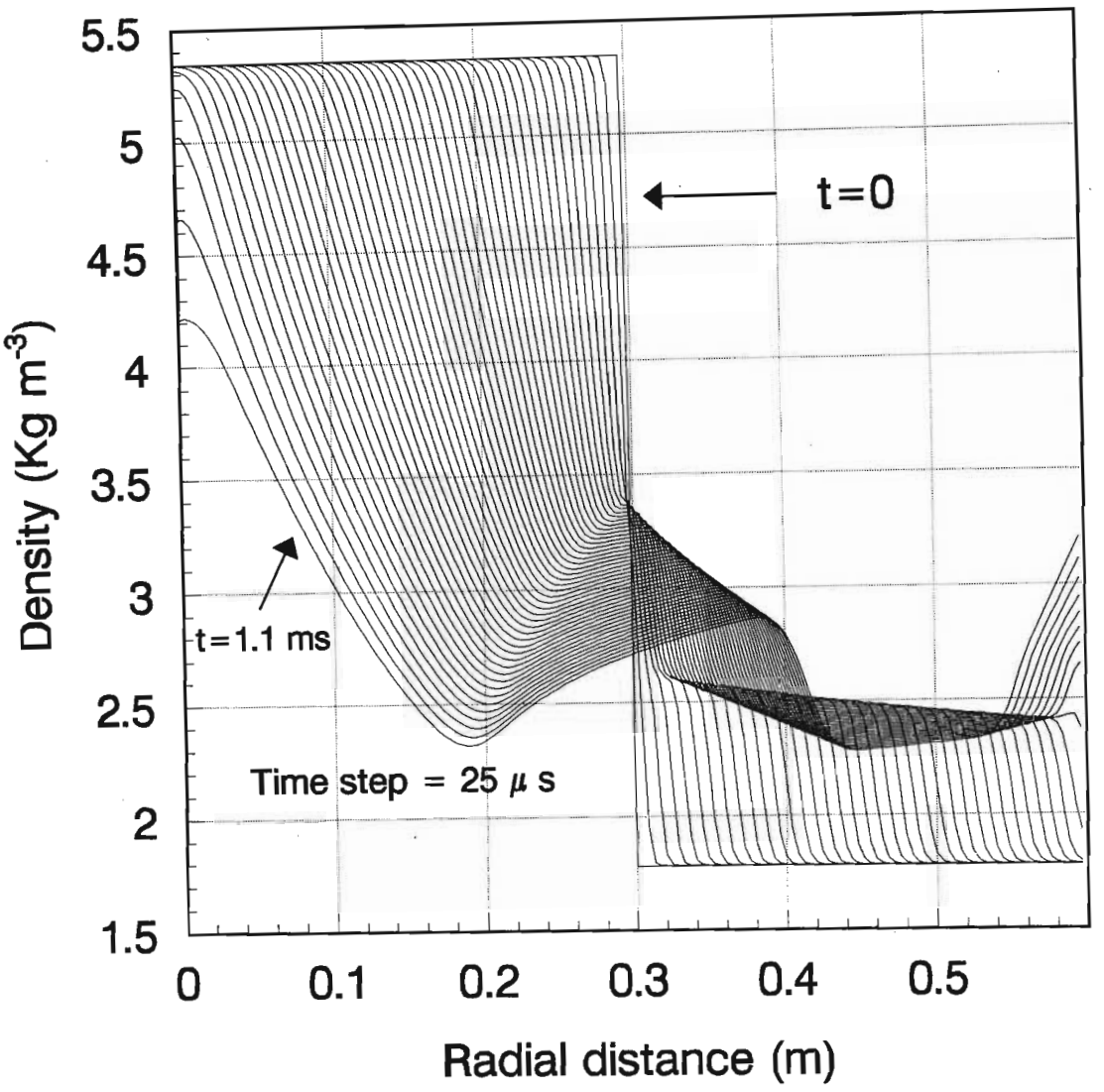

Figure 3.12: Time evolution of density profiles inside an expanding gas cylinder, 0.6 m in diameter and pressurised to 3 *bar*.

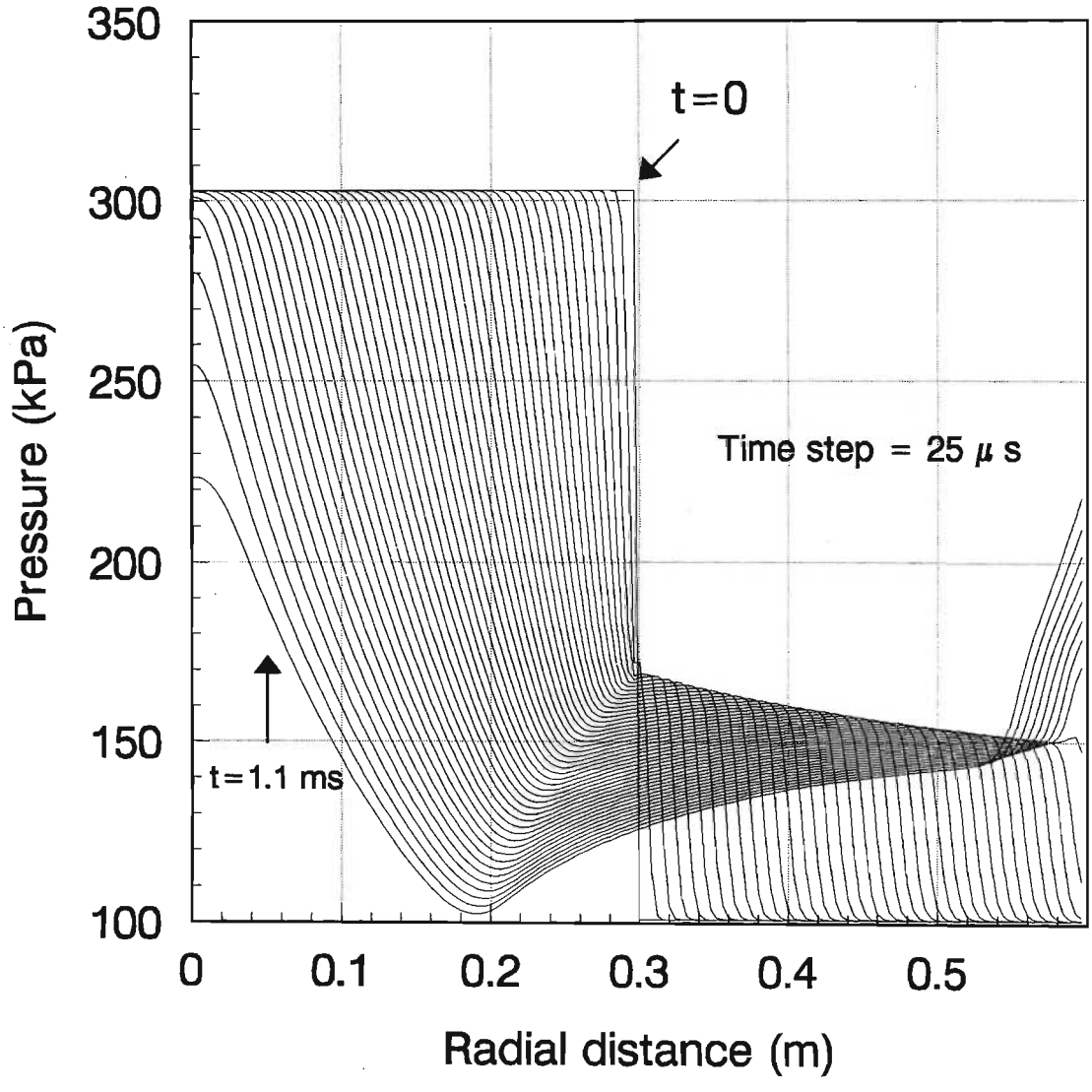

Figure 3.13: Time evolution of pressure profiles inside an expanding gas cylinder, 0.6 m in diameter and pressurised to 3 bar.

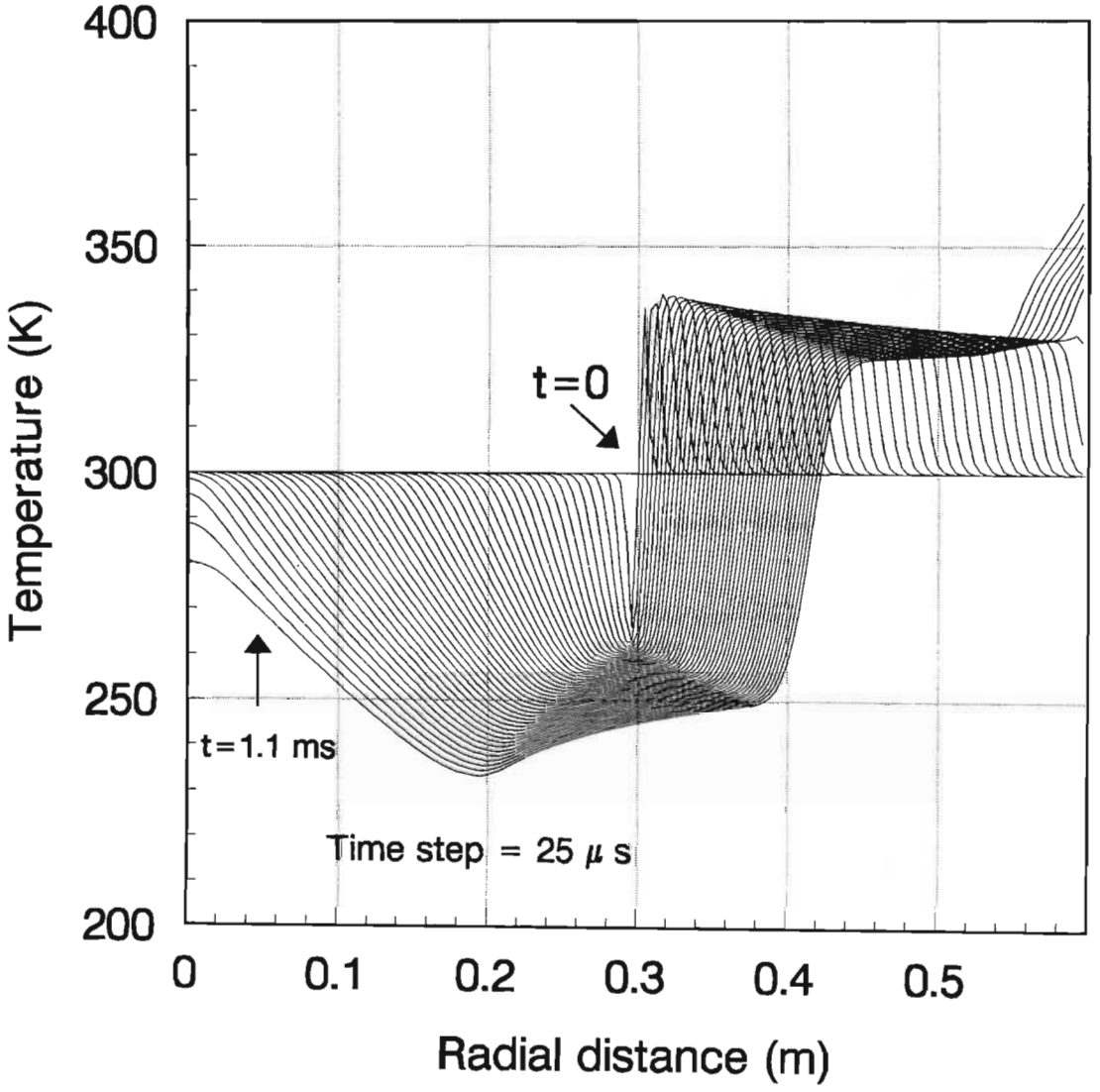

Figure 3.14: Time evolution of temperature profiles inside an expanding gas cylinder, 0.6 m in diameter and pressurised to 3 bar.

by:

$$C = (\mid u \mid + c)\frac{\delta t}{\delta y} \leq 1, \tag{3.17}$$

where u is the fluid velocity and c is the sound speed in the fluid. The Courant number stipulates that in a time step δt, the disturbance cannot travel greater than a distance δy. For the above simulation with initial pressure of 8 *bar* the maximum Courant number in the radial direction for $\delta t = 2.5\ \mu s$ and $\delta y = 2\ mm$ is $C = 0.48$.

From figures 3.9 to 3.14 it is evident that the rarefraction wave speed is the same for both pressure ratios. The rarefraction wave speed is given by the sound speed in the gas.

The speed of sound in an ideal gas is given by:

$$c = \sqrt{\gamma \overline{R} T}, \tag{3.18}$$

where γ is the ratio of specific heats of the gas, $\overline{R}$ is the gas constant specific to the gas, and T is the temperature of the gas in Kelvin.

From equation 3.18, the speed of the rarefraction wave, for a particular gas, is only dependent on temperature. In the FLIC simulation of the gas expansion, the initial temperature inside the gas cylinder was assumed to be equal to the temperature of the surrounding atmospheric region ($T = 300\ K$). From figure 3.11 and 3.14 it is evident that the rarefraction wave head, before reaching the centre of the cylinder, only sees a temperature of 300 K. This

results in the rarefraction wave speeds being equal and constant for the two different pressure ratios.

The speed of sound in carbon dioxide at $T = 300\ K$ is:

$$\begin{aligned} c &= \sqrt{1.3 \times 189 \times 300} \\ &= 271.5\ ms^{-1}. \end{aligned}$$

From figure 3.9 the rarefraction wave takes approximately 1 ms to travel the 0.3 m to the centre of the gas cylinder. This corresponds to a velocity of 300 ms^{-1}. The error in the simulated velocity is 10.5 %.

For the expansion of the gas cylinder initially pressurised to 8 bar, the minimum temperature reached is approximately $-75°\ C$, corresponding to a pressure of approximately 140 kPa. If one considers the phase diagram for carbon dioxide (triple point at 517.6 kPa and $-56.6°\ C$), no condensation or sublimation will occur in the cylinder during the expansion.

It is important to note that the computed gas expansion has assumed that the physical restriction, which contained the gas inside the cylinder, is instantaneously removed. This is not practically possible since there will always be a finite time before the restriction is removed. This will have an effect on the gas expansion.

The computed density profiles can be converted to refractive index profiles by using equation 3.1. The refractive index of carbon dioxide at standard temperature and pressure for sodium light is 1.00045. The density of carbon dioxide at 101 kPa is 1.957 kgm^{-3}. From equation 3.1 the value of k is

thus $2.30 \times 10^{-4}\ m^3kg^{-1}$. The density profiles of figure 3.9 and figure 3.12 are converted to refractive index profiles by using equation 3.1 and are given in figure 3.15 and figure 3.16. The region inside the cylinder has only been shown since this is the only region of interest for lensing. The value of k is specific for sodium light. Dispersion effects on k due to light of different wavelengths is neglected.

In section 3.3 it was stated that if laser light is incident on a cylinder of gas with a radial refractive index profile given by equation 3.2 and constant along the length of the cylinder, the light will be focused to a point. If one examines the refractive index profiles of figure 3.15 and figure 3.16, it is evident that a profile similar in shape to that described by equation 3.2 exists when the rarefraction wave reaches the centre of the gas cylinder ($t \approx 1\ ms$). This similarity is restricted to a short distance ($\leq 3\ mm$) from the centre of the gas cylinder. The PGL diameter will thus have to be apertured down so that the region suitable for focusing is only selected.

The focal length of a 3 m long PGL, 30 cm in radius and pressurised to 8 bar was calculated in section 3.4 to be 10 m. The refractive index profile was assumed to be linear. From figure 3.15, considering the refractive index at $t = 1\ ms$, it is clear that the focal length calculated is inaccurate since the refractive index profile is by no means linear over the whole radius of the cylinder.

To compute the optimum focal length and focal quality of the PGL, one needs to numerically raytrace through the computed radial refractive index profiles of the PGL, for the different times after the initiation of gas expansion. This is performed by solving the paraxial ray equation (equation 3.6), using the 4^{th} order Runge-Kutte numerical technique, for the rays propagating through the PGL. To show the light ray paths through the PGL, a raytrace

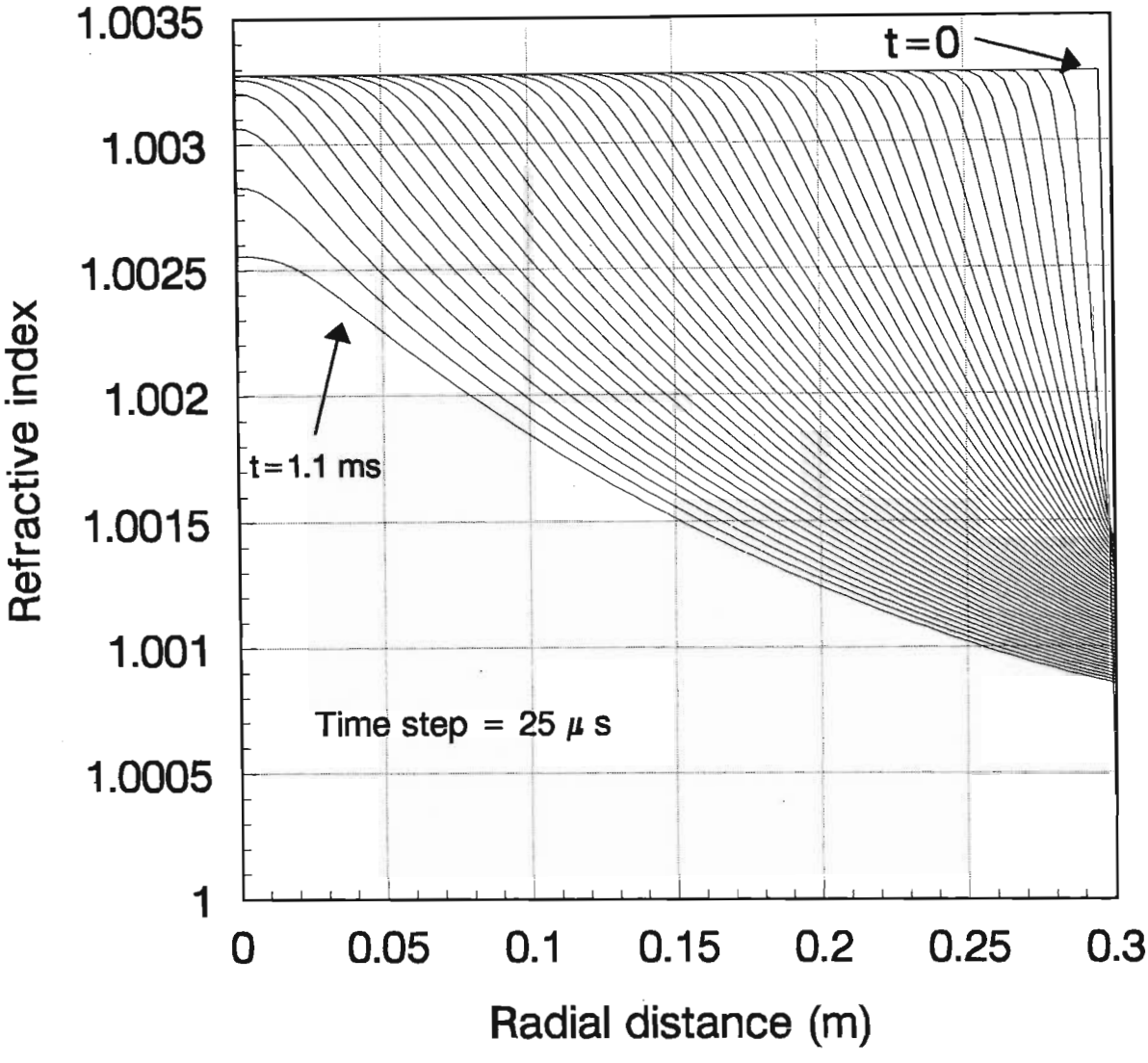

Figure 3.15: Time evolution of refractive index profiles inside an expanding gas cylinder, 0.6 m in diameter and pressurised to 8 bar.

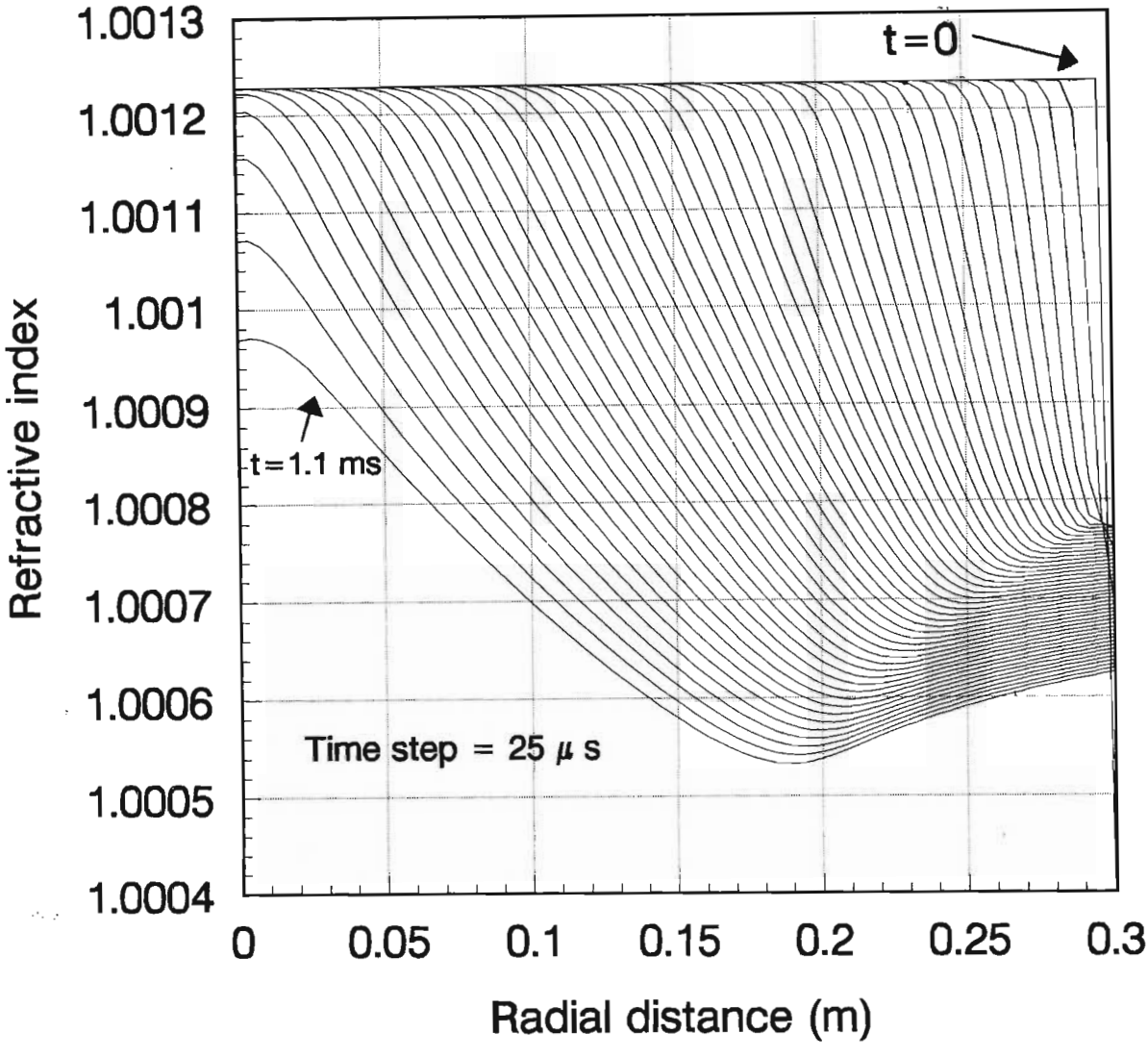

Figure 3.16: Time evolution of refractive index profiles inside an expanding gas cylinder, 0.6 m in diameter and pressurised to 3 bar.

through a slice in the y-z plane of the PGL is adequate. However, to evaluate a three-dimensional intensity distribution of the focus one has to raytrace through the whole cylindrical PGL. This is performed by raytracing an initial random mesh of rays through the PGL and performing a histogram of the ray positions in the focal plane. The above method and computer code, to determine the three-dimensional intensity distribution of the focus, was developed by Lisi to determine the focal quality of a spinning pipe gas lens [Lisi *et al.* (1993a)].

The accuracy of the raytracing technique was determined by comparing the focal length obtained by numerically raytracing through a radial refractive index given by equation 3.4 ($\alpha = 0.467$), for a lens 3 m in length and 10 cm in diameter, assuming that $\frac{n_0}{n} \simeq 1$; with the focal length obtained from the analytical solution of the ray path inside the lens given by equation 3.8. For the numerical raytrace, with a step size of 100 μm, the focal length of the lens is 0.36702 m from the end of the lens. For the analytic solution, the focal length of the lens is 0.36712453 m from the end of the lens. The numerical raytraced value is accurate to the third decimal place. If the numerical step size is reduced to 1 μm the focal length is 0.36712350 m. This result is accurate to the fifth decimal place.

A numerical raytrace was performed through the refractive index profiles of the proposed PGL given in figure 3.15 (8 *bar* pressure) for a lens 1.5 m in length. A step size of 100 μm was used to reduce the computational time. The ray paths through the lens for different times after the initiation of gas expansion are given in figures 3.17 to 3.19. The PGL proposed in section 3.4 was 3 m long. For such a lens focusing is achieved inside the PGL. The length of the proposed PGL was thus reduced to 1.5 m.

From figures 3.17 to 3.19 it is evident that the PGL produces a sharp ring

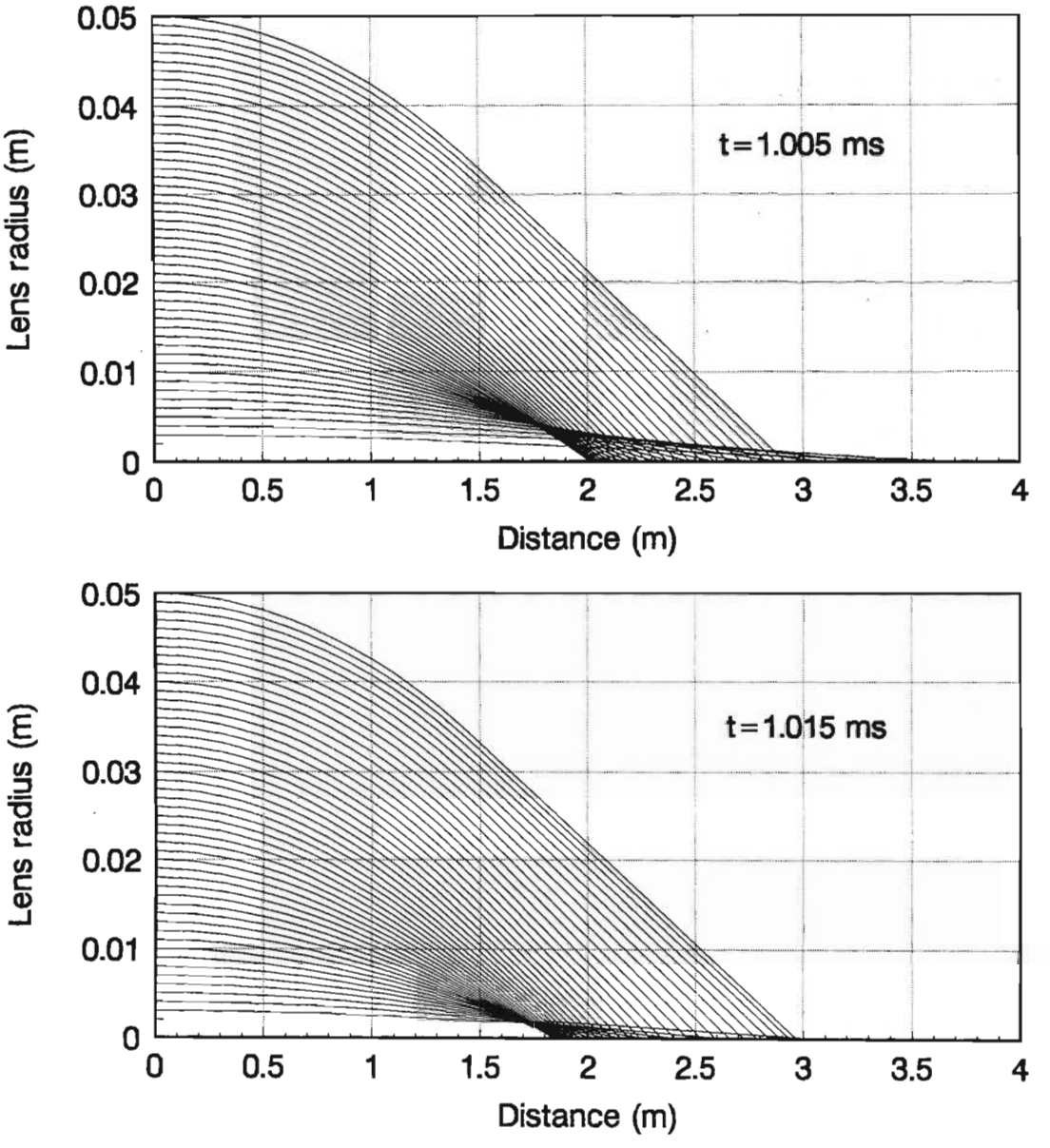

Figure 3.17: Numerical raytrace through a PGL, 1.5 m in length, 0.6 m in diameter and pressurised to 8 bar, for $t = 1.005\ ms$ and $t = 1.015\ ms$ after the initiation of gas expansion.

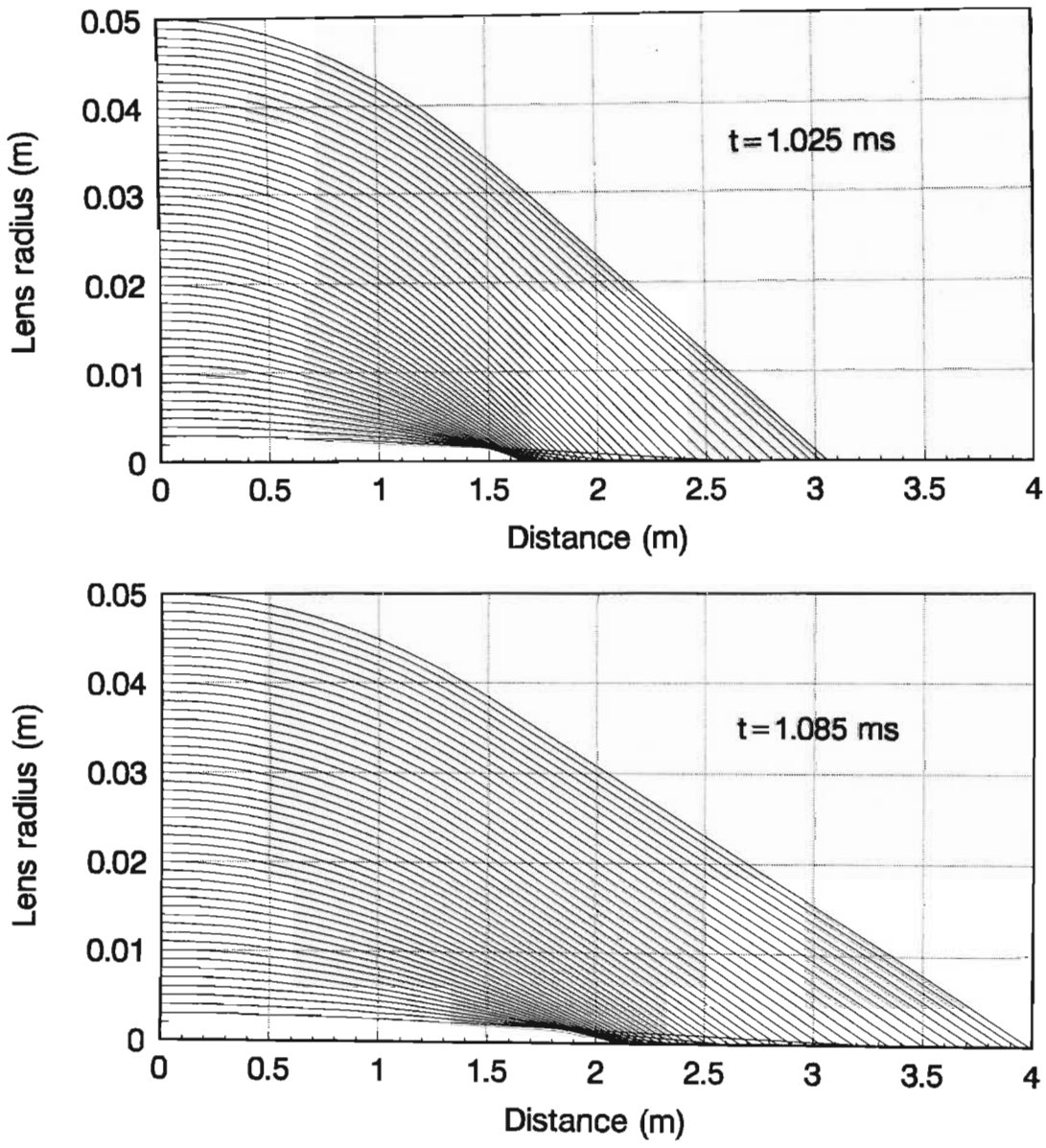

Figure 3.18: Numerical raytrace through a PGL, 1.5 m in length, 0.6 m in diameter and pressurised to 8 bar, for $t = 1.025\ ms$ and $t = 1.085\ ms$ after the initiation of gas expansion.

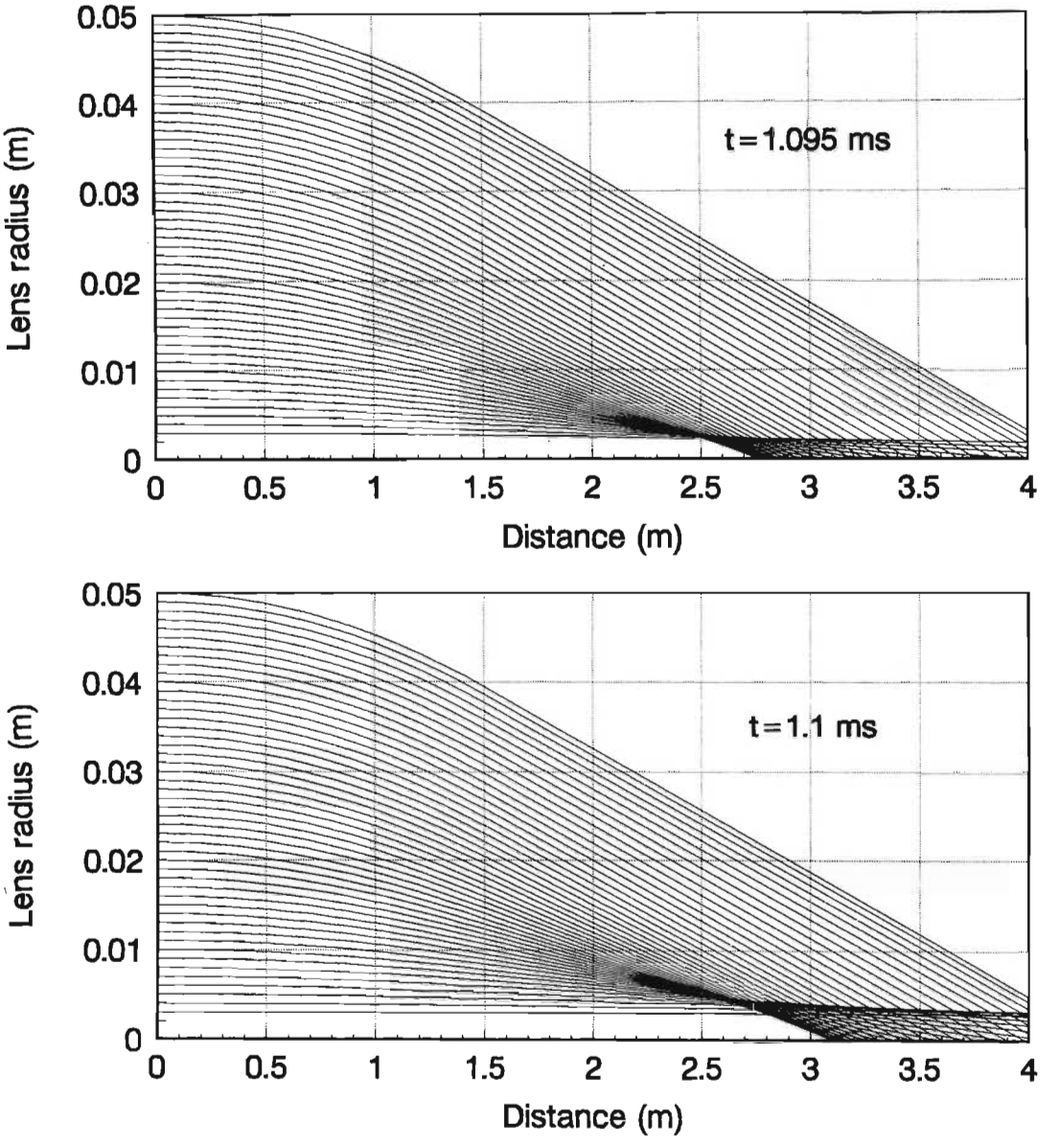

Figure 3.19: Numerical raytrace through a PGL, 1.5 m in length, 0.6 m in diameter and pressurised to 8 bar, for $t = 1.095\ ms$ and $t = 1.1\ ms$ after the initiation of gas expansion.

focus. The diameter and position of this ring focus, together with the optical diameter of the lens, is dependent on the time that laser light is passed through the PGL after the initiation of gas expansion. The optical diameter of the lens is defined as the lens diameter that produces an acceptable focus. An acceptable focus is a focus which contains a high percentage of the initial laser beam energy. If one defocuses the ring focus, the PGL at $t = 1.025\ ms$, apertured down to 5 cm in diameter, has a focal length of 20 cm (measured from the end of the 1.5 m long PGL) and a full width half maximum (FWHM) focal spot diameter of 550 μm. A three-dimensional relative intensity distribution of the focus is given in figure 3.20. The region depicted in figure 3.20 contains 99 % of the initial laser beam energy.

A problem associated with previous gas lenses, e.g. the spinning pipe gas lens [Notcutt *et al.* (1988)], is their scalability. Convection currents in large diameter spinning pipe gas lenses reduce the optical quality of the lens. An important feature of the simulated PGL is that it is scaleable.

If the diameter of the PGL is increased, the radial region suitable for focusing is also increased. A numerical raytrace through the radial refractive index field at 2.02 ms after the initiation of gas expansion for a PGL 1.5 m long, 1.2 m in diameter and pressurised to 8 bar is given in figure 3.21. A three-dimensional relative intensity distribution of the focus for the PGL apertured down to 10 cm in diameter is given in figure 3.22. The PGL has a focal length of 3.55 m from the end of the lens and a focal spot diameter (FWHM) of approximately 500 μm. The region depicted in figure 3.22 contains 88 % of the initial laser beam energy.

The focal length, optical diameter and focal spot diameter of the PGL are also dependent on the length of the PGL and the initial pressure inside the PGL. These two parameters effect the amount of refraction experienced by

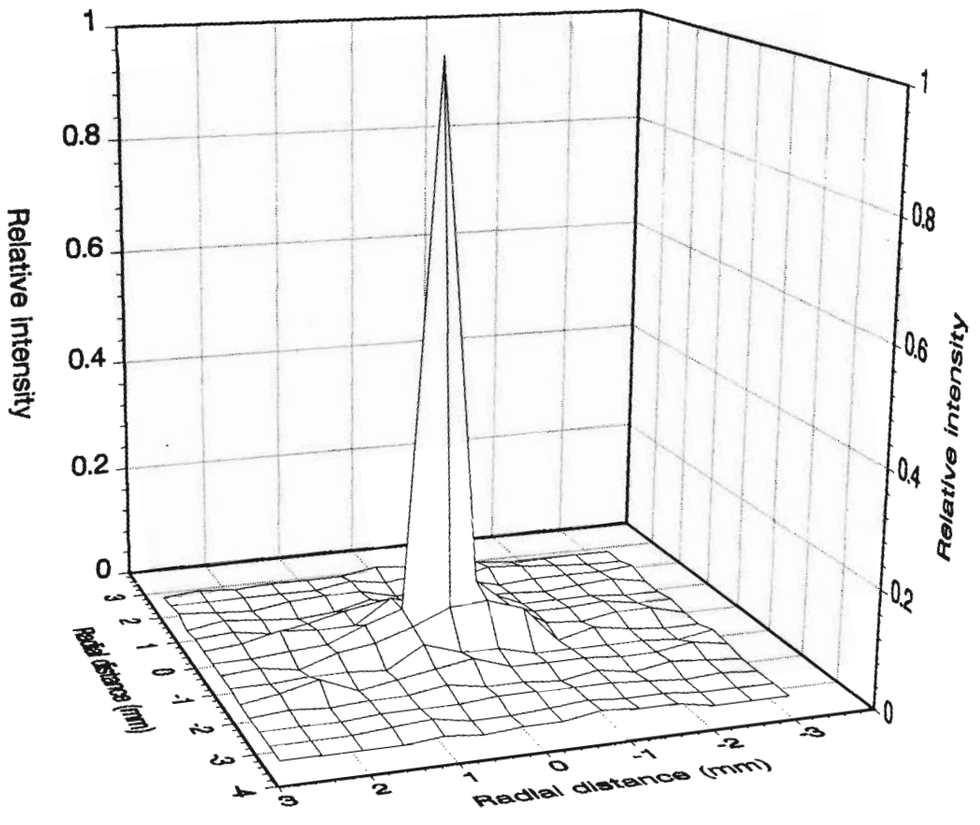

Figure 3.20: Three-dimensional relative intensity distribution of the focal spot of a PGL, 1.5 m in length, 0.6 m in diameter, pressurised to 8 bar, apertured down to 5 cm in diameter, at $t = 1.025$ ms after the initiation of gas expansion.

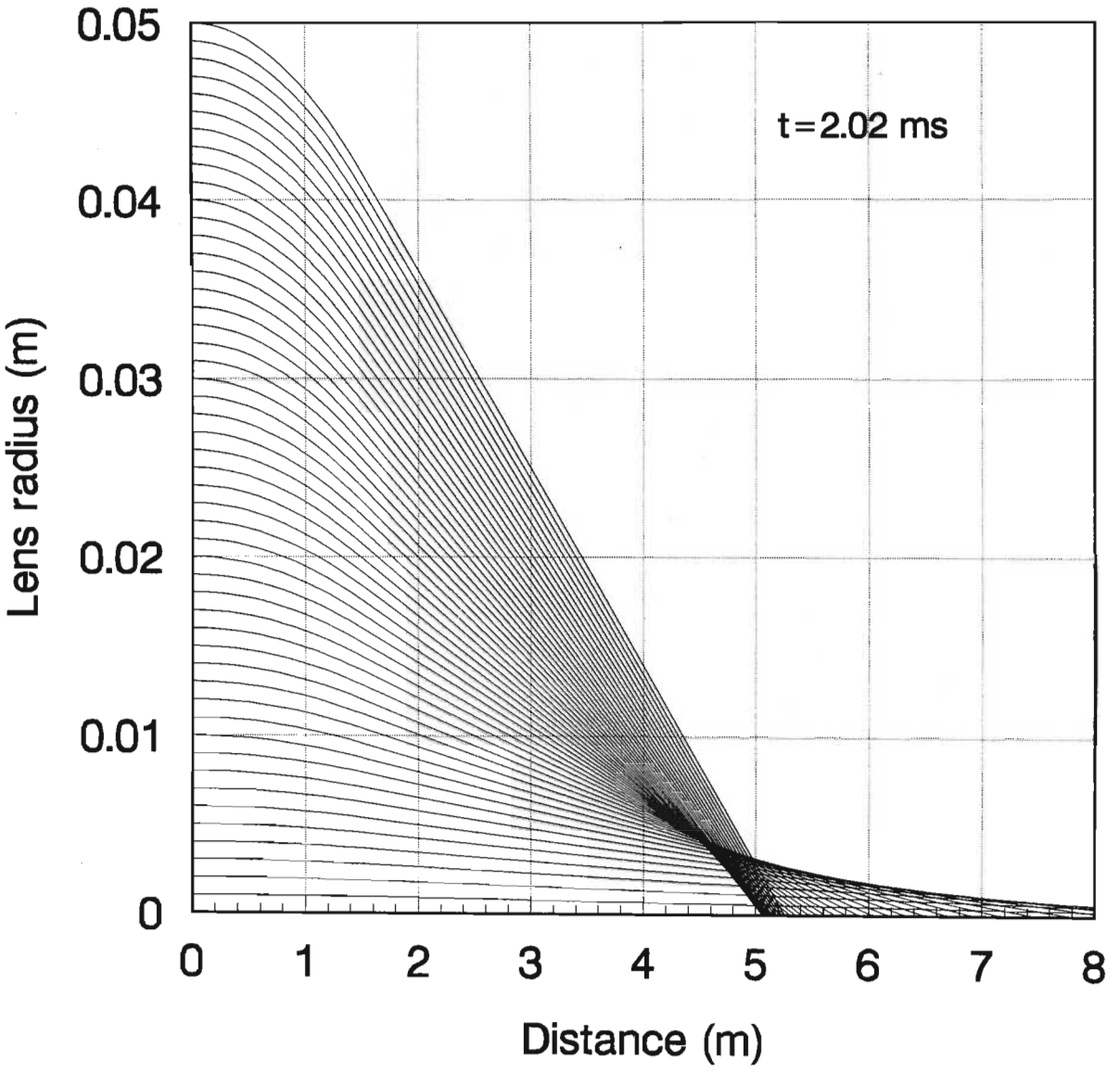

Figure 3.21: Numerical raytrace through a PGL, 1.5 m in length, 1.2 m in diameter and pressurised to 8 bar, for $t = 2.02$ ms after the initiation of gas expansion.

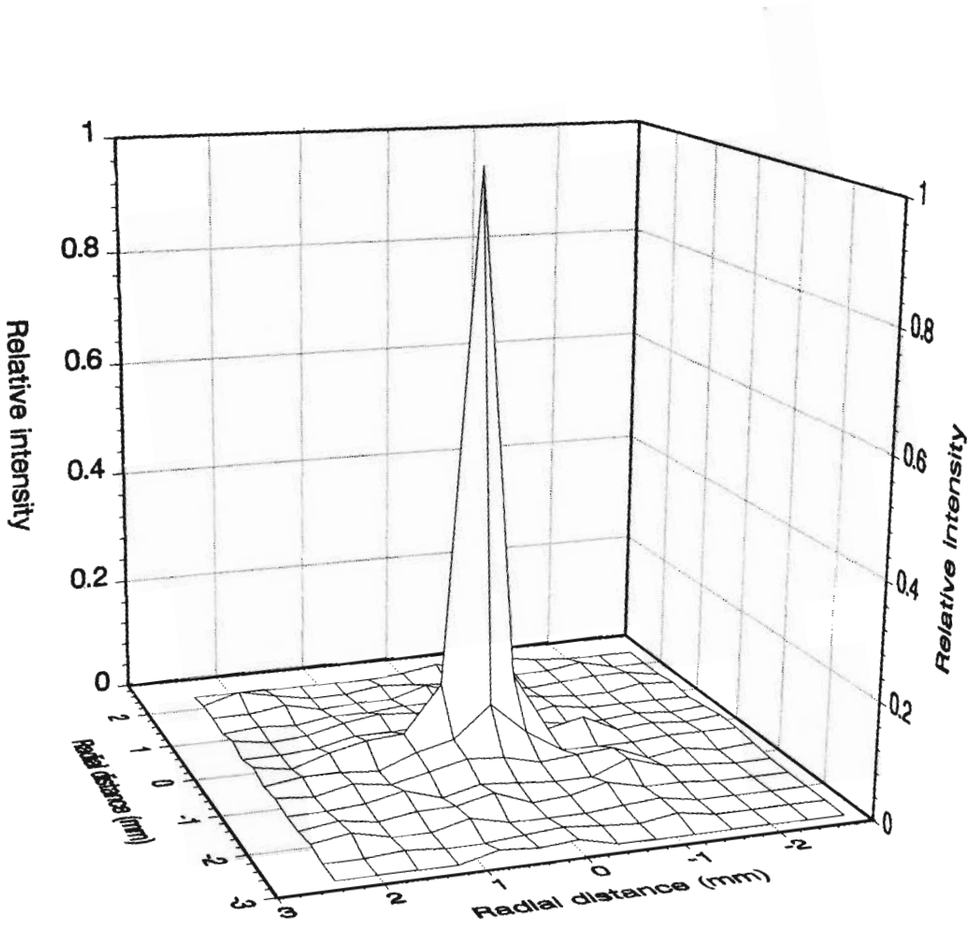

Figure 3.22: Three-dimensional relative intensity distribution of the focal spot of a PGL, 1.5 m in length, 1.2 m in diameter, pressurised to 8 bar, apertured down to 10 cm in diameter, at $t = 2.02$ ms after the initiation of gas expansion.

the light propagating in the PGL.

If one decreases the initial pressure inside the PGL, the radial refractive index gradients will decrease, resulting in the light propagating through the PGL experiencing less refraction. This decrease in gradient is evident if one compares figure 3.15 and 3.16. A decrease in refraction will result in a longer focal length and will have an effect on the optical lens diameter and focal spot diameter.

If one reduces the length of the PGL one reduces the amount of refraction the light propagating through the radial refractive index will experience. This will reduce the focal length of the PGL and will have an effect on the optical diameter and focal spot diameter of the lens.

In designing a PGL the length and diameter of the PGL, together with the initial pressure ratios, have to be chosen so as to give the desired lens optical diameter, focal spot size and focal length. If one has control over the initiation of the gas expansion and resultant flow (i.e. by fast valves), then one may be able to shape the refractive index profile to a shape better suited to maximise the lens optical diameter and minimise the focal spot diameter, for a particular focal length. This is beyond the scope of this work.

The above simulation of the performance of the proposed PGL as a focusing lens has shown that the PGL will act as a focusing element. It has shown that the optical diameter is small in comparison with the physical PGL diameter and that a sharp focus will be obtained. In the simulation several assumptions have been made which could have an effect on the lensing properties of the PGL:

- the gas has been assumed to be ideal

- the gas has assumed to be inviscid
- the gas expansion has been assumed to have been instantaneously initiated and unimpeded.

To accurately characterise the performance of the PGL as a focusing element and to test the accuracy of the numerical simulation of its performance, a PGL has to be built and tested. This will be performed in the near future by the Laser Group of the University of Natal.

3.6 Pulsed Refraction Experiment

To investigate certain practical aspects of the proposed PGL design, laser beam deflection studies were performed on a beam deflection device. A diagram of the gas-dynamic beam deflection device is given in figure 3.23. The concept is as follows: a rectangular slab of high pressure, high density, high refractive index gas is contained inside a rectangular metal box with a long rectangular window on top of the box and two optical slit apertures on either side of the box. The long window is opened allowing a plane rarefraction wave to propagate back towards the lower wall of the box. If a laser beam is directed through the box, it will be refracted by the propagating rarefraction wave. The beam deflection device can be seen as a slice in the y-z plane of the proposed PGL (figure 3.3).

The main engineering problem encountered in the proposed proof-of-principle PGL design was the opening mechanism of the gas chamber. The beam deflection device was used to develop a suitable opening mechanism.

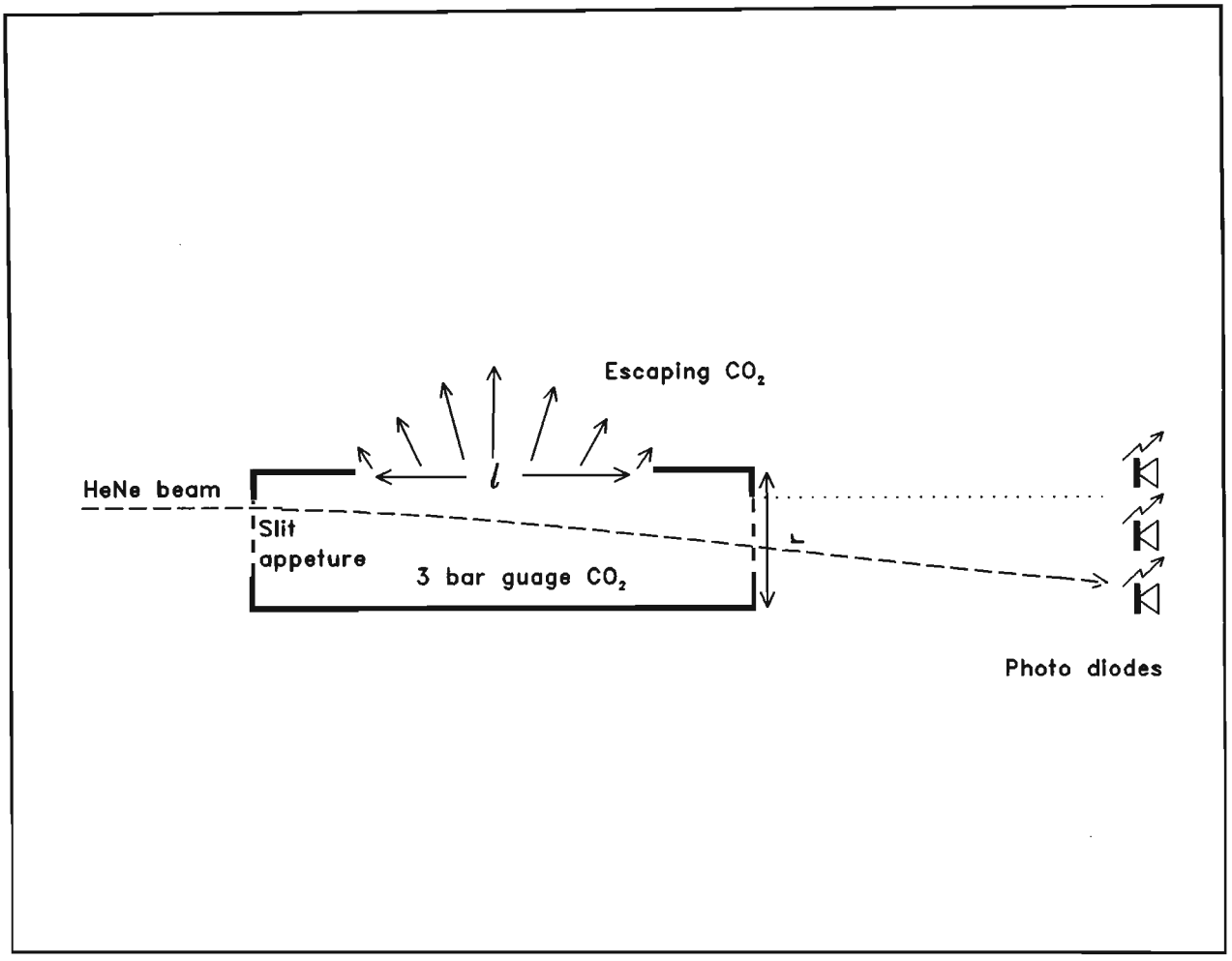

Figure 3.23: Pulsed beam deflection device.

The rarefraction wave propagates at the speed of sound in the gas, reaching the rear wall at time $t = \frac{r}{c}$. Thus, for a 30 cm deep box, assuming $c \simeq$ 300 ms the rarefraction wave will take approximately 1 ms to reach the rear wall of the box. To obtain a refractive index profile suitable for beam deflection, the window must be opened in a fraction of the time that the rarefraction wave takes to travel to the rear wall of the box ($\approx$ 0.1 ms). Commercial gate valves could not be used since they operate at least two orders of magnitude slower and only into vacuum. After considering many options on the window opening mechanism, shattering a 3 mm thick glass slide was chosen. Shattering the glass slide by over-pressurising the chamber resulted in a non-uniform and slow opening of the window. (The box is topped with a wooden structure to contain the glass fragments and the glass is held in position with a clamp and two rubber gaskets). To overcome the problem of slow opening, a 1 mm perspex flat was placed over the glass. A copper wire was placed between the glass and the perspex flat and connected to a 2 kJ capacitor bank. The box was pressurised to just below glass rupture point ($\approx$ 4 bar) and the exploding wire detonated. Fast opening of the window was obtained.

In developing the opening mechanism a further problem was encountered. Initially the chamber was pressurised with air, but on shattering of the glass window and subsequent depressurisation of the chamber, the laser beam disappeared and did not reappear for several seconds. It is estimated that adiabatic expansion from 4 bar lowers the temperature to approximately $-60°$ C, which is well below the condensation temperature of air. A TV camera placed in front of the box showed that the PGL was behaving as a cloud chamber, water vapour in the air condensing to micro droplets. A white cloud was seen escaping out of the top of the box. Shortly before the beam re-appeared, the laser path was evidenced by scattered red light inside the box. This problem was solved by pressurising the chamber with dry

carbon dioxide gas which has a condensation temperature lower than that of moist air.

To summarise, successful operation requires:

- rapid and complete opening of the window to obtain a steep density profile needed for deflection.
- choice of a gas with a high refractive index for maximum deflection and low condensation temperature.

3.6.1 Experimental Setup

The experimental setup is shown in figure 3.24. A Helium-Neon (HeNe) laser beam (1 *cm* in diameter) was directed through the beam deflection device, 5 *cm* below the glass slide, onto a vertical photo-diode array. This array consisted of 10 photo-diodes spaced 1 cm apart. The photo-diodes were configured in an on/off mode i.e. to output a 5 V volt pulse only when light was incident on them. The laser beam was positioned 1 *cm* above the first photo-diode.

The chamber was pressurised with carbon dioxide gas to 4 bar and the glass window was opened by closing switch S1, exploding the zigzag wire and shattering the glass slide. The HeNe beam was deflected down the photo-diode array and their on/off states were recorded by digital oscilloscopes.

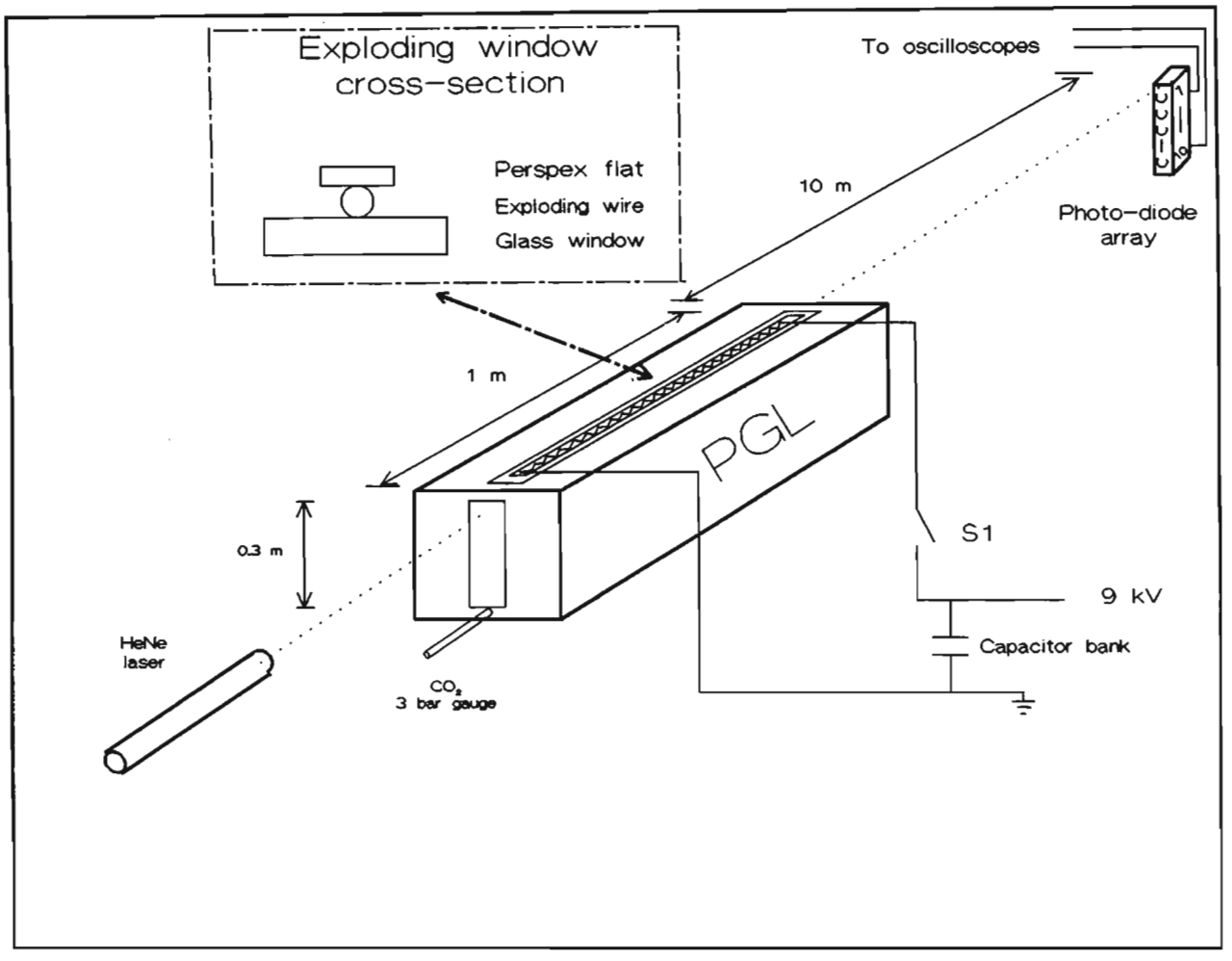

Figure 3.24: Beam deflection device experimental setup.

3.6.2 Results

Typical oscilloscope traces are shown in figure 3.25. After shattering the glass window, the HeNe beam deflected down through the first photo-diode (not shown in figure 3.25), triggering the oscilloscopes. Approximately 0.6 ms after the oscilloscopes were triggered, the beam passed through the second photo-diode (2 $mrad$ downward deflection) and $\approx$ 0.4 ms later, the beam passed through the third photo-diode (3 $mrad$ downward deflection). No signal was observed on the fourth photo-diode.

The deflections of the laser beam observed after 2 ms are possibly due to the gas flow inside the chamber after the rarefraction wave reaches the rear wall of the box. A further possibility is the smearing of the 1 cm in diameter HeNe laser beam during deflection, resulting in the beam intensity being below that required to trigger the photo-diodes.

The beam deflection results were not reproducible from shot to shot. This was due to the difficulty in repeating the opening conditions of the chamber by the method of shattering the glass window.

3.6.3 Beam Defection Device Simulation

The FLIC computational scheme used to simulate the cylindrical PGL operation in section 3.5.2 was used to simulate the beam deflection device operation. The computational mesh is given in figure 3.26. The mesh is a cartesian co-ordinate system of cells where each cell is a right parallelepiped with dimensions given by equations A.1 to A.3. Boundaries 1, 2, 3, 4 and 6 are closed, allowing the gas only to expand out the device through the open

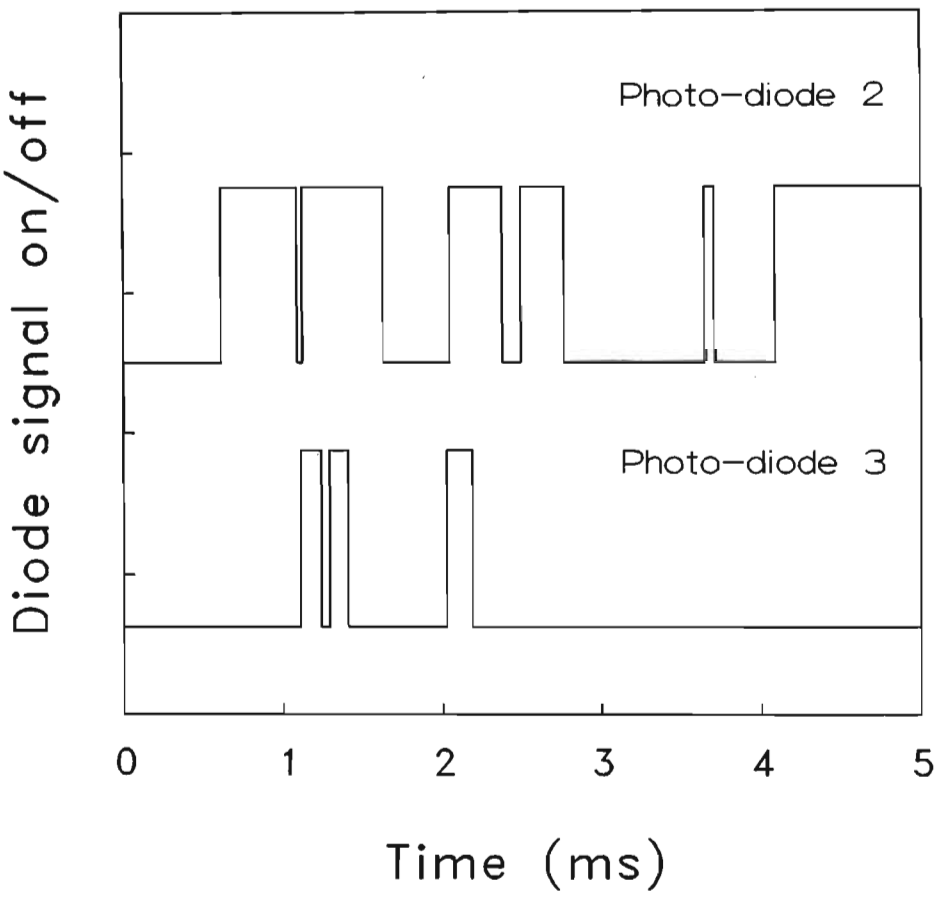

Figure 3.25: Typical photo-diode deflection traces of the beam deflection device.

boundary 5. Cells 2 to 150, in the y direction, model the conditions inside the device while cells 151 to 300 model the conditions outside the device. The computational mesh represents half the beam deflection device. It is assumed that the two halves are mirror images of each other.

The beam deflection device is pressurised with carbon dioxide gas to 4 *bar*. The diaphragm, containing the high pressure gas inside the device, is instantaneously removed and the gas is assumed to expand into a region of carbon dioxide gas at atmospheric pressure. A three dimensional plot of the refractive index within the device, 0.75 ms after initiation of gas expansion, is given in figure 3.27. Two rarefraction waves are evident: one wave propagates down to the rear wall of the device while a second wave propagates sideways to the enclosed side wall of the device. Vortex action around the flow corner of the device (y=0.3 m, z=0.5 m) is evident.

The laser beam entering the chamber at $y = 0.25\ m$ experiences minor refraction in the enclosed region of the device ($z < 0.5\ m$) since the refractive index gradients, perpendicular to the laser beam, are small. Major refraction is experienced by the laser beam in the open region of the device ($z > 0.5\ m$). A time evolution of the refractive index profiles within the chamber for $z = 0.9\ m$ are given in figure 3.28. The observed features; the propagating rarefraction wave, contact surface and shock wave, are similar to those seen in figures 3.9 and 3.12. The oscillations at the shock front are due to no explicit artificial viscosity terms ($K = 0, B = 0$) being used in the simulation. The above curves were computed for $\delta z = 1\ cm$, $\delta y = 2\ mm$ and $\delta t = 2.5\ \mu s$.

Laser beam deflection commences when the rarefraction wave traverses the initial laser beam position ($y = 0.25\ m$). From figure 3.28 this occurs approximately 0.18 ms after the initiation of gas expansion. Maximum deflection is obtained when the refractive index gradient reaches a maximum at the initial

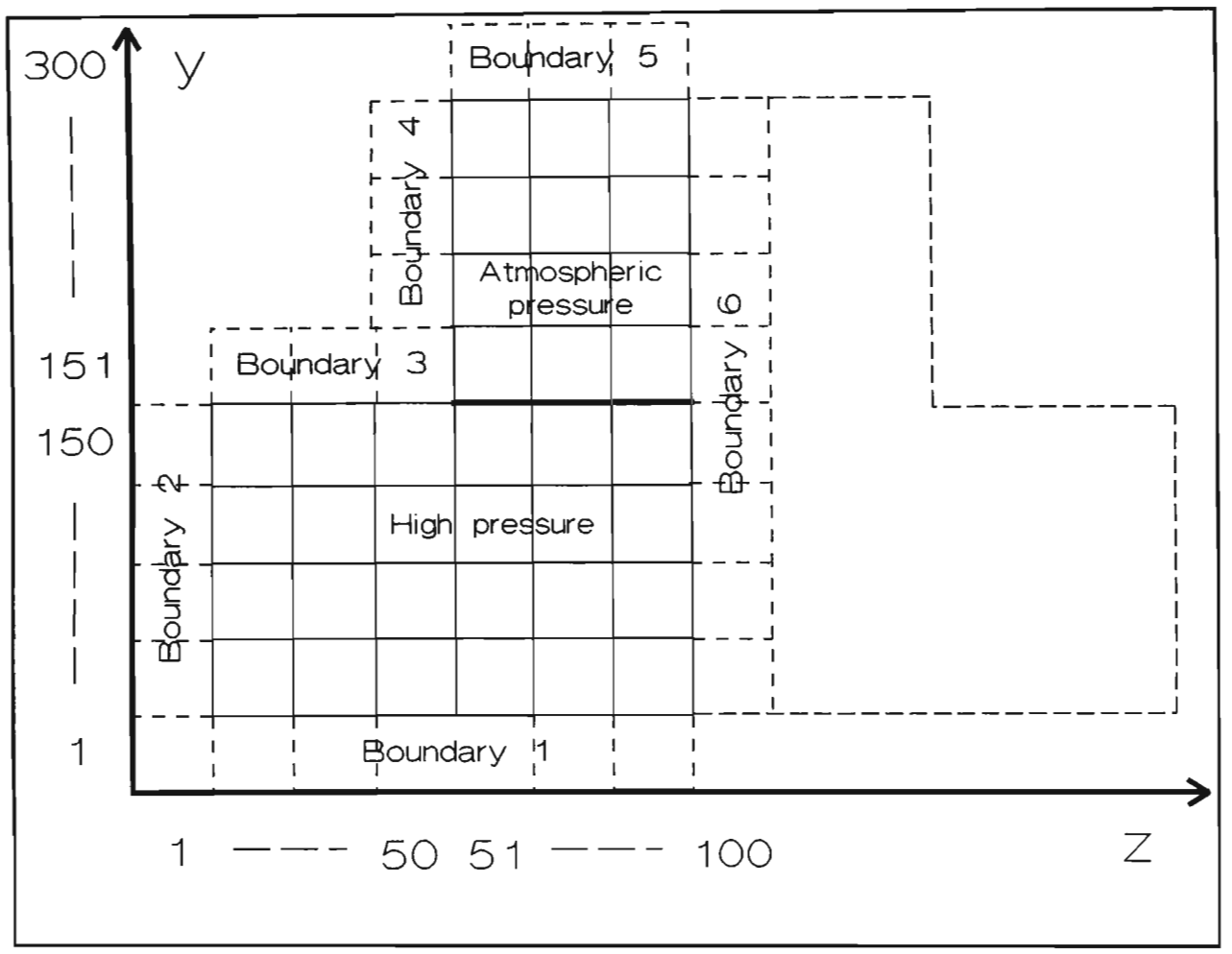

Figure 3.26: Beam deflection device computational mesh.

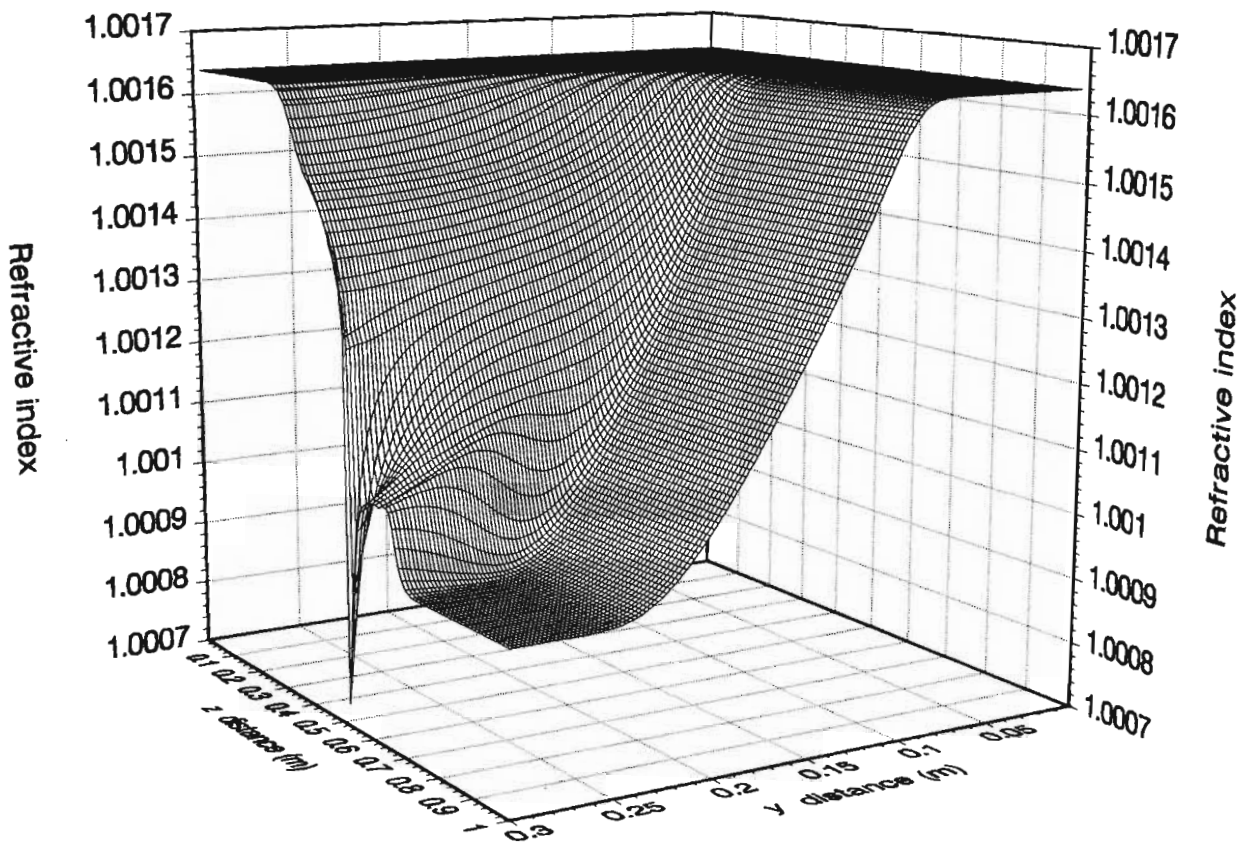

Figure 3.27: A three-dimensional representation of the refractive index profile inside the beam deflection device 0.75 ms after initiation of gas expansion.

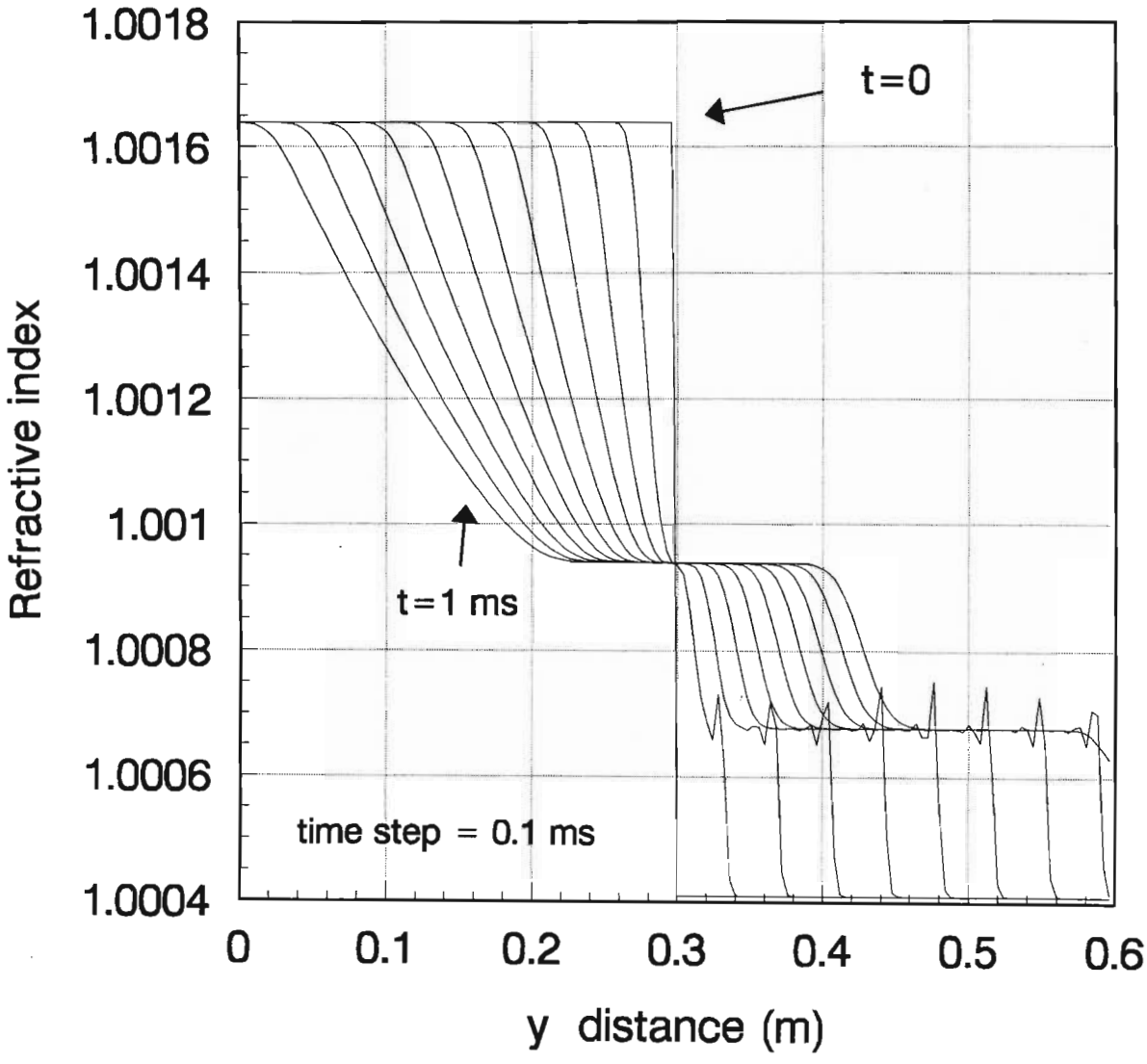

Figure 3.28: A time evolution of the refractive index profiles inside the beam deflection device at $z = 0.9\ ms$.

laser beam position. This occurs approximately 0.2 ms after the initiation of gas expansion. The refractive index profile at this time is approximately linear and the graded index formula (equation 3.11) can be used to estimate the deflection of the laser beam. The deflection is 15 $mrad$. This corresponds to a downward deflection of 15 cm over 10 m. At 1 ms the refractive index gradient at $y = 0.25$ m is approximately 0, thus no significant beam deflection will occur.

When comparing the simulated and experimentally measured laser beam deflection, it is important to note that the timing of the simulated data is relative to the initiation of gas expansion, while the timing of the experimental data is relative to the triggering of the first photo-diode which is 1 cm below the initial undeflected beam.

Considering this timing difference, the simulated and the experimental laser beam deflections, do not agree. The maximum measured deflection of 3 cm occurred at 1 ms while the maximum simulated deflection of 15 cm occurred at 0.2 ms.

This leads one to conclude that the initiation of the gas expansion by rupturing the glass is not instantaneous and uniform, over the length of the window, as assumed in the simulation and that this does have an effect on the expansion of the gas. For a non-instantaneous opening, the beam deflection device will empty at a slower rate and the refractive index gradients will not be as steep as in an instantaneous opening.

There are two possible solutions to circumvent this problem. Firstly, the opening of the beam deflection device can be incorporated into the simulation to obtain a more accurate model of the system. If one assumes that the glass slide does not shatter, but moves as a whole, the glass slide can be

incorporated into the computer code as a closed boundary. The position of this boundary, at each time step of the calculation cycle, would be determined from the pressure acting on the glass slide. The gas would expand out the device through the side boundaries, opened by the moving closed boundary. To simulate a non-uniform opening, over the whole length of the window, some of the cells making up the closed boundary could be opened. This would allow gas expansion vertically and laterally which is more realistic. Secondly, the method of initiating the gas expansion can be modified to be more uniform and instantaneous to match the performed simulations. A possible solution could be the method used in shock tubes: to use a material like mylar instead of glass, pressurise it near to breakpoint and shattering the mylar using an exploding wire [Perry and Kantrowitz (1951)].

3.7 Conclusion

The computer simulations of the proposed proof-of-principle PGL have shown that the PGL can be used as a focusing lens if the initiation of gas expansion is instantaneous and that the gas flow is not impeded by the physical construction of the PGL. An experiment performed on a beam deflection device showed that the proposed opening mechanism is not instantaneous as assumed in the simulation. The opening mechanism of the PGL has to be modified to decrease the opening time. The opening process must be incorporated into the computer simulation to obtain a better model for the PGL operation and lensing properties.

Chapter 4

The Colliding Shock Lens

4.1 Introduction

Gas lenses have traditionally been continuous wave devices. The concept of pulsed gas lenses, where an inhomogeneous gas medium momentarily focuses laser light, offers many potential applications: optical switches and optical isolators to name but a few. The Pulsed Gas Lens (PGL), presented in Chapter 3, was designed to focus large diameter laser beams and consequently it is a bulky device. A small, robust and portable pulsed gas lens, capable of focusing small diameter laser beams which are commonly found in commercial lasers, would have vast industrial and research applications.

In the experiment described in this chapter [Buccellato *et al.* (1993b)] a pulsed gas lens, using converging shock waves, is presented: the Colliding Shock Lens (CSL). The formation of the lensing region and the lensing properties of the CSL were investigated using the Refractive Fringe Diagnostic

(RFD). A numerical simulation of the CSL was performed to model the behaviour of the lens. Future development and applications of the CSL are discussed.

4.2 Converging Shock Waves: a brief historical review

The converging shock wave problem has received a great deal of interest, both theoretically and experimentally. The interest in converging shock waves lies in the localised region of high density, pressure and temperature obtained on implosion. This region has offered a number of applications in the fields of applied physics and engineering e.g. thermonuclear fusion and material science.

4.2.1 Theoretical Review

The first analytical solution for the converging cylindrical and spherical shock wave problem, for ideal gases, was presented by Guderley [Guderley (1942)]. This was followed by the solutions of Butler [Butler (1954)] and Stanyukovich [Stanyukovich (1960)]. In these self-similar solutions, the flow variables do not depend on position and time independently. They depend on a particular combination of them. Due to the requirement of no characteristic length and infinitely strong shock waves, the applicability of these solutions are limited to the region near the implosion centre. The similarity solution models the asymptotic nature of all converging shock waves irrespective of their generation.

Lee [Lee (1967)] extended the self-similar solution to include the finite strength of the shock wave, for earlier times, in the implosion process. His quasi-similar solution asymptotically approaches the self-similar solution on convergence. However, this solution is still restricted to a small region near the implosion centre.

Bach and Lee [Bach and Lee (1969)] presented an analytic solution for the initial stages of convergence for a spherical and cylindrical shock wave generated by the uniform and instantaneous energy deposition at a spherical or cylindrical surface. This solution is restricted to small distances from the shock wave formation surface.

To accurately model the converging shock wave process, a numerical solution is needed to solve the time dependent equations of motion governing the flow process. Various numerical solutions have been presented which model this process for different methods of shock wave formation.

The cylindrical shock tube has been widely used in numerical models as a method of producing converging cylindrical shock waves. A diaphragm separates a cylindrical region of stationary high pressure gas from a central cylindrical region of stationary low pressure gas. When the diaphragm is instantaneously removed, a converging shock wave is produced. After convergence, a reflected diverging shock wave is formed.

Payne [Payne (1957)] used the finite difference method of Lax to model this process (a detailed description of the different types of finite difference methods is given by Roach [Roach (1985)]). Lapidus [Lapidus (1971)], using a Cartesian method in two-space dimensions, and Abarbanel and Goldberg [Abarbanel and Goldberg (1972)], using the Lax-Wendroff finite difference method, concluded that the simulation of Payne did not accurately model

the shock wave speed. Sod [Sod (1977)] proposed the random choice method of Glimm [Glimm (1965)] with operator splitting. The results obtained were in general agreement with those obtained by Payne, Lapidus, and Abarbanel and Goldberg. However, the time of arrival of the converging shock wave at the implosion centre was only in agreement with that of Abarbanel and Goldberg. An advantage of this method was the sharpness of the shock front and contact discontinuity obtained. The previous methods lacked this feature. Ben-Artzi and Falcovitz [Ben-Artzi and Falcovitz (1986)] employed a second order upwind differencing scheme to simulate this process. Their results were in agreement with those of Abarbanel and Goldberg and Sod. Recently, Srivastava *et al.* [Srivastava *et al.* (1992)] have employed the finite difference scheme of Rusanov to model the flow of cylindrical and spherical shock waves generated by large initial pressure ratios. Previous methods only considered moderate initial pressure differences.

Instantaneous energy deposition on a spherical or cylindrical surface has also been used in numerical simulations of converging shock waves as a method of shock wave generation. This has been achieved by coating cylindrical or spherical surfaces with explosives. On detonation a converging shock wave is produced. A reflected diverging shock wave is formed after shock wave convergence.

Matsuo has applied different numerical methods to model cylindrical converging shock waves produced in this fashion. The solution obtained using the method of integral relations [Matsuo (1979)] matched the solution of Bach and Lee near the cylindrical surface and was smoothly continuous to Guderley's solution near the implosion centre. The self-similar limit of Guderley, on implosion, was not reached. A problem associated with the method of integral relations was the deterioration of the convergence of the method near the vicinity of the implosion centre.

The method of characteristics and the random choice method [Matsuo (1988)] were found to model the convergence process accurately. The solution approached the self-similar limit of Guderley on implosion and Guderley's self-similar solution was found to hold near the vicinity of implosion, but only for a small distance behind the shock front. The self-similar distribution of particle velocity was found to be accurate for a large region behind the shock front.

Several finite difference methods with explicit artificial viscosity were tested [Matsuo (1988)] to model the converging shock wave process. The second order MacCormack scheme was found give the best results. However, no indication of the different types of schemes tested is given. The results compared favourably with those obtained with the method of characteristics and the random choice method except for the region near the implosion centre. The artificial viscosity term which was needed to stabilize the solution, smeared the shock front near the implosion centre.

In view of the accuracy obtained with the random choice method in modeling the converging shock wave process, this method was used to model the reflected divergent shock wave obtained after shock wave convergence [Matsuo (1990)]. The results obtained compared favourably with experimental results and highlighted the credibility of the numerical method.

The problem of converging spherical shock waves has been dealt with by Saito and Glass [Saito and Glass (1982)] to model their hemispherical, explosive driven, implosion chamber. Using the random choice method of Glimm and operator splitting, reasonable accord with experimental results was obtained.

4.2.2 Experimental Review

The first experimental production of converging cylindrical shock waves was performed by Perry and Kantrowitz [Perry and Kantrowitz (1951)]. They used a cylindrical shock tube, with a centered tear drop shaped body near the end of the shock tube, to turn a planar shock wave by 90° and force it to converge (figure 4.1(a)). Schlieren photographs of the converging shock wave and the resultant reflected diverging shock wave, showed the process to be stable for weak shock waves (figure 4.1(b)). A decrease in stability was observed for strong imploding shock waves. A similar technique was used by Wu *et al.* [Wu *et al.* (1980)] to produce converging cylindrical shock waves. An annular shock tube with an axisymmetric area contraction at the end of the shock tube was used to turn the shock wave by 90° and force it to converge (figure 4.2(a)). Shadowgraphs were used to study the stability of the convergence process. It was found that the converging shock wave was stable except near the implosion centre where a breakdown in shock front curvature was evident (figure 4.2(b)). This instability was found to be more pronounced if the initial cylindrical symmetry of the converging shock wave was perturbed [Wu *et al.* (1981)].

Dennen and Wilson [Dennen and Wilson (1962)] produced converging cylindrical shock waves by exploding thin metal films over the inner surface of glass cylinders. Using Schlieren photography, the time-space relation of the converging shocks were found to be approximated by Guderley's solution.

Imploding detonation waves can be used to produce converging cylindrical shock waves. Lee and Lee [Lee and Lee (1965)] used a cylindrical exploding detonation wave in an exploding chamber, to produce an imploding detonation wave in an adjacent implosion chamber. The chambers were filled with an equi-molar acetylene-oxygen mixture. Near implosion, the chemical

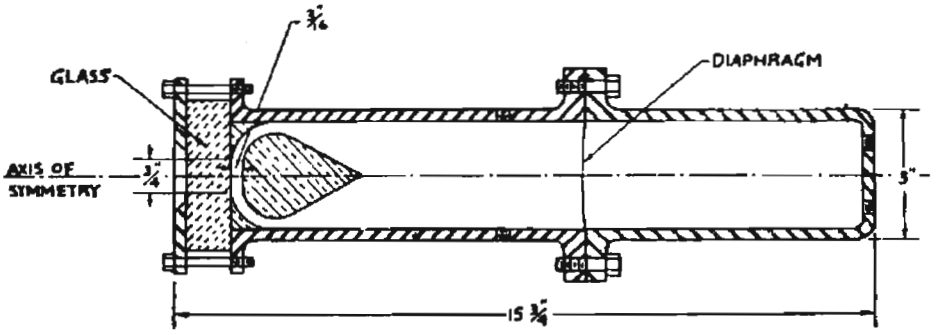

a)

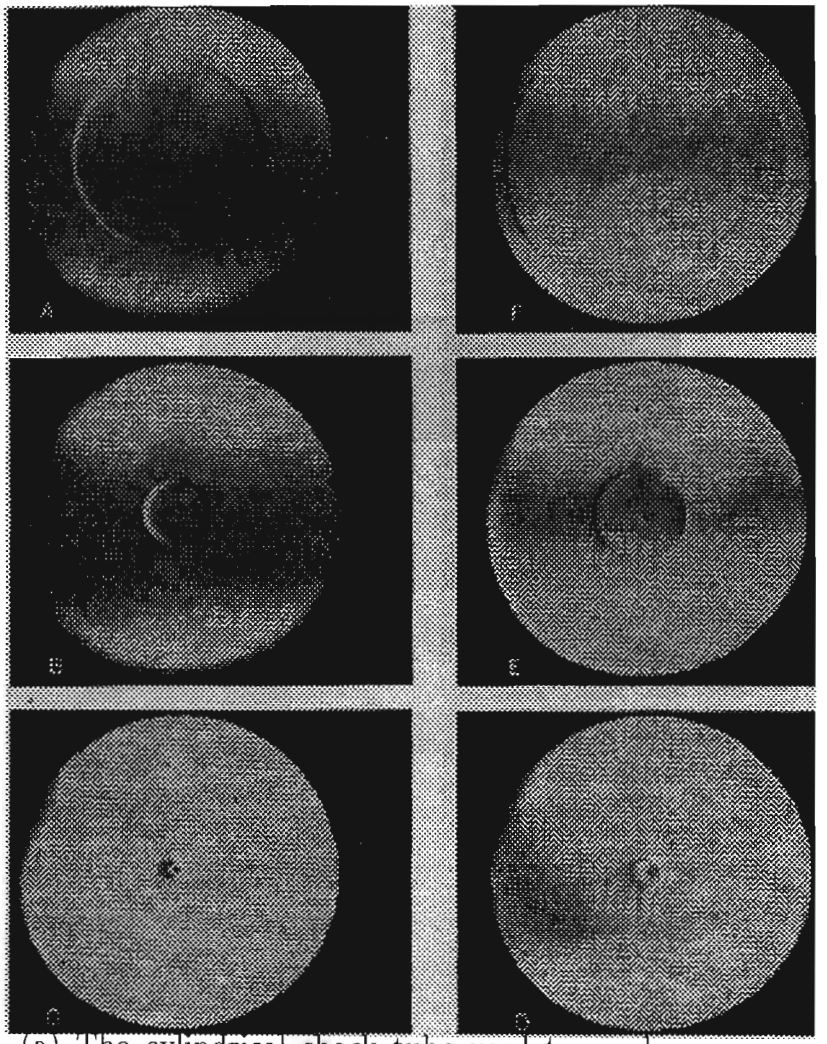

b)

Figure 4.1: (a) The cylindrical shock tube used to produce a converging cylindrical shock wave. (b) Schlieren photographs of the convergence process [Perry and Kantrowitz (1951)].

a)

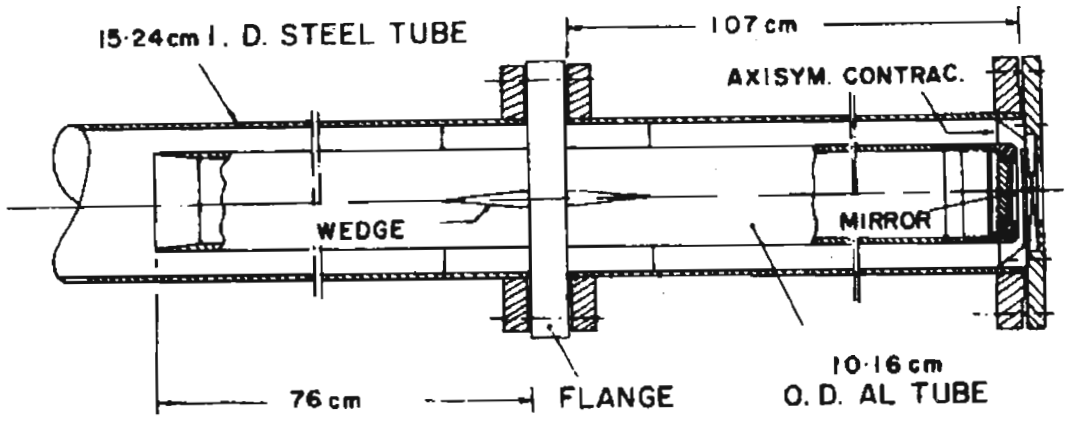

b)

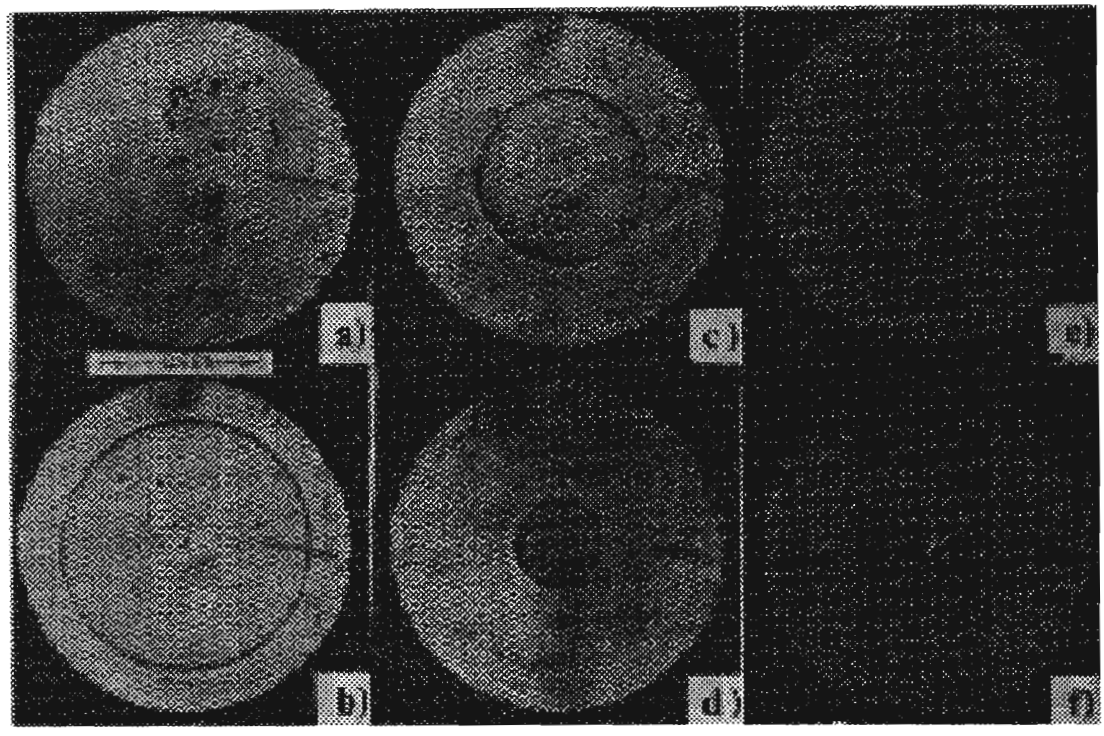

Figure 4.2: (a) The annular shock tube used to produce a converging cylindrical shock wave. (b) Shadowgraphs of the convergence process [Wu *et al.* (1980)].

energy released at the detonation wavefront is much less than the pressure energy driving the wave. The detonation wave then approaches a strong converging shock wave. Ahlborn and Huni [Ahlborn and Huni (1969)], using a similar device as Lee and Lee, photographically showed that converging detonation waves were stable. Knystautas *et al.* [Knystautas *et al.* (1969)] developed a different technique to produce converging detonation waves (figure 4.3(a)). Planar detonation wavelets were used to create a converging polygonal shaped wavefront. On convergence, the curvature of the polygonal shaped wavefront was smoothed and a cylindrical shaped wavefront was obtained. Schlieren photographs show that the implosion and resultant expansion process is stable (figure 4.3(b)).

Exploding detonation waves reflected off a hemispherical surface can be used to produce converging shock waves. The UTIAS implosion chamber at the University of Toronto, Canada, has been used to study this process. An exploding wire, at the origin of a hemispherical chamber which is filled with a combustible gas at high pressure, produces an exploding detonation wave. On reflection with the hemispherical wall, the exploding detonation wave produces an imploding hemispherical shock wave. If the hemispherical wall is coated with explosives, the gaseous exploding detonation wave detonates the explosive shell and a strong imploding shock wave is produced (figure 4.4). Several spectroscopic investigations have been performed on this device for different initial conditions [Roberts and Glass (1971), Roig and Glass (1977), Saito and Glass (1982)].

Converging cylindrical shock waves have been generated in atmospheric air by detonating explosives over cylindrical surfaces (figure 4.5(a)). The explosives were detonated by exploding wires. Numerous studies have been performed by Matsuo at Kumamoto University, Japan. Using streak and framing cameras it was found that the imploding shock waves were self-

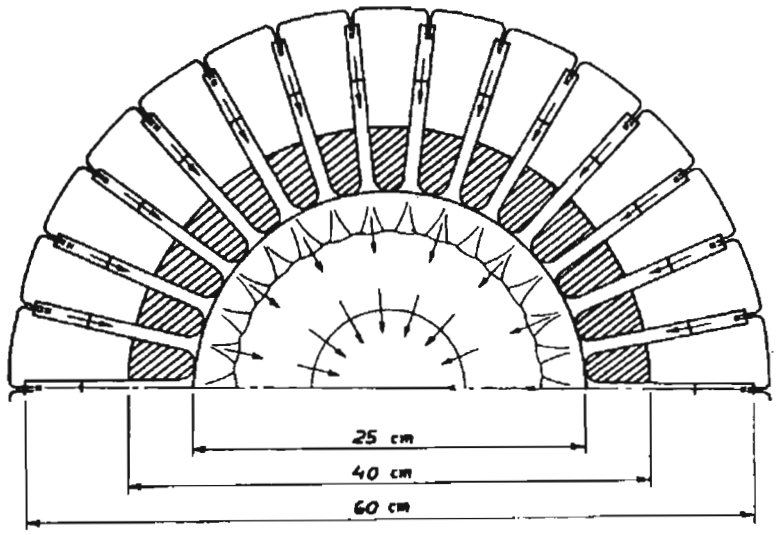

a)

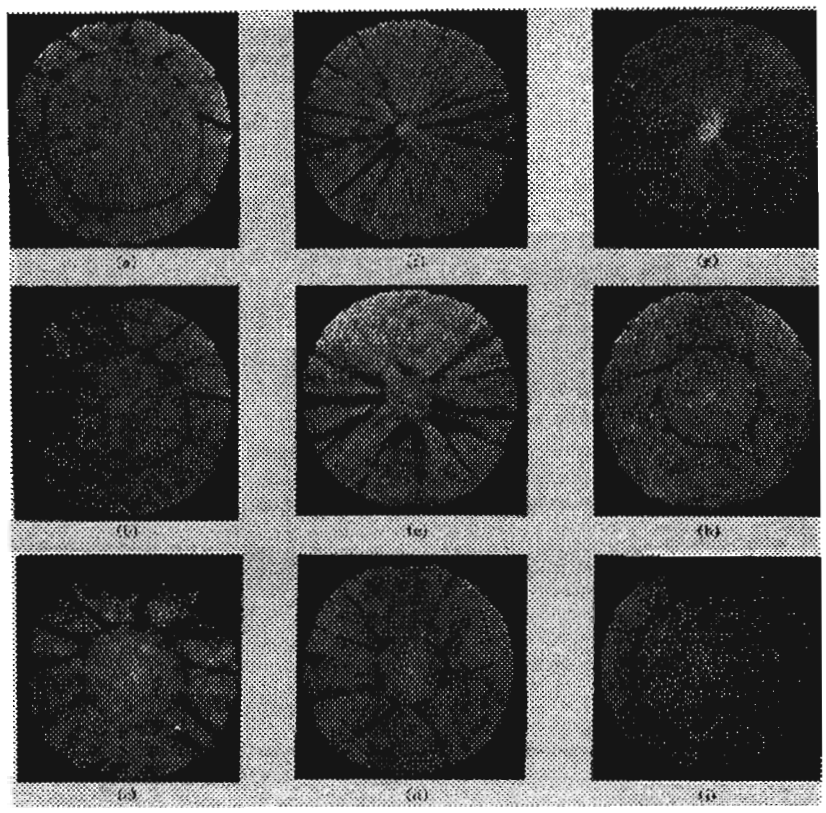

b)

Figure 4.3: (a) The initiation method of cylindrical converging detonation waves. (b) Schlieren photographs of the implosion process [Knystautas *et al.* (1969)].

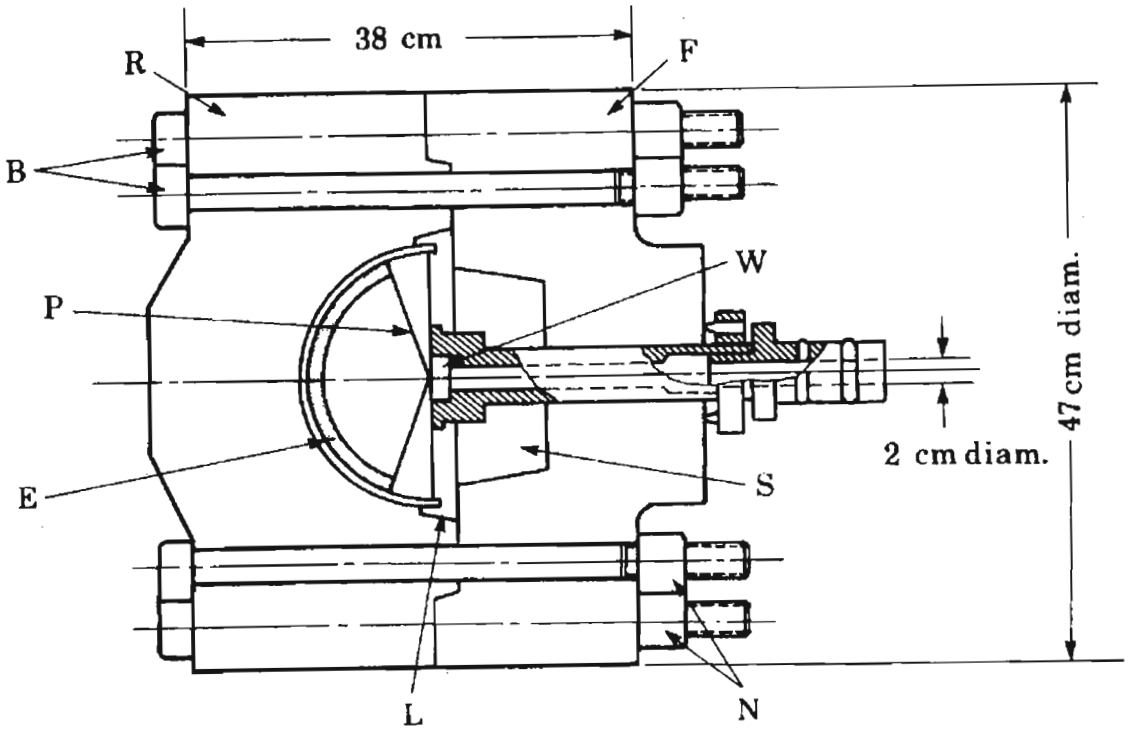

UTIAS implosion chamber: B, bolts; P, protecting plate; E, PETN explosive liner; L, liner plate; F, front plate; R, rear plate; S, segmented cone; N, nuts; W, Plexiglas window.

Figure 4.4: The UTIAS implosion chamber [Saito and Glass (1982)].

luminous [Matsuo and Nakamura (1980)]. In the same study, the time-space relation of the converging shock front was determined by electrical ionization probes. It was found that the measured shock front trajectories were in good agreement with Guderley's prediction over a wide region near implosion. By increasing the quantity of explosives, it was found that stronger and more stable converging shock waves were produced (figure 4.5(b)) [Matsuo and Nakamura (1981)]. The reflected divergent shock wave was also found to be very stable. The stability of the implosion process was studied by laser shadowgraphy and a spectroscopic study was performed [Matsuo *et al.* (1984)]. It was found that the converging cylindrical shock wave, near the implosion centre, was slightly unstable (figure 4.5(c)). This instability was reduced by improving the uniformity of the wire explosion which detonated the explosives (figure 4.5(d)) [Matsuo *et al.* (1985)]. Spectroscopic temperature measurements for different quantities of explosives were also performed. The measured temperatures on implosion were found to be approximately proportional to the square root of the initiation energy.

The region of high pressure, temperature and density near the implosion centre has been used for various applications. The UTIAS hemispherical implosion chamber has been used as a hypervelocity launcher [Flagg and Glass (1968)]. A barrel was connected to the origin of the hemispherical chamber and a plastic projectile was driven to large velocities by the imploding shock wave. A similar arrangement was used for a hypervelocity shock tube [Glass *et al.* (1974)]. The imploding spherical shock wave produced a strong planar shock wave in a cylindrical shock tube which was connected to the origin of the hemispherical chamber. Industrial diamonds have been synthesised by the compression of graphite powder, at the origin of the hemispherical implosion chamber, by the imploding shock wave [Glass and Sharma (1976)]. Neutrons and γ rays, resulting from the fusion of deuterium, have been produced by the hemispherical implosion of a shock wave in a stoichiometric

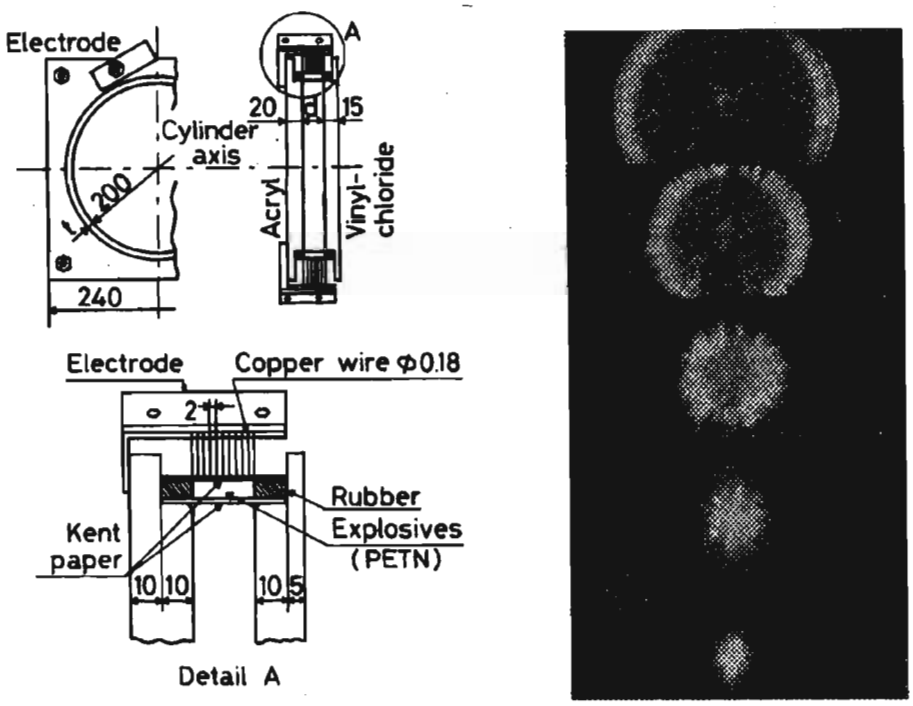

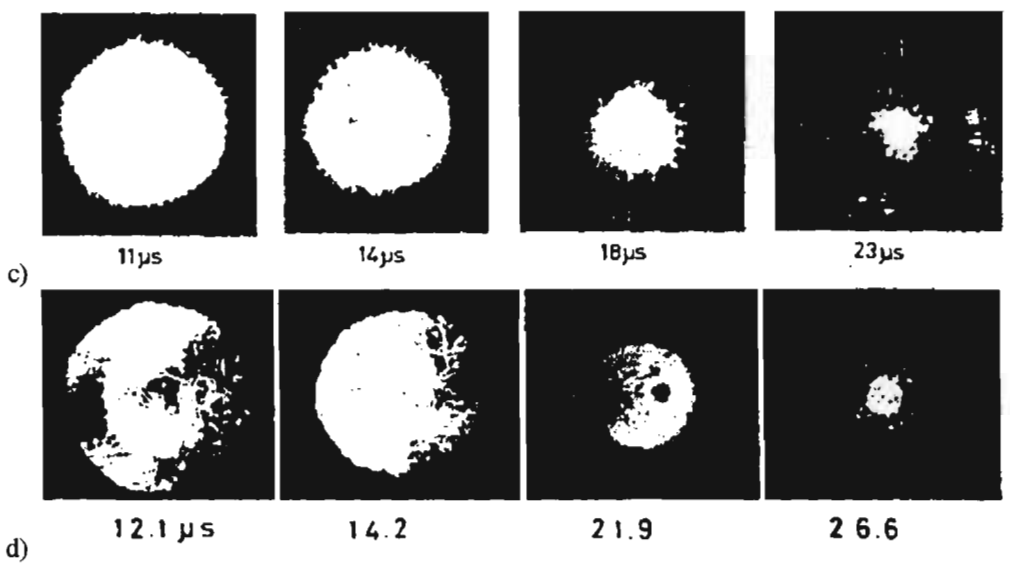

Figure 4.5: (a) The implosion chamber used to produce converging cylindrical shock waves (dimensions in mm). (b) Framing camera photographs of the implosion process. (c) Shadowgraphs of an unstable implosion. (d) Shadowgraphs of a stable implosion. [Matsuo *et al.* (1980) (1981) (1984) (1985)]

mixture of deuterium-oxygen [Glass and Sagie (1982)].

The above applications have concentrated on the implosion region of the converging shock waves. The CSL utilises the reflected region, after convergence, to focus laser light.

4.3 The Colliding Shock Lens Principle

Diverging spherical shock waves, originating from equi-spaced points on a circumference, produce a cylindrically symmetric converging shock wave. After implosion, a cylindrically symmetric diverging shock wave is formed. The region bounded by this reflected diverging shock wave has been found to be suitable to focus laser light. This process, from shock wave generation to lens formation, will be dealt with in more detail.

An electric arc discharge, between two electrodes in atmospheric air, can be used to produce a diverging spherical shock wave. If a capacitor, charged to a high voltage, is discharged through the electrodes, an electrically conducting channel is briefly formed between the electrodes. The sharp rise in current, in the arc channel, rapidly heats the channel to a high temperature by the process of Joule heating. This process is limited by the half-period of the discharge. The sharp rise in temperature is accompanied by a sharp increase in pressure in the arc channel. A diverging cylindrical shock wave is produced [Craggs (1978)]. This shock wave gradually becomes spherical in shape after travelling a distance greater than the electrode separation.

The time evolution of the radial density profile of a diverging shock wave, produced by an electric arc discharge, is given in figure 4.6 [Hamamoto *et*

al. (1981)]. Initially the shock wave is characterised by a sharp rise and fall in density. As the shock wave propagates the energy of the shock wave is distributed over a larger area and the shock wave weakens. Dissipative effects (eg. viscosity and heat conduction) also weaken the propagating shock wave. With time the shock front becomes less steep, the peak density decreases and the regions behind the shock front flatten out.

If several diverging spherical shock waves are generated from points equidistant on a circumference, shock collisions between the expanding shock waves will occur. The region of interest for the CSL is the interior region of the shock initiation circle. The expanding spherical shocks will experience two different types of collisions [Courant and Friedrichs (1948)]. These collisions can be understood by considering a plane shock wave propagating in a channel with an inclined wall (figure 4.7). The collision of a shock wave with a rigid wall is analogous to two shock waves colliding with each other. The incident plane shock, on interaction with the inclined wall, will experience Mach reflection if the inclination angle (θ) is small. A small inclination angle implies a large included angle between the colliding shocks. A reflected Mach shock and a Mach tail will be formed. The Mach shock front has a slight curvature. The Mach number of the Mach shock is higher than the incident shock wave. Schwendeman and Whitham [Schwendeman and Whitham (1987)], in their numerical simulation of converging shocks, found that Mach reflection occurs for $\theta \leq 65°$. This was found to be consistent with other reported experimental values. For larger values of θ, regular reflection will occur. With regular reflection the resultant flow pattern may be described interms of an incident and reflected shock front. This type of reflection does not produce the Mach system shown in figure 4.7.

Perry and Kantrowitz [Perry and Kantrowitz (1951)] recognised that the uniform distribution of curvature along the Mach shock, due to Mach reflection,

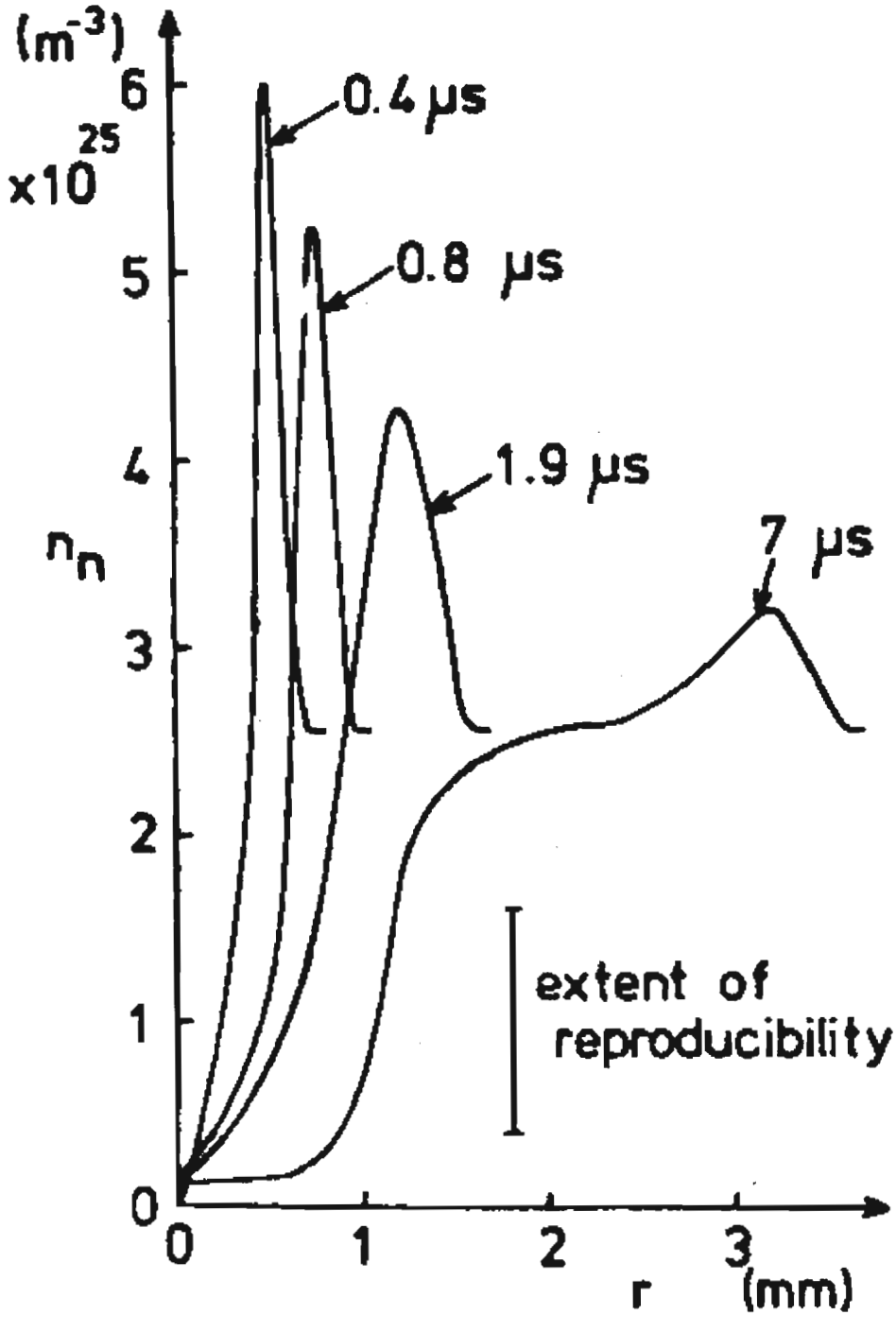

Figure 4.6: Time evolution of the radial density (n_n) structure of a diverging shock wave produced by an electric arc discharge [Hamamoto *et al.* (1981)].

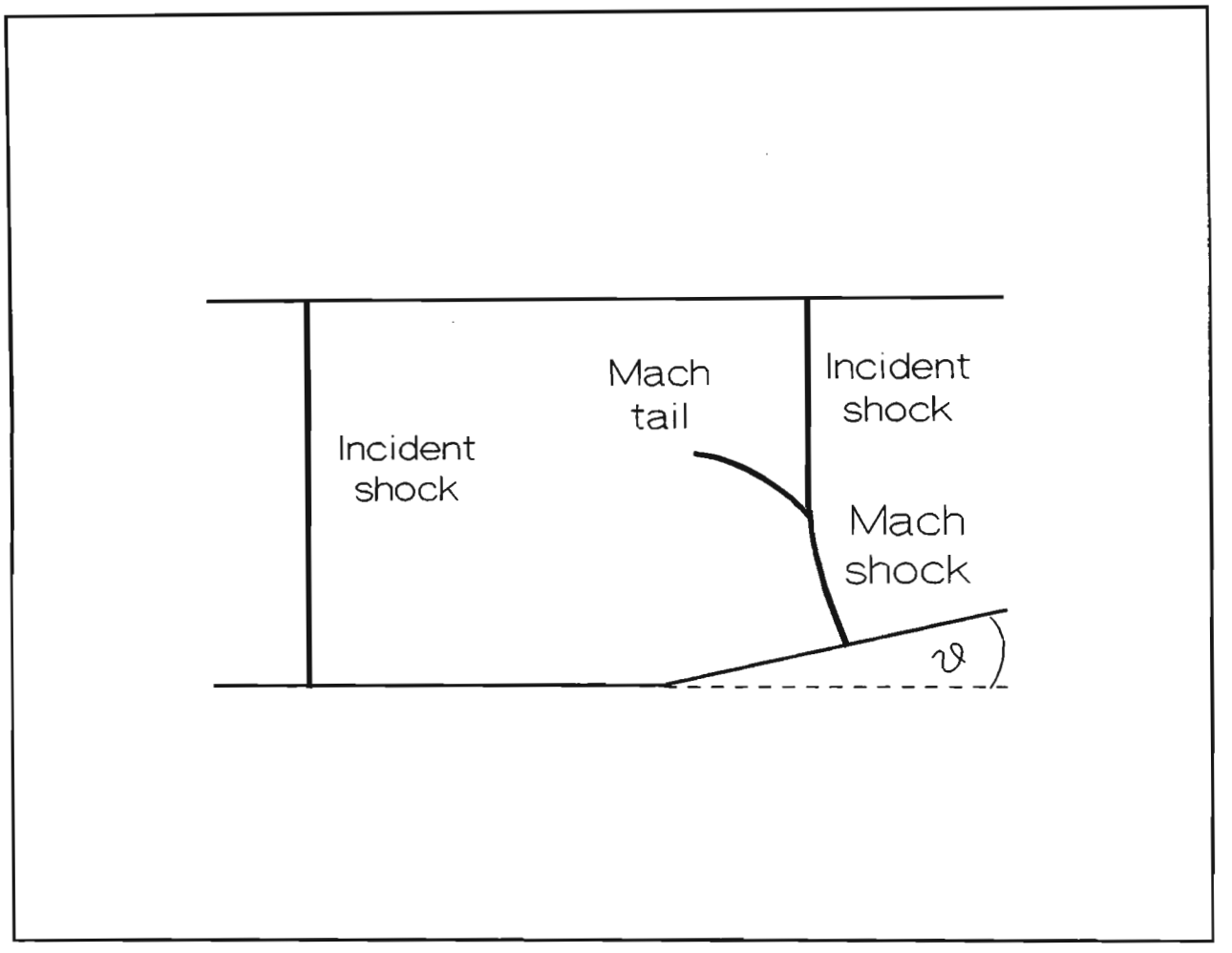

Figure 4.7: A plane shock propagating in a channel with an inclined wall.

would give converging cylindrical shock waves a "stability of form ". Any initial deviation from cylindrical symmetry of the converging shock wave or any disturbance encountered during convergence would be damped out. Knystautas *et al.* [Knystautas *et al.* (1969)] used this feature to produce a stable converging cylindrical detonation front from a regular polygonal shaped detonation front which was made from planar detonation wavelets. Schwendeman and Whitham [Schwendeman and Whitham (1987)] performed a numerical study on converging cylindrical shock waves with polygonal shaped cross-sections. They established that converging cylindrical shock waves, with polygonal shaped cross-sections, are stable. Converging cylindrical shock waves, with regular polygonal shaped cross-sections, were found to regain their initial shape after successive time intervals. For cross-sections close to a polygonal shape or a perturbed circular shape, a polygonal shape cross-section was obtained during convergence. However, their analysis assumed that the Mach shocks had no shock front curvature. Mach shock curvature will smoothen out the polygonal shaped cross-section of the converging cylindrically symmetric shock wave and a circular cross-section will be reached.

If one considers a cross-section of the expanding spherical shock waves, the mechanism for the formation of the cylindrically symmetric converging shock wave can be readily understood. A cross-section of the CSL is given in figure 4.8. Diverging circular shock waves originate from equi-spaced points on a circumference (figure 4.8(a)). A time will be reached, in the expansion process, where the circular shock waves begin to collide with each other (figure 4.8(b)). This initial collision is a head-on collision and regular reflection will occur. Further shock expansion will result in an increase in the collision angle between adjacent expanding circular shock fronts, and Mach reflection will predominate. The resultant Mach shocks propagate faster than the expanding circular shocks and a quasi-polygonal shaped converging shock wave will be formed (figure 4.8(c)). With subsequent circular shock expansion and

continued Mach reflection, a stable circular cross-section will be reached (figure 4.8(d)). For simplicity, the Mach shocks in figure 4.8 have only been shown in the interior region of the diverging shock wave initiation circle. Mach reflection also occurs in the region exterior to this circle where shock collisions occur.

As the converging cylindrically symmetric shock wave approaches the implosion axis, it experiences self-amplification. During convergence, the shock frontal area is reduced and the converging shock wave energy is concentrated within a smaller region behind the shock front. This process speeds up and strengthens the converging shock wave. On implosion, the shock strength should be infinite. However, dissipation due to conduction and radiation processes limit the strength of the shock wave on implosion. After implosion, the converging cylindrically symmetric shock wave is reflected and a diverging cylindrically symmetric shock wave is formed.

Introducing the full symmetry of the converging shock wave problem, a simplified three-dimensional representation of the cylindrically symmetric converging shock wave, formed by diverging spherical shock waves, is given in figure 4.9(a). For clarity not all the shock fronts have been shown. The converging shock shape resembles a centrally pinched cylinder. The central region of this pinched cylinder implodes sooner than the ends of the cylinder. The reflected cylindrically symmetric diverging shock wave is thus cigar shaped, as shown in figure 4.9(b). This cigar shaped region is the lensing region of the CSL.

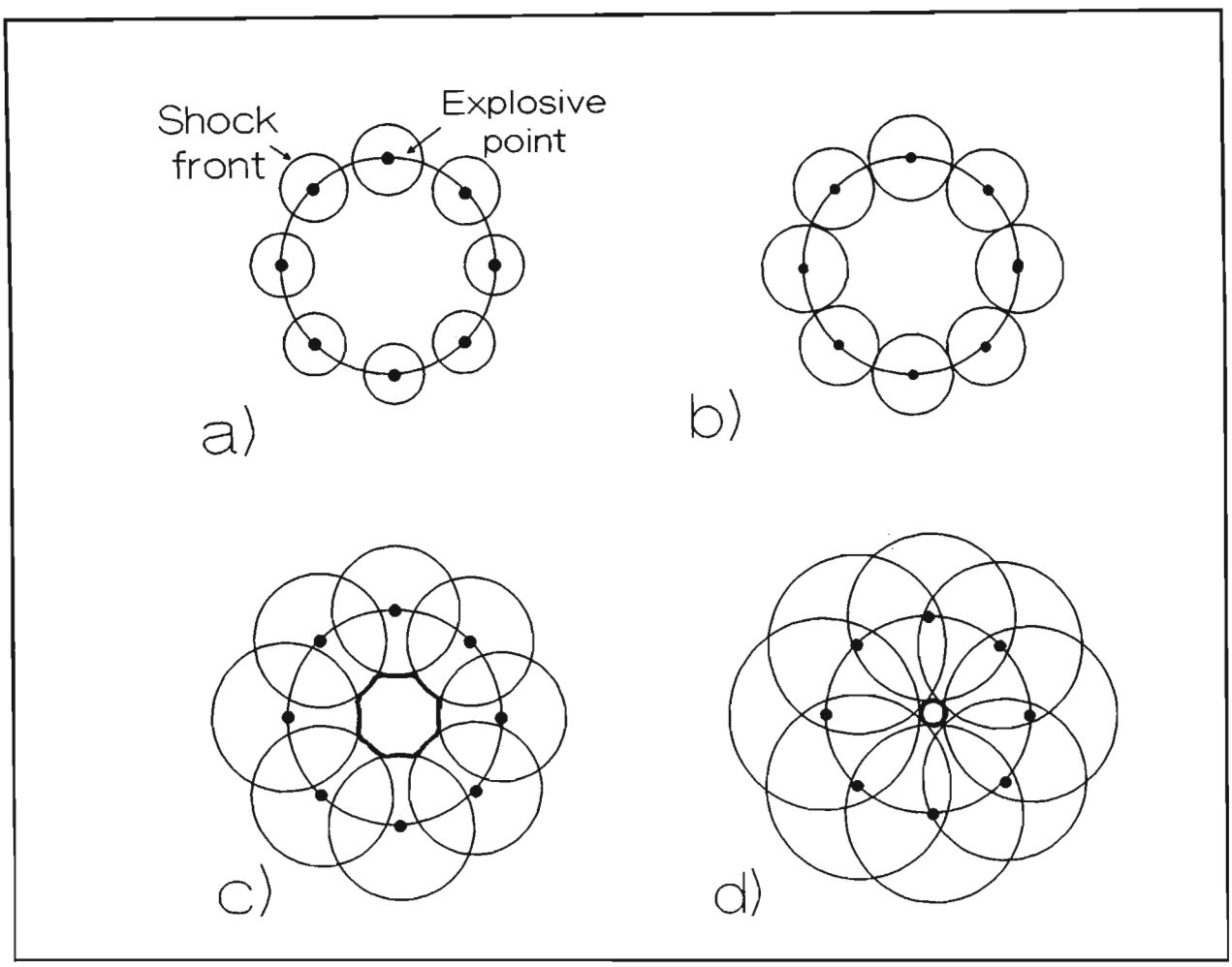

Figure 4.8: A cross-section of the expanding spherical shock waves for different times after initiation.

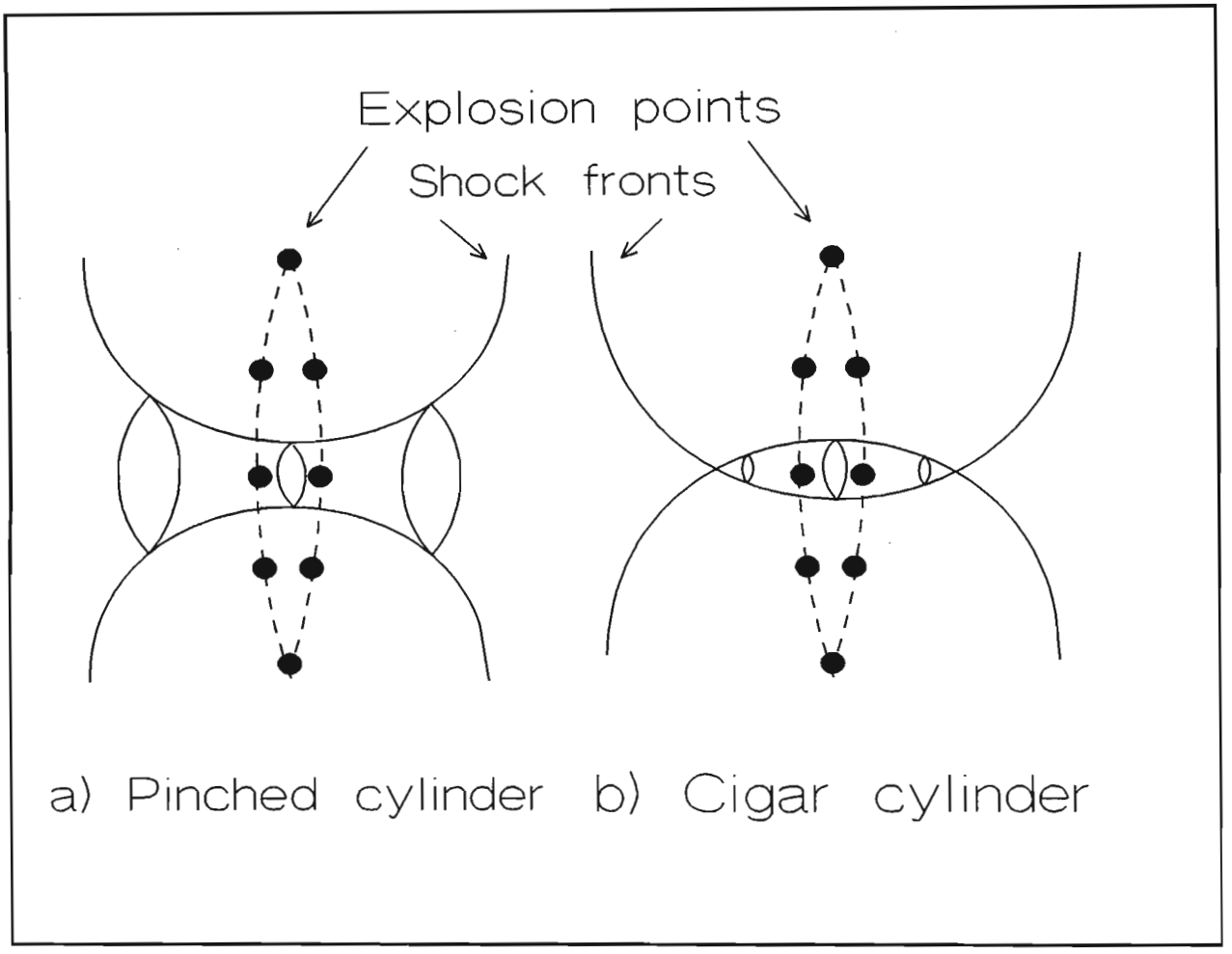

Figure 4.9: A simplified three-dimensional representation of the cylindrically symmetric: a) converging shock wave, b) reflected diverging shock wave.

4.4 The Refractive Fringe Diagnostic of Shock Waves

The Refractive Fringe Diagnostic (RFD) has been used in the CSL investigation as a diagnostic tool. The RFD was initially developed as a laser produced plasma diagnostic. This is discussed in Chapter 2. This diagnostic tool has recently been extended to study shock waves. Waltham *et al.* [Waltham *et al.* (1987)] investigated the shock structure produced by a de Laval nozzle. Bacon *et al.* [Bacon *et al.* (1989)] studied diverging cylindrical shock waves produced by arc discharges in atmospheric air. This study was extended to diverging spherical shock waves by Michaelis *et al.* [Michaelis *et al.* (1991b)].

The RFD utilises a defocused shadowgraphic technique to study density fields. A laser probe beam incident on a density field is refracted. Refracted light rays interfere with each other and with unrefracted light rays to form a fringe pattern. Density field features can be deduced from this fringe pattern. A fringe pattern of a diverging spherical shock wave for a late time after shock wave initiation, is given in figure 4.10(a). The corresponding radial fringe intensity plot is given in figure 4.10(b). The fringe pattern can be conceptually understood by tracing light rays through the radial density field of the diverging spherical shock, shown in figure 4.10(c). To get a broad picture of the process, light rays traversing the density field tangentially are only considered since these are the rays which experience the most refraction. This diagram is reproduced from the paper of Michaelis *et al.* (1991b).

Light rays traversing the shock rear (3) are refracted in the direction of increasing refractive index and interfere with unrefracted light rays which traverse the undisturbed region ahead of the shock front (1). The outer

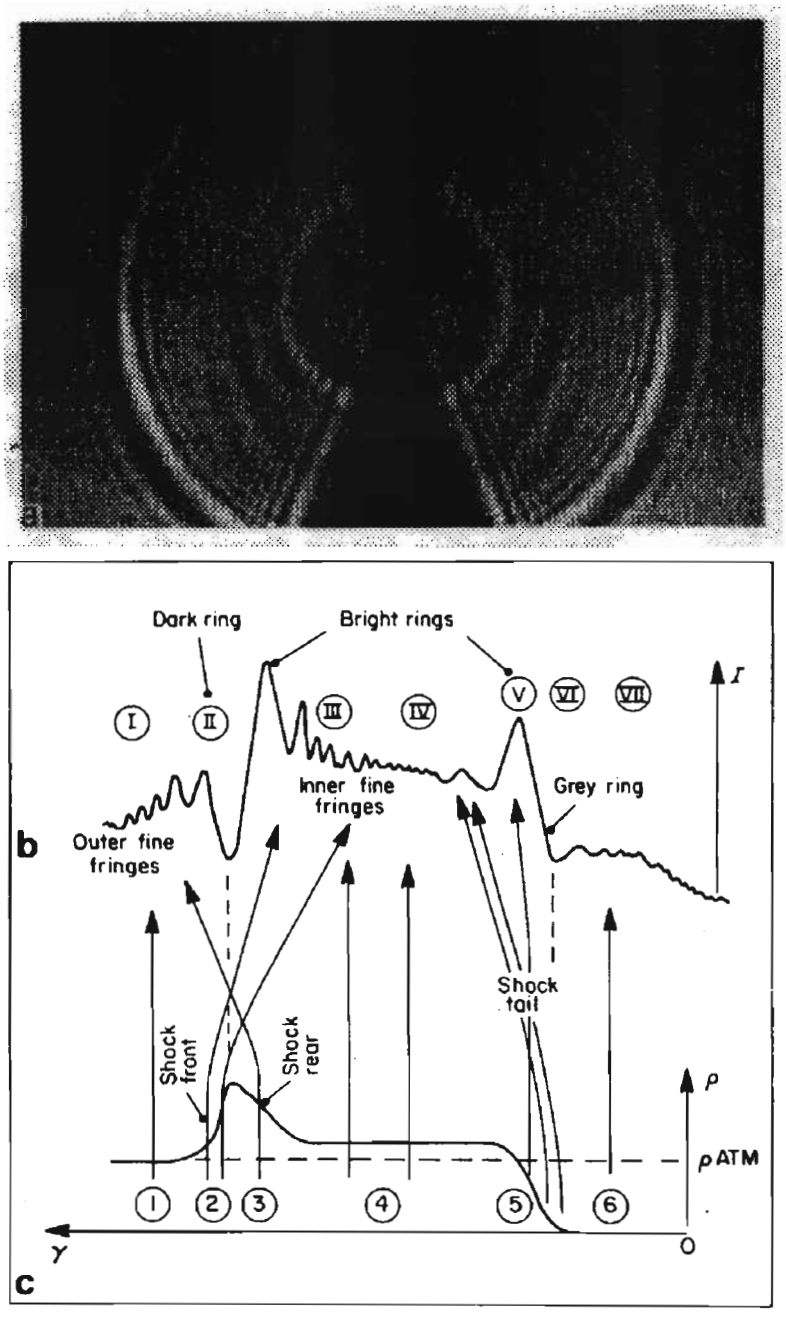

Figure 4.10: (a) RFD fringe pattern of a diverging shock wave, (b) the radial fringe intensity plot, (c) the shock wave radial density field.

fine fringe illumination pattern of region I is formed. Light rays traversing the shock front are strongly refracted inwards and interfere with the light rays traversing the shock saddle (4). The light rays traversing the shock saddle experience negligible refraction. The inner fine fringes of region III are formed. The fanning of the light rays from region 2 and 3 produce a dark ring (II). Light rays traversing the shock tail (5) are weakly refracted outward and interfere with unrefracted light rays traversing the shock saddle to form broad fringes (IV). A dark ring is formed (VI) in the region where the light has been refracted out from. Negligible refraction is experienced by light rays traversing the central vacuum region (6) and no fringe pattern is observed in region VII.

The fringe pattern of a diverging spherical shock wave for an earlier time than figure 4.10(a), where the shock rear (5) and the shock saddle (4) have not yet been formed, would only have the illumination regions I, II and III.

To determine quantitative information from the fringe interference pattern, an intelligent computer code is needed. A raytrace through a predicted radial density field, taking into account the spherical symmetry, must be performed to determine the illumination pattern of the resultant interference fringes. This illumination pattern must be compared to the experimental fringe illumination pattern. The initial prediction of the density field must be modified, by successive raytraces and comparisons, until the fringe illumination patterns match. The coding of the comparison and the resultant modifications needed to the density field, is not trivial. A different approach would be to train a neural network to deconvolve the density field from the illumination pattern of the fringes. However, the fringe patterns offer a great deal of qualitative information. Numerous inner fine fringes fanned over a wide region (III) suggests a steep shock front while the converse is suggested by fewer and broader fringes. The same argument holds for the shock rear

and shock tail. A dark ring suggests that light has been refracted out from that region.

4.5 Experimental Details

4.5.1 The Colliding Shock Lens

A schematic of the CSL, is shown in figure 4.11. Diverging spherical shock waves are created at points equi-spaced on a circumference (diameter d_e) by eight pairs of opposing electrodes of diameter 0.85 mm. For simplicity only four pairs of electrodes are shown in figure 4.11. An arc gap spacing of 1 mm was used. The gaps were connected in series in order to have approximately simultaneous breakdown. Breakdown was achieved by discharging a capacitor C, through the CSL to ground. The electrodes were mounted on two opposite plexiglass plates with a circular hole in the centre (diameter d_h), allowing a laser beam to be directed along the axis of the CSL. The electrode configuration used in this investigation was an eight arc CSL with $d_e = 11\ mm$ and $d_h = 7.5\ mm$.

4.5.2 System Configuration

Two different experimental arrangements were used in the CSL investigation. The CSL firing circuitry was identical in both arrangements. The difference lies in the type of diagnostic tool and laser used.

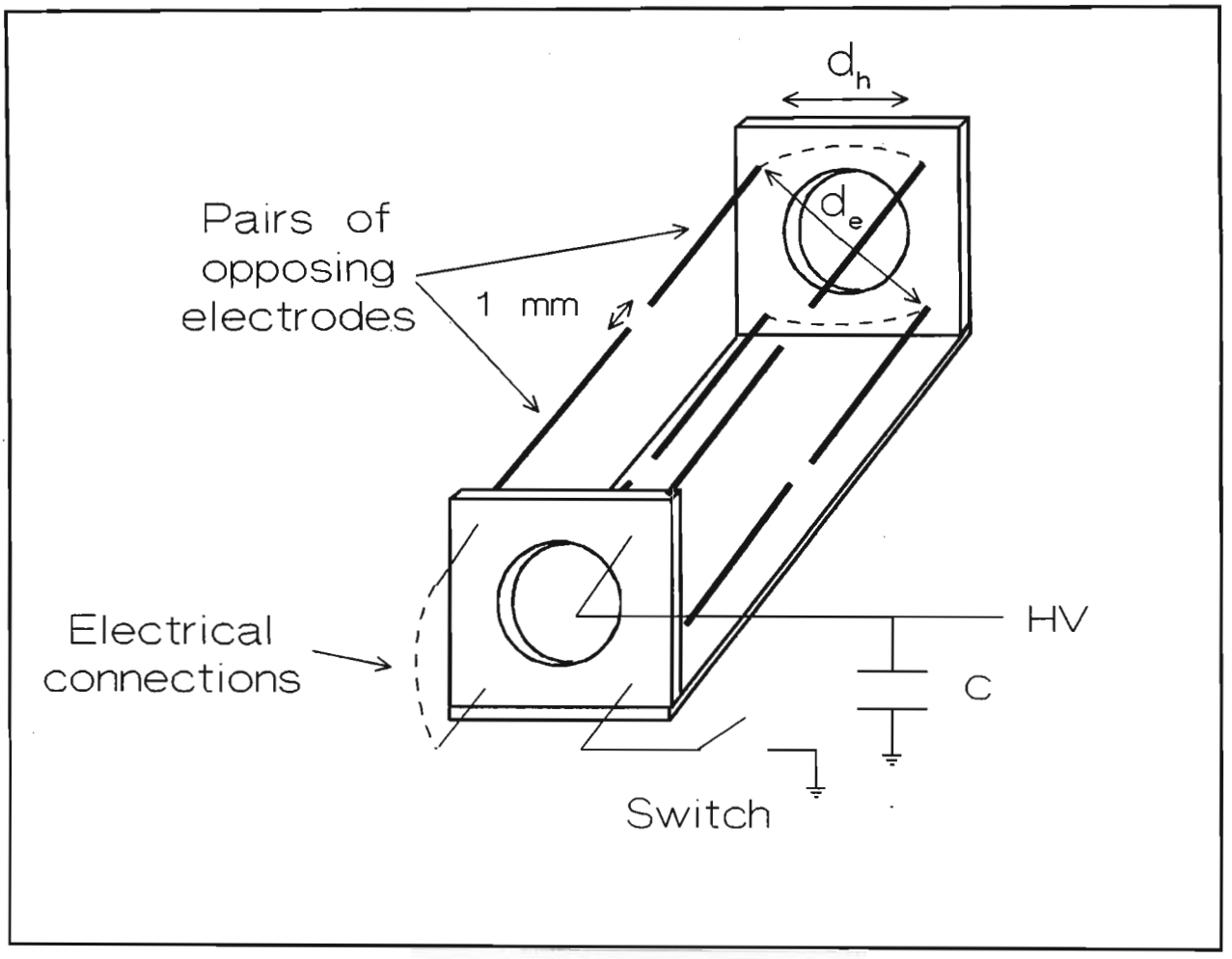

Figure 4.11: Four electrode CSL.

RFD Configuration

The experimental set up to investigate the lensing properties of the CSL and the mechanism responsible for the formation of the lensing region of the CSL, is shown in figure 4.12. A PC was used to synchronise the triggering of the CSL with the image digitiser (Oculus 200 real time frame grabber). When the image digitiser was activated, a TTL signal from the PC was stepped up to 30 KV by the pulse generator. This signal was used to fire the CSL by breaking down the pressurised spark gap.

The firing circuitry of the CSL is driven by an 18 kV DC power supply. The 18 kV power supply charged the 1 nF capacitor and, through a 10 H inductor, the capacitor C. The CSL was connected in parallel with the 10 H inductor. The CSL was fired by breaking down the pressurised spark gap, shorting the 1 nF capacitor to ground. Due to the high impedance of the 10 H inductor, the capacitor C discharged through the CSL to ground. The value of the capacitor C determined the energy provided to the electric arc discharges. A 5 nF capacitor (C) was used for all the experimental investigations.

Synchronism between the firing of the CSL and the probing Nitrogen laser ($FWHM \simeq 1\ ns$) was achieved via a Rogowsky coil in the CSL circuitry. When the pressurised spark gap was broken down, the induced signal in the Rogowsky coil was delayed via a variable delay box before triggering the Nitrogen laser. This enabled one to probe the CSL at different times after the firing of the CSL. These times were recorded by a digital oscilloscope (HP 54502A). When the CSL was fired the Rogowsky coil in the CSL circuitry triggered the oscilloscope and the signal from the Rogowsky coil in the Nitrogen laser's triggering circuitry was recorded. The jitter between firing the CSL and triggering the Nitrogen laser was approximately 50 ns.

The Nitrogen laser was telescoped and spatially filtered (laser beam divergence was 0.5 $mrad$) and directed through the collision region of the CSL onto a TV (Hitachi HVT20E) camera face plate through an imaging lens ($f = 20\ cm$) and a Nitrogen interference filter (330 $nm, bandwidth = 10\ nm$).

The delay between activating the image digitiser and firing the Nitrogen laser, with the variable delay set to minimum, was less than 3 μs. The loss of information on the digitised image was negligible since the image digitiser takes 50 ms to grab one frame.

Burn Pattern

The experimental setup to investigate the quality of the burn pattern of the CSL is shown in figure 4.13. A diffraction limited ruby laser beam ($FWHM \simeq 30\ ns, E \simeq 0.5\ J$) was directed through the lensing region of the CSL onto photographic paper placed 39 cm from the CSL. The delay between the firing of the Ruby laser and the firing of the CSL was set so that the CSL's focal length was 39 cm. The Ruby laser has a 1 ms delay between receiving the trigger pulse from the PC and emitting laser light. For comparison, a burn pattern was obtained using a glass convex lens of equal focal length and apertured to 1.5 mm.

4.6 Results

The lensing properties and the formation of the lensing region of the CSL were investigated using the setup shown in figure 4.12. Images of the colliding shock waves were recorded at different times after shock wave initiation for

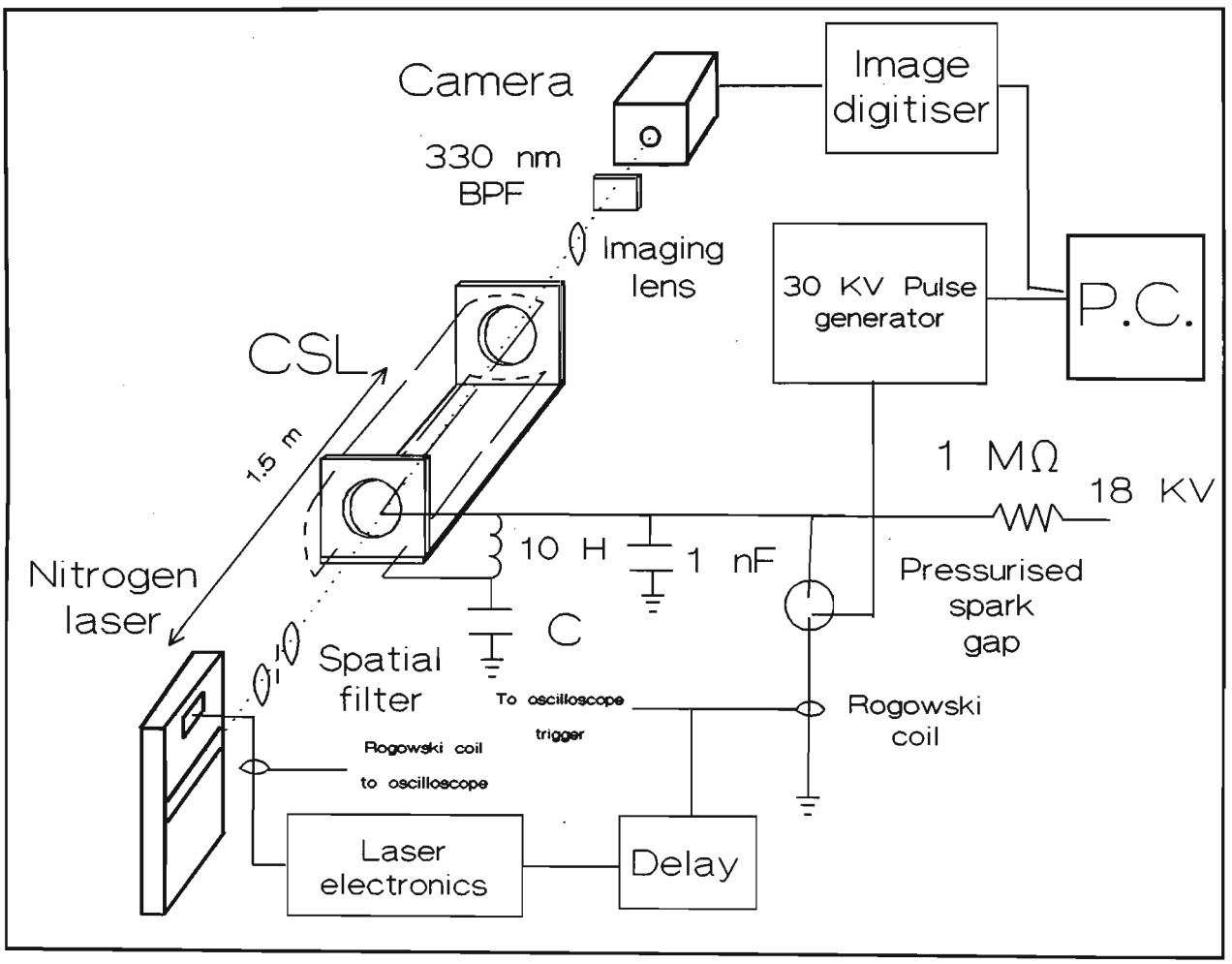

Figure 4.12: RFD system arrangement.

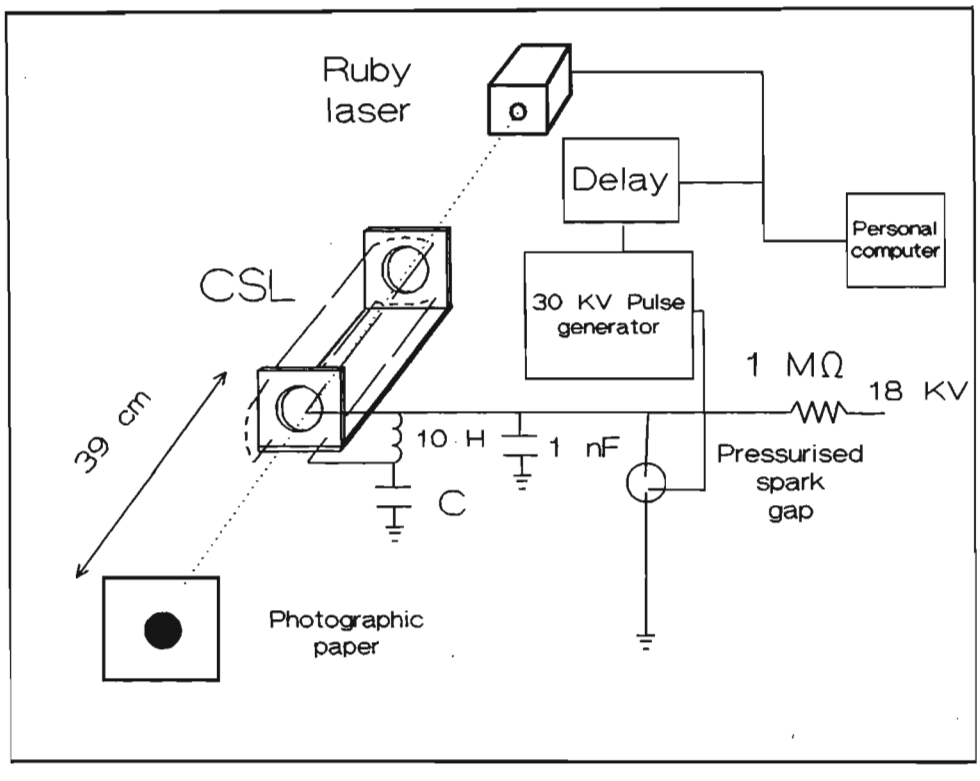

Figure 4.13: Burn pattern system arrangement.

different distances from the CSL. The intensity response of the TV camera is non-linear thus the intensity pattern of the recorded images were linearised using a linearisation curve specific to the TV camera [Waltham (1991)].

A time sequence for the colliding spherical shock waves, imaged on the shock collision plane, is shown in figure 4.14. The shock collision plane is the plane of the arc gap spacings between opposing electrodes. A similar sequence imaged 19 *cm* from the shock collision plane is shown in figure 4.15. The diverging shock waves produced by the arc discharges, (figure 4.14(a), figure 4.15(a)-(d)), produce a cylindrically symmetric converging shock wave ((figure 4.14(b), figure 4.15(e)-(f)). After convergence, a diverging reflected shock wave is formed (figure 4.14(c) and (d), figure 4.15(g)-(p)). Focusing is achieved in figure 4.15(i). Interference patterns behind the diverging shock fronts are evident in figures 4.15(j)-(m).

Focal spot images were recorded at different distances from the CSL. These distances, as a function of the time taken for focusing to occur after the firing of the CSL, are given in figure 4.16. The associated effective lens diameters for the measured foci were determined from the colliding shock wave time sequence imaged on the colliding shock plane (figure 4.14). Figure 4.14 shows only a few selected images of the time sequence. The effective lens diameter is the maximum diameter of the diverging cylindrically symmetric shock wave. These diameters as a function of time, after the firing of the CSL, are given in figure 4.17. The full width half maximum (FWHM) focal spot diameters associated with the focal lengths given in figure 4.16 are shown in figure 4.18. The measured focal spot sizes are compared with the theoretical diffraction limited spot size (FWHM) given by:

$$\phi_{diff} \approx \frac{1.22\lambda f_{length}}{\phi_{lens}}, \tag{4.1}$$

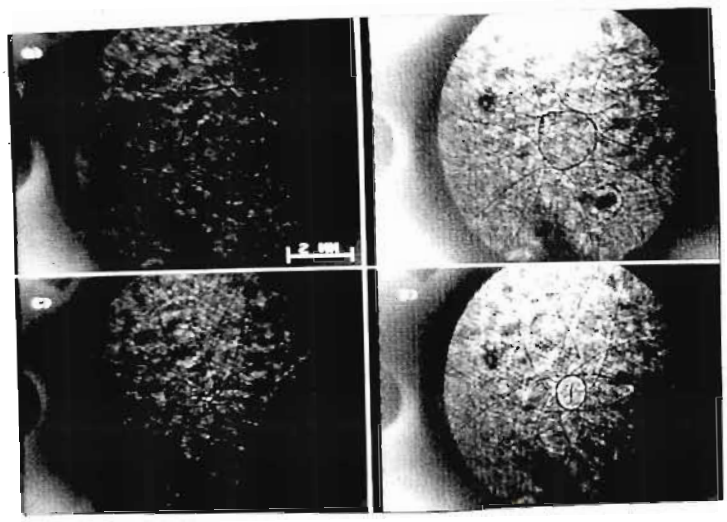

Figure 4.14: A time sequence for eight colliding shock waves imaged in the plane of collision at (a) 6.7 μs, (b) 8.5 μs, (c) 10.4 μs, (d) 11.3 μs.

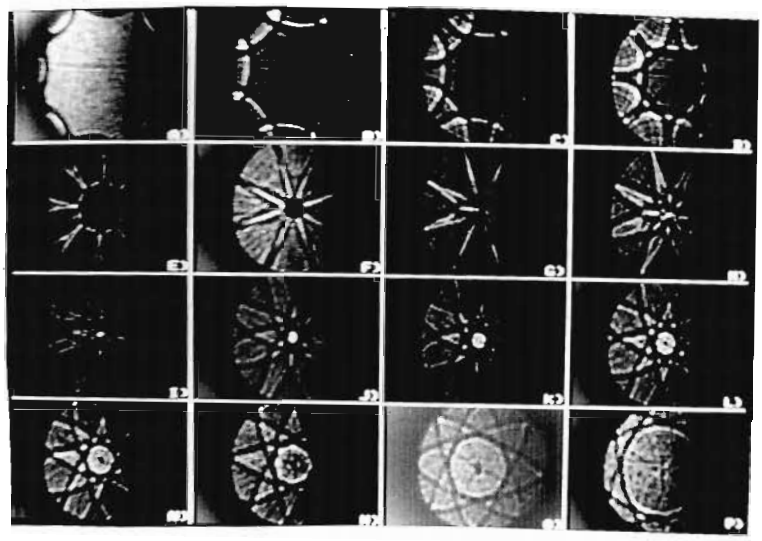

Figure 4.15: A time sequence for eight colliding shock waves imaged 19 *cm* from the CSL at (a) 3.2 μs, (b) 5 μs, (c) 6 μs, (d) 6.9 μs,(e) 8 μs, (f) 10 μs, (g) 10.4 μs, (h) 10.9 μs, (i) 11.3 μs, (j) 11.6 μs, (k) 11.8 μs, (l) 12.2 μs, (m) 12.4 μs, (n) 13.1 μs, (o) 14 μs, (p) 15.6 μs.

where λ is the wavelength of the Nitrogen laser (337 nm), f_{length} is the focal length of the lens given by figure 4.16 and ϕ_{lens} is the effective lens diameter given by figure 4.17 [Hecht (1989)].

A typical focal spot image, 39 cm from the CSL is shown in figure 4.19. An identical focal spot obtained with an additional filter ($ND = 1$) is shown in figure 4.20. The filter was needed to prevent the TV camera from saturating. A three-dimensional representation of the relative intensity of the central region of figure 4.20 is shown in figure 4.21. The associated contour plot is shown in figure 4.22. The position of the dark rings surrounding the focal spot in figure 4.19 were compared with Airy disk theory. A plot of the normalised dark fringe position (relative to the centre of the bright disk) versus fringe number, for two different focal spot images is given in, figure 4.23. The position of the dark fringes were normalised using:

$$x = \frac{\phi_{lens} 2\pi r}{\lambda f_{length}} \tag{4.2}$$

where ϕ_{lens} is the lens diameter, r is the dark fringe radius, λ is the wavelength of the Nitrogen laser (337 nm) and f_{length} is the lens focal length [Hecht (1989)].

To investigate the shape of the lensing region of the CSL the setup shown in figure 4.12 was used with the CSL rotated vertically by 90°. An image of the colliding shock waves, after initial shock wave convergence, is shown in figure 4.24. A central cigar shaped region is evident.

The burn pattern of the CSL focus was investigated using the setup shown in figure 4.13. A CSL focus burn pattern on photographic paper, 39 cm from the CSL, is given in figure 4.25(a). The photographic paper was pre-

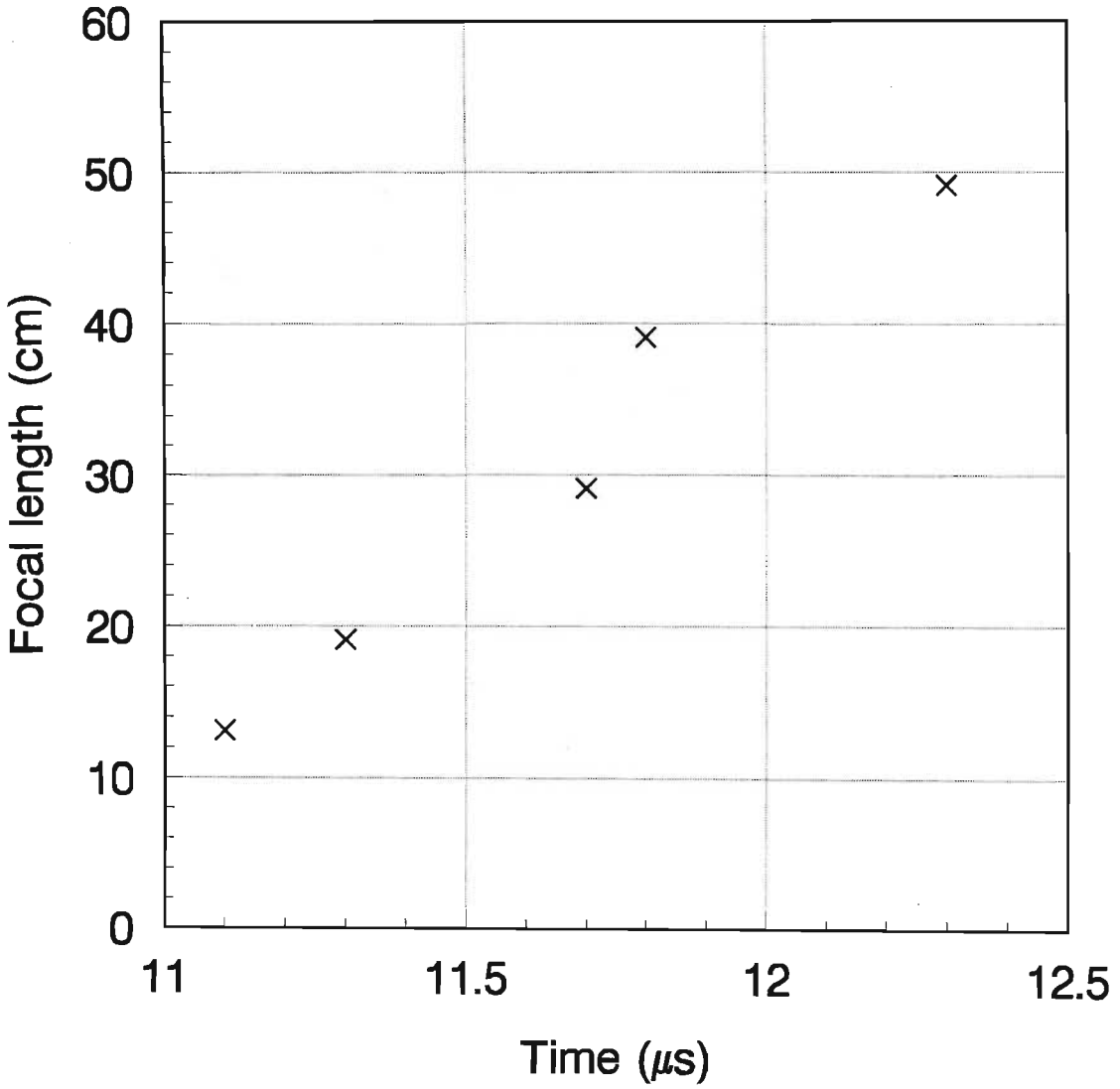

Figure 4.16: Focal length for the eight arc CSL at different times after arcing.

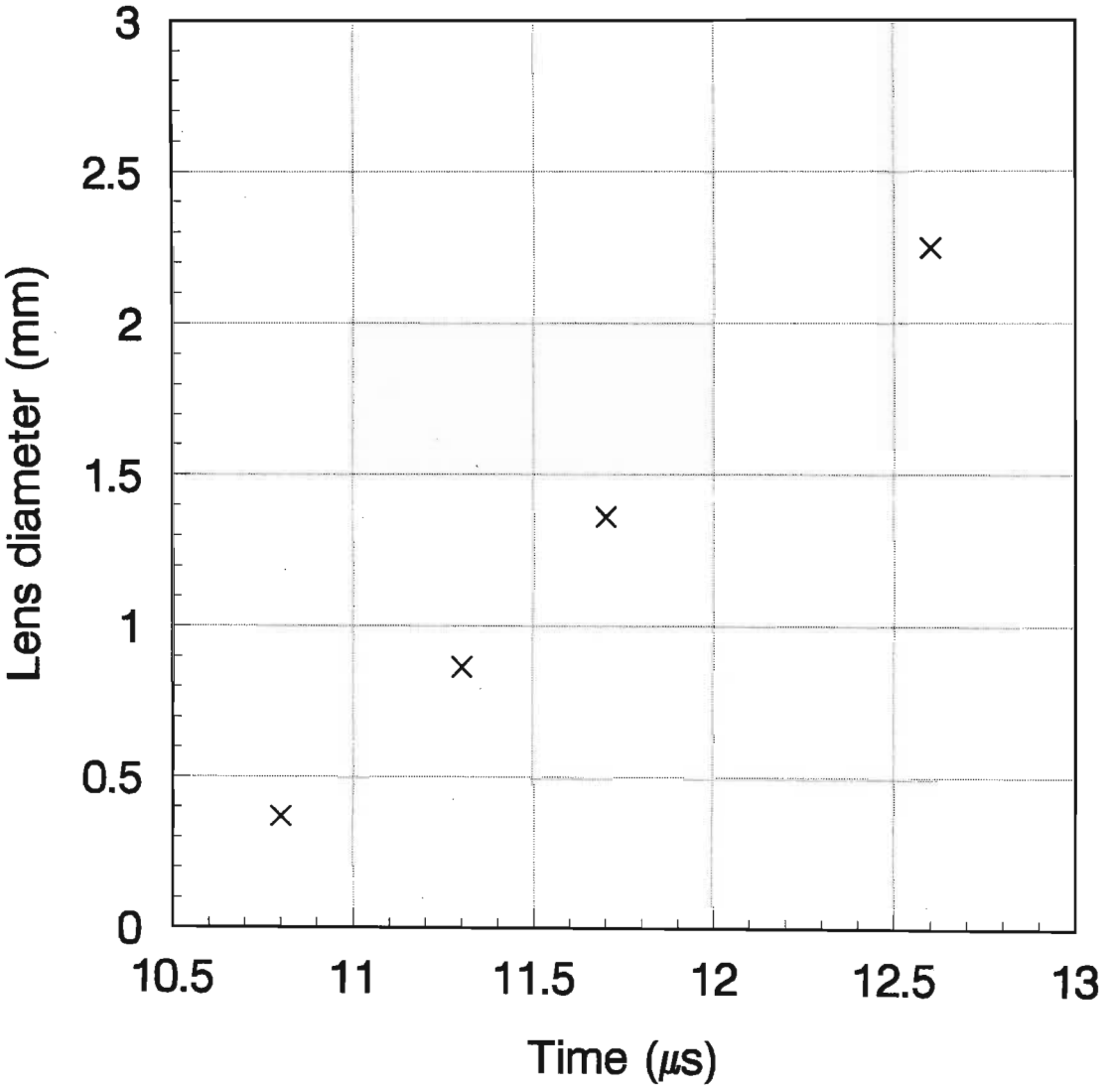

Figure 4.17: Effective lens diameter for the eight arc CSL at different times after arcing.

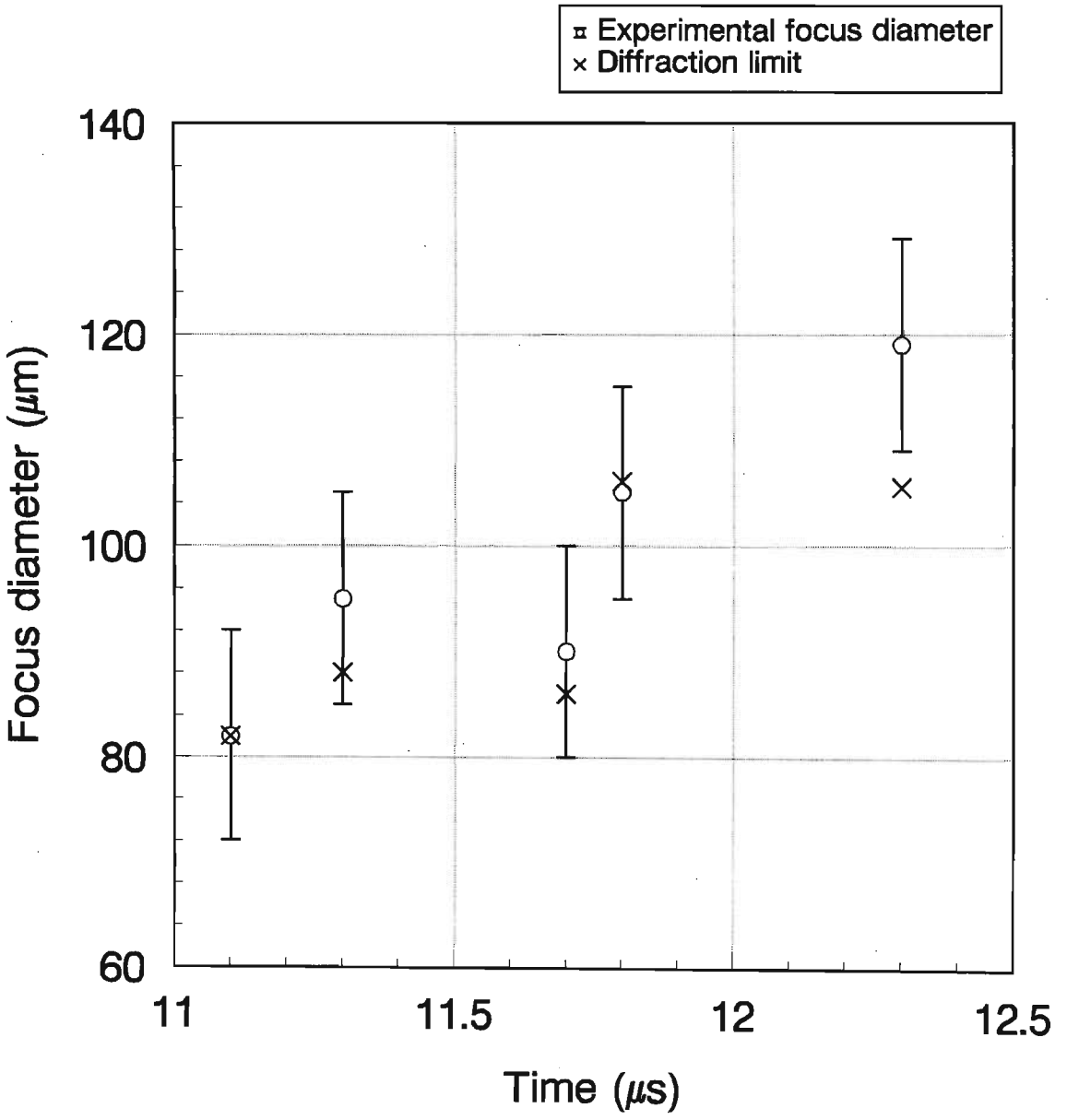

Figure 4.18: Comparison of focus diameters (FWHM) with the diffraction limit for the eight arc CSL at different times after arcing.

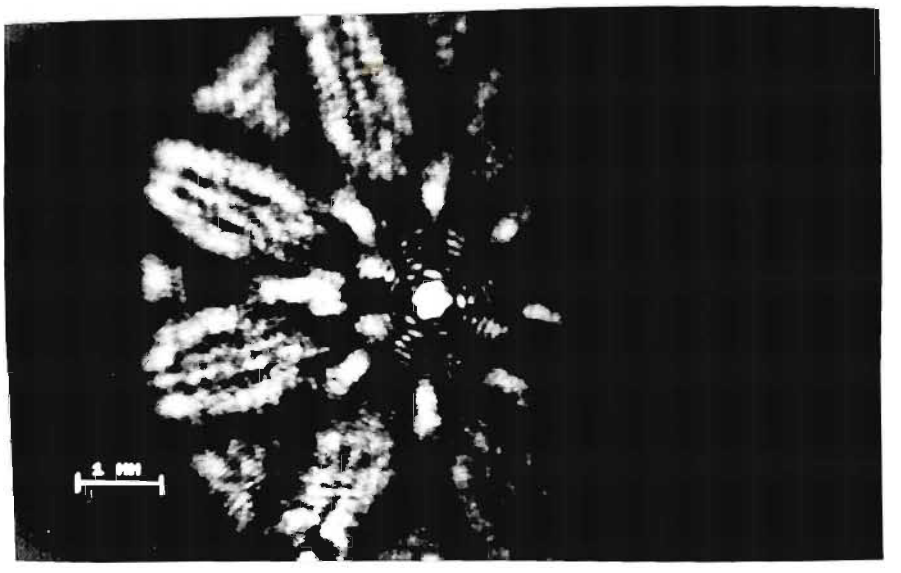

Figure 4.19: Eight arc CSL focal spot (focal length = 39 cm, delay = 11.8 μs).

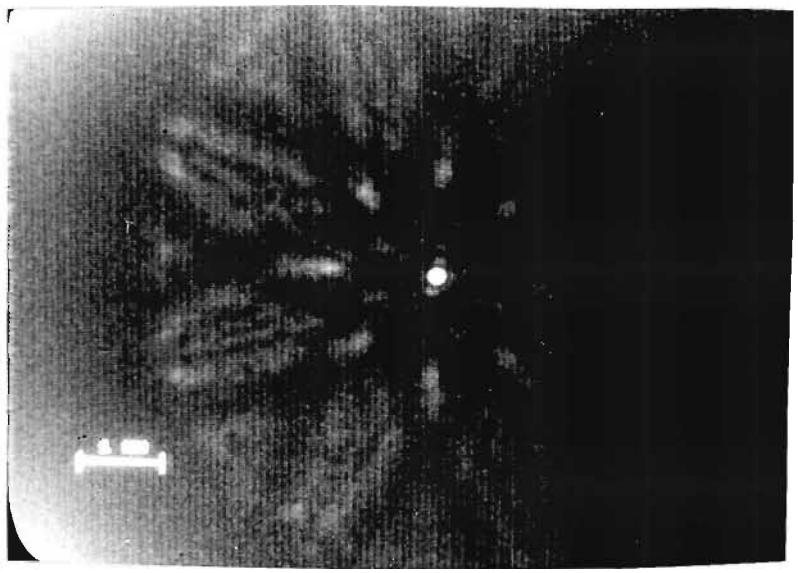

Figure 4.20: Eight arc CSL focal spot with an additional filter (focal length $= 39\ cm$, delay $= 11.8\ \mu s$).

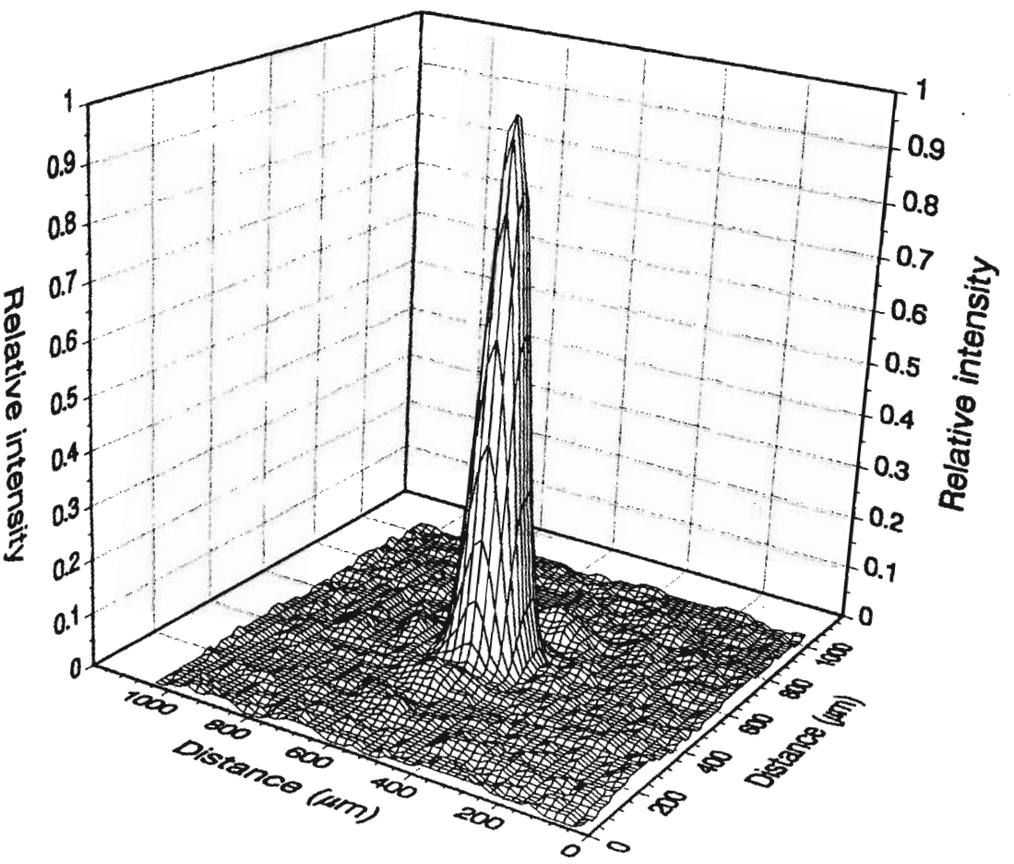

Figure 4.21: A three-dimensional relative intensity distribution of the focal spot (focal length = 39 cm, delay = 11.8 μs).

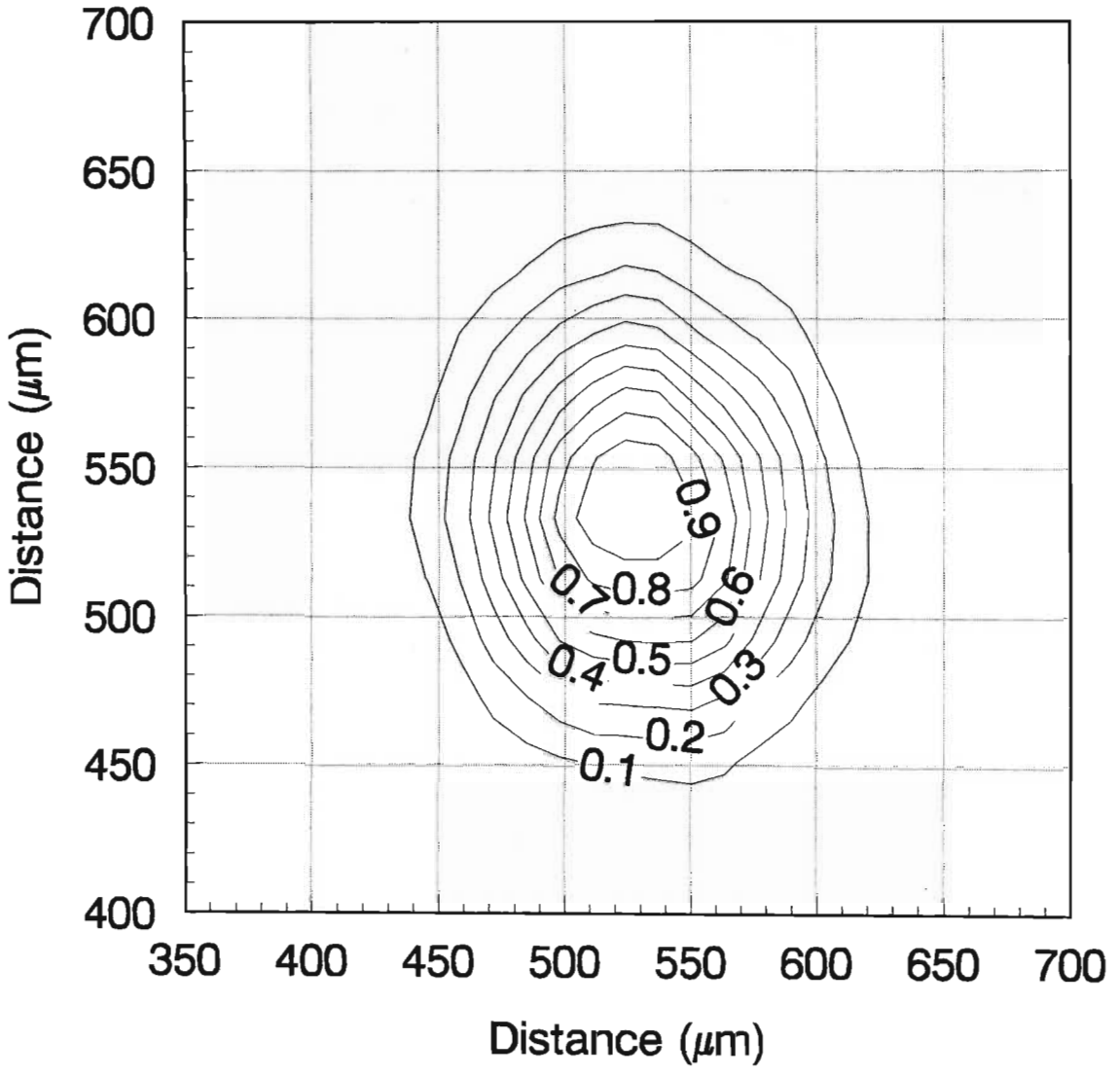

Figure 4.22: A relative intensity contour plot of the focal spot (focal length = 39 cm, delay = 11.8 μs).

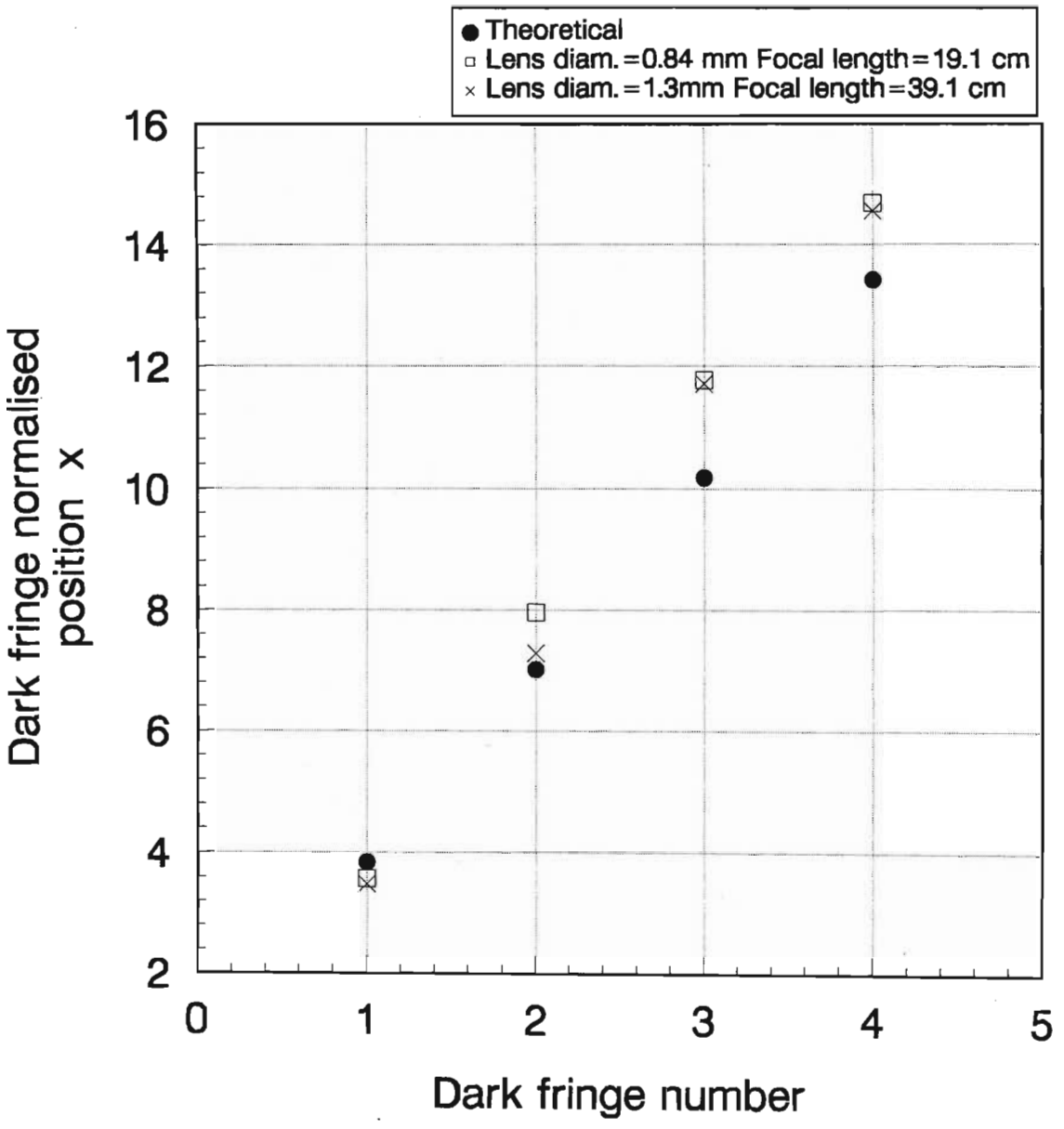

Figure 4.23: Comparison with Airy theory. Dark fringe number versus dark fringe normalized position $x = \frac{2\pi\phi_{lens}r}{\lambda f_{length}}$, r = dark fringe radius, ϕ_{lens},f_{length} = lens diameter, focal length.

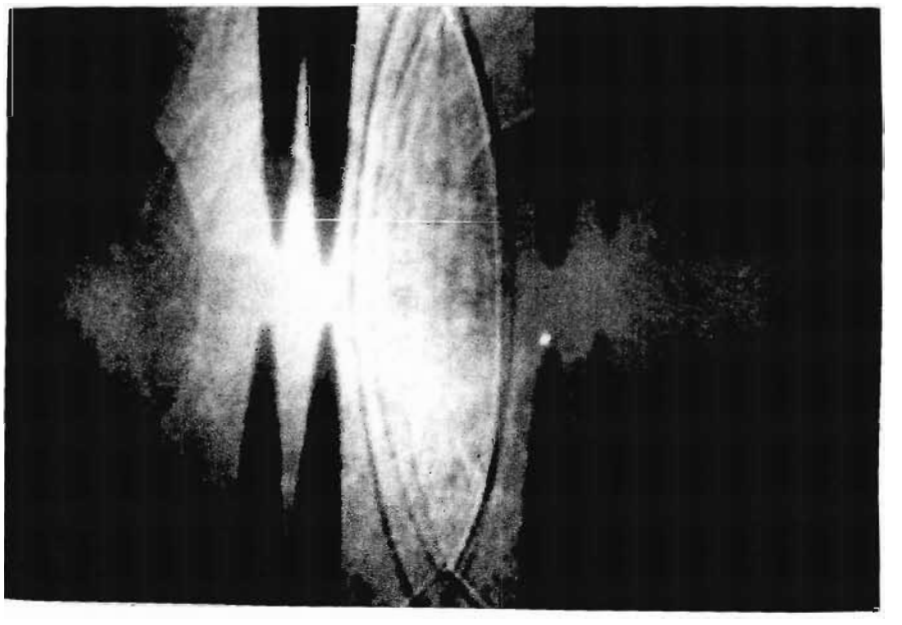

Figure 4.24: Eight arc CSL imaged side on, on the collision plane.

viously exposed to sunlight to obtain a faint pink colour. Exposure to high intensity laser light turned the pink colour to a deep red colour. The central white region of figure 4.25(a) represents a region of very high intensity light where the photographic emulsion was completely burnt off. This region is approximately $200\mu m$ in diameter. The speckled region surrounding the central white region represents a region of high intensity light where the photographic emulsion was partially burnt off. The dark region surrounding the burnt regions represents a region of lower intensity light where the photographic paper turned from a faint pink colour to a deep red colour. The white region surrounding the burn region represents a region where the photographic paper was not exposed to light and remained pink in colour.

A focus burn pattern for a glass lens, of focal length 39 cm and apertured to 1.5 mm, is given in figure 4.25(b). The central white region where the photographic emulsion was completely burnt off is approximately 200 μm in diameter.

4.7 Discussion

The mechanism responsible for the formation of the lensing region of the CSL can be understood with reference to figure 4.15. The curvature distribution mechanism of Mach reflection, as proposed by Perry and Kantrowitz [Perry and Kantrowitz (1951)], produces the stable cylindrically symmetric converging shock wave (figure 4.15(e)-(f)) from the diverging spherical shock waves (figure 4.15(a)-(d)). The expanding spherical shock waves (figure 4.15(a)) collide and the emergence of reflected Mach shocks are evident as broad, dark regions at the collision points (figure 4.15(b)). This implies a strong shock wave in this region. With continued spherical shock expansion and

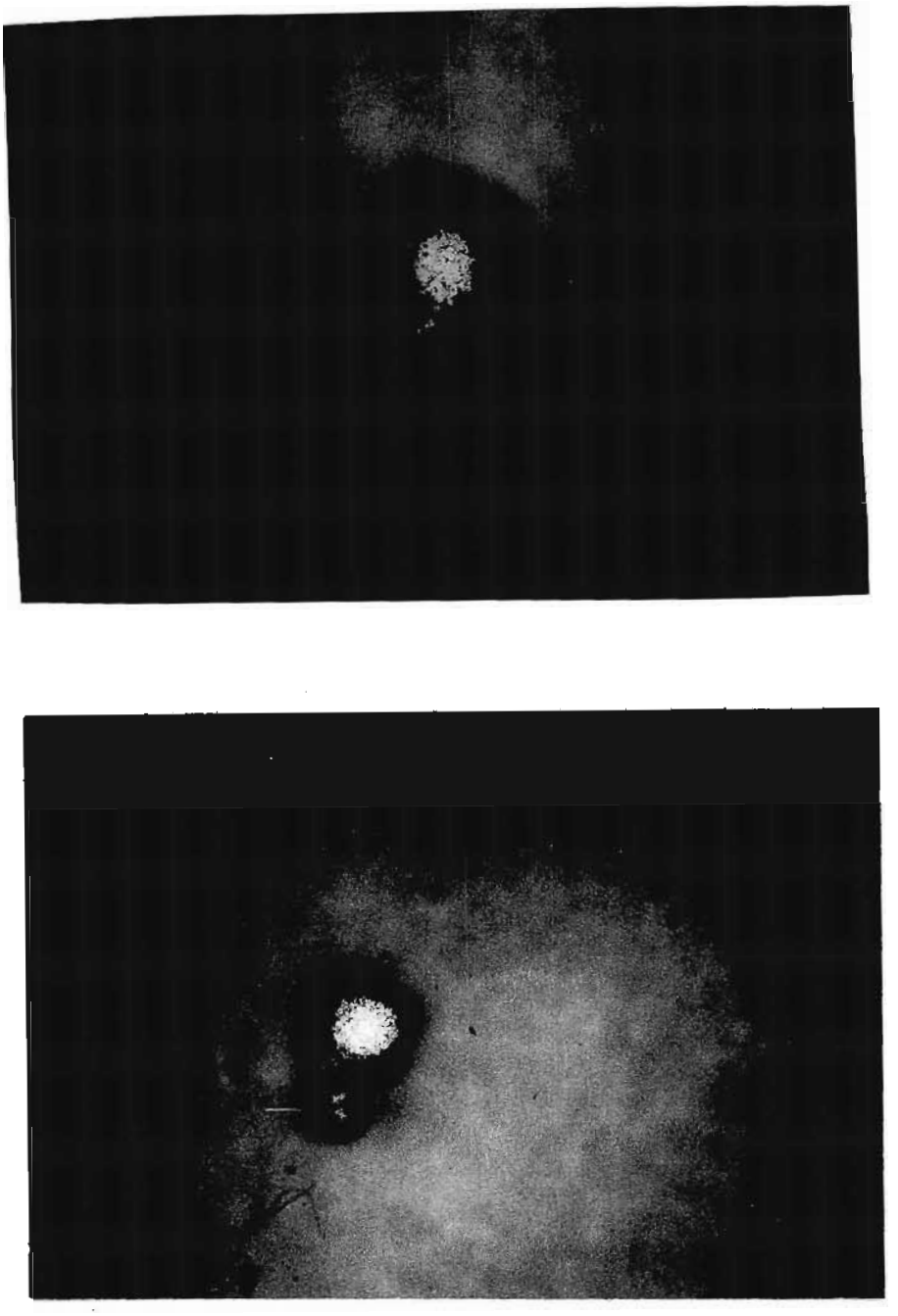

Figure 4.25: (a) Eight arc CSL burn pattern (focal length = 39 cm, delay = 11.8 μs) (b) equivalent glass lens burn pattern (focal length = 39 cm, aperture size = 2.5 mm).

collision the Mach shocks become more pronounced (figure 4.15(c)) and a cylindrically symmetric converging shock wave with an irregular polygonal cross-section is formed (figure 4.15(d)). A circular cross-section is obtained by further shock expansion and collision (figure 4.15(e)). The broad dark fringe implies a strong shock. The curvature of the Mach shocks are not readily seen from figures 4.15(b)-(d). The curvature distribution mechanism give the converging cylindrically symmetric shock wave a "stability of form". The converging shock wave is stable (figure 4.15(e)-(f)). On implosion ($t = 10.3\ \mu s$) one has a localised high density region. After implosion a reflected diverging cylindrically symmetric shock wave (figures 4.15(g)-(p)) is formed. The stability of the diverging shock wave confirms the stability of the converging shock wave process. The region bounded by the cylindrically symmetric diverging shock wave is the lensing region of the CSL.

The shape of the lensing region resembles a cigar (figure 4.24). The cigar viewed down the optical axis can be seen as consisting of many circular shock waves in different stages of divergence and convergence. The ends of the cigar are experiencing early divergence while the centre of the cigar is experiencing late divergence.

The growth of this cigar, due to continued shock wave expansion, gives the CSL unique features. As the cigar expands the maximum diameter of the cigar increases. The maximum diameter of the cigar is the effective diameter of the CSL (figure 4.17). This diameter is determined from the colliding shock wave images, imaged on the shock collision plane (figure 4.14). With the growth of the cigar the density field inside the cigar changes and the focal length was found to increase with time (figure 4.16). With the increase in the lens diameter and focal length with time, the diffraction limited focal spot size will also vary with time. The measured focal spot diameters compared favourably with their respective diffraction limited spot sizes (figure 4.18).

This gives an indication of the quality of the gas lens.

The use of equation 4.1, to determine the theoretical diffraction limited spot size (FWHM) of the CSL, is valid for a plane wave incident upon a circular aperture. The CSL must thus be placed in the near field of the laser and the CSL f-number must be significantly less than the inverse of the far field laser beam divergence. From figure 4.12 the CSL is $1,5\ m$ from the Nitrogen laser. The CSL is thus located in the near field of the laser since for a beam diameter of 2 mm, the Rayleigh range is approximately 18 m. From figure 4.16, the maximum focal length of the CSL is 49 cm. This focal length corresponds to a lens diameter of 2 mm (figure 4.17). The lens f-number is 245. The far field beam divergence of the laser is approximately 0.5 $mrad$. The lens f-number is thus much less than the inverse of the far field laser beam divergence (i.e. 2000).

From the magnified focal spot image, imaged 39 cm from the CSL (figure 4.19), certain features are clearly evident. The central bright spot is the focal spot of the CSL. From the three-dimensional relative intensity plot (figure 4.21) of the filtered focal spot image (figure 4.20), the majority of the light is concentrated within a 200 μm square region around the focal spot. The focal spot size (FWHM) is 104 μm (figure 4.22). The circular fringes surrounding the central bright spot were initially thought to be Airy rings. Their normalised dark fringe position were compared with Airy disk theory and reasonable accord was obtained (figure 4.23). However, the probable cause of these fringes is due to interference between rays of light originating from different points of the laser beam but refracted into the same interference zone. These fringes were observed by Lisi [Lisi (1994)] in a numerical raytrace through a CSL. The star patterns seen in figure 4.19 and figures 4.15(f)-(i) are due to collisions of the shock waves which experienced initial head on collision outside the field of view of figure 4.15(a). The prop-

agation of these shock waves, behind the converging shock wave, can be seen in figure 4.15(b)-(e).

The effect of the growth of the cigar is evident in figure 4.15: focusing occurs on the imaged plane in figure 4.15(i) while the central bright region in figures 4.15(j)-(m) represent focusing at further distances from the imaged plane. The interference fringes in these bright regions are due to interference between rays of light which have been slightly refracted by the lensing region of the CSL but by different amounts.

The burn pattern of the CSL compared favourably with the burn pattern of the glass lens. The high intensity region where the photographic emulsion was burnt off, for both lenses, is equal in size. However, the surrounding region is larger for the CSL than the glass lens. Interference fringes are evident around the central burn spot of the CSL while no fringes are evident around the glass lens central burn spot. This highlights the fact that these fringes are interference fringes and not Airy rings. The secondary burn spot in the glass lens burn spot is due to secondary reflections from the prisms used to steer the ruby laser through the CSL. These prisms are not shown in figure 4.13.

The possibility of operating the CSL at a high repetition rate was investigated. The maximum frequency of operation of the CSL is limited by the time taken for the flow field inside the CSL to reach equilibrium after shock wave generation. The converging shock wave imploded 10.3 μs after shock wave generation. One would expect the diverging shock wave to take a similar time to reach the electrodes. A reasonable estimate for equilibrium to be reached inside the CSL would then be an order of magnitude higher than double the convergence time, i.e. approximately 200 μs. This corresponds to a maximum frequency of operation of approximately 5 kHz.

The CSL firing circuitry (figure 4.12) is an oscillator. The frequency of oscillation can be set by adjusting the pressure or the electrode separation of the spark gap. The maximum oscillation frequency is limited by the charge time of the capacitors. The charge time is given by: $RC = 18\ ms$. The maximum frequency of operation of the CSL is then approximately 50 Hz. The CSL was operated at 10 Hz and the focus was found to be stable. The operating frequency of the CSL was limited by the repetition rate of the Nitrogen laser. The CSL operation was found to be insensitive to surrounding conditions. While the CSL was operated at 10 Hz, pressurised air was blown through the CSL and no effect on the focus was visible.

The experimental investigations have not dealt with the effects of CSL diameter, number of electrodes, discharge current characteristics and initial shock wave energy on the lensing properties of the CSL. This work is currently being undertaken by the Laser Group of the University of Natal.

4.8 Colliding Shock Lens Simulation

The experimental investigation of the CSL, determined the lensing properties of the CSL and the mechanism responsible for the formation of the lensing region of the CSL. The structure of the lensing region was not investigated. A numerical simulation of the CSL was performed to investigate the refractive index field of the lensing region of the CSL.

The FLIC scheme [Gentry *et al.* (1966)], used to model the operation of the PGL in Section 3.5.2, was modified to model the CSL operation. A full description of the FLIC scheme is given in Appendix A.

The computational mesh used to model the converging cylindrically symmetric shock wave and the resultant reflected cylindrically symmetric shock wave, is given in figure 4.26. This simulation models the evolution of the converging shock wave given in figure 4.9(a) and the formation of the resultant diverging shock wave given in figure 4.9(b). A slice in the y-z plane is only considered. The collision of the shock wave with a rigid wall is analogous to two shock waves colliding head-on. The mesh is a cylindrical co-ordinate system of 400 × 200 cells with $\delta z = \delta r = 25\ \mu m$. Boundary 1 is closed and the rest are open. The initial shock wave position and speed ($M_1 = 1.5$) were determined from the experimental investigation. The shock wave density, pressure and temperature profiles were assumed to be square and 1 mm wide. The density, pressure and temperature values of the shock wave were determined from the Rankine-Hugoniot equations which can be expressed as [Gaydon and Hurle (1963)]:

$$\frac{\rho_2}{\rho_1} = \frac{(\gamma+1)M_1^2}{(\gamma-1)M_1^2+2}, \tag{4.3}$$

$$\frac{P_2}{P_1} = \frac{2\gamma M_1^2 - (\gamma-1)}{(\gamma+1)}, \tag{4.4}$$

$$\frac{T_2}{T_1} = \frac{(\gamma M_1^2 - \frac{\gamma-1}{2})(\frac{\gamma-1}{2}M_1^2+1)}{(\frac{\gamma+1}{2})^2 M_1^2}, \tag{4.5}$$

where γ is the ratio of specific heat ($\gamma = 1.4$ for air). The subscript 1 denotes the ambient conditions and subscript 2 denotes the shock wave conditions. The time step (δt) used in the simulation was 1 ns. The maximum Courant number (equation 3.17) was less than 0.1. No artificial viscosity terms (K, B) were used in the simulation.

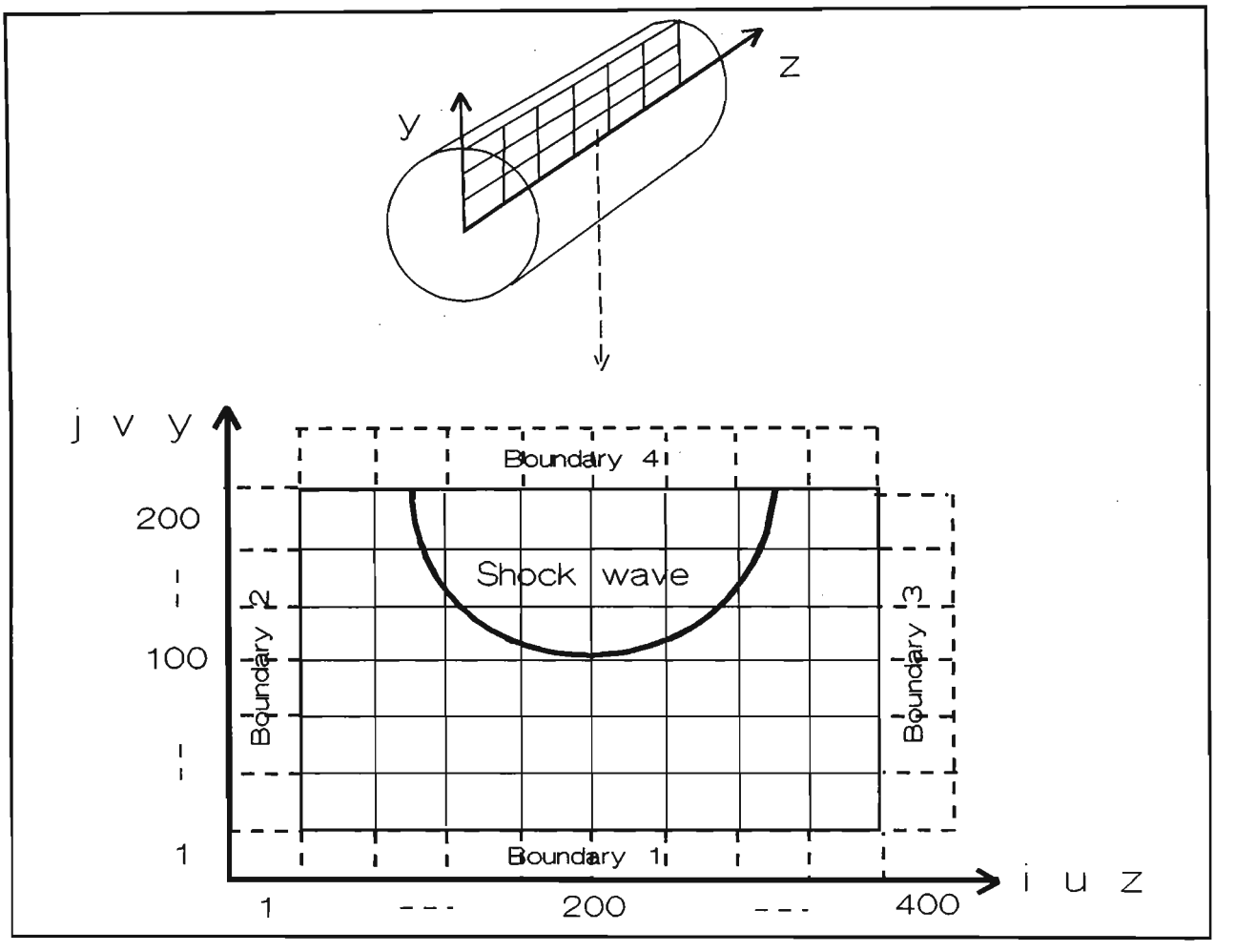

Figure 4.26: The CSL computational mesh.

The time evolution of the refractive index profiles of the converging and diverging shock wave, for $i = 100$ in figure 4.26, is given in figure 4.27 and figure 4.28, respectively. The shock wave strengthens during convergence and weakens during divergence. The initial reflected shock wave has a steep shock front and rear. With time the shock front and shock rear gradients decrease. The region behind the shock front flattens out and decreases with time. The oscillations behind the shock front are due the absence of artificial viscosity terms in the simulation. Artificial viscosity was found to make the solution unstable during collision with the rigid boundary. A three-dimensional representation of the refractive index field of the CSL, 1 μs after initial shock wave reflection (figure 4.28), is given in figure 4.29. Only half the lensing region is shown in figure 4.29. This is the cigar region referred to in previous sections. The refractive index increases sharply near the edges of the cigar and a depression is visible in the centre of the cigar. The CSL is a complex graded index lens with both axial and radial gradients. A light beam incident on this cylindrically symmetric region will experience considerable refraction in the peripheral regions where the refractive index gradients are large. The outer shell of the cigar is thus responsible for the lensing properties of the CSL. The converging shock wave can be seen skirting the lensing region of the CSL in figure 4.29

The time evolution of the radial change in optical path length between light propagating through the lensing region of the CSL and light propagating through normal atmospheric conditions, is given in figure 4.30. The focal lengths of the CSL, for different times after initial shock convergence, were determined from figure 4.30. The computed focal lengths are compared with the experimental focal lengths in figure 4.31. The computed focal lengths are shorter than the experimental focal lengths. The associated lens diameters for the computed focal lengths were determined from the position of the shock front in figure 4.28. The computed lens diameters are compared with

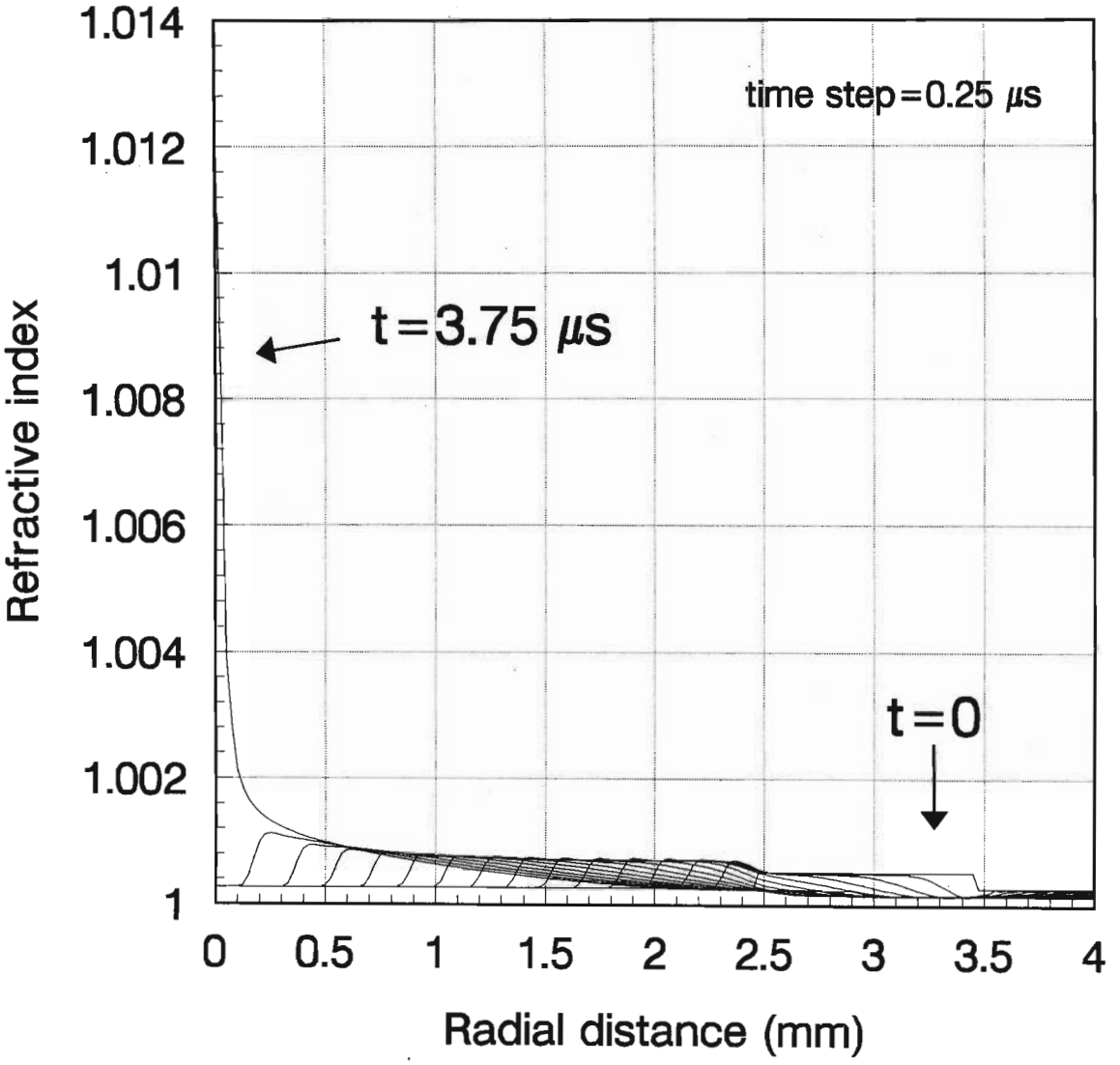

Figure 4.27: Time evolution of the computed refractive index profiles of the converging shock wave.

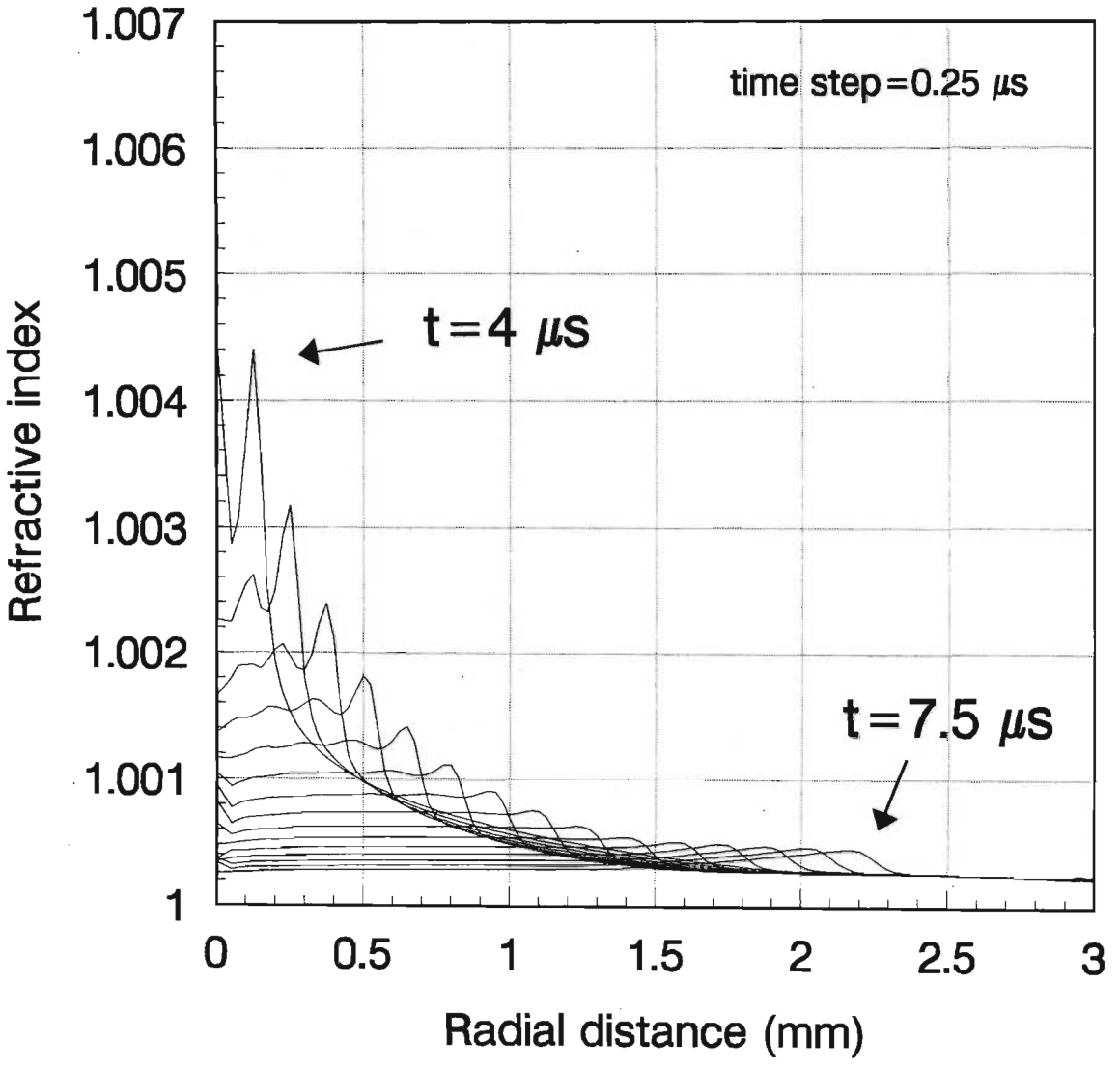

Figure 4.28: Time evolution of the computed refractive index profiles of the diverging shock wave.

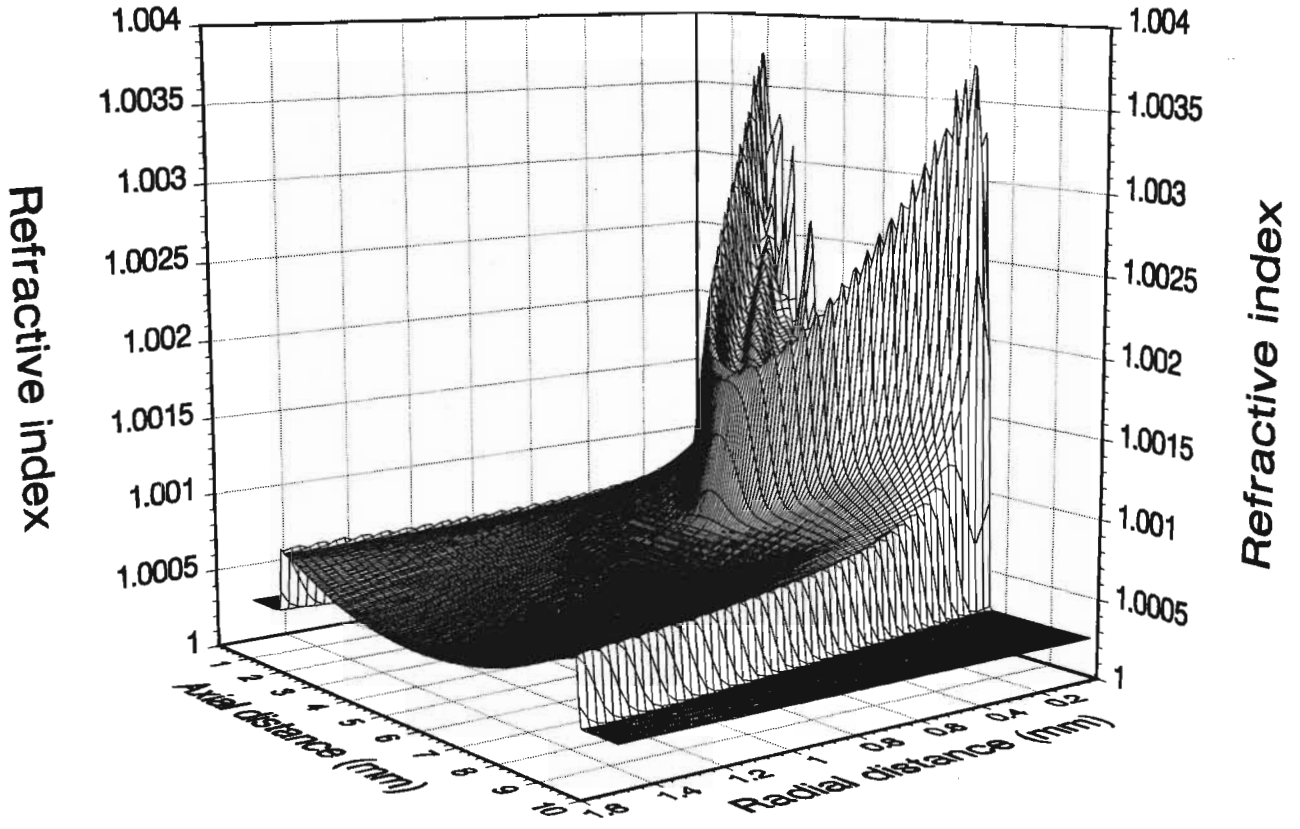

Figure 4.29: A three-dimensional representation of the refractive index field of the CSL 1 μs after initial shock wave reflection.

the experimental lens diameters in figure 4.32. The lens diameters for early times compare favourably but for late times the computed lens diameters are larger than the experimentally observed lens diameters. These discrepancies can be attributed to viscosity and conduction processes not being included in the simulation and the initial shock profile not being characteristic of the shock wave. Viscosity and conduction weaken the shock wave. The speed of the shock wave is then slower than computed (accounting for the discrepancy in figure 4.32) and the refractive index values of the lensing region are lower than computed (accounting for the discrepancy in figure 4.31). The method employed to determine the focal length of the CSL from the radial change in optical path length through the CSL, is an approximate method. It assumes that there is no light ray deflection inside the lensing region of the CSL. This will have a minor effect on figure 4.31.

Although the CSL simulation is not perfectly accurate, it does enable one to establish certain features of the CSL. The variation of the computed focal lengths with lens diameter is given in figure 4.33. The focal lengths increase sharply with lens diameter and a maximum useful lens diameter of approximately 4 *mm* is reached. This small lens diameter limits the usefulness of CSL. The lens diameter of the CSL can be increased by increasing the diameter of the CSL. This will increase the size of the lensing region. A simulation of a CSL, double the size of the CSL used in the experiment, was performed. The initial shock width, Mach number and shock front position relative to boundary 1 and boundary 4 (figure 4.26) was identical to the previous simulation. The variation of focal length with lens diameter is compared with the previously simulated (small) CSL in figure 4.33. For the same focal length the big CSL has a larger lens diameter than the small CSL. A maximum useful lens diameter of approximately 6 *mm* is reached. This shows that the lens diameter can be increased by scaling up the diameter of the CSL. Obviously, more energy is needed to produce the initial shock wave in the

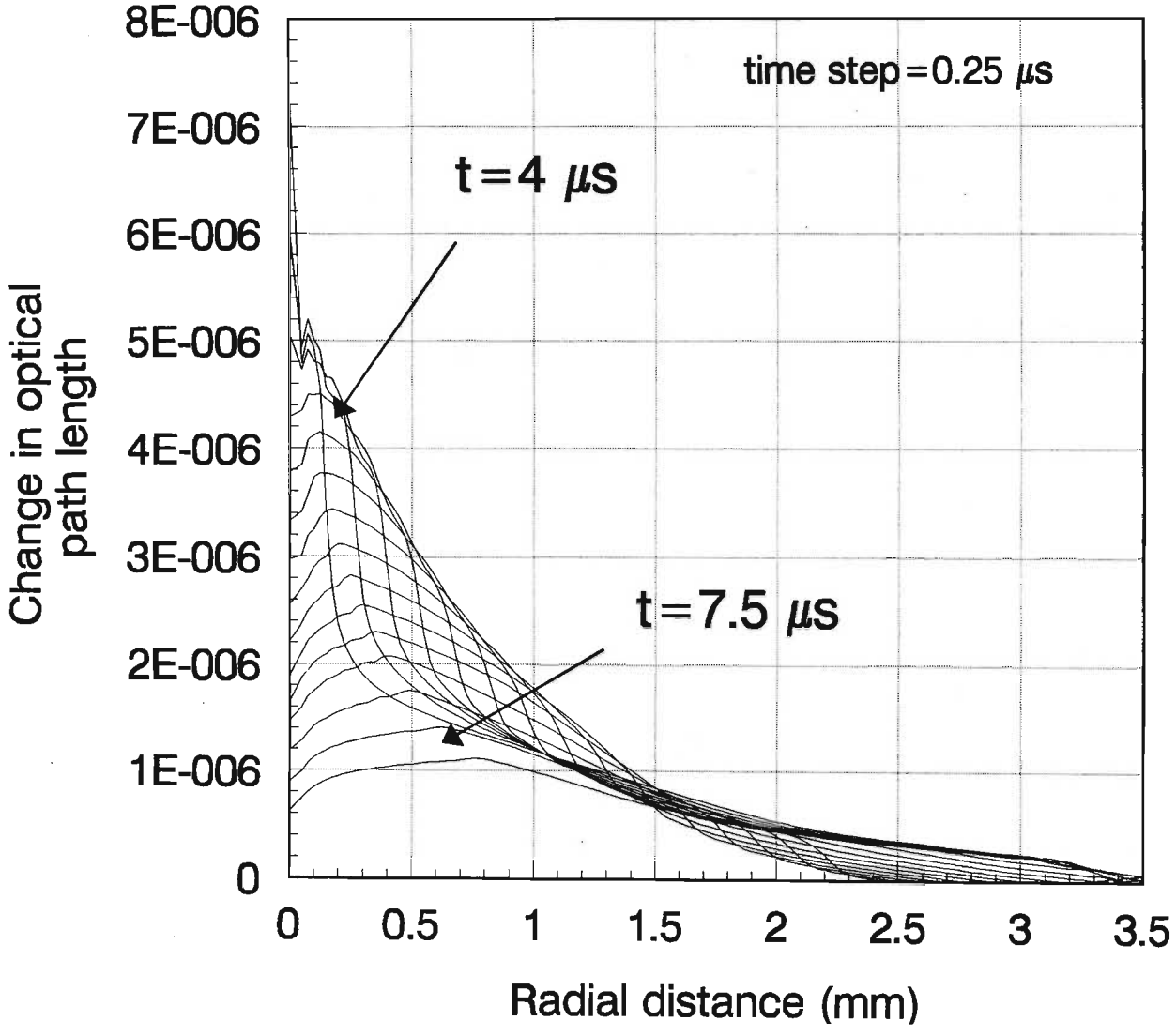

Figure 4.30: Time evolution of the radial change in the optical path length through the CSL.

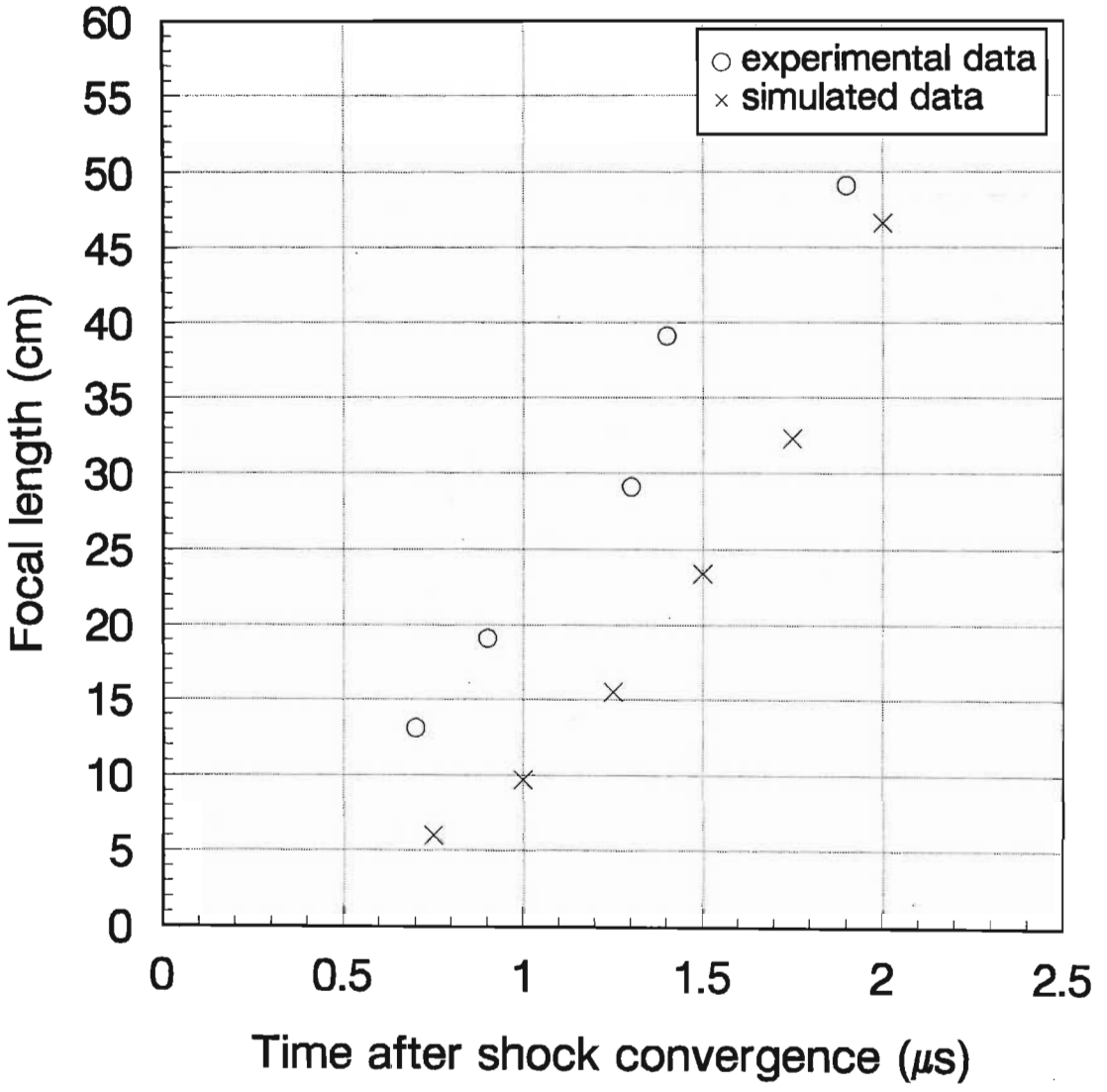

Figure 4.31: A comparison between computed and experimental focal lengths.

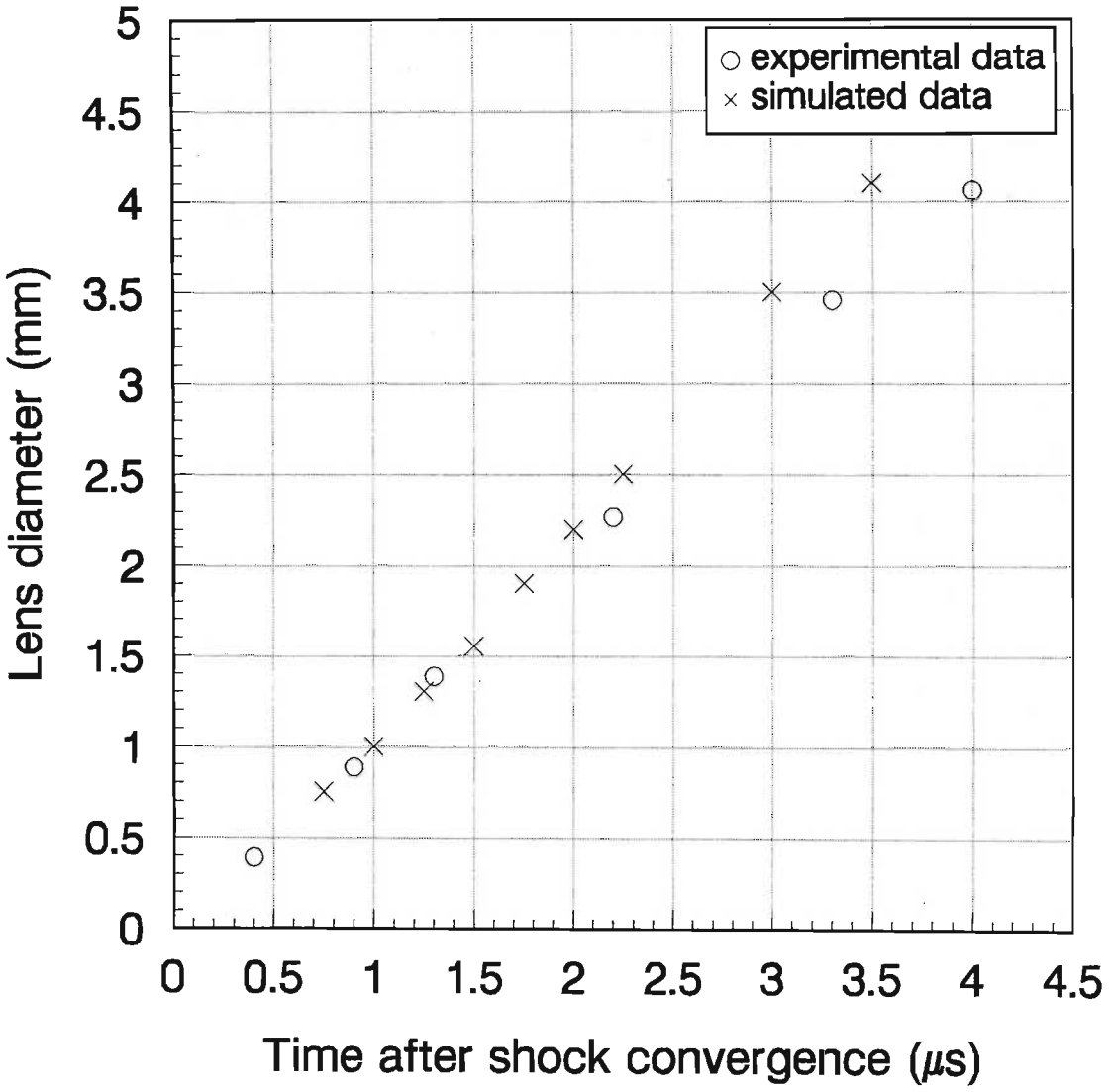

Figure 4.32: A comparison between computed and experimental lens diameters.

simulation of the big CSL than the small CSL.

Scaling up the CSL diameter can also be achieved by increasing the ambient pressure. A simulation of the small CSL operating in an atmosphere of 303 kPa was performed and the results are shown in figure 4.33. The small CSL operating at the higher ambient pressure has a larger lens diameter for the same focal length than the small CSL operating in normal atmospheric conditions. The useful maximum lens diameters are approximately equal for both cases. To generate the same shock strength for both cases, more energy is needed to be given to the shock waves for the CSL operating at 303 kPa.

4.9 Applications of the Colliding Shock Lens

The CSL has a great application potential [Michaelis *et al.* (1993)]. Its varifocal nature and high repetition rate offer the CSL unique applications.

The CSL can be used in conventional industrial applications. The CSL can be coupled to a high power, high repetition rate laser for drilling, cutting and welding applications. The CSL has certain distinct advantages over conventional lenses: the CSL is relatively inexpensive; it is insensitive to dust and dirt; it can focus higher power laser beams and the focal length can be adjusted. A limitation in the industrial application of the CSL is the lens diameter. Work is currently under way to increase the CSL lens diameter to an industrially acceptable size.

Optical switching with spatial filtering and optical isolation could be performed with the CSL. The CSL would form part of a confocal telescope with a pinhole in the focal plane.

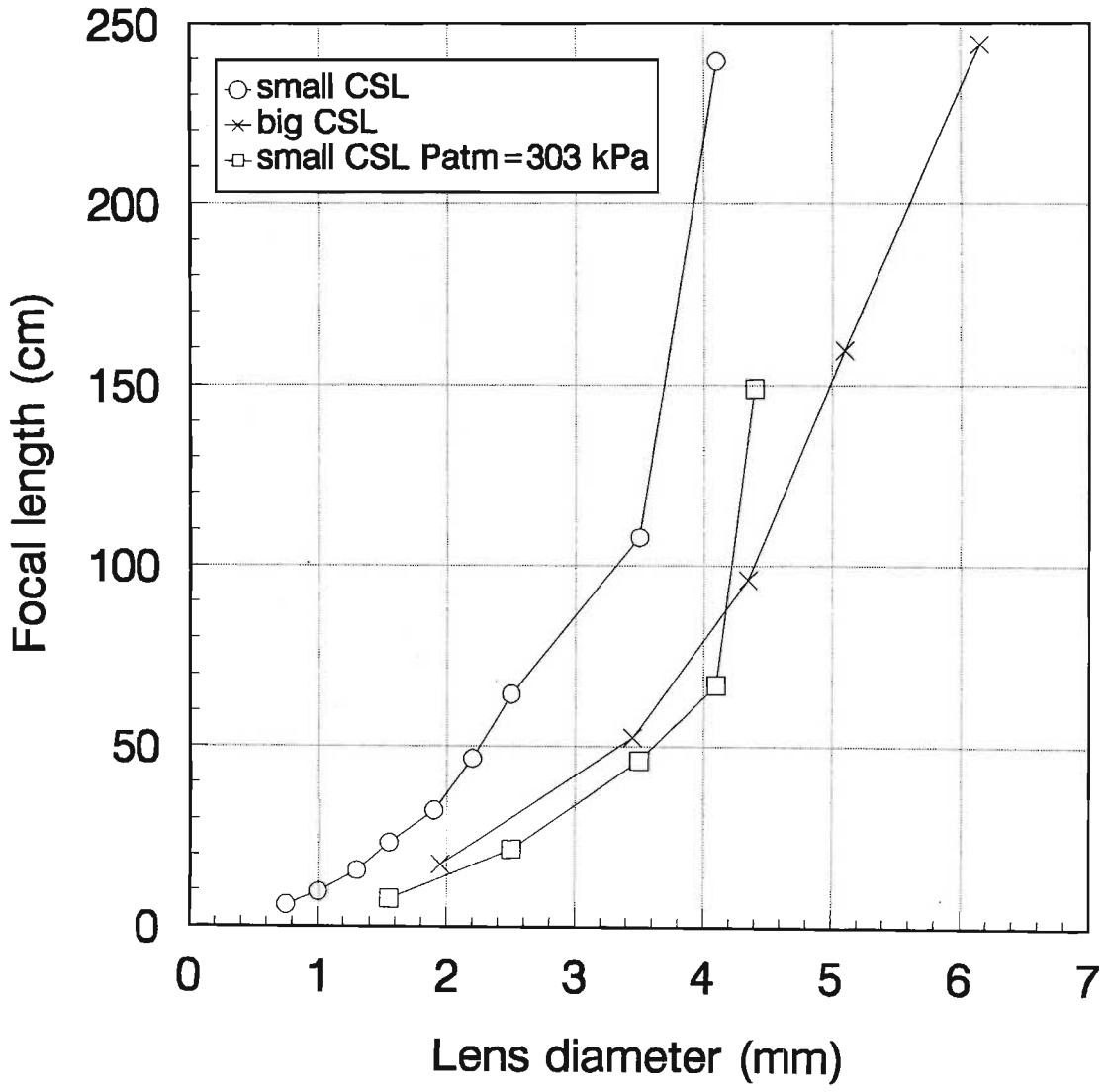

Figure 4.33: Variation of focal length with lens diameter for different CSL.

The CSL has been used as an all gas Q-switch for a Ruby laser [Lisi *et al.* (1993b)]. A CSL placed in tandem with a spinning pipe gas lens inside a laser cavity, produced a giant pulse when the lenses were confocal. A pulse width (FWHM) of 375 ns was obtained

4.10 Conclusion

The CSL is a varifocal lens where the lens diameter and focal length increase with time. The optical quality of the CSL is comparable with conventional lenses. A draw back encountered with the CSL is its small lens diameter. A numerical simulation of the CSL was presented and good agreement with the experimental results was obtained. The simulation was used to investigate the scalability of the lens. It was established that the CSL lens diameter could be increased by increasing the physical dimensions of the CSL. Due to the varifocal nature, high repetition rate and insensitivity to surrounding conditions, the CSL has vast potential applications.

Chapter 5

Conclusions and Summary

This thesis investigated the effects of the refraction of a laser beam through three different phase objects, i.e. a laser produced plasma, an expanding cylinder of gas and a diverging cylindrically symmetric shock wave. The investigation included the assessment of the accuracy of a diagnostic tool for laser produced plasmas and the demonstration of two novel types of gas lenses.

5.1 Comparative Electron Density Measurements for the Refractive Fringe Diagnostic and Nomarski Interferometry

The Refractive Fringe Diagnostic, as an electron density diagnostic tool for laser produced plasmas, was found to over-estimate the electron densities by

an order of magnitude, for the type of laser produced plasmas investigated. The errors were due to the assumptions inherent in the Refractive Fringe Diagnostic, i.e. parabolic ray paths in the plasma and planar wavefronts at the object plane. The errors due to the deviation from the assumed plasma symmetry were not investigated. It was concluded that the Refractive Fringe Diagnostic was a useful "quick look and see" diagnostic tool for laser produced plasmas due to its simplicity in setup and fringe data analysis.

5.2 The Pulsed Gas Lens

A proof-of-principle design of a Pulsed Gas Lens was presented. A numerical simulation of the operation of the Pulsed Gas Lens showed that the lens could be used as a focusing element. A beam deflection device, built to model the operation of the Pulsed Gas Lens, showed that the opening mechanism played an important part in the operation of the lens. The venting mechanism in the simulation was assumed to open instantaneously which was not the case for the beam deflection device. The opening mechanism must be modified to decrease the opening time and to produce a uniform opening.

Future work on the Pulsed Gas Lens will address the problem of the opening mechanism and the incorporation of the opening mechanism into the simulation of the gas expansion. A more accurate assessment of the feasibility of using the Pulsed Gas Lens as a focusing element will be obtained. This work is presently being undertaken by the next generation of Laser Group students.

5.3 The Colliding Shock Lens

Diverging spherical shock waves produced by electric discharges, equi-spaced on a circumference, produced a converging cylindrically symmetric shock wave. The region bounded by the reflected diverging cylindrically symmetric shock wave was found to focus laser light. The optical quality of the Colliding Shock Lens was found to be comparable to equivalent conventional glass lenses. The expansion of the lensing region gives the Colliding Shock Lens the unique feature of being a varifocal lens, i.e. the focal length and lens diameter increase with time. A limitation of the lens was the small lens diameter. A numerical simulation of the Colliding Shock Lens showed that by increasing the physical size of the lens and the input electrical energy, the lens diameter could be increased.

Currently work is being performed in scaling up the lens diameter of the Colliding Shock Lens.

Appendix A

Fluid in Cell Differencing Method

The Fluid in Cell (FLIC) method of Gentry *et al.* [Gentry *et al.* (1966)] used to solve the time dependent equations of motion for compressible fluid flow, in two dimensions, is summarized in this appendix. This summary closely follows the mathematical description of the method given by Gentry *et al.* in their paper and has been included to help the reader gain a better understanding of the simulations performed in the text. The boundary conditions used in the simulation are also discussed in this appendix.

The FLIC method, subdivides the flow field under consideration into a number of cells. A typical mesh is given in figure A.1.

If a cartesian co-ordinate system is used, each cell is a right parallelpiped with dimension $\delta r, \delta z$ and of unit depth. If a cylindrical co-ordinate system is used each cell is a rectangular torus with inner radius $j\ \delta r$ and outer radius

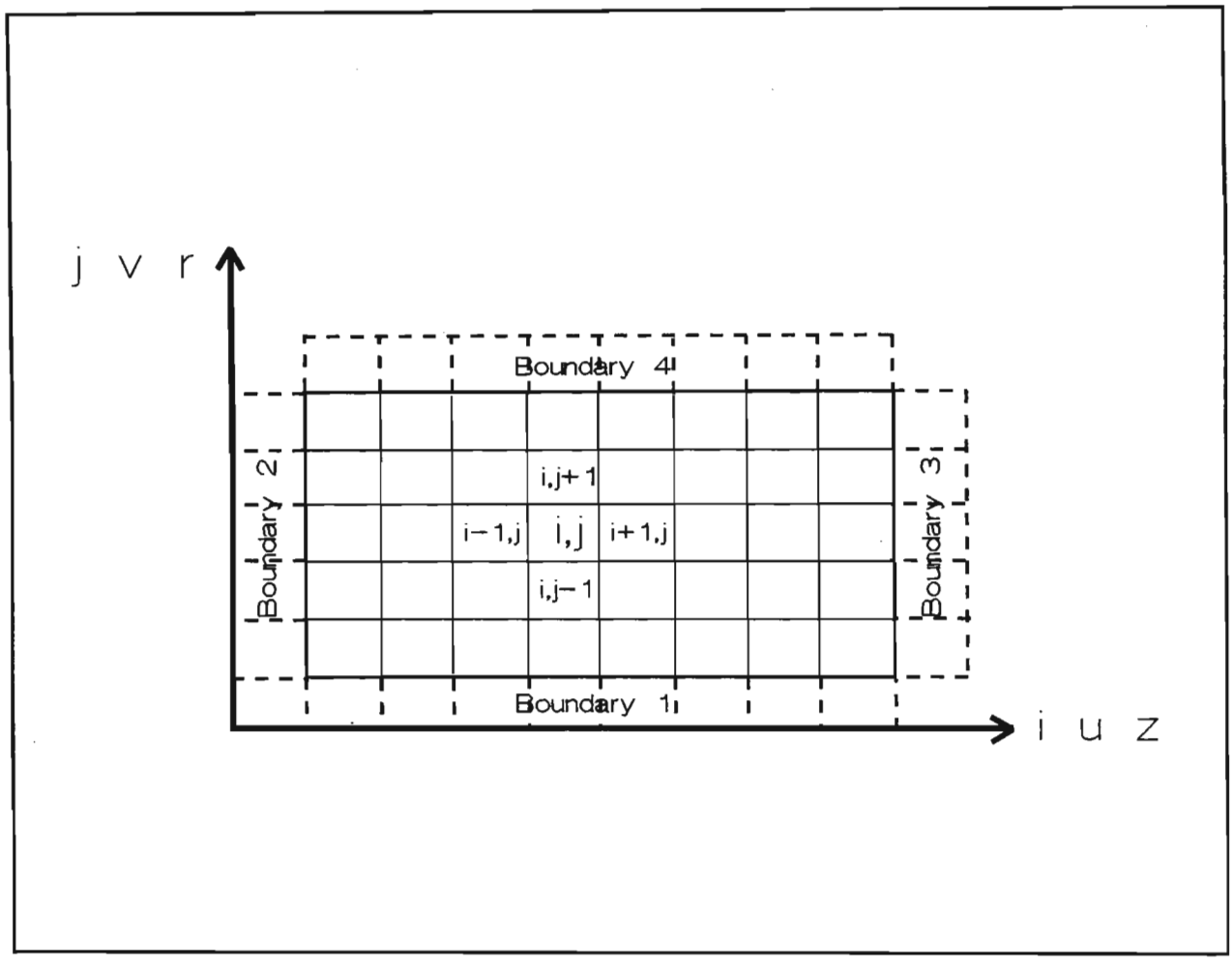

Figure A.1: FLIC computational mesh

$(j+1)\ \delta r$ and width δz. S_j^z is defined as the area of contact between cells (i,j) and $(i+1,j)$, open to flow in the z direction. Similarly, $S^r_{j+\frac{1}{2}}$ is defined as the area of contact between cells (i,j) and $(i,j+1)$, open to flow in the r direction. V_j is the volume of cell (i,j).

For cartesian co-ordinates:

$$V_j = \delta r \delta z \tag{A.1}$$

$$S_j^z = \delta r \tag{A.2}$$

$$S^r_{j+\frac{1}{2}} = \delta z. \tag{A.3}$$

For cylindrical co-ordinates:

$$V_j = 2\pi(j+\frac{1}{2})\delta r^2 \delta z \tag{A.4}$$

$$S_j^z = 2\pi(j+\frac{1}{2})\delta r^2 \tag{A.5}$$

$$S^r_{j+\frac{1}{2}} = 2\pi(j+1)\delta r \delta z. \tag{A.6}$$

The start of the calculation cycle at time $t = n\delta t$ where δt is the time increment and n is a time increment counter with initial value 0, each cell (i,j) is given an initial value of density $(\rho^n_{i,j})$, z-velocity component $(u^n_{i,j})$, r-velocity component $(v^n_{i,j})$ and pressure $(p^n_{i,j})$. The specific internal energy $(I^n_{i,j})$ for each cell (i,j) is calculated using the equation of state:

$$I^n_{i,j} = \frac{p^n_{i,j}}{(\gamma-1)\rho^n_{i,j}}, \tag{A.7}$$

where γ is the ratio of specific heat of the gas used.

The flow variables of each cell is advanced in time using the finite difference approximation for the equations of motion of the fluid. At time $t = (n+1)\delta t$ intermediate values for velocity $(\tilde{v}^n_{i,j}, \tilde{u}^n_{i,j})$ and specific internal energy $(\tilde{I}^n_{i,j})$ are calculated taking into account acceleration effects due to the pressure gradients:

$$\tilde{u}^n_{i,j} = u^n_{i,j} - \frac{\delta t}{\rho^n_{i,j}\delta z}((p+q)^n_{i+\frac{1}{2},j} - (p+q)^n_{i-\frac{1}{2},j}) \tag{A.8}$$

$$\begin{aligned}\tilde{v}^n_{i,j} &= v^n_{i,j} - \frac{\delta t}{\rho^n_{i,j}}(\frac{1}{2V_j}(S^r_{j+\frac{1}{2}}(p^n_{i,j+1} - p^n_{i,j}) \\ &- S^r_{j-\frac{1}{2}}(p^n_{i,j-1} - p^n_{i,j})) \\ &+ \frac{1}{\delta r}(q^n_{i,j+\frac{1}{2}} - q^n_{i,j-\frac{1}{2}}))\end{aligned} \tag{A.9}$$

$$\begin{aligned}\tilde{I}^n_{i,j} &= I^n_{i,j} - \frac{\delta t}{\rho^n_{i,j}V_j}(p^n_{i,j}(S^r_{j+\frac{1}{2}}\overline{v}^n_{i,j+\frac{1}{2}} - S^r_{j-\frac{1}{2}}\overline{v}^n_{i,j-\frac{1}{2}}) \\ &+ \frac{1}{2}q^n_{i,j+\frac{1}{2}}(S^r_{j+1}\overline{v}^n_{i,j+1} + S^r_j\overline{v}^n_{i,j}) \\ &- \frac{1}{2}q^n_{i,j-\frac{1}{2}}(S^r_j\overline{v}^n_{i,j} + S^r_{j-1}\overline{v}^n_{i,j-1}) \\ &- \overline{v}^n_{i,j}S^r_j(q^n_{i,j+\frac{1}{2}} - q^n_{i,j-\frac{1}{2}}) \\ &- \overline{u}^n_{i,j}S^z_j(q^n_{i+\frac{1}{2},j} - q^n_{i-\frac{1}{2},j}) \\ &+ S^z_j(\overline{u}^n_{i+\frac{1}{2},j}(p^n_{i,j} + q^n_{i+\frac{1}{2},j}) \\ &- \overline{u}^n_{i-\frac{1}{2},j}(p^n_{i,j} + q^n_{i-\frac{1}{2},j}))).\end{aligned} \tag{A.10}$$

Note: for simplification the following type of notation was used,

$$p^n_{i+\frac{1}{2},j} = \frac{1}{2}(p^n_{i,j} + p^n_{i+1,j}) \tag{A.11}$$

$$\overline{u}^n_{i,j} = \frac{1}{2}(u^n_{i,j} + \tilde{u}^n_{i,j}). \tag{A.12}$$

The quantity $q^n_{i+\frac{1}{2},j}$ is an explicit artificial viscosity term added to the pressure term to enhance the stability of the difference equations in regions where the fluid velocity is small compared to the local sound speed $c^n_{i,j}$.

If $K(u^2+v^2)^n_{i+\frac{1}{2},j} < (c^2)^n_{i+\frac{1}{2},j}$ and $u^n_{i,j} > u^n_{i+1,j}$ then:

$$q^n_{i+\frac{1}{2},j} = Bc^n_{i+\frac{1}{2},j}\rho^n_{i+\frac{1}{2},j}(u^n_{i,j} - u^n_{i+1,j}), \tag{A.13}$$

otherwise,

$$q^n_{i+\frac{1}{2},j} = 0. \tag{A.14}$$

If $K(u^2+v^2)^n_{i,j+\frac{1}{2}} < (c^2)^n_{i,j+\frac{1}{2}}$ and $v^n_{i,j} > v^n_{i,j+1}$ then:

$$q^n_{i,j+\frac{1}{2}} = Bc^n_{i,j+\frac{1}{2}}\rho^n_{i,j+\frac{1}{2}}(v^n_{i,j} - v^n_{i,j+1}), \tag{A.15}$$

otherwise,

$$q^n_{i,j+\frac{1}{2}} = 0. \tag{A.16}$$

The quantitiy K and B are specified by the user. K determines the maximum value of the Mach number at a cell interface for which the artificial viscosity term will be applied. B denotes the magnitude of the viscous pressure term.

From the intermediate values of velocities calculated, the mass flow across the cell boundaries can be determined. This mass flow is proportional to the density of the donor cell. If $\Delta M^n_{i+\frac{1}{2},j}$ is the mass flow across the area S^z_j between cell (i,j) and $(i+1,j)$ during time δt and similarly $\Delta M^n_{i,j+\frac{1}{2}}$ is the mass flow across the area $S^r_{j+\frac{1}{2}}$ between cell (i,j) and $(i,j+1)$ during time δt then:

$$\Delta M^n_{i+\frac{1}{2},j} = S^z_j \rho^n_{i,j} \tilde{u}^n_{i+\frac{1}{2},j} \delta t \quad if \ \tilde{u}^n_{i+\frac{1}{2},j} > 0 \tag{A.17}$$

$$= S^z_j \rho^n_{i+1,j} \tilde{u}^n_{i+\frac{1}{2},j} \delta t \quad if \ \tilde{u}^n_{i+\frac{1}{2},j} < 0 \tag{A.18}$$

$$\Delta M^n_{i,j+\frac{1}{2}} = S^r_{j+\frac{1}{2}} \rho^n_{i,j} \tilde{v}^n_{i,j+\frac{1}{2}} \delta t \quad if \ \tilde{v}^n_{i,j+\frac{1}{2}} > 0 \tag{A.19}$$

$$= S^r_{j+\frac{1}{2}} \rho^n_{i,j+1} \tilde{v}^n_{i,j+\frac{1}{2}} \delta t \quad if \ \tilde{v}^n_{i,j+\frac{1}{2}} < 0. \tag{A.20}$$

Applying the law of conservation of mass, the density in each cell at time $t = (n+1)\delta t$, can be determined:

$$\rho^{n+1}_{i,j} = \rho^n_{i,j} + \frac{1}{V_j}(\Delta M^n_{i,j-\frac{1}{2}} + \Delta M^n_{i-\frac{1}{2},j} - \Delta M^n_{i,j+\frac{1}{2}} - \Delta M^n_{i+\frac{1}{2},j}). \tag{A.21}$$

Conservation of momentum and energy is used to determine new values of velocity and energy components of each cell, corresponding to $t = (n+1)\delta t$, assuming that the mass which crosses the cell boundaries carries the intermediate components of velocity and specific internal energy of the donor cell, using the relarionship of the form:

$$
\begin{aligned}
F_{i,j}^{n+1} &= \frac{1}{\rho_{i,j}^{n+1} V_j}(T_{i,j}(1)\tilde{F}_{i-1,j}^{n}\Delta M_{i-\frac{1}{2},j}^{n} + T_{i,j}(2)\tilde{F}_{i,j-1}^{n}\Delta M_{i,j-\frac{1}{2}}^{n} \\
&- T_{i,j}(3)\tilde{F}_{i+1,j}^{n}\Delta M_{i+\frac{1}{2},j}^{n} - T_{i,j}(4)\tilde{F}_{i,j+1}^{n}\Delta M_{i,j+\frac{1}{2}}^{n} \\
&+ \tilde{F}_{i,j}^{n}(\rho_{i,j}^{n} V_j + (1 - T_{i,j}(1))\Delta M_{i-\frac{1}{2},j}^{n} + (1 - T_{i,j}(2))\Delta M_{i,j-\frac{1}{2}}^{n} \\
&- (1 - T_{i,j}(3))\Delta M_{i+\frac{1}{2},j}^{n} - (1 - T_{i,j}(4))\Delta M_{i,j+\frac{1}{2}}^{n})), \qquad \text{(A.22)}
\end{aligned}
$$

where:

$$
F_{i,j} = \begin{pmatrix} u_{i,j}^{n} \\ v_{i,j}^{n} \\ E_{i,j}^{n} \end{pmatrix}, \qquad \text{(A.23)}
$$

and

$$
\begin{aligned}
T_{i,j}(k) &= 1 \text{ if fluid flows into cell } (i,j) \text{ across side } k \\
T_{i,j}(k) &= 0 \text{ if fluid flows out of cell } (i,j) \text{ across side } k.
\end{aligned}
$$

Note: $k = 1$ corresponds to the left boundary of a cell, $k = 2$ corresponds to the bottom boundary of a cell, $k = 3$ corresponds to the right boundary of a cell and $k = 4$ corresponds to the top boundary of a cell.

The specific internal energy of each cell is found using the relation:

$$
I_{i,j}^{n+1} = E_{i,j}^{n+1} - \frac{1}{2}(u^2 + v^2)_{i,j}^{n+1}. \qquad \text{(A.24)}
$$

Equation A.7 is used to compute the new pressures in each cell. This calculation cycle is repeated until the desired time is reached.

The above difference equations are applicable to interior cells which are not adjacent to one of the boundaries of the computing mesh. The boundary of the computing mesh is made up of fictitious cells and the type of boundary determines the value of the flow variables in these cells.

For an open output boundary the flow variables in the fictitious boundary cells are made equal to the values in the adjacent interior cells. This allows flow of mass and energy across the boundary. For a closed boundary no mass and energy can flow across the boundary. This requires that the velocity component of the fictitious boundary cell, normal to the boundary, be made equal in magnitude but opposite in direction to that of the interior adjacent cell. All other flow variables are treated in the same way as the open boundary. If the boundary has a corner then the fictitious corner boundary cell is assigned two sets of flow variables depending from which cell the calculation is being made.

The above boundary conditions stipulated by Gentry *et al.* were found by Meintjies (1975) to introduce reflections from the output boundaries into the computational mesh. When dealing with output boundaries Meintjies suggested that the flow variables in each fictitious cell not be set equal to the adjacent value but be set equal to a linear interpolated value from two adjacent cells, eg: the density of a fictitious boundary cell, $\rho^n_{i+1,j}$, is given by:

$$\rho^n_{i+1,j} = 2\rho^n_{i,j} + \rho^n_{i-1,j}. \tag{A.25}$$

The boundary flow variables suggested by Meintjies (1975) were used in the

PGL simulation.

References

ABERBANEL S., GOLDBERG M.
J. Comput. Phys., **10** 1 (1972)

AHLBORN B., HUNI J.P.
AIAA J., **7** (6) 1191 (1969)

ATTWOOD D.T., SWEENEY D.W., AUERBACH J.M., LEE P.H.Y.
Phys. Rev. Lett., **40** 184 (1978)

BACH G.G., LEE J.H.
J. Fluid Mech., **37** 513 (1969)

BACON M., CAMPBELL R.N., CUNNINGHAM P.F., MICHAELIS M.M.
J. Appl. Phys., **66** (3) 1075 (1989)

BASOV N.G., ZAKHARENKOV YU.A., ZOREV N.N., SKLIZKOV G.V., RUPASOV A.A., SHIKANOV A.S.
"Heating and Compression of Thermonuclear Targets by Laser Beam", Cambridge University Press, Cambridge (1986)

BASOV N.G., LEBO I.G., ROZANOV V.B.
"The Physics of Laser Induced Thermonuclear Fusion", Knowlege Press, Moskow (1988)

BEN-ARTZI M., FALCOVITZ J.
SIAM J. Sci. Stat. Comput., **7** 744 (1986)

BENATTAR R., POPOVICS C., SIGEL R.
Rev. Sci. Instrum., **50** 1583 (1979)

BENATTAR R., POPOVICS C.
J. Appl. Phys., **54** (2) 603 (1983)

BORN M., WOLF E.
"Principles of Optics", Pergamon, London (1965)

BUCCELLATO R., CUNNINGHAM P.F., MICHAELIS M.M., PRAUSE A.
Laser and Particle Beams, **10** 697 (1992)

BUCCELLATO R., MICHAELIS M.M., DEMPERS C.A., PRAUSE A.
Opt. & Laser Technol., **25** (4) 247 (1993a)

BUCCELLATO R., LISI N., MICHAELIS M.M.
Opt. Comms., **101** 350 (1993b)

BUTLER D.S.
Armament Research and Development Establishment, Rep. no. 54/54 (1954)

BUTLER T.D.

AIAA J. **4** (3) 460 (1966)

CAMPBELL R.N.
"Refractive Fringe Diagnostic of Plasma", Ph.D. thesis, Univesity of Natal, Durban (1985)

CHEN F.F.
"Introduction to Plasma Physics", Plenum, New York (1974)

COURANT R., FRIEDRICHS K.O., LEWY H.
Mathematische Annalen, **100** 32 (1928)

COURANT R., FRIEDRICHS K.O.
"Supersonic Flow and Shock Waves", Interscience, New York (1948)

CRAGGS J.D.
"Electrical Breakdown of Gases" ed. Meek J.M., Craggs J.D.; Wiley-Interscience, Chichester (1978)

CUNNINGHAM P.F., CAMPBELL R.N., MICHAELIS M.M.
J. Phys.E.: Sci. Instrum., **19** 957 (1986a)

CUNNINGHAM P.F., CAMPBELL R.N., MICHAELIS M.M., BHAGWANDIN N.
S. Afr. J. Phys., **9** 103 (1986b)

DENNEN R.S., WILSON L.N.
"Exploding Wires", Plenum, New York (1962)

DEUTSCH M., BENIAMINY I.
Appl. Phys. Lett., **41** 27 (1982)

EINSTEIN A.
Physikalische Zeitschrift, **18** 121 (1917)

EVANS M.E., HARLOW F.H.
LASL Rept. No. la-2139, Los Alamos, New Mexico (1957)

EVTUSHENKO T.P., ZAIDEL A.N., OSTROVSKAYA G.V.,
OSTROVSKII YU.T., CHELIDZ T.YA.
"Recent advances in Plasma Diagnostics", Consultants Bureau, New York (1971)

FEDOSEJEVS R., BURGESS M.D.J., ENRIGHT G.D., RICHARDSON M.C.
Phys. Rev. Lett., **43** 1664 (1979)

FLAGG R.F., GLASS I.I.
Phys. Fluids, **11** 2282 (1968)

FLETCHER A., MURPHY T., YOUNG A.
Proc. R. Soc. Lond., **223** 216 (1954)

FROMM J.E.
LASL Rept. No. 2535, Los Alamos, New Mexico (1961)

GAYDON A.G., HURLE I.R.
"The Shock Tube in High-Temperature Chemical Physics", Chapman and Hall, London (1963)

GENTRY R.A., MARTIN R.E., DALY B.J.
J. Compt. Phys., **1** 87 (1966)

GLASS I.I., CHAN S.K., BRODE H.L.
AIAA J., **12** (3) 367 (1974)

GLASS I.I., SHARMA S.P.
AIAA J., **14** (3) 402 (1976)

GLASS I.I., SAGIE D.
Phys. Fluids, **25** (2) 269 (1982)

GLIMM J.
J. Comm. Pure Appl. Math., **18** 697 (1965)

GORDON J.P., ZEIGER H.J., TOWNES C.H.
Phys. Rev., **99** 1264 (1955)

GUDERLEY G.
Luftfahrtforchung, **19** 302 (1942)

HALL T.A.
"Laser-Plasma Interactions 3" ed. M.B. Hooper; SUSSP Publications, Edinburgh (1986)

HAMAMOTO M., MURAOKA K., AKAZAKI M.
Jpn. J. Appl. Phys., **19** (6) L293 (1980)

HARLOW F.F., AMSDEN A.A.

LASL Rept. No. la-4100, Los Alamos, New mexico (1970)

HECHT E.
"Optics", Addison-Wesley, Reading (1989)

HONIG R.E., WOOLSTON J.R.
Appl. Phys. Lett., **2** 138 (1963)

HUGHES T.P.
"Plasma and Laser Light", Adam Hilger, Bristol (1975)

JAVAN A., BENNETT W.R. JR, HERRIOT D.R.
Phys. Rev. Lett., **6** 106 (1961)

JET TEAM
Nuclear Fusion, **32** 187 (1992)

KARE J.T.
SDIO Workshop on Laser Propulsion (1987)

KEILMANN F.
Plasma Phys., **14** 111 (1972)

KEY M. H.
"Laser-Plasma Interactions 3" ed. M.B. Hooper; SUSSP Publications, Edinburgh (1986)

KNYSTAUTAS R., LEE B.H.K., LEE J.H.S.
Phys. Fluids Suppl. I, **12** 165 (1969)

KOGELSCHATZ U., SCHNEIDER W.R.
Appl. Opt., **11** 1822 (1972)

LAPIDUS A.
J. Comput. Phys., **8** 106 (1971)

LAX P.D.
Comm. Pure and Appl. Math., **9** 267 (1954)

LEE B.H.K.
AIAA J., **5** (11) 1997 (1967)

LEE J.H., LEE B.H.K.
Phys. Fluids, **8** (12) 2148 (1965)

LINLOR W. I.
Appl. Phys. Lett., **3** 210 (1963)

LISI N., BUCCELLATO R., MICHAELIS M.M.
Opt. & Laser Technol., in press (1993a)

LISI N., MICHAELIS M.M., BUCCELLATO R., KUPPEM M., PRAUSE A.
submitted to *Phys. Rev. Lett.* (1993b)

LISI N.
Ph.D. thesis, University of Natal, Durban, forthcoming (1994)

MAIMAN T.H., HOSKINS R.H., D'HAENENS I.J., ASAWA C.K.
Phys. Rev., **123** 1151 (1961)

MAKER P.D., TERHUNE R.W., SAVAGE R.W.
Proc. 3rd Int. Conf. on Quantum Electron. ed. P. Grivet and N. Bloembergen; Columbia University Press, New York (1963)

MATSUO H.
Phys. Fluids, **22** (9) 1618 (1979)

MATSUO H., NAKAMURA Y.
J. Appl. Phys., **51** (6) 3126 (1980)

MATSUO H., NAKAMURA Y.
J. Appl. Phys., **52** (7) 4503 (1981)

MATSUO H., EBIHARA K., NAGAYAMA K.
J. Appl. Phys., **55** (1) 271 (1984)

MATSUO H., EBIHARA K., OHYA Y., SANEMATSU H.
J. Appl. Phys., **58** (7) 2487 (1985)

MATSUO H., OHYA Y., FUJIWARA K., KUDOH H.
J. Comput. Phys., **75** 384 (1988)

MATSUO H., FUJIWARA K.
Phys. Fluids A, **2** (2) 266 (1990)

MEINTJIES K.
M.Sc. Thesis, University of the Witwatersrand, Johannesburg (1975)

MEYERAND R.G., HAUGHT A.F.

Phys. Rev. Lett., **11** 401 (1963)

MICHAELIS M.M., WILLI O.
Opt. Comm., **36** 153 (1981)

MICHAELIS M.M, BHAGWANDIN N., CUNNINGHAM P.
Opt. Comm., **52** 371 (1985)

MICHAELIS M.M., CUNNINGHAM P.F.,CAZALET R.S., WALTHAM J.A., NOTCUTT M.
Laser and Particle Beams, **9** 641 (1991a)

MICHAELIS M.M., WALTHAM J.A., CUNNINGHAM P.F.
Opt. & Laser Technol., **23** (5) 283 (1991b)

MICHAELIS M.M., BUCCELLATO R., LISI N., KUPPEN M.
Laser and Particle Beams, in press (1993)

MORETTI G. ABBETT M.
AIAA J., **4** (12) 2136 (1966)

NOMARSKI M.G.
Journal de la Physique et le Radium, **16** 95 (1955)

NOTCUTT M., MICHAELIS M.M., CUNNINGHAM P.F., WALTHAM J.A.
Opt. & Laser Technol., **20** (5) 243 (1988)

PAYNE R.B.
J. Fluid Mech., **2** 185 (1957)

PAWLOWICZ W.
SINS-2103/P-V/PP/A, Soltan Institute for Nuclear Studies, Internal Report (1990a)

PAWLOWICZ W.
SINS-2120/P-V/PP/A, Soltan Institute for Nuclear Studies, Internal Report (1990b)

PERRY R.W., KANTROWITZ A.
J. Appl. Phys., **22** (7) 878 (1951)

PHIPPS C.R.
Laser and Particle Beams, **7** 835 (1989)

PITTS J.
UCRL Rept. No. 92558, Lawrence Livermore National Laboratory (1985)

RAVEN A., WILLI O.
Phys. Rev. Lett., **43** 278 (1979)

RICHARDSON L.F.
Trans. R. Soc. Lond. A., **210** 307 (1910)

ROACHE P.J.
J. Compt. Phys., **10** 169 (1972)

ROACHE P.J.
"Computational Fluid Dynamics", Hermosa, New Mexico (1985)

ROIG R.A., GLASS I.I.
Phys. Fluids, **20** (10) 1651 (1977)

ROBERTS D.E., GLASS I.I.
Phys. Fluids Lett., **14** (8) 1662 (1971)

SAITO T., GLASS I.I.
Proc. R. Soc. Lond. A, **384** 217 (1982)

SCHAWLOW A.L., TOWNES C.H.
Phys. Rev., **112** 1940 (1958)

SCHREIBER P.W., HUNTER A.M.,II , SMITH D.R. JR.
Plasma Phys., **15** 635 (1973)

SCHWENDEMAN D.W., WHITHAM G.B.
Proc. R. Soc. Lond. A, **413** 297 (1987)

SHAPIRO A.H.
The Dynamics and Thermodynamics of Compressible Fluid Flow, Ronald Press , New York (1954)

SOD G.A.
J. Fluid Mech., **83** 785 (1977)

SOD G.A.
J. Compt. Phys., **27** 1 (1978)

SRIVASTAVA R.C., LEUTLOFF D., ROESNER K.G.

Astrophys. Space. Sci., **192** 1 (1992)

STANYUKOVICH K.P.
"Unsteady Motion of Continuous Media", Pergamon, Oxford (1960)

SWEENEY D.W., ATTWOOD D.T., COLEMAN L.W.
Appl. Opt., **15** 1126 (1976)

THOM A.
Proc. R. Soc. Lond. A., **141** 651 (1933)

VERBER C.M., ADELMAN A.H.
Appl. Phys. Lett., **2** 220 (1963)

VEST C.M.
Appl. Opt., **14** 1601 (1975)

VON NEUMANN J., RICHTMYER R.D.
J. Appl. Phys., **21** 232 (1950)

WALTHAM J.A., CUNNINGHAM P.F., MICHAELIS M.M.,
CAMPBELL R.N., NOTCUTT, M.
Opt. & Laser Technol., **19** (4) 203 (1987)

WALTHAM J.A.
Ph.D. Thesis, University of Natal, Durban (1991)

WOOD R.W.
"Physical Optics", Macmillan, New York (1905)

Wu J.H.T., Neemeh R.A., Ostrowski P.P.
AIAA J., **18** (1) 47 (1980)

Wu J.H.T., Neemeh R.A., Ostrowski P.P.
AIAA J., **19** (3) 257 (1981)

Optics Communications 101 (1993) 350–355
North-Holland

OPTICS
COMMUNICATIONS

Colliding shock lens

R. Buccellato, N. Lisi and M.M. Michaelis
Plasma Physics Research Institute, University of Natal, Durban, South Africa

Received 7 December 1992; revised manuscript received 8 March 1993

A pulsed colliding shock lens is developed where the shocks were generated by electric discharges. Near diffraction limited focusing was observed.

1. Introduction

Gas lenses have recently been shown to be more versatile than expected [1,2]. Continuous wave gas lenses have industrial potential and even show promise in astronomy [3]. In ref. [4] we consider a macroscopic pulsed gas lens that could be used as a final focusing element in a laser driven thermonuclear fusion experiment. In this article we describe a novel type of pulsed gas lens which would be suitable for operation in series with a small pulsed gas laser: the colliding shock lens (CSL).

2. Colliding shock lens principle

When two spherical shocks collide, the interaction depends on their strength [5]. At low Mach number (M_0) the waves simply pass unmodified through one another. At intermediate M_0 they pass but are somewhat delayed. At higher M_0, there is a period of stagnation during which the fronts merge into a high density plane slab, and at very high M_0 the collision generates turbulence. When several shocks are launched from explosion points placed on the arc of a circle, one might expect similar behaviour to that of the double shock interaction. Moreover, since many shocks now collide at one point, nonlinearities in the shock interaction are expected to occur at lower M_0 than for two colliding shocks. The regime of interest here, is at an intermediate M_0 when the fronts interact in a nonlinear but orderly manner.

When several spherical shocks, produced by arc discharges, expand from points equi-spaced on a circumference, a cylindrically symmetric converging shockfront is formed. Schwendeman and Witham [6] have noted that converging cylindrical shocks with regular polygonal shaped cross-sections are stable and tend towards a circular cross-section. Converging cylindrically symmetric shock waves produce a condition of high pressure, temperature and density in the region of implosion. After the spherical shock converges to a point, a regular and stable [7] axi-symmetric cigar shaped expanding density distribution results. It is in this region that we expect the density distribution to act as a graded index lens.

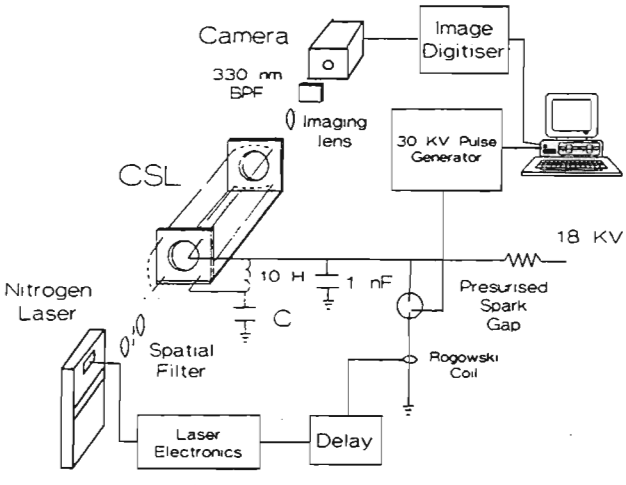

Fig. 1. Experimental setup.

3. Experimental setup

A schematic representation of the experimental setup, including the colliding shock lens, is shown in fig. 1. The spherical shocks were created at points equi-spaced on a circumference (diameter 11 mm) by eight pairs of opposing electrodes (for simplicity only four pairs of electrodes are shown in fig. 1). We utilized needles of diameter 0.85 mm and an arc gap spacing of 1 mm. The electrodes were mounted on two opposite plexiglass plates with a circular hole in the center (diameter 7.5 mm) allowing a laser beam to be directed along the axis of the CSL. The gaps were connected in series in order to have approximately simultaneous breakdown. A spatially filtered nitrogen laser beam (fwhm ≈ 1 ns) was directed through the collision region onto a T.V. camera face plate through an imaging lens and a nitrogen interference filter (330 nm, bandwidth 10 nm). A PC synchronised the triggering of the CSL with the image digitiser. A Rogowsky coil in the CSL circuitry triggered the nitrogen laser via a variable delay box. The value of the capacitor C determines the energy provided to the colliding shocks. A 5 nF capacitor was used.

4. Results

The CSL properties were investigated by recording images at different distances from the CSL and at different delays. Parasitic fringes were due to the interference filter.

A time sequence for the colliding shocks is given in fig. 2 ($M_0 \approx 1.5$). After the eight shocks have collided (figs. 2f, 2g) a high density expanding region

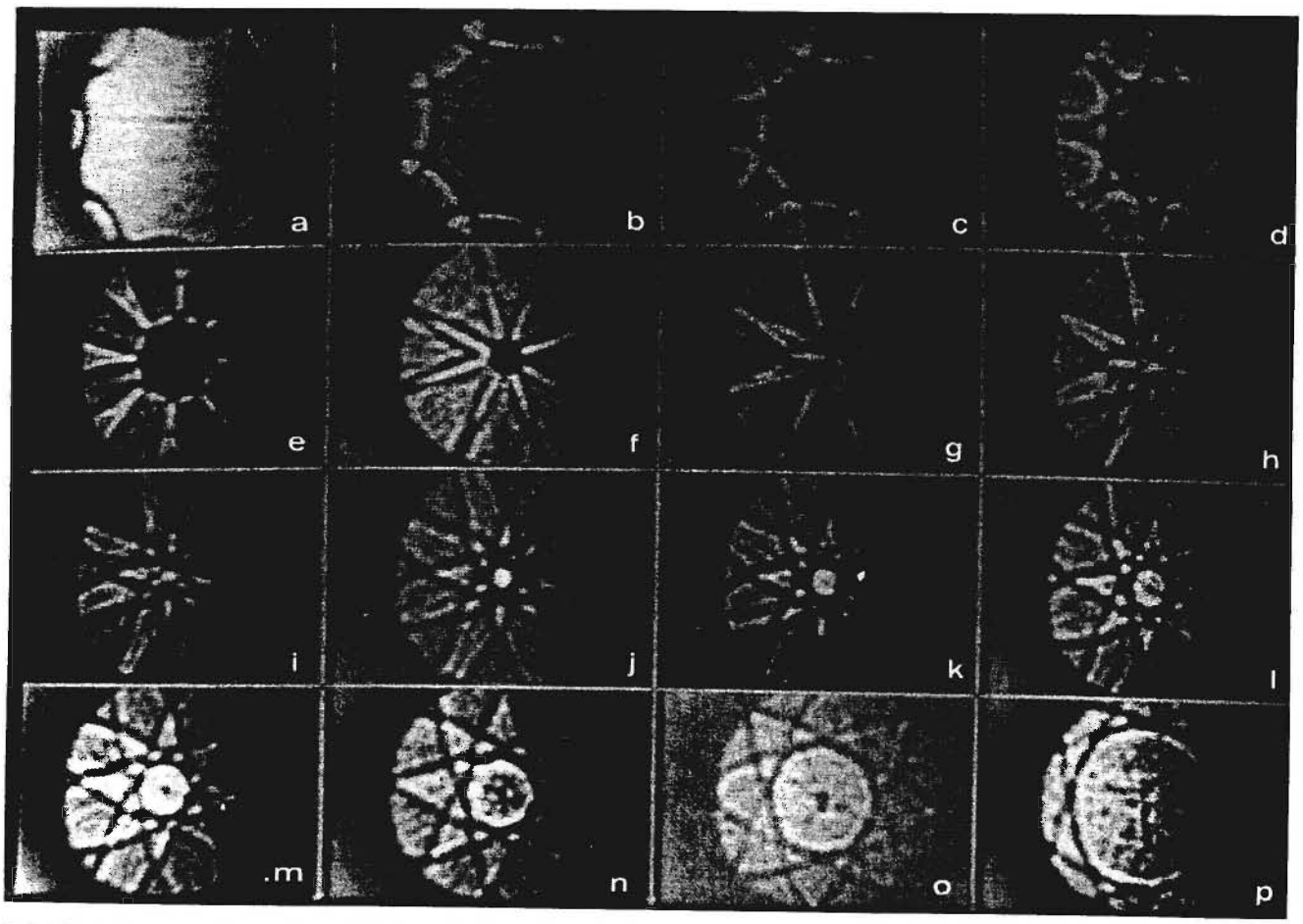

Fig. 2. Time sequence of an eight arc CSL imaged 19 cm from the CSL at (a) 3.2 μs, (b) 5 μs, (c) 6 μs, (d) 6.9 μs, (e) 8 μs, (f) 10 μs, (g) 10.4 μs, (h) 10.9 μs, (i) 11.3 μs, (j) 11.6 μs, (k) 11.8 μs, (l) 12.2 μs, (m) 12.4 μs, (n) 13.1 μs, (o) 14 μs, (p) 15.6 μs.

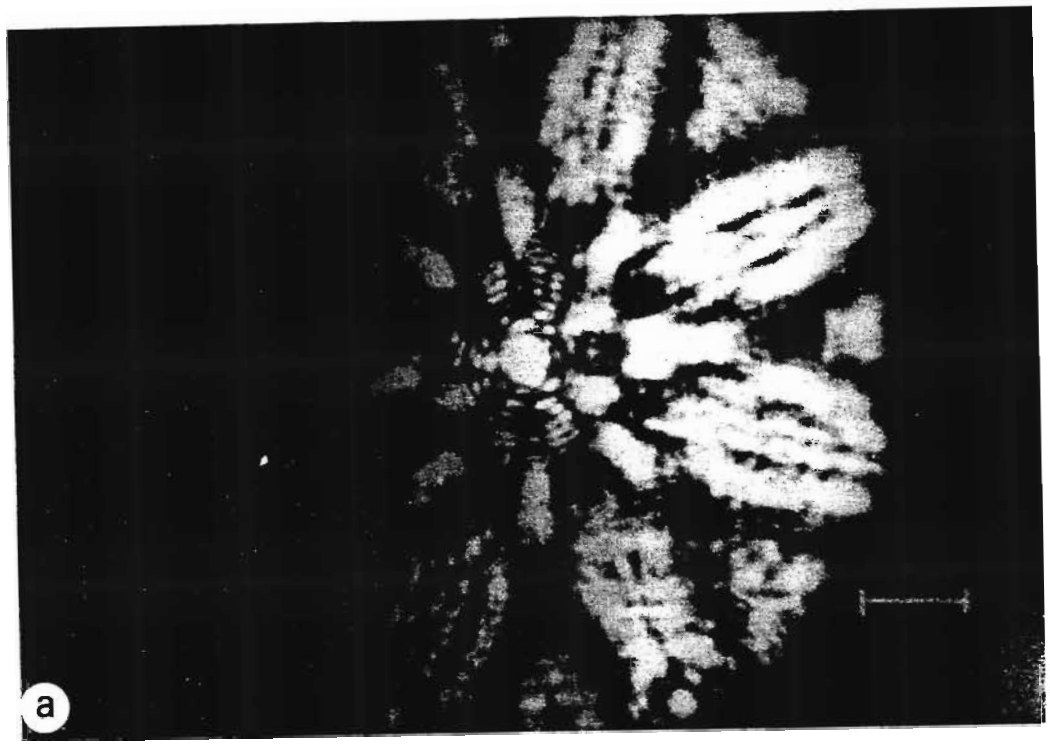

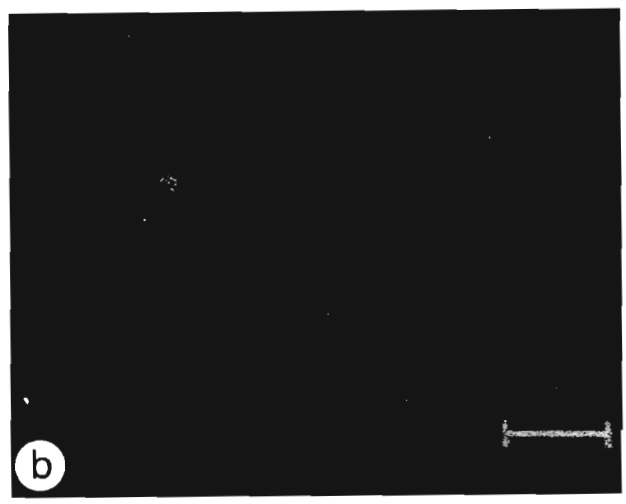

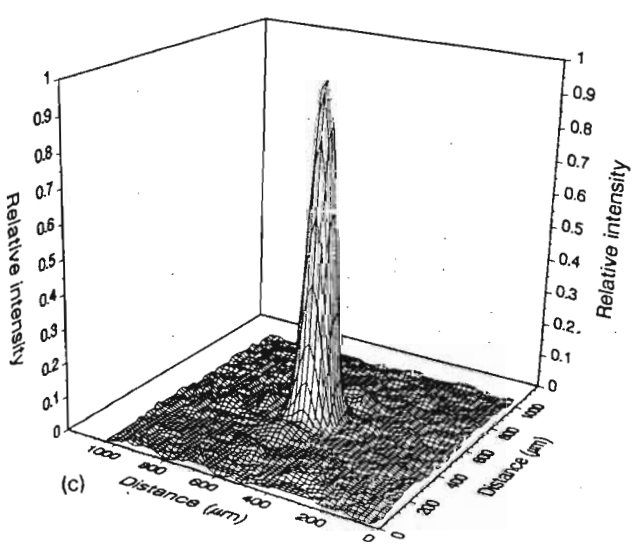

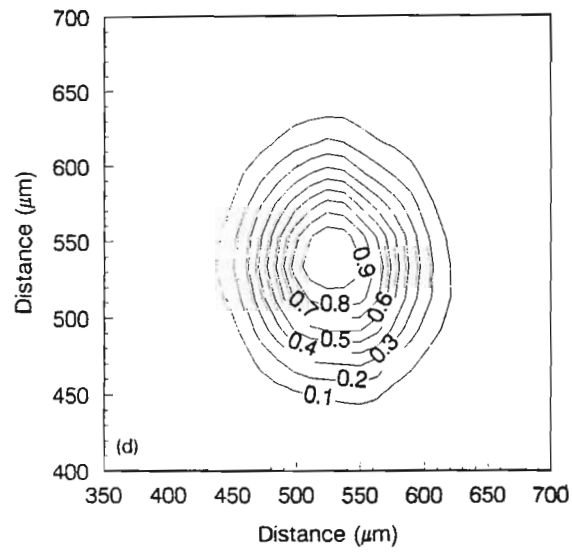

Fig. 3. (a) Eight arc CSL focal spot (focal length 39 cm, delay 11.8 μs). (b) Focal spot with an additional filter. (c) 3D relative intensity distribution of the central region. (d) Relative intensity contour plot of the central region (bar = 1 mm).

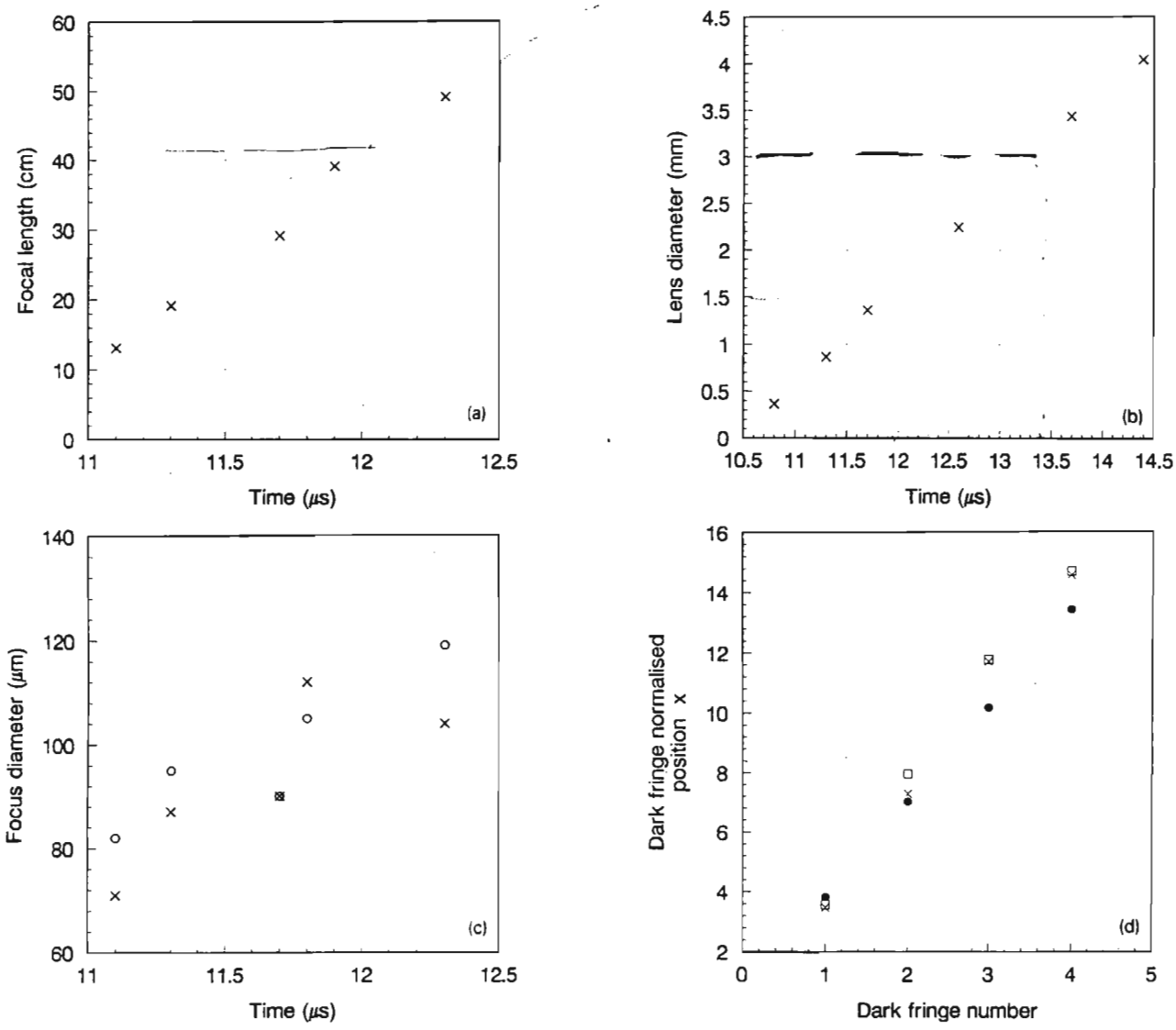

Fig. 4. (a) Focal length of eight arc CSL at different times after arcing. (b) Effective lens diameter. (c) Comparison of focus diameters (fwhm) with time, ○: experimental focus diameter, ×: diffraction limit. (d) Dark fringe number versus dark fringe normalized position $x=(\pi D d_f)/(\lambda f)$, d_f is the dark fringe position, D, f are the lens diameter and focal length, respectively. ● Theoretical, □: lens diameter of 0.84 mm, focal length is 19.1 cm; ×: lens diameter of 1.3 mm and focal length of 39.1 cm.

is created (figs. 2h, 2p). Focusing is achieved in figs. 2h and 2i. Figures 2j–m show the typical diffraction pattern when focusing is achieved closer to the TV camera. Figure 3a shows the focusing obtained with the eight arc CSL ($C=5$ nF) at a distance of 39 cm. The image in fig. 3b was recorded with an addition filter (ND=1). A three-dimensional representation of the relative intensity of the central region is shown in fig. 3c and the associated contour plot is shown in fig. 3d. The fwhm focal spot diameter is 100 μm. The CSL is a varifocal lens in which the focal length increases with time: fig. 4a. The effective lens diameter was obtained by imaging on the shock collision plane. Due to the expansion of the shockfront after the collision, the effective lens diameter increases with time (fig. 4b). Consequently, the relative diffraction limited focal spot size is expected to vary with time and is consistent with the measured focal spot size (fig. 4c). The position of the rings surrounding the central spot (fig. 3a) is in reasonable agreement with

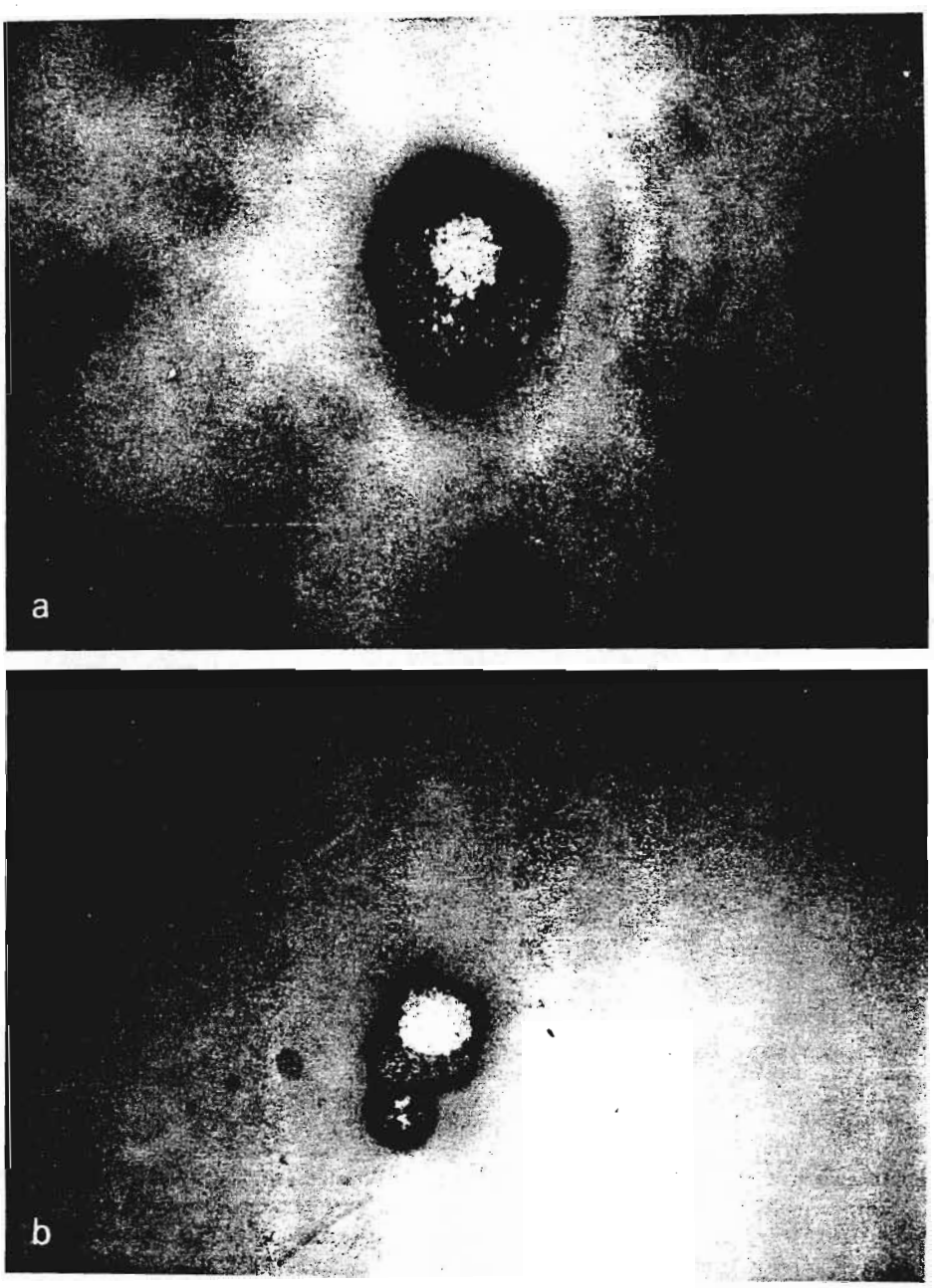

Fig. 5. (a) Eight arc CSL burn pattern (focal length 39 cm, delay 11.8 μs). (b) Equivalent glass lens burn pattern.

the theoretical Airy rings value (fig. 4d).

The CSL was used to focus a ruby laser beam (fwhm $\approx$ 30 ns, $E \approx 0.5$ J) onto photographic paper in order to obtain a burn pattern. We chose a focal length of 39 cm. The diffraction limited ruby beam was directed through the lensing region and the burn pattern shown in fig. 5a was obtained. For comparison a glass convex lens of equal focal length was apertured to 1.5 mm. This is the effective aperture of the CSL. The burn pattern of fig. 5b was obtained. The secondary spot in the lower region of the burn patter is due to secondary reflections by the prisms used to direct the beam through the lens. The central burnt regions for both lenses were approximately 200 μm in diameter.

5. Conclusion

We have developed a novel type of focusing device, the colliding shock lens, where near diffraction limited focusing was observed. Although the useful aperture of this lens is small we are in the process of scaling up its dimensions.

Acknowledgements

Useful discussions were held with P.F. Cunningham and A. Prause. We thank W. de Beer, D. Davies and B. Buhrman for their technical assistance, and the Laser Applications and Research Institute of South Africa (LARISA) and the Foundation for Research and Development (FRD) for financial support.

References

[1] B.L. Xie, S.J. Xia and Q.T. Chow, Chinese Phys. Lett. 2 (1985) 509.
[2] M.M. Michaelis, P.F. Cunningham, R.S. Cazalet, J.Z. Waltham and M. Notcutt, Laser and Particle Beams 9 (1991) 641.
[3] M.M. Michaelis, C.A. Dempers, M. Kosch, A. Prause, M. Notcutt, P.F. Cunningham and J.A. Waltham, Nature 353 (1991) 547.
[4] R. Buccellato, M.M. Michaelis, C.A. Dempers, A. Prause and P.F. Cunningham, Optics and Laser Technology, to be published.
[5] R. Courant and K.O. Friedrichs, Supersonic flow and shock waves (Interscience, New York, 1948) p. 297.
[6] D.W. Schwendeman and G.B. Whitham, Proc. R. Soc. Lond. A 413 (1987) 297.
[7] H. Matsuo and Y. Nakamura, J. Appl. Phys. 52 (1981) 4503.

Optical quality and temperature profile of a spinning pipe gas lens

N. LISI, R. BUCCELLATO, M. M. MICHAELIS

A spatially resolved temperature measurement in a spinning pipe gas lens of aperture 2.25 cm and length 1 m, is presented. Ray tracing through the measured refractive index profile was performed. We show that by reducing the optical aperture of the lens (to 1 cm), an angular resolution of twice the diffraction limited is obtainable.

KEYWORDS: gas lenses, optical quality, temperature measurement

Introduction

Gas lenses were first developed at Bell Laboratories[1] shortly after the invention of the laser, but fell into oblivion owing to their main applications—optical communication and power transmission—avering themselves as impractical. Recently, there has been a resurgence of interest with the realization that gas lenses may be used to focus lasers and drill holes[2] and may even earn a role in telescopy.[3] Thermal gradient gas lenses are typically long focal length, small aperture devices. In early versions the lens consisted of a small cross-section metal pipe in which gas was fluxed along the optical axis.[1] The obvious difficulty that was encountered in scaling up the aperture and keeping the focal length short is the consequent increase in the temperature radial gradients. These larger gradients give rise to convection currents which impair or even destroy the action of the lens.[4] Some improvement could be obtained by spinning the lens,[2] in order to eliminate the convection cells. In this case the gas flow stops being laminar and no analytical theory is available. In Ref. 5 the temperature profile was measured for a fluxed small diameter gas lens and the results showed good agreement with the theory. We have measured the temperature profile of a spinning pipe gas lens both along the optical axis and along the vertical section: the latter to look for the eventual gravitational effect on the temperature distribution of the gas. We performed this measurement to quantify the optical quality of the device.

Experimental details

Our aim was to measure the gas temperature inside the heated spinning pipe with a spatial resolution of the order of 1 mm along the radius of the lens and 1 cm along its optical axis. Our detector consisted of a NiCr thermocouple, made of two 200 μm diameter wires. The thermocouple was secured via a thermally insulated material on a thin steel wire ($d = 400\,\mu$m) as a support suspended by two XYZ mounts. The experimental set-up, shown in Fig. 1 allows us to move our probe in the lens with the required precision. The probe thermocouple was referenced to a second NiCr thermocouple, submerged in a mixture of ice and water at 273.3 K. The output voltage was

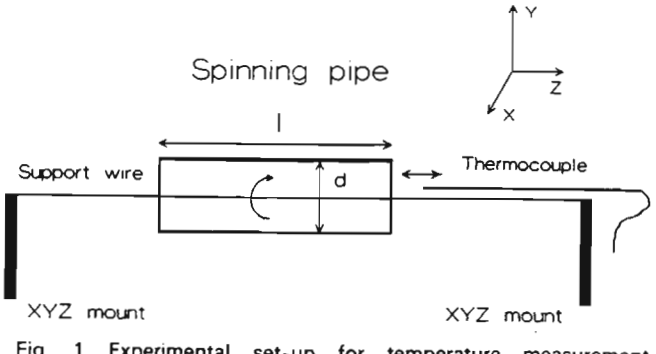

Fig. 1 Experimental set-up for temperature measurement. $D = 2.25$ cm, $L = 100$ cm

The authors are at the Plasma Physics Research Institute, University of Natal, Durban, South Africa. Received 14 June 1993. Revised 12 August 1993.

0030-3992/94/010025-03

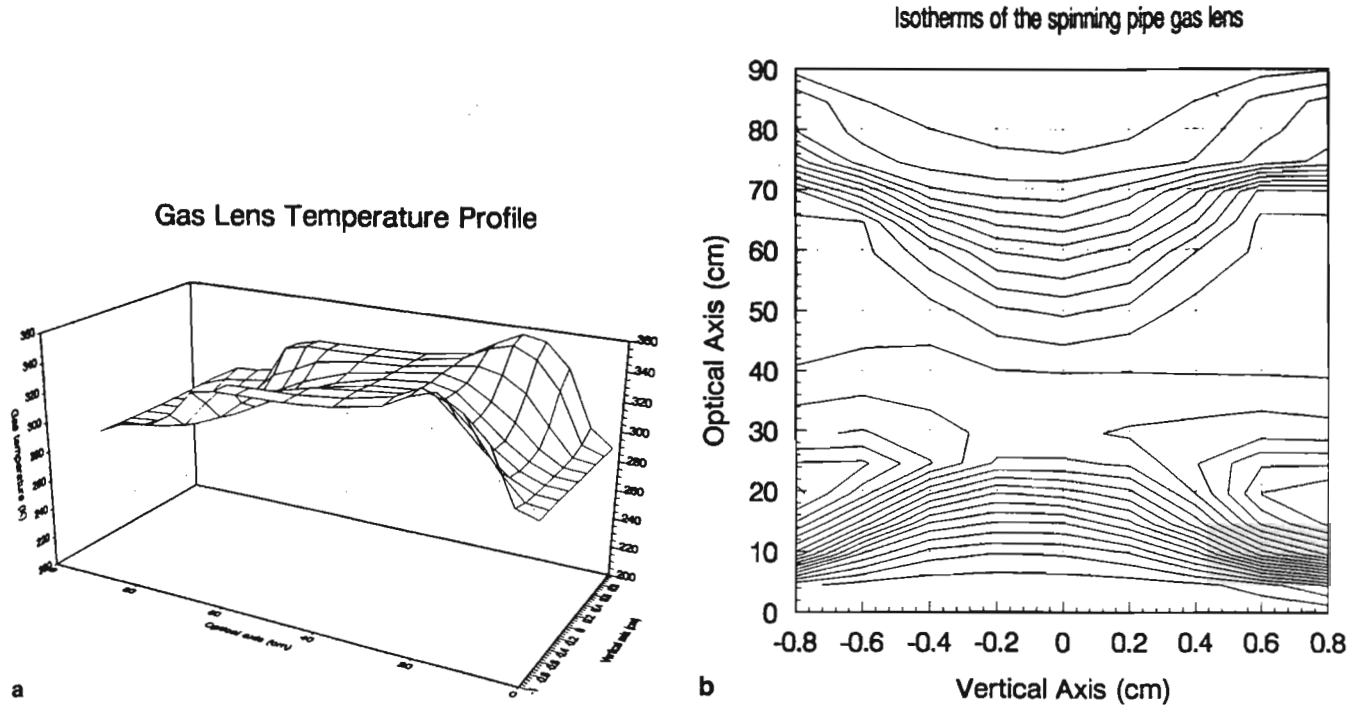

Fig. 2 Measured temperature profile: (a) three-dimensional plot; (b) isotherms

read on a Keithley 199 Voltmeter and the measured voltage values were then normalized according to the polynominal for type k thermocouples.[6]

In Fig. 2(a) we show the temperature profile. The temperature distribution is flat in the middle region of the pipe where the co-rotating vortices[7] meet and there is almost no longitudinal gas flow while two regions of strong transverse thermal gradients are present near the edges of the pipe. The asymmetry between these two regions is due to the asymmetry in the heating of the pipe. It was found empirically that the lens works better under such conditions. During the experiment, we kept the rotational speed of the lens at 30 Hz and the temperature of the pipe at 400 K, which gave a focal length of 2 m. Figure 2(b) shows the vertical asymmetry caused by gravity in greater detail. This vertical asymmetry has an important effect on the performance of the lens, as described later.

Some observations about the experiment

After changing the measurement position, our probe requires, typically, some seconds to reach a steady asymptotic value. We noted that the gas flow inside the spinning pipe is very sensitive to the flow conditions surrounding the lens, such as draughts in the laboratory. Large fluctuations in local temperature are sometimes observed corresponding to small external perturbations. To obtain reproducible results, as with all gas lens experiments, a still environment is essential. We also verified that there was no horizontal ($\pm X$) axis asymmetry. The finite size of the probe could possibly have an effect on the gas flow. We assumed, justified by the reproducibility of the results with different geometries, the effect to be negligible.

Ray tracing

The refractive index profile is obtained from the temperature distribution with the help of the equation

$$(n-1)=\frac{(n_0-1)T_0}{T} \tag{1}$$

where n_0 is the reference refractive index at temperature T_0.

We numerically solved the ray equation in the paraxial approximation for the three-dimensional refractive index profile obtained by interpolating the experimental points. To reduce computational time, our interpolation is with splines along the vertical direction (Y), linear along the optical axis (Z) and with a combination of sine and cosine terms to get the refractive index value off the Y axis. A fully three-dimensional smooth interpolation is time consuming and the paraxial ray equation requires smooth gradients only in the direction transverse to the propagation. The program can give a histogram representation of the light intensity from an input object at any image plane. We chose computationally to image two distant point sources decreasing their angular separation until they became unresolvable on the focal plane. We tried to apply the Rayleigh criteria of resolution, which is non-trivial when the focus resembles more a ring (Fig. 3(a)) than a Bessel function.

Some images were recently taken with the same gas lens,[3] and the best results were obtained limiting the aperture to 1 cm, and features close to the diffraction limit were observed. For the full aperture device (2.0 cm) the limit resolution obtainable is 0.3 mrad (see Fig. 4) which is very poor if compared with the diffraction limit. By limiting the useful aperture to 1 cm it is possible to obtain a resolution of 0.2 mrad

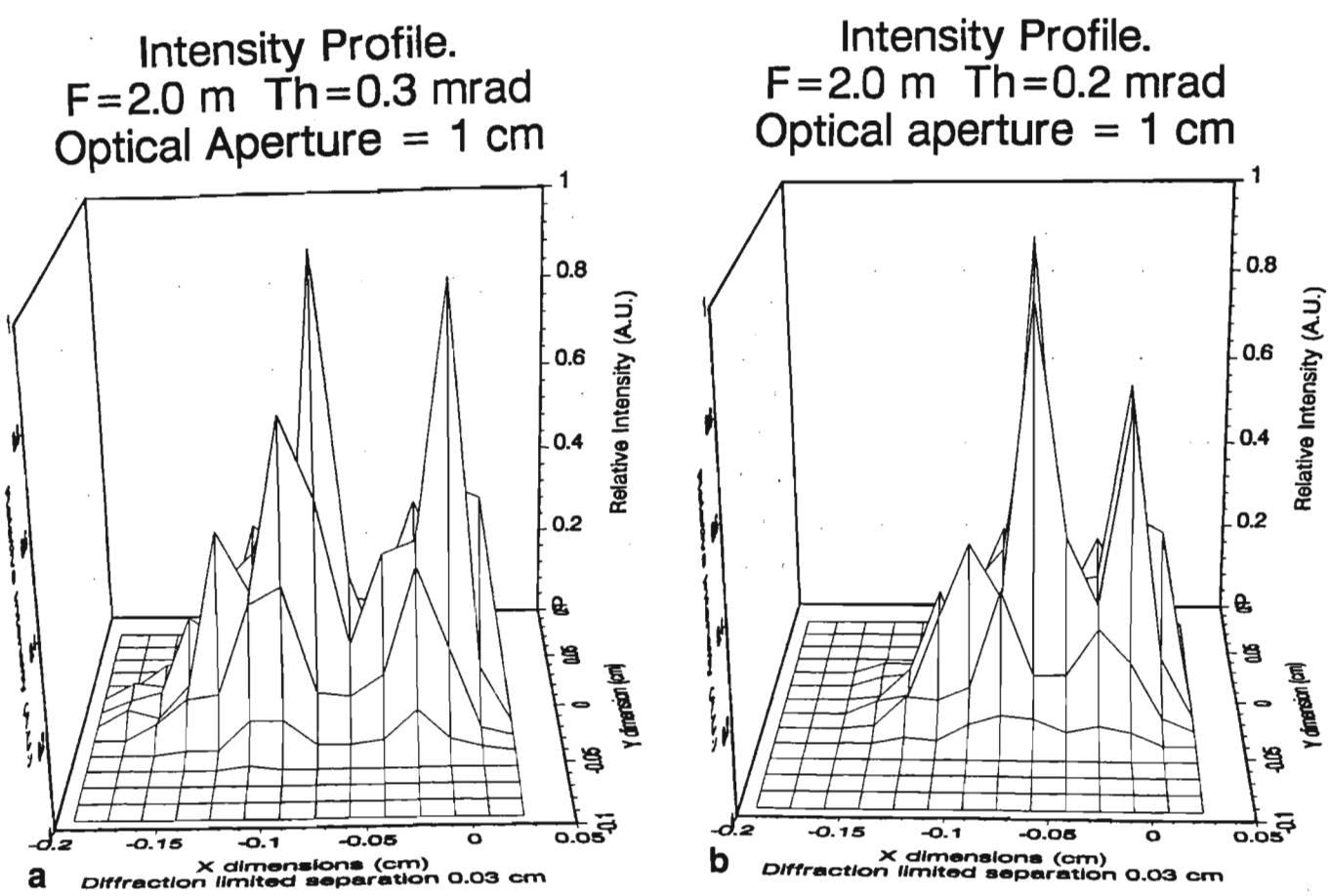

Fig. 3 Computed intensity profile for two point sources at infinity, optical aperture 1 cm: (a) angular separation 0.3 mrad; (b) angular separation 0.2 mrad

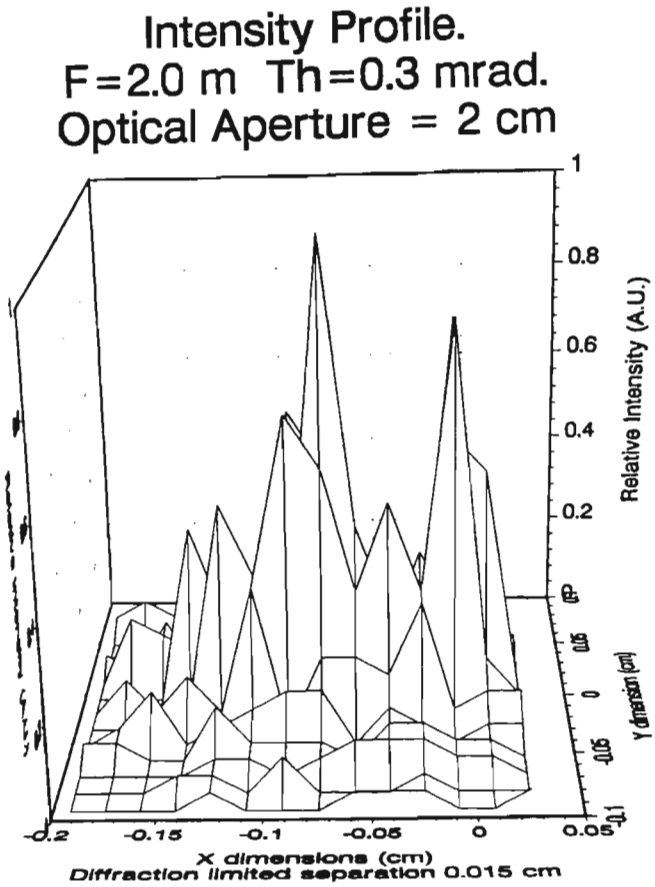

Fig. 4 Computed intensity profile for two point sources at infinity, optical aperture 2 cm, angular separation 0.3 mrad

(Fig. 3(b)), which is only about twice the diffraction limit. It can be easily seen that the outer rays are too weakly refracted to arrive in the same focus as the inner rays. Another feature, visible both in Fig. 3 and Fig. 4, is that the focus is displaced along the vertical, below the optical axis, due to the effect of gravity on the temperature distribution (see Fig. 2(b)).

Conclusions

Ray tracing through the measured refractive index profile of a spinning pipe gas lens, satisfactorily explains two important features: the decrease in optical quality as the optical aperture approaches that of the pipe, and the lowering of the image centre due to gravity. Reasonable numerical agreement is obtained.

References

1 **Marcuse D.**, Theory of thermal gradient gas lens, *IEEE Trans Microwave Theory and Techniques* **MTT-13** (1965) 734
2 **Nottcutt M., Michaelis M. M., Cunningham P. F., Waltham J. A.**, Spinning pipe gas lens, *Opt Laser Technol* **20** (1988) 243.
3 **Michaelis M. M., Dempers C. A., Kosch M., Prause A., Nottcutt, M., Cunningham P. F., Waltham J. A.**, A gas-lens telescope, *Nature* **353** (1991) 547
4 **Gloge D.**, *Bell Syst Tech J* **46** (1967) 357
5 **Steier W. H.**, Measurement of a thermal gradient gas lens, *IEEE Trans Microwave Theory and Techniques* **MTT-13** (1965) 740
6 *Practical Temperature Measurements*, Hewlett Packard, Application Note 290, 8
7 **Michaelis M. M., Cunningham P. F., Cazalet R. S., Waltham J. A., Nottcutt M.**, Gas lens applications, *Laser and Particle Beams* **9** (1991) 641

J. Phys. D: Appl. Phys. 24 (1991) 1744–1747. Printed in the UK

Ion flows from laser-irradiated microcylinders

P F Cunningham, R Buccelato, J A Waltham, M M Michaelis and A Prause

Plasma Physics Research Institute, Department of Physics, University of Natal, Durban 4001, South Africa

Received 10 October 1990, in final form 4 April 1991

Abstract. Hollow aluminium microcylinders were irradiated internally through a circular aperture located in one wall using a pulsed ruby laser beam. Plasma formation and ion flows were monitored using a Nomarski interferometer and an array of Faraday cups. A collimation of ion energy along the cylinder axis was observed.

1. Introduction

Recently, much interest has been shown in the internal irradiation of hollow microcylinders. They are a promising target configuration for x-ray lasers (Balmer and Weber 1988, Lin *et al* 1988, Miura *et al* 1989). Furthermore, when viewed axially, they represent a convenient cross section for the study of plasma behaviour and energy transport in hollow spheres (Földes *et al* 1987). A recent publication has described the temporal development of the contained plasma in these cylinders, viewed with a Nomarski interferometer (Cunningham *et al* 1988). Another describes the temporal behaviour of the x-ray emission (Weber *et al* 1988).

A description of ions collimated into one plane by the irradiation of a solid target with a laser line focus has recently appeared in this journal (Waltham *et al* 1989). A collimated ion beam may have applications in fields such as accelerator physics. Very little is known of the behaviour of the flow of ions from laser-irradiated microcylinders. In this paper we report preliminary results of a highly directional emission of ions along the axis of internally irradiated microcylinders.

2. Experimental arrangement

The experimental arrangement used to monitor the plasma flow from laser-irradiated microcylinders is shown schematically in figure 1. The plasma was produced using a Q-switched ruby laser having typical output energies of 250 mJ in 50 ns FWHM with a multimodal spatial beam profile. This laser radiation was directed onto the back wall of the hollow microcylinder, after focusing through a circular entrance hole in its front wall, using an $f/1.5$ lens triplet. The aluminium cylinders were aligned with their axes orthogonal to the incoming ruby beam. Typical cylinder parameters for this investigation were $l \simeq 1$ cm, $r_c = 350$ μm and $r_d = 150$ μm, where l, r_c and r_d are the cylinder length, internal radius and entrance hole radius respectively. The vacuum chamber was evacuated to pressures less than 10^{-5} Torr.

The main diagnostic was an array of charge collecting Faraday cups (Raven *et al* 1980) arranged at various angles in the horizontal plane about the cylinder axis at distances approximately 20 cm from it. The temporally resolved ion flux signals (figure 2) were downloaded onto an IBM PC for further analysis using an array of GPIB linked Thurlby 524 digital storage adaptors.

The position of the focal plane of the lens was found by using the Foucault technique on a 30 μm diameter

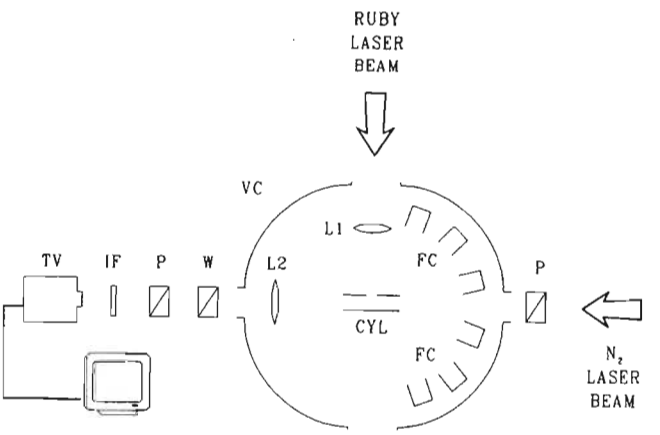

Figure 1. The experimental arrangement used in this investigation. VC: vacuum chamber; L1: focusing lens; L2: imaging lens; CYL: hollow microcylinder (not to scale); FC: Faraday cups; P: polariser; W: Wollaston prism; IF: bandpass filter for the N_2–laser wavelength; TV: TV camera linked up to a video analysis system.

0022-3727/91/101744+04$03.50

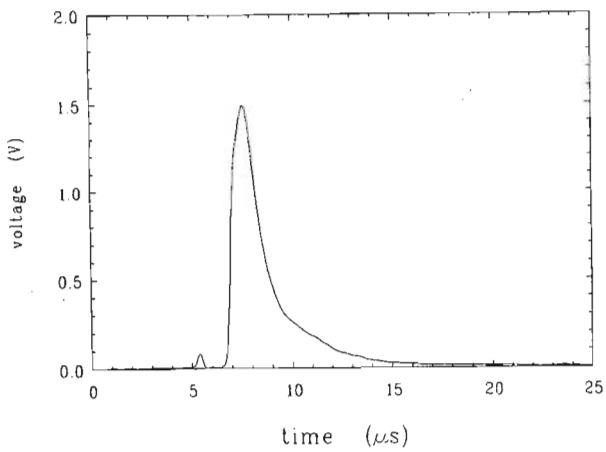

Figure 2. A typical recorded ion trace of voltage as a function of time.

Nickel wire, placed near the focal point of the lens. Once the wire was found to be in the focal plane to within the desired accuracy, its position was recorded on a TV imaging system. The wire could then be replaced with the microcylinder target, the back wall of which could be positioned at the focal plane to an overall accuracy of approximately 50 μm. A detailed description of this positioning technique may be found in the thesis by Waltham (1991). Focal diameters observed on planar film indicate that focal spot sizes of approximately 60 μm were produced, which is consistent with the $f\mathrm{d}\theta$ estimate for the laser configuration used. If the curved back wall of the microcylinder is considered to approximate a plane target, laser intensities of approximately 10^{11} W cm^{-2} on target were used.

A nitrogen laser of pulse length 1 ns FWHM was used for both cylinder alignment and optical probing of the plasma. The beam path of the N_2-laser was orthogonal to that of the ruby laser and hence coaxial with the target cylinder. The time of arrival of the N_2-laser pulse at the cylinder was synchronized to the plasma event using an in-line laser-triggered spark gap (Cunningham *et al* 1986), triggered by a fraction of the ruby laser beam. Optical probing of the plasma was achieved using a Nomarski interferometer, the components of which are depicted in figure 1. More detailed descriptions of this type of interferometer may be found elsewhere (e.g. Cunningham *et al* 1988).

3. Results

A typical Nomarski interferogram of the microcylinder, obtained approximately 10 ns after the peak intensity of the ruby radiation, is shown in figure 3, and serves to give an indication of the various phenomena taking place within the closed geometry configuration. Figure 4 shows a three-dimensional plot of line integrated plasma density for a cross section of the microcylinder, calculated from the interferogram by measuring the fringe shift versus location on the microcylinder cross section. Primary plasma formation was observed on the back wall of the cylinder, where the main laser energy

Figure 3. A typical Nomarski interferometer image taken approximately 10 ns after the peak intensity of the plasma producing ruby laser beam. The ruby beam was incident from the left.

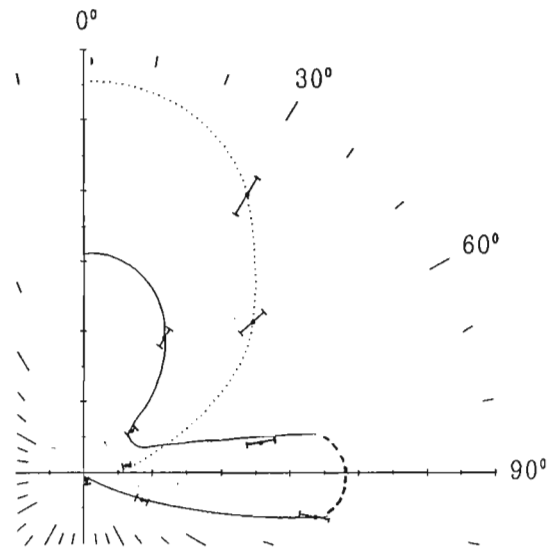

Figure 4. Three-dimensional plot of line integrated plasma density for a cross section (*xy*-plane) of the microcylinder.

was dumped. The fringes in that region are curved. The fringes on the front wall of the cylinder bend the opposite way thus indicating the existence of neutrals produced by the back reflection of the laser beam off the back wall. This Nomarski image also showed that plasma production external to the circular entrance hole was negligible.

A typical voltage versus time trace produced by the collected ions is shown in figure 2. The preliminary small amplitude spike was produced by UV and x-ray emission from the plasma inducing the photoemission of electrons from the collector, and was useful for confirming time $t = 0$, the time of plasma production.

If it is assumed that both the average ion charge and various recombination effects are independent of the asymptotic expansion angle, then the number of ions received by each cup per unit time is proportional to the signal voltage, i.e.

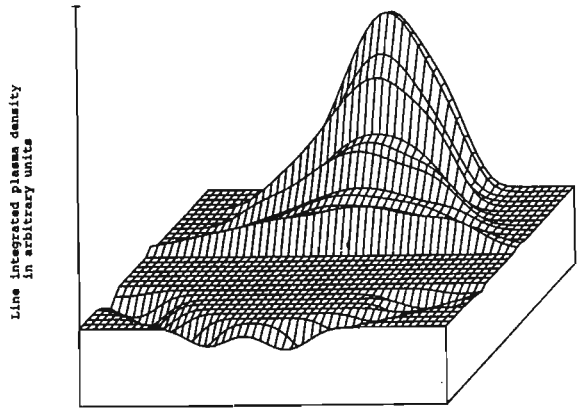

Figure 5. Plots of the total relative ion energy per cup, E_r, versus θ for a microcylinder (full line) and a planar (dotted line) target. N.B. The broken line is an extrapolation.

$$\frac{dN}{dt} = kV(t)$$

and thus the total relative ion energy collected by each cup is

$$E_r = \frac{m_{Al}\, k\, d^2}{2} \int_0^\infty \frac{V(t)}{t^2}\, dt$$

where d is the target to cup distance and m_{Al} is the ionic mass of aluminium.

Typical polar plots of E_r as a function of the angle θ are shown in figure 5. The angle θ was defined to be that angle between the plasma producing laser beam and the ion collector. The solid curve is the curve interpolated from the results obtained from irradiating a hollow microcylinder. The presence of the Nomarski interferometer precluded ion measurements around $\theta = 90°$ and the ruby beam focusing lens precluded measurements at $\theta \leqslant 25°$. The dotted curve interpolates the results obtained when a planar target was irradiated under similar conditions, and is included for comparison.

By assuming symmetries in the expansion of the plasma into three dimensions, a proportional estimate of the total energy contained in the plasma expansion was obtained. Figure 5 shows a plot of the total energy E_r versus θ. The indicated error bars have been calculated as follows: since we assume the aforementioned proportionality factor k to be constant, only $V(t)$ and t contribute to uncertainties of E_r. With the voltage reading having a manufacturer specified accuracy of 3% and the accuracy of the time reading being half a subdivision on the scope (hence approximately 3% accuracy in the vicinity of the main peak) the resulting uncertainty of E_r is 7%. It was thus found that the energy contained in the ions expanding in all directions from the irradiated microcylinder was up to 25% of that contained in the ions expanding from the planar target. Furthermore, in the case of expansion from the microcylinder target, the ions expanding in the direction of the plasma producing laser beam account for typically 66% of the total ion expansion energy from this target. These ions may be from the primary plasma formed on the rear wall of the cylinder, since the 300 μm hole should not have closed during the event. A small contribution from ions expanding from the outside edge of the hole might also be possible, produced by the edge of the ruby beam or slight beam misalignment.

4. Discussion

A flux of ion energy parallel to the cylinder's axis was observed, with the velocity of these ions normally greater than those expanding in the direction of the ruby beam. Furthermore, as may be seen from figure 5, the half angle $\theta_{EN/2}$, (i.e. the angle at which the ion energy drops to half of its maximum value), was significantly narrower for these axial ions than for those ions moving in the direction of the plasma producing laser beam. The observations of ion flux in the axial direction represent a lower limit. A more rigorous experiment planned will have a Faraday cup placed on axis (in the path of the Nomarski interferometer).

The mechanism for these effects is not fully understood at present. The observed movement of ions along the cylinder length may be due to multiple reflections off the inside walls. Ion–ion scattering in regions where primary ions collide with either reflected ions or with secondary ions from the inside front wall may contribute to this effect. The higher velocity of ions in the axial direction suggests an interaction process. A possible mechanism might be the acceleration of axial ions by a negative surface charge of the cylinder wall. Such a surface charge might originate from the charge separation of plasma electrons and ions due to the higher velocity of the former (von Engel). Another possible explanation is that the walls of the cylinder stabilize the plasma. This is the same effect as that described by Hübner in which a z-pinch is stabilized by the conducting walls of the z-pinch vessel. A later experiment using a microcylinder made of non-conductive material may be a good check for this theory.

We notice the ratio of the measured total ion energy from the cylinders to total ion energy from an equivalent planar target does not exceed 0.25. This may be due to absorption of the primary ions on the inside of the cylinder walls, to a far greater than anticipated collimation of ion energy along the axis of the cylinder, or to slight misalignment of the ruby beam on the entrance hole.

The secondary plasma in the region of the entrance hole may have been created by UV and x-ray radiation originating from the rear wall and by secondary electron emission produced by the expanding primary plasma ions. Reflection of laser light from the rear wall is expected to have been insignificant at the laser irradiances used as far as plasma production is concerned.

A future experiment will incorporate a larger array of collectors in order to observe the full ion flow profile in alignment investigations. The aspect ratio of cylinder length to inside diameter and target material will be varied to ascertain the collimation mechanism. Additionally, we will bias the microcylinders and put a

magnetic field along the axis of the microcylinder. The influence of these fields on the ion collimation should give us valuable information on the extent to which the collimation is due to surface charges on the cylinder wall or to the plasma stabilization effect. Information may be gained about the plasma evolution and collisions by probing with a Nomarski interferometer set-up at a range of times.

Acknowledgments

Thanks are extended to Mr W de Beer and Mr R Atkinson for technical assistance and to the FRD for financial support. Useful discussions with Drs Mike Alport and Gerd Wintermeyer are gratefully acknowledged.

References

Balmer J E and Weber R 1988 *Helv. Phys. Acta* **61** 132

Cunningham P F, Campbell R N and Michaelis M M 1986 *J. Phys. E: Sci. Instrum.* **19** 957

Cunningham P F, Weber R, Lädrach P and Balmer J E 1988 *Opt. Commun.* **68** 412

Földes I B Pakula R, Sakabe S and Sigel R 1987 *Appl. Phys.* B **43** 117

Hübner K *Einführung in die Plasmaphysik* chap 'Plasma stability'

Lin Z, Yu W, Tan W, Chen W, Zheng Y, Gu M, Zhang H, Wang G, Tsui J, Cheng R and Deng X 1988 *Opt. Commun.* **65** 445

Miura E, Daido H, Kitagawa K, Kato Y, Nishihara K, Nakai S and Yamanaka C 1989 *Appl. Phys. Lett.* **55** 223

Raven A, Rumsby P T and Watson J 1980 *Rev. Sci. Instrum.* **51** 351

von Engel A *Ionized Gases* 2nd edn chap 'Glow discharge'

Waltham J A, Cunningham P F, Michaelis M M and Notcutt M 1989 *J. Phys. D: Appl. Phys.* **22** 766

Waltham J A 1991 Investigations of laser-produced plasmas and associated phenomena *PhD Thesis* University of Natal

Weber R, Cunningham P F and Balmer J E 1988 *Appl. Phys. Lett.* **53** 2596

Laser and Particle Beams (1992), *vol.* 10, *no.* 4, *pp.* 697–706
Printed in the United States of America

Comparative electron density measurements for the refractive fringe diagnostic and Nomarski interferometry

By R. BUCCELLATO, P.F. CUNNINGHAM, M.M. MICHAELIS AND A. PRAUSE
Plasma Physics Research Institute, Department of Physics, University of Natal, Durban, South Africa

(Received 11 December 1991; accepted 2 March 1992)

Massive carbon targets were irradiated with a pulsed ruby laser and the laser-produced plasma electron densities were *simultaneously* evaluated using Nomarski interferometry and the refractive fringe diagnostic. An agreement of half an order of magnitude between the two diagnostics was obtained.

1. Introduction

With the growing importance of fusion by irradiation with laser light and the subsequent implosion of fusion microspheres, a knowledge of the electron density profiles of the laser-produced plasma (LPP) surrounding the microspheres is required. Electron density profiles of LPP can be determined by optical probing.

Interferometers are the most widely used optical probes and numerous studies have been performed (Reintjes *et al.* 1976; Attwood *et al.* 1978; Fedosejevs *et al.* 1979).

The refraction of a probe beam through a phase object can be used to study the phase object concerned (Evtushenko *et al.* 1971; Keilmann 1972; Kogelschatz and Schneider 1972; Schreiber *et al.* 1973; Benattar and Popovics 1983). The first quantitative refractive fringe diagnostic to evaluate the electron density profiles of LPP was proposed by Michaelis and Willi (1981) and was later revised by Cunningham *et al.* (1986a). This diagnostic has been applied in the study of flames (Michaelis *et al.* 1985) and shocks in air (Waltham *et al.* 1987; Bacon *et al.* 1989).

The refractive fringe diagnostic (RFD) is a simple method of diagnosing the electron density profiles of LPP. However, the accuracy of this method has not been determined. We report here a comparative study between a Nomarski interferometer and the RFD in determining the electron density profiles of LPP based upon experimental data obtained from the same laser shot.

2. Theory

The refractive index of a fully ionized plasma is given approximately by

$$n = \sqrt{1 - N_e/N_c}, \tag{1}$$

where N_e is the electron density and N_c is the critical electron density. The critical electron density of a probing light beam with vacuum wavelength λ is given by

$$N_c = \frac{4\pi^2 m_e \epsilon_0 c^2}{\lambda^2 e^2}. \tag{2}$$

 0263-0346/92 $5.00 + .00

the differentiation of $\phi(y)$, by an order of magnitude. The refractive index is given by (Deutsch and Beniaminy 1982)

$$n(r) = -\frac{1}{\pi}\left\{\frac{\phi(r_0) - \phi(r)}{\sqrt{r_0^2 - r^2}} + \int_r^{r_0} \frac{[\phi(y) - \phi(r)]y}{(y^2 - r^2)^{3/2}}\,\mathrm{d}y\right\}. \tag{6}$$

2.2. *Nomarski interferometer*

The Nomarski interferometer consists of two polarizers, a Wollaston prism and a lens (see figure 2). The plasma is imaged onto the camera by the lens. Two images are created on the camera by the Wollaston prism. Interference between these two images is achieved by the two polarizers, which are either orthogonal or parallel to each other. The advantages of using a Nomarski interferometer are outlined in Benattar *et al.* (1979).

The fringes on the resultant interferogram represent isophase contours, i.e., the change in the OPL between the light traversing the plasma and that not traversing the plasma, which can be given by geometric arguments (assuming negligible refraction; Pawlowicz 1990)

$$\phi(y) - 2\sqrt{r_0^2 - y^2} \equiv \psi(y), \tag{7}$$

form visible fringes when $\psi(y)$ is an integral number of wavelengths, λ,

$$\psi(y) = F\lambda, \tag{8}$$

where $F = 0,1,2\ldots,n$. Let us perform the integration implied in equation (5) on our experimental data $\psi(y)$:

$$-\frac{1}{\pi}\int_r^{r_0} \frac{\psi'(y)}{\sqrt{y^2 - r^2}}\,\mathrm{d}y = -\frac{1}{\pi}\int_r^{r_0} \frac{\phi'(y)}{\sqrt{y^2 - r^2}}\,\mathrm{d}y + \frac{1}{\pi}\int_r^{r_0} \frac{2y}{\sqrt{(r_0^2 - y^2)(y^2 - r^2)}}\,\mathrm{d}y,$$

$$= n(r) - 1, \tag{9}$$

$$\equiv \Delta n(r). \tag{10}$$

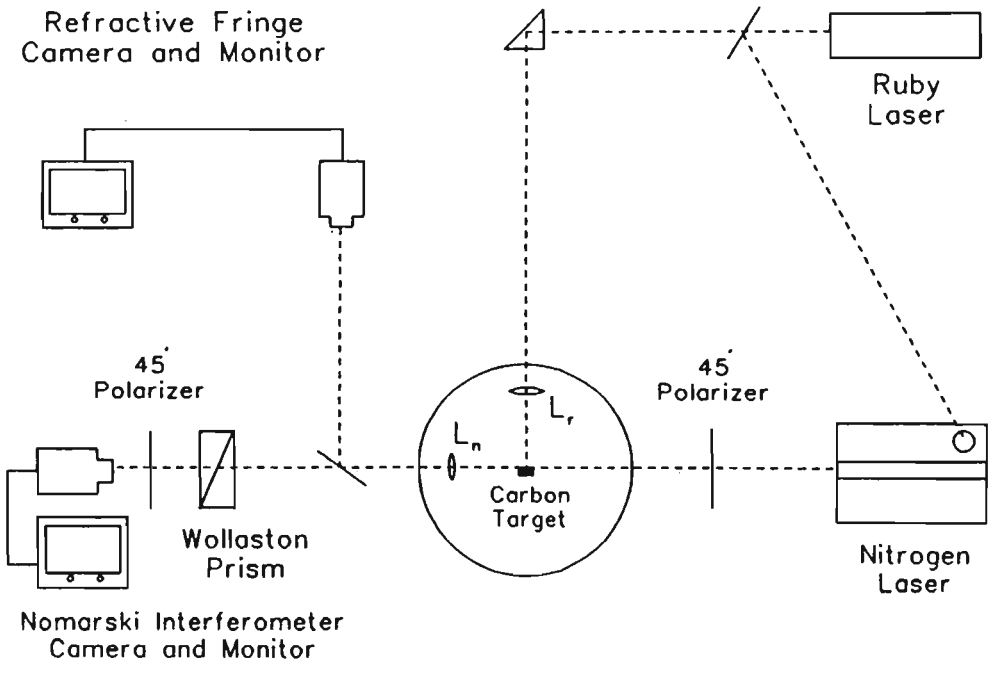

FIGURE 2. Experimental setup.

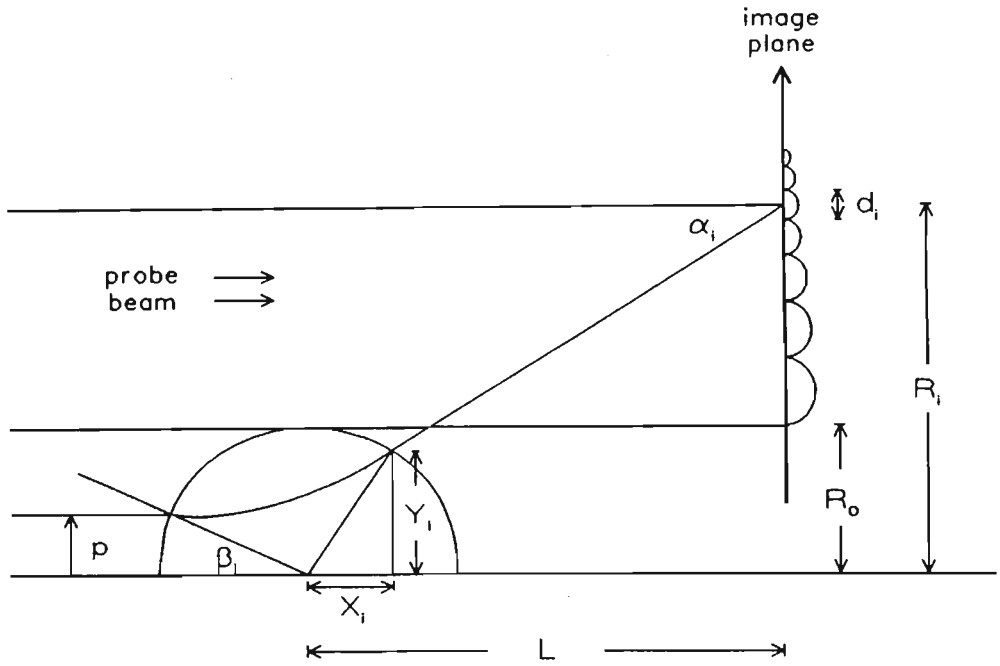

FIGURE 3. Geometry of the RFD.

where

$$r_i = R_0\left[\frac{\sin\beta_i}{\cos(\alpha_i/2)} + \frac{1}{2}\tan(\alpha_i/2)\cos(\beta_i + \alpha_i/2)\right]. \tag{20}$$

α is determined by the fringe spacings

$$\alpha_i = \sin^{-1}(\lambda/d_i) \tag{21}$$

and β is given by

$$\beta_i = \tan^{-1}\left(\frac{Y_i}{X_i}\right) - \alpha_i. \tag{22}$$

The electron density profile of the defocused shadowgraph can be evaluated from the fringe separation by using equations (1), (19), and (20).

A constraint in applying the RFD exists. The use of ray optic techniques is only justified if (Born and Wolf 1965)

$$\left|\frac{\partial N_e}{\partial y}\right| \ll 2\,\frac{N_c - N_e}{\lambda_{\text{vacuum}}}, \tag{23}$$

where λ_{vacuum} is the probe wavelength in vacuum.

It is also important to note some of the assumptions that the RFD makes and will be repeated here, i.e., *there must be spherical or cylindrical plasma symmetry and parabolic light ray paths in the plasma.*

3. Experimental arrangement

The experimental arrangement is shown schematically in figure 2. A Q-switched ruby laser, with a 5-mm mode selecting pinhole within the laser cavity, was focused onto massive carbon targets in a vacuum chamber evacuated to pressures less than 10^{-5} torr. An $f/1.5$

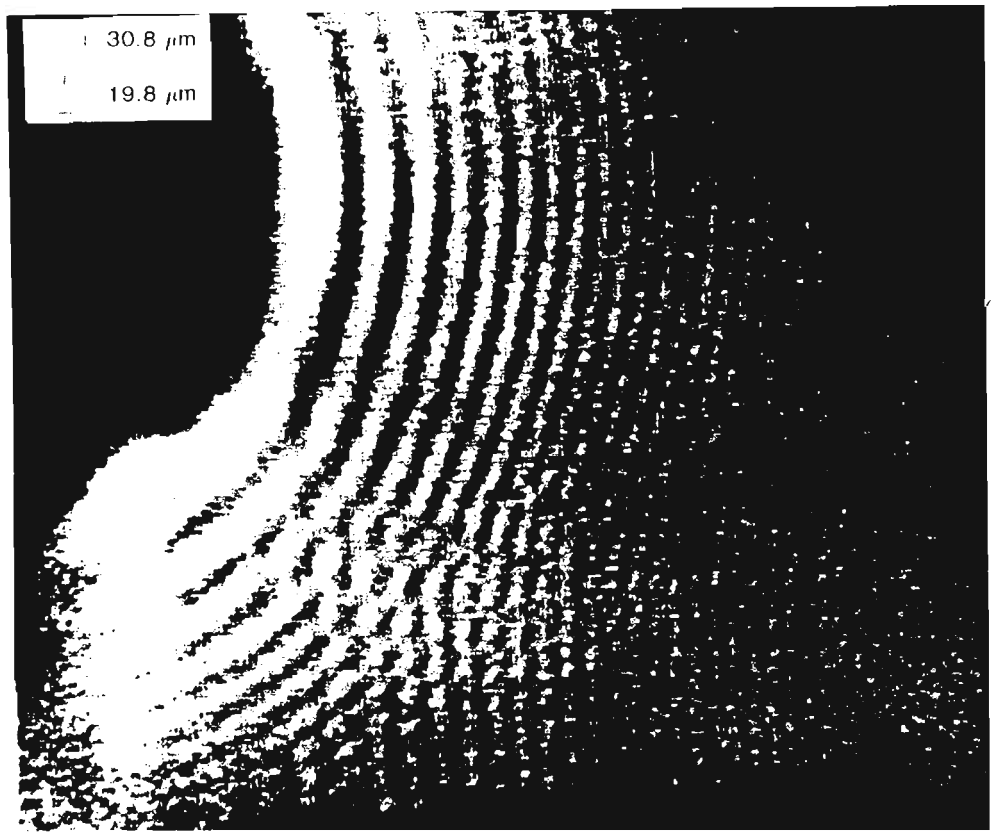

(a)

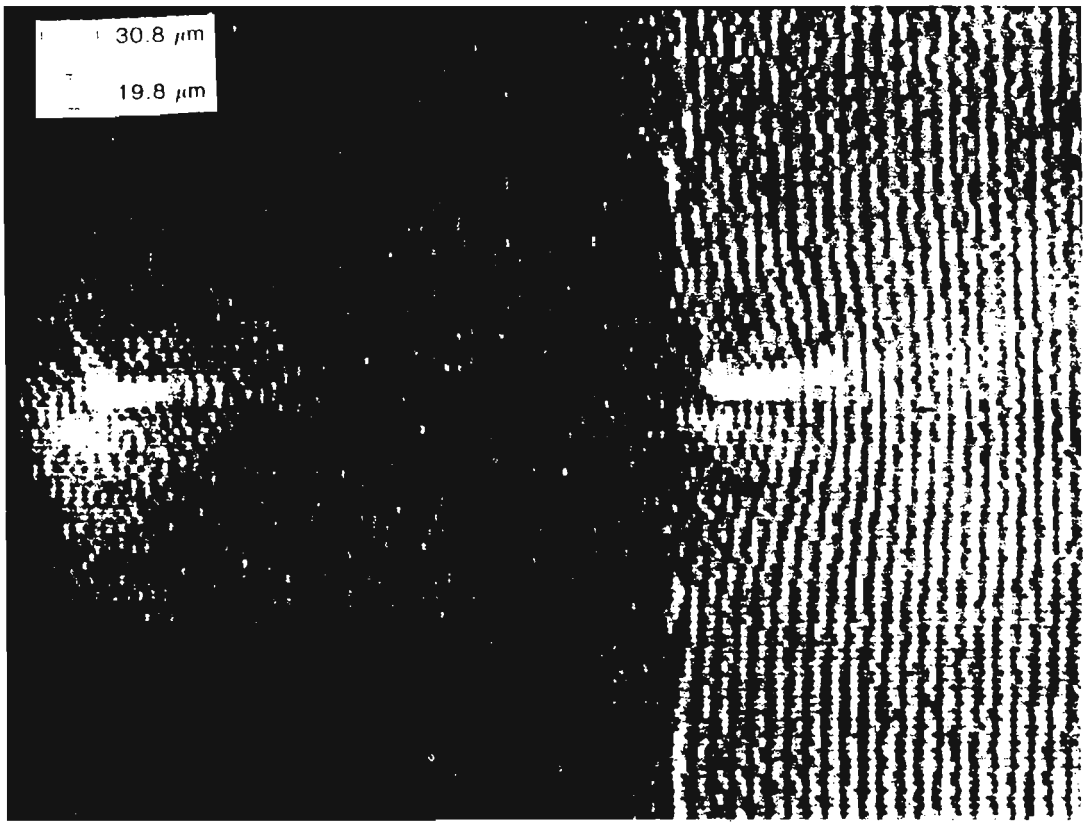

(b)

FIGURE 4. (a) Nomarski interferogram of LPP at irradiance 3.5×10^{11} W cm^{-2}. (b) Corresponding RFD defocused shadowgraph.

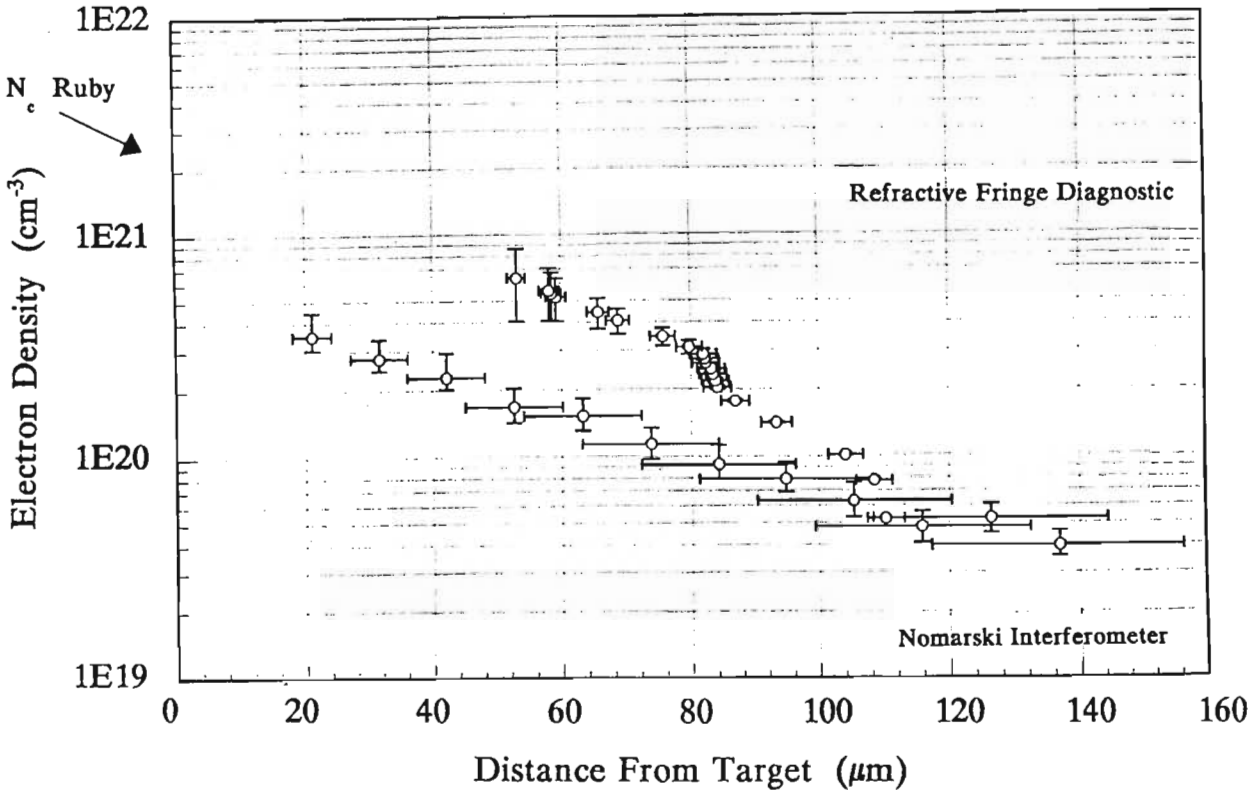

FIGURE 6. Comparison between the electron density profiles evaluated on the ruby laser axis from the RFD defocused shadowgraph and the Nomarski interferogram.

trivial. The RFD compared favorably with conventional Nomarski interferometry in determining the electron density profiles of LPP. An agreement of half an order of magnitude was obtained between the two diagnostics. The discrepancy can be attributed to the lack of cylindrical symmetry of the LPP upon which the RFD was formulated and the incorrect assumption that the probing rays in a plasma follow parabolic paths.

Acknowledgments

Thanks are extended to W. de Beer and R. Atkinson and their staff for technical assistance and to the Foundation for Research and Development and the Laser Applications Research Institute of South Africa for financial support. Useful discussions were held with Dr. R.L. Mace and J.A.R. Waltham and are gratefully acknowledged.

REFERENCES

ATTWOOD, D.T. *et al.* 1978 *Phys. Rev. Lett.* **40**, 184.
BACON, M. *et al.* 1989 *J. Appl. Phys.* **66**, 1075.
BASOV, N.G. *et al.* 1980 *Sov. J. Plasma Phys.* **6**, 642.
BENATTAR, R. *et al.* 1979 *Rev. Sci. Instrum.* **50**, 1583.
BENATTAR, R. & POPOVICS, C. 1983 *J. Appl. Phys.* **54**, 603.
BOCKASTEN, K. 1961 *J. Optic. Soc. Am.* **51**, 943.
BORN, M. & WOLF, E. 1965 *Principles of Optics* (Pergamon Press Ltd., London, UK).
CUNNINGHAM, P.F. *et al.* 1986a *J. Phys. E. Sci. Instrum.* **19**, 957.
CUNNINGHAM, P.F. *et al.* 1986b *S. Afr. J. Phys.* **9**, 103.

Pulsed gas lenses

R. BUCCELLATO, M.M. MICHAELIS, C.A. DEMPERS, A. PRAUSE, P.F. CUNNINGHAM

The concept of a pulsed gas lens is proposed. Potential applications are envisaged and preliminary experiments with pulsed ray refraction are reported.

KEYWORDS: gas lenses, fusion studies, refraction

Introduction

With the recent success of the JET experiment in generating over one megawatt of thermonuclear power[1], fusion has come a major step closer to being a realistic source of energy. The impressive results obtained by the magnetic fusion community will undoubtedly benefit all types of controlled fusion research. Just as there exist several types of fission power station, from the less than man-size power plants on board satellites to the GW fast breeder reactor, so will there exist several types of fusion reactor. Whilst the Tokamak is a sensible choice as the central power generator for a large industrial conglomeration, its minimum electrical output (1 GW) makes it an inconvenient choice for less developed regions.

In the African context in particular, a laser fusion power station with its variable output ($100\ \text{MW} < P_e < 1\ \text{GW}$) is a more appealing concept. It is not generally realized that laser-fusion break-even (thermonuclear power out = electrical power in) could occur before the turn of the century. The classified Halite-Centurion program has shown that a radiation drive in the region of 10 MJ produces a large (but undisclosed) thermonuclear yield. On the basis of these and other results Lawrence Livermore National Laboratory hopes to be granted funds to build a Laser Microfusion Facility with a MJ neodymium glass laser as its driver, before 1999. The Japan Osaka team are meanwhile confident that their 100 kJ 'Gekko Upgrade' will approach break-even in the nearer future.

A somewhat neglected question is: 'Beyond break-even, beyond single pulse yield, what optics?'

All Inertial Confinement Fusion (ICF) reactor studies locate the optics many metres from the 'microfusion' centre. This is because neutron and α particle damage calculations show that no solid-state optical component (lens, frequency doubler/tripler or $\lambda/10$ mirror surface) will resist the several shots per second loading required for reactor operation. In one Los Alamos National Laboratory conceptual design the first lens is 80 m from the target[2]. Livermore Laboratories chose 10 m (see Ref. 3) as do Basov *et al.*[4] at the Lebedev.

Our group has already proposed[5] that a pulsed gas lens (PGL) may help to overcome this problem, thereby considerably reducing the size of a future ICF reactor.

Pulsed gas lens applications

The first application we envisage (and the only one seriously considered in this article) is that of gas laser driven thermonuclear fusion. In particular we consider the HF laser proposed at Los Alamos Laboratory by Phipps *et al.*[2]. Whilst it is likely that ICF will be demonstrated with the Nova Upgrade solid-state laser, relatively few engineers envisage such a laser as a reactor driver. Nova can only fire a few shots per day. Even with specially designed flash lamp shields Nova Upgrade will only improve on this by an order of magnitude. Gas lasers can be far more economical and could be designed to fire at a high repetition rate.

A cursory examination of Phipps' proposed 170 MJ HF laser system (Fig. 1) shows it to consist of three main components: the amplifiers, the Pressure Gradient Interface (PGI) and the target chamber.

The function of the PGI is simply to isolate the target from the laser in such a manner that the gas pressure is always below that at which plasma forms and laser light is absorbed. The PGI essentially consists of a large number of fast butterfly valves, opening onto a vacuum chamber so that the PGI pressure rises from high vacuum to 1/3 bar over 80 m.

The authors are at the Plasma Physics Research Institute, University of Natal, Durban, South Africa. Received 12 November 1992. Revised 3 March 1993. Accepted 15 March 1993.

0030-3992/93/040247-04

In a power station one might envisage a large number of fast butterfly valves as in Phipps' design[2]. The PGL could be designed to serve a triple purpose: first as the final focusing lens; second as a nuclear and debris shield for the expensive oscillator optics up-beam; and thirdly as the exhaust gas extraction system for the gas laser: Fig. 2(b). The lens parameters would be similar to those of the single pulse system. An important question is, however, that of the power consumption of the lens. For the above parameters the energy per gas fill is of order

$$pV = 6.4 \times 10^5 \text{ J}$$

or $\simeq 10^6$ J per lens for a relatively inefficient fast fill. A ten-beam direct drive system would thus require 10 MJ per target. This may seem large when compared with an estimated laser output of similar magnitude, but not when one considers that the best lasers have a 'wall plug efficiency' of about 10%.

Pulsed refraction experiments

We have conducted laser-beam deflection studies preparatory to operating a full-scale pulsed gas lens. These studies have usefully identified a number of non-evident problems. Figure 3(a) is a diagram of the gas-dynamic beam deflection device. The concept is as follows: a rectangular slab of high-pressure, high-density, high-refractive index gas is contained inside a box with a long rectangular window on top and two optical slit apertures on either side. The long window is instantaneously opened allowing a plane rarefraction wave to propagate back towards the lower wall of the box. This rarefraction wave propagates at the speed of sound in the gas (c_s), reaching the rear wall at time $t = r/c_s$. Thus, for a 30 cm deep box the near optimum density profile (and thus refractive index profile) may exist at $1/4 \text{ ms} \lesssim t \lesssim 1/2 \text{ ms}$ (Fig. 3(b)).

Instantaneous opening of the window is required to obtain the desired density profile needed for beam deflection. The above argument shows that instantaneous here means $t \approx 1/10$ ms. Commercial valves operate at least two orders of magnitude

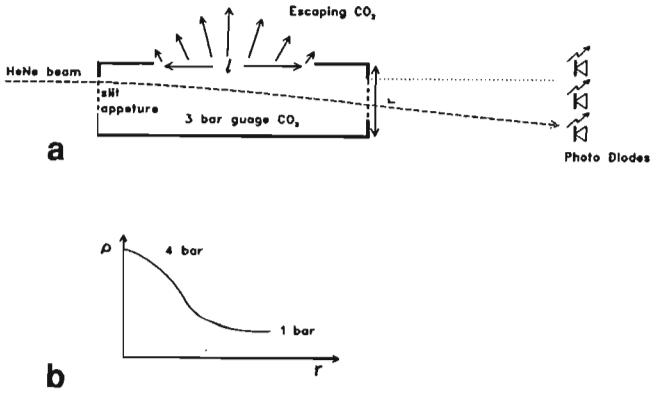

Fig. 3 (a) Pulsed beam deflection device. (b) Density profile (schematic)

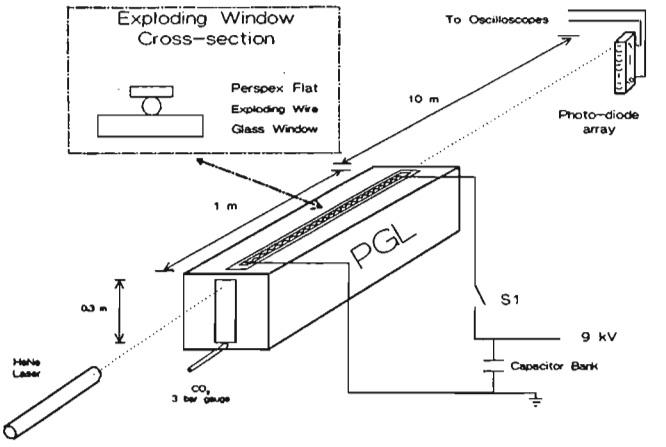

Fig. 4 Experimental set-up

slower and only in vacuum. After considering many options we chose to shatter a 3 mm thick glass slide. Shattering the glass slide by over-pressurizing the chamber resulted in a non-uniform and slow opening of the window. (The box is topped with a wooden structure to contain the glass fragments and the glass is held in position with a clamp and two rubber gaskets.) To overcome the problem of slow opening, a 1 mm Perspex flat was placed over the glass. A copper wire was placed between the glass and the Perspex flat and connected to a 2 kJ capacitor bank. The box was pressurized to just below glass rupture point ($\approx$3 bar gauge) and the exploding wire detonated. Fast opening of the window was obtained.

Initially the chamber was pressurized with air, but on shattering of the glass window and subsequent depressurization of the chamber, the HeNe beam disappeared and did not reappear for several seconds. It is estimated that adiabatic expansion from 3 bar lowers the temperature to $\approx -60°C$, which is well below the condensation temperature of air. A TV camera placed in front of the box showed that the PGL was behaving as a cloud chamber, water vapour in the air condensing to micro droplets. A white cloud was seen escaping out of the top of the box. Shortly before the beam re-appeared, the laser path was shown by scattered red light inside the box. This problem was solved by pressurizing the chamber with dry CO_2 gas which has a condensation temperature lower than that of moist air.

To summarize, successful operation requires

- rapid and complete opening of the window to obtain a steep density profile needed for deflection;
- choice of a gas with a high refractive index for maximum deflection and low condensation temperature.

The experimental set-up is shown in Fig. 4. A HeNe laser beam was directed through the PGL onto a vertical photodiode array. This array consisted of ten photodiodes spaced 1 cm apart. The photodiodes were configured in an on/off mode, that is to output a 5 V pulse only when light was incident on them. The laser beam was positioned just above the first photodiode.

LPB 380

Laser and Particle Beams (1994), *vol.* 12, *no.* 3, *pp.* 000–000
Printed in the United States of America

Applications of the colliding shock lens

By M.M. MICHAELIS, N. LISI, R. KUPPEN, R. BUCCELLATO AND A. PRAUSE
Department of Physics, University of Natal, Durban, South Africa

(Received 10 January 1994; accepted 19 January 1994)

The colliding shock lens is described briefly. Possible applications, industrial drilling and cutting, laser Q-switching and spatial filtering, ultrahigh-power applications, and "all gas lasers" are proposed. The time evolution, scaleability, and repetition rate operation are investigated.

1. Introduction

At a previous ECLIM, we described work with continuous gas lenses (Michaelis *et al.* 1991a). A novel pulsed gas lens has now been developed relying on the interaction of converging shocks in air. Here we report on the initial studies of the parameters of this lens undertaken to see which applications, if any, show promise. The article is divided into four parts: a brief description of the colliding shock lens (CSL); a list of potential applications suitable for the CSL; a study of the performance of various CSL designs; and concluding remarks.

2. The colliding shock lens

Gas lenses invented at Bell Labs in the early 1960s were soon discarded as bulky devices with a narrow field of view. A slight renewal of interest has resulted from a demonstration that they are able to focus laser light to drill holes (Notcutt *et al.* 1988; Michaelis *et al.* 1991a) or to generate laser-produced plasmas (Waltham *et al.* 1990). We have shown that they have sufficiently good optical quality to serve as objective lenses in telescopy (Michaelis *et al.* 1991b). We have also proposed that large aperture pulsed gas lenses could play an important part as the final focusing element in a laser-driven fusion reactor (Buccellato *et al.* 1993a). More recently (Buccellato *et al.* 1993b) we have described a different type of pulsed gas lens, the CSL.

The simplest CSL consists of 16 needles disposed in opposition on the arc of a circle (figure 1a). Eight electric arcs are struck between opposing points and generate eight shock waves that converge at the center. A cigar-shaped region of high gas density gradient results. If a pulsed laser is synchronized soon (100 ns) after the shock collision and directed through the center, it can produce a focus. Figures 1b and 1c show other CSL designs with different number of arcs and different diameters. We distinguish between the "electrical diameter," that of the circle of arcs, and the optical aperture, that of the effective lens. The optical aperture turns out to be an order of magnitude smaller than the electrical diameter. It is not yet clear whether the optical aperture will scale with the system geometry or with the typical shock width dimensions. The former would mean that the *f*-number could remain more or less constant with increasing optical aperture; the latter, that it does not scale at all. A first attempt at scaling up the first 1.2-cm electrical aperture device to 3 cm

 0263-0346/94 $5.00 + .00

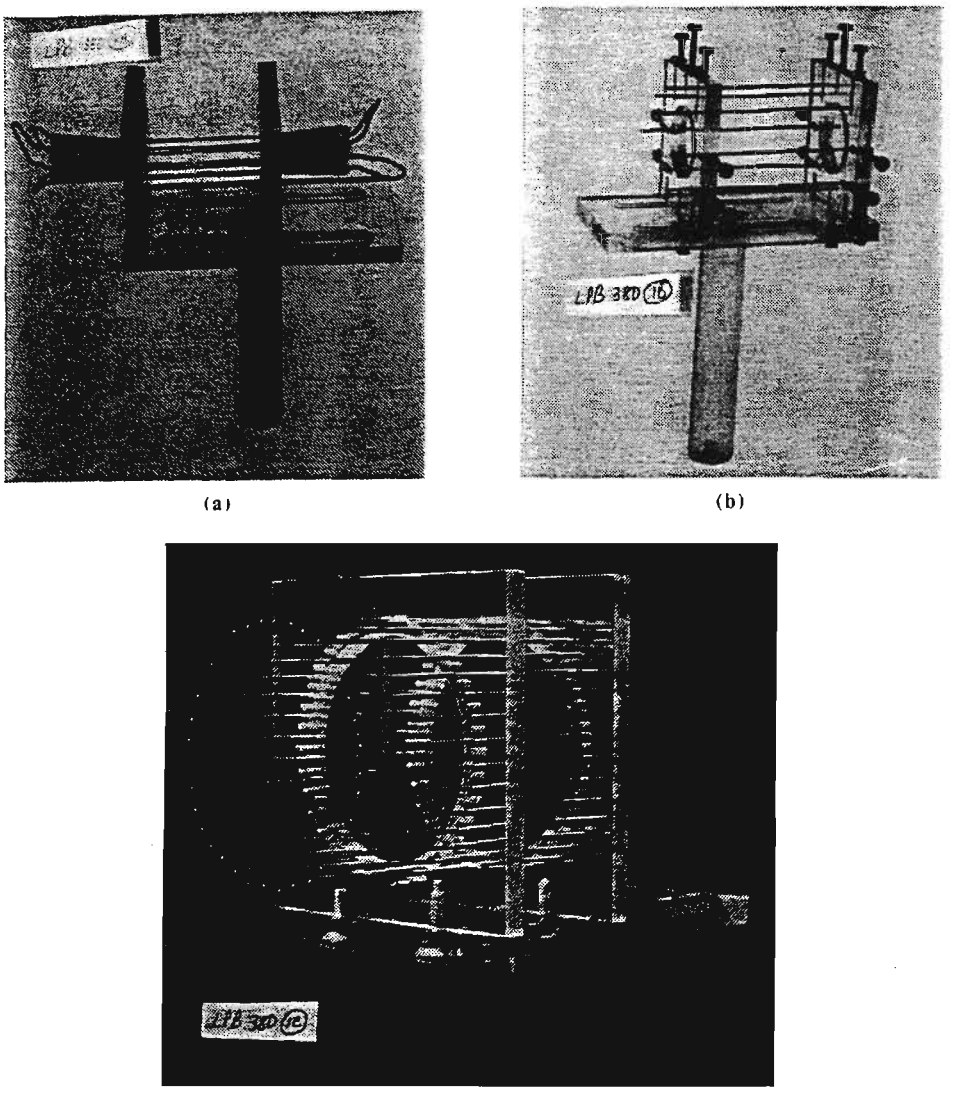

FIGURE 1. Colliding shock lenses. (a) 16-pin, 8-arc device. Electric diameter 1.2 cm. Optical aperture 2 mm. (b) 3-cm electric diameter device. Optical aperture approximately 3 mm. (c) 36-pin, 3-cm electric diameter device.

(figure 1b) indicates that the truth lies somewhere in between. Increasing the number of pins (figure 1c) did not have any obvious effect.

Depending on the time at which the pulsed laser is fired with respect to the arcs, a variety of illumination patterns results: figure 2 shows a sequence obtained with an eight-arc device. The frames are taken directly with a lensless television camera disposed 40 cm away from the center of the lens. The first three frames show the shock waves propagating almost undisturbed through one another. The detailed illumination pattern (i.e., dark and bright rings, coarse and fine fringes) is best understood by referring to articles on refractive fringe diagnostics (Bacon *et al.* 1989; Michaelis *et al.* 1991*c*). The next frames show nonlinear interaction between the shock waves resulting in noncylindrically symmetric illumination pat-

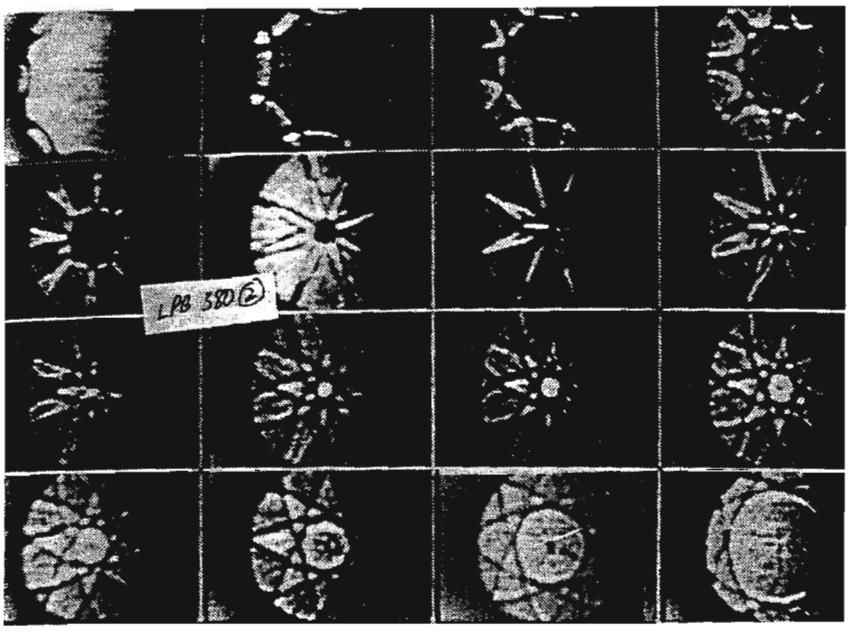

FIGURE 2. Illumination patterns 40 cm from the lens of figure 1a, at various times after the arcs: 3.2, 5, 6, 6.9, 8, 10, 10.4, 10.9, 11.3, 11.6, 11.8, 12.2, 12.4, 13.1, 14, 15.6 μs.

terns. The interesting point is that after the shocks have collided at the center, there is a cylindrically symmetric core. The shocks have forgotten where they originated. A sharp focus is seen in the seventh frame. An enlargement of the focal region (figure 3) shows an interesting set of Airy ring-like patterns centered on the strongly saturated focus.

3. Potential applications

3.1. *Drilling, cutting, and welding*

A good reason why lasers have not penetrated every industrial workshop is that their output windows and lenses are expensive and sensitive devices. We have already shown that CO_2 lasers coupled to gas lenses are capable of drilling through thick steel sheets (Michaelis *et al.* 1991a). However, the lenses we used were unwieldy CW devices with very long focal lengths (of the order of 80 cm.) The "dream" gas lens for this purpose would be a short focal length device (10 cm) capable of being "rep-rated" (100 Hz), with an optical aperture of at least 1 cm and minimal power consumption and weight.

3.2. *Q-switching and spatial filtering*

The combination of a CSL and a pinhole within the laser resonator could in principle serve to simultaneously Q-switch and spatially filter a laser oscillator. The pinhole would need to be under vacuum or, if the pulse is short enough, in helium gas to prevent breakdown. But Q-switching requires opening times of about 10–100 ns (Siegman 1986). For engineering applications, the focal length should not vary too quickly; whereas for Q-switching and beam handling (e.g., isolator) functions, fast switching is essential.

FIGURE 3. Magnified central region of 11.3-μs frame. (Bar = 1 mm)

3.3. *Ultrahigh-power and "all gas" lasers*

It is well known that even under clean room conditions lenses operating for pulse lengths of tens of nanoseconds start to fail at intensities in the GW/cm^2 range. Also, multiphoton processes at ultrahigh intensities render conventionally transmitting materials opaque or absorbing. We have previously pointed out that gas lenses could help alleviate these problems (Michaelis *et al.* 1991a). We foresee, without having the means to observe it, that very high powers may heat the gas and change the characteristics of the lens, just as in atmospheric "thermal blooming" (Barnard 1989). But for intermediate powers, the CSL could fill the present gap.

The final application we envisage is that of an "all gas" (or nearly all gas) system. Conventional pulsed gas laser systems are designed with beam diameters corresponding to the breakdown thresholds of solid optical components. A combination of aerodynamic windows and diverging and converging gas lenses could give gas laser design a new degree of freedom.

4. Performance of the CSL

All the applications listed above pose the following questions:

a. How good is the focus? Is it near diffraction limited?
b. How short is the focal length?
c. How quickly do CSLs switch, and how long do they last?
d. How large is the aperture, and is any light lost?
e. Can they be "rep-rated"? How much power do they consume?

FIGURE 4. 130-μm burn pattern in aluminum foil obtained with lens of figure 1b.

a. From the very first experiments, we realized that this was somewhat surprisingly, given the limited number of arcs, an excellent lens. Figure 4 shows a burn pattern in aluminium foil obtained with an eight-arc lens. The optical aperture of the lens was 3 mm and the focal length 40 cm, so the diffraction limit would give a 130-μm hole. The central hole is approximately 130 μm.

b. The shortest focal length for an eight-arc device is about 20 cm. This is too long for many applications. We have already begun testing a double-ring device, and there is no apparent reason why several rings should not reduce the focal length to the 10-cm range.

c. For this purpose we have measured the switching ability. Our experimental apparatus is very simple and consists of a 10-mW HeNe laser followed by the CSL and a receiving photodiode at a distance L with a pinhole of diameter Φ immediately in front of it. We vary the distance L, the diameter Φ, and also the energy delivered to the shocks by changing the discharge capacitor. Figure 5 shows a typical switching time curve. In figure 6 we show how the switching risetime and the maximum signal vary with the pinhole size Φ at a fixed distance L, and in figure 7 we show how the same quantities vary with the focal length L for fixed Φ. As can be seen from switching curves like those in figure 5, the fall time of the signal is always comparable with the rise time (to within, say 50%), the latter being a less critical quantity for Q-switching. The signals have been normalized to the signal produced by a 3-mm aperture, 50-cm focal length, spherical glass lens on the same photodiode and a pinhole $\Phi = 250$ μm. Figure 8 is like figure 6, but for a capacitor value of 1 μF. We believe that by increasing the shock energy we can make the switching faster.

The present CSL is thus a little too slow for Q-switching. But we have a concept for speeding it up that involves a multiple lens. Another problem in using this device for Q-switching is that it requires the presence of a pinhole in the cavity and the concomitant possibility of too high a radiation flux through it. Our idea is that this system could be worthwhile for cheaply Q-switching a small laser system.

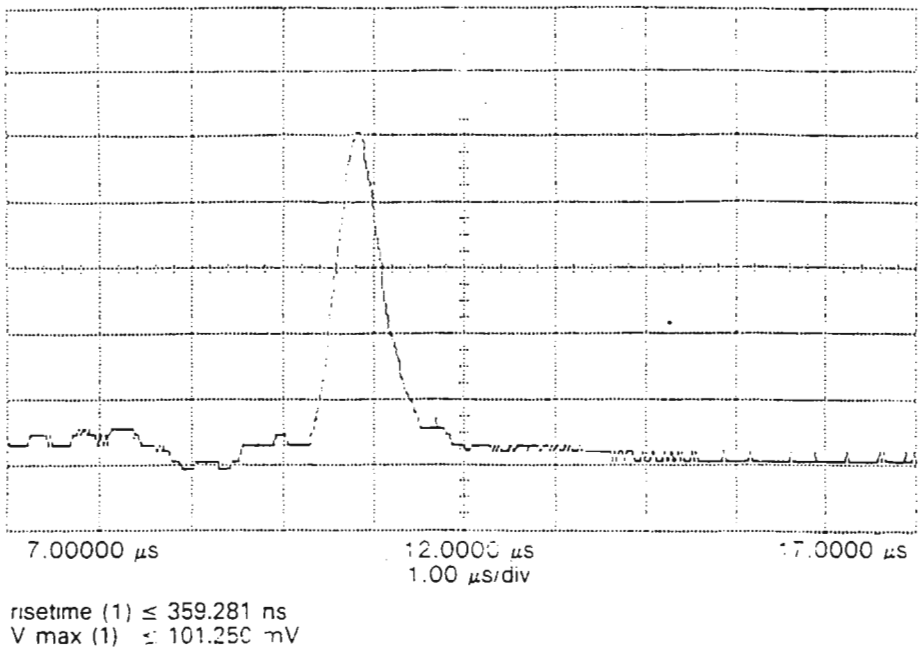

FIGURE 5. Switching curve. L = 40 cm. Φ = 300 μm. C = 5 nF.

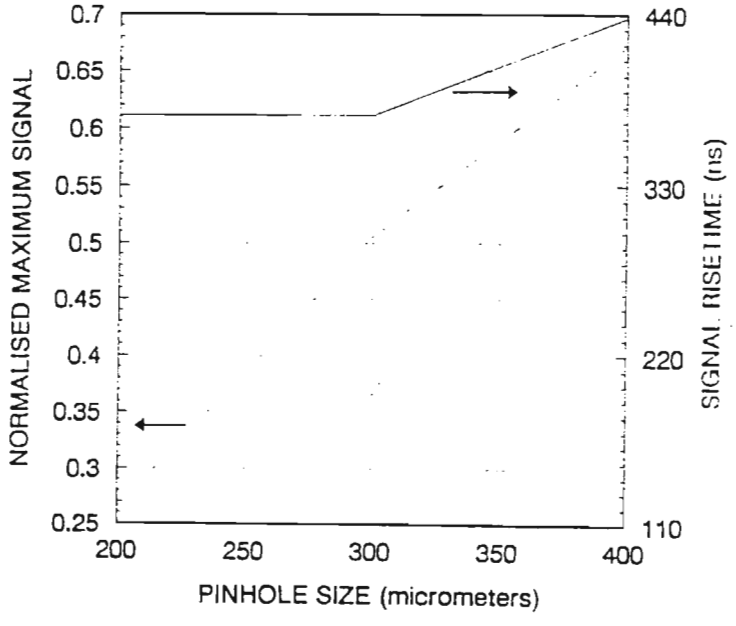

FIGURE 6. Switching rise time and maximum normalized signal versus pinhole size for L = 40 cm. C = 5 nF.

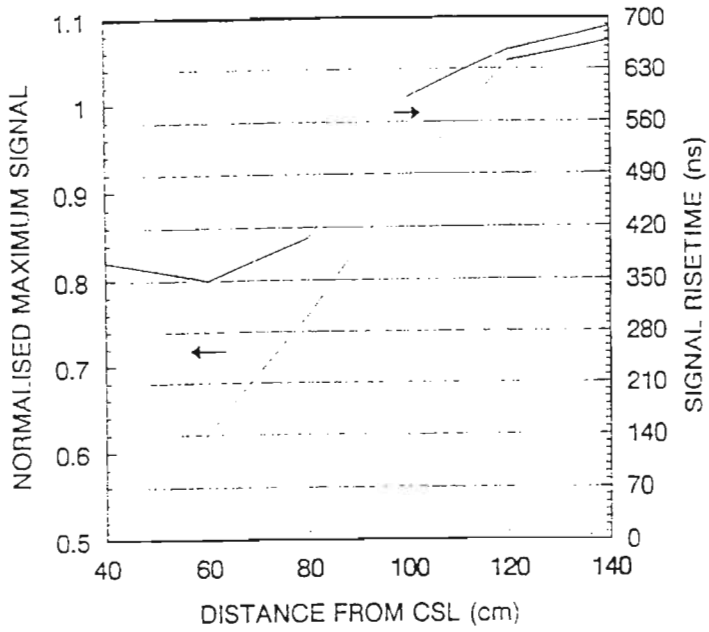

FIGURE 7. Switching rise time and maximum normalized signal versus distance from the CSL for Φ = 300 μm.

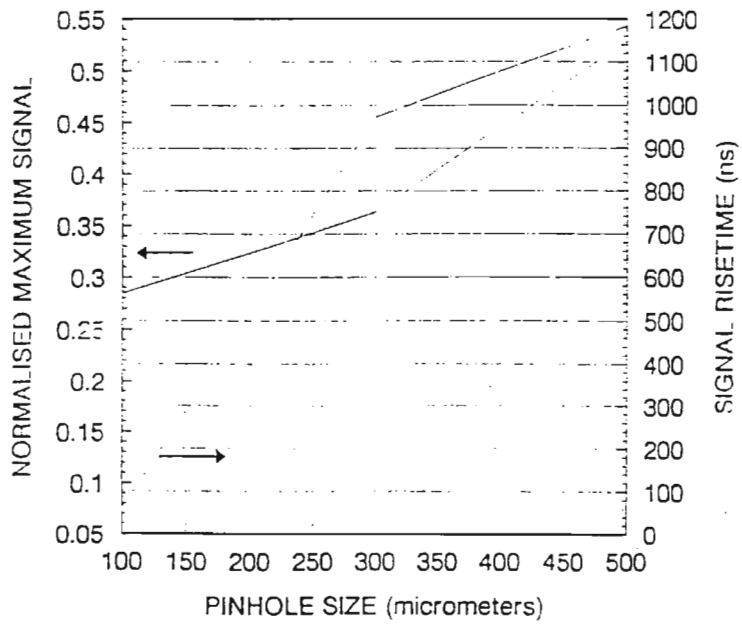

FIGURE 8. Switching rise time and maximum normalized signal versus pinhole size for L = 40 cm, C = 1 nF.

d. Possibly the worst feature of CSLs is the large electro-optic aspect ratio. The largest aperture obtained so far was only 4 mm. We plan to test a 10-cm electrical diameter lens in the hope of obtaining an 8-mm optical aperture. Another worrying feature of these lenses is that they are lossy. This, we believe, is inherent to their shock wave structure. The rear of the reflected shock refracts some light "in the wrong direction." This is to be expected from refractive fringe studies of shocks (Michaelis *et al.* 1991c). Orientatively we estimate the loss to be about 10%, slightly larger than that due to reflection in conventional lenses.

e. The question of "rep-rating" the lens has only been partially answered experimentally for want of a suitable high-voltage power supply. Operation at 10 Hz confirmed our expectations that the lens could run at moderate frequencies without degradation of the focus. At this repetition rate a typical switching curve such as that in figure 5 remains virtually unaltered. Based on dimension and speed of sound arguments, we would expect the limiting period to be of the order

$$\frac{\text{electrical aperature}}{\text{sound speed}} \approx 1 \text{ ms}.$$

The corresponding "rep-rate" would be 1 kHz, a useful frequency for industrial applications. The final question is that of power consumption. At a rep rate of $f = 1$ kHz, our present eight-pin lens would consume

$$W = f \cdot 1/2 \cdot CV^2 = 1 \text{ kw} \qquad (C = 5 \text{ nF}, V = 20 \text{ kV}).$$

This is a considerable amount of pulsed power. To reduce this we tested an enclosed CSL that confines the arcs to two rather than three dimensions. An order of magnitude reduction in energy consumption occurs. However, that may be counteracted by the necessity of increasing the electrical diameter.

5. Conclusion

The novel CSL appears to be on the borderline of becoming a promising optical component. The focus is good, but the lens is slightly lossy. The lens focuses quickly, but not quite quickly enough for efficient Q-switching. The aperture is disappointingly small but might be scaleable. The lens may be rep-rated but consumers appreciable electrical power and could be incredibly noisy.

Acknowledgments

This work was supported in part by the Plasma Physics Research Institute (P.P.R.I.) and the Laser Applications Research Institute (L.A.R.I.S.A.).

REFERENCES

Barnard, J.J. 1989 *Appl. Opt.* **28**, 438.
Bacon, M. *et al.* 1989 *J. Appl. Phys.* **66(3)**, 1075.
Buccellato, R. *et al.* 1993a *Opt. Laser Technol.* (in press).
Buccellato, R. *et al.* 1993b *Opt. Commun.* (in press).
Michaelis, M.M. *et al.* 1991a *Laser Particle Beams* **9**, 641.
Michaelis, M.M. *et al.* 1991b *Nature* **353**, 547.
Michaelis, M.M. *et al.* 1991c *Opt. Laser Technol.* **23**, 283.
Notcutt, M. *et al.* 1988 *Opt. Laser Technol.* **20(5)**, 243.
Siegman, A.E. 1986 *Lasers* (University Science Books)
Waltham, J.A. *et al.* 1990 *Laser Particle Beams* **8(1)**, 361.

The Colliding Shock Lens as an Intracavity Q-Switch Element *

N. Lisi M.M. Michaelis R. Buccellato M. Kuppen

A. Prause

University of Natal, South Africa

9 November 1993

Abstract

We show how a varifocal pulsed gas lens, the Colliding Shock Lens, can be utilized as an intracavity element to Q-switch a ruby laser. By placing the shock lens in tandem with a second lens a giant pulse is obtained. The second lens may be a conventional glass lens or a continuous wave gas lens.

*Applied Optics (Oct 94), in press

Quality factor or "Q-switching" of lasers is an important method of enhancing the power of pulsed lasers [1]. Mechanical Q-switches and dye cell switches have generally been discarded in favour of triggerable opto-electronic devices based on rotation of polarization using the Kerr or Pockels effect. In this letter we will discuss another form of triggerable Q-switching which makes use of a new kind of gas lens. This lens, the Colliding Shock Lens [2] was developed in our laboratory, in step with the recent revival of interest in gas lens optics [3, 4].

The principle of Colliding Shock Q-switching (CS-QS), relies on the insertion of a steady state converging lens and of the rapidly varying CSL in a laser cavity. In Fig. 1 we show the evolution of the CSL focal length and lens diameter with time. When the CSL is switched off, the steady state lens renders the cavity unstable. Only when the CSL is switched on and while the focal regions of the two lenses overlap, does the laser cavity become stable and the losses low. If this condition is achieved when the population inversion is at its peak in the active medium, lasing occurs in the form of a giant pulse.

In the experiment designed to test the CS-QS concept, a commercial ruby laser [5] was modified to incorporate the additional Q-switching components. Fig. 2(a) is a schematic of the experiment. The laser consists of a ruby head, a full reflector R1, and an output coupler R2. The Q-switching components are a Colliding Shock Lens L2, a continuous lens L1, and a fluorescence sensing photodiode PD1.

The CSL consists of eight arc discharges, struck simultaneously between pairs of opposing points located on the arc of a circle as illustrated in Fig. 2(b). Each point explosion produces an expanding spherical shock wave. After the eight shock waves collide at the center of the circle, a cigar shaped, high density, axially symmetric core expands outwards. Lensing is due to the radially symmetric density gradients within the expanding region. As the lens diameter increases, the density diminishes and the focal length in-

creases as depicted in Fig. 1. The CSL used for these experiments, was specially chosen for its fast switching and large optical aperture. It consists of a 5.0 cm diameter cylinder closed at both ends. The end plates which carry the sixteen pins forming the eight gaps, are 1.0 cm apart. The gaps are set to 1.5 mm and the diameter of the circle of pins is 3.0 cm. The central apertures are 1.0 cm in diameter. A 100 nF capacitor, charged to 17 kV, is connected to the eight gaps in series via a triggerable spark gap. This series connection ensures simultaneous arcing.

The lens L1 can be either a conventional solid state device or a continuous wave gas lens. The Spinning Pipe Gas Lens [6] used in some experiments, consists of a 1.0 m long, 2.0 cm diameter heated tube, spun at 30 Hz. The rotation centrifuges warm air out of the two ends and causes cold air to be aspired along the axis. The resulting density and refractive index gradient produces a long focal length lens, the quality of which fluctuates [7]. The focal length can be varied from 1.5 m to several meters (as measured from the center of the pipe) by changing the pipe temperature and rotation speed. The two flat end mirrors are a full reflector $R_1 = 96\%$, and an output coupler $R_2 = 45\%$.

The operation sequence for all CS-QS experiments is the following. First the ruby flashlamp is fired and the PD1 photodiode detects the fluorescence signal from the active medium. This signal is electronically delayed and used as a trigger for the CSL master spark gap circuit. The signal from the photodiode PD2, placed behind the full reflector R1, is read by a storage oscilloscope and gives the laser pulse waveform. The laser beam energy is measured with an energy meter. A burn pattern of the attenuated beam at the focus of a lens is used to measure the divergence.

The cavity is operated in three different modes described below in detail. Mode a, maximises the output energy and beam diameter. Mode b, minimises the Q-switched laser pulse duration. Mode c, explores the feasability of a cavity with intracavity beam expansion optics consisting entirely of gas.

The stability of the laser resonator can be determined in terms of a complex parameter m. In the formalism of ray matrix optics this is half the trace of the round trip resonator matrix [8]. For an unstable resonator, abs(m) > 1. In this case we can introduce the magnification M as

$$M = \begin{cases} m + (m^2 - 1)^{1/2} & \text{if } m > 1 \text{ (Positive Branch)} \\ m - (m^2 - 1)^{1/2} & \text{if } m < -1 \text{ (Negative Branch)} \end{cases} \quad (1)$$

where M is the amplification of the beam cross section per round trip and can be related to the cavity losses. When abs(m) < 1 the cavity is stable and abs(m) $= 1$ for a plane parallel configuration, which corresponds to the confocal situation of the intracavity "telescope".

Mode a: L1 is a 200 cm focal length glass lens. The lens separation d is 250 cm. The condition abs(m) $= 1$ is achieved when $f_{\mathrm{CSL}} = 50$ cm. The CSL lens aperture (d_{CSL}) is 3.0 mm (see Fig. 1) and the beam fills the ruby rod (10 mm). At slightly later times, the resonator becomes stable and we expect lasing to occur. A drawback of this operating condition is that the cavity is long (3.0 m) as is consequently the risetime of the laser pulse. In this case the initial magnification of the resonator (before the CSL is operated) is low: $M = 2.8$. We must therefore operate the flashlamp below 4.3 kV to avoid free running lasing. A 2.0 J laser pulse of duration 360 ns (FWHM) is observed 39 μs after the shock generation which corresponds to 5 μs after the shock collision. Fig. 3 shows the pulse waveform.

Mode b: L1 is a 50 cm focal length glass lens ($d = 100$ cm). Again $m = 1$ is achieved when $f_l = 50$ cm, $d_{\mathrm{CSL}} = 3.0$ mm and the beam diameter on the output coupler is expected to be 3.0 mm. The initial magnification M is now 4.4 and free running is inhibited at any flashlamp voltage. We operated at 4.5 kV. In this case we expect shorter pulses and a very narrow beam together with lower energy. A 100 mJ pulse, of duration 175 ns (FWHM) is observed 39.5 μs after the CSL is fired (see Fig. 3). On a few occasions when

the CSL alignment appeared to be optimised, a pulse length of about 50 ns was observed.

Mode c: L1 is a spinning pipe gas lens operated at 200 cm focal length. For this "all gas" Q-switch we expected similar performance to mode a. Fig. 3 shows a 375 ns (FWHM) pulse similar to that of mode a. However, the energy for this mode is slightly higher (3.0 J). The absence of reflective losses in the cavity appears to outweigh the effect of the spinning pipe gas lens aberrations.

In Table I we summarize the results of the experiment. The energy values reported in this paper are the maximum values obtained over a large number of experiments. Although the fluctuations are large, especially for mode c, due in this case to the unstable behaviour of the Spinning Pipe Gas Lens [6], we noted that the operations do not critically depend on the cavity alignment and gas lens aberrations.

We now examine in greater detail the evolution of the cavity geometry after the CSL shocks have collided and how this affects the cavity losses. The losses can be split into two terms. The first term is constant and takes into account diffraction, surface reflections from lens L1, and ruby rod surface imperfections.

The second term depends on the cavity geometry and will vary explicitly with time. If no apertures are present in the cavity, the losses depend only on the parameter m and can be calculated according to the following loss formula

$$L = \begin{cases} 1 - 1/M^2 & \text{if abs}(m) > 1 \\ 0 & \text{if abs}(m) \leq 1 \end{cases} \tag{2}$$

where L is the fractional intensity loss of an "input beam" entering the output coupler and whose linear magnification over one round trip is M. The

evolution of M and the corresponding L is shown in Fig. 4 for mode a.

A simple model of the laser system was developed. Due to the presence of apertures in the cavity such as the ruby rod external diameter and the CSL aperture, the expression for the loss term is more complex than that given by Eq. (2) and depends on the "input beam" cross section. It coincides with Eq. (2) only for light traveling close to the optical axis. Taking this into account the calculation of the losses as a function of the distance from the optical axis was performed using the formalism of matrix optics. The laser beam was subdivided into a collection of annular beams. The laser rate equations were solved for each annulus, using the fourth order Runge Kutta numerical method with variable step size. Independently an approximate computation of the beam divergence is performed for the resonator geometry that exists when lasing is at its peak. We generate a uniform planar distribution of rays at the position of the ruby rod and we follow the path of each of the rays for a given number of round trips, recording the values of their angle at the output coupler. These values are used to calculate the beam diameter and divergence.

Fig. 5 shows the computed laser beam intensity waveform in the centre of the beam, for modes a, b, and c. The computed values of the laser energy, pulselength, beam diameter, and divergence are summarized in Table II. The discrepancy between the measured and computed pulselength can be attributed to the aberrations of the gas lenses which are not included in the actual model.

In conclusion we have demonstrated a novel Q-switching configuration that can use only gas optics. The advantages of the method are: no damage threshold, both for high peak power and average power; absence of polarization and polarizer. A major disadvantage is the necessity of having a long cavity which results in a long laser pulse. Improvements in colliding shock lens design and performance may correct this problem.

Acknowledgments

We thank W. de Beer and D. Davies for unflagging technical support, P. Di Lazzaro for discussions, and the FRD for financial support.

References

[1] W. Koechner, *Solid State Laser Engineering* (Springer Verlag, Berlin-Heidelberg-New York, 1988) Second Edition, 402

[2] R. Buccellato, N. Lisi, and M. M. Michaelis, Opt. Comm. **101**, 350 (1993)

[3] M. M. Michaelis, C. A. Dempers, M. Kosch, A. Prause, M. Notcutt, P. F. Cunningham, and J. A. Waltham, Nature **353**, 547 (1991)

[4] B. L. Xie, S. J. Xia, and Q. T. Chow, Chin. Phys. Lett. **2**, 509 (1985)

[5] A 1975 model K1 Korad ruby laser.

[6] M. Notcutt, M. M. Michaelis, P. F. Cunningham, and J. A. Waltham, Optics and Laser Technology **20**, 243 (1988)

[7] N. Lisi, R. Buccellato, and M. M. Michaelis, Optics and Laser Technology, accepted for publication

[8] A. E. Siegman, *Lasers* (University Science Book, Mill Valley, California, 1986) 599

Figure Captions

Fig. 1 Colliding Shock Lens characteristics. Evolution of focal length and effective diameter after the shock collision.

Fig. 2(a) Schematic of the CS-QS experiment.

Fig. 2(b) Colliding Shock Lens geometry.

Fig. 3 Measured laser pulse intensity waveforms.

Fig. 4 Evolution of the cavity magnification m and losses L for paraxial rays (mode a).

Fig. 5 Computed laser pulse intensities in the center of the beam.

Tables

Table I: Summary of the results of the Colliding Shock Q-Switching experiment. $E_{\max}$ is the maximum recorded value of the output energy in the three different resonator geometry. t_p is the typical pulse duration (FWHM). d is the laser spot diameter and div is the divergence.

	$E_{\max}$/J	t_p/ns	d/mm	div/mrad
Mode a	2.0	360	8.0	1.0
Mode b	0.1	175	2.0	3.3
Mode c	3.0	375	8.0	1.4

Table II: Summary of the computational results of the Colliding Shock Q-Switching. $E_{\max}$ is the energy, t_p is the FWHM pulse duration, d is the laser beam diameter, and div is the divergence.

	$E_{\max}$/J	t_p/ns	d/mm	div/mrad
Mode a	2.0	225	10.0	1.0
Mode b	0.13	105	2.8	4.0
Mode c	3.0	200	10.0	0.9

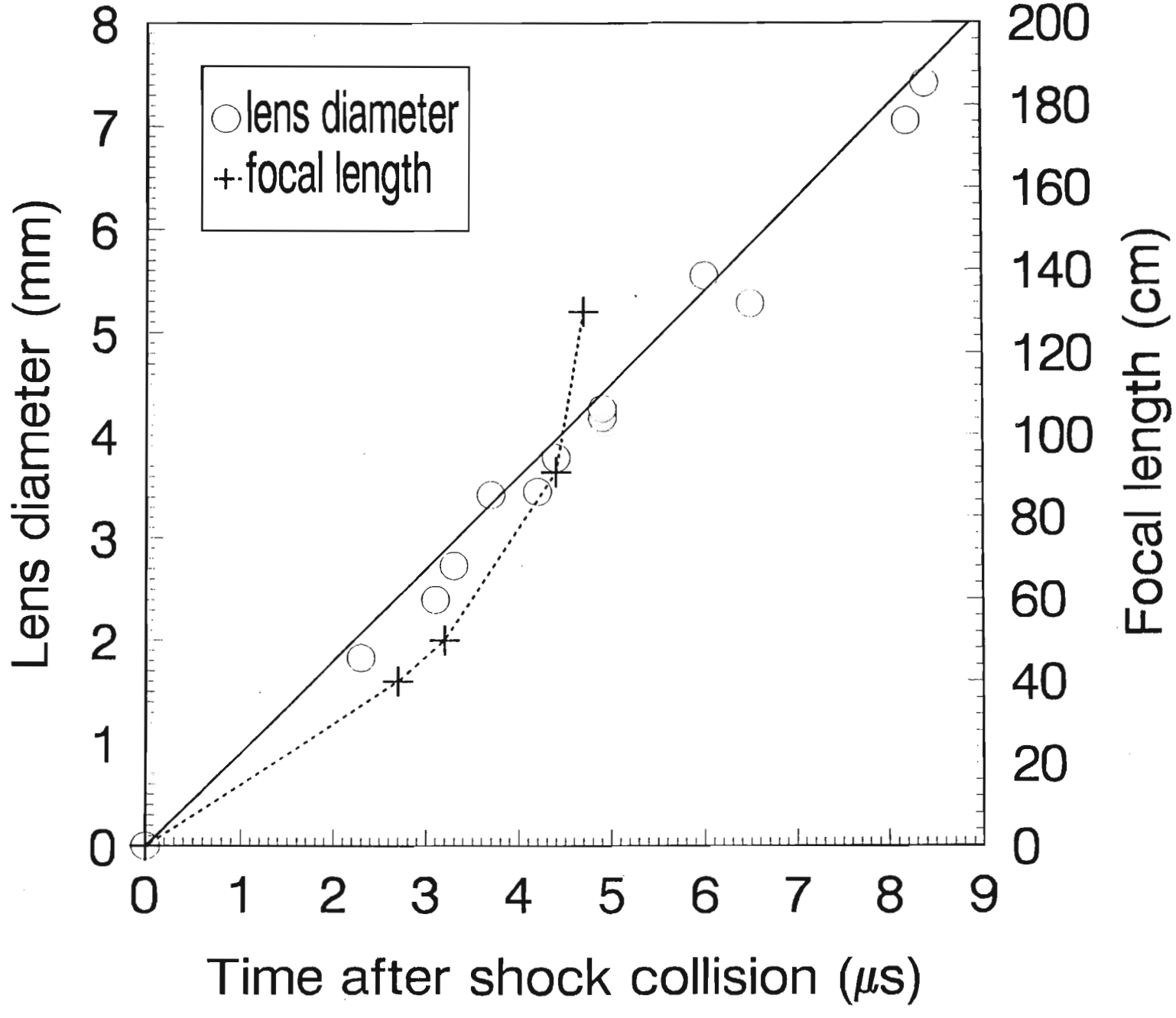
lens diameter
focal length
Lens diameter (mm)
Focal length (cm)
Time after shock collision (μs)
0
1
2
3
4
5
6
7
8
9
0
20
40
60
80
100
120
140
160
180
200

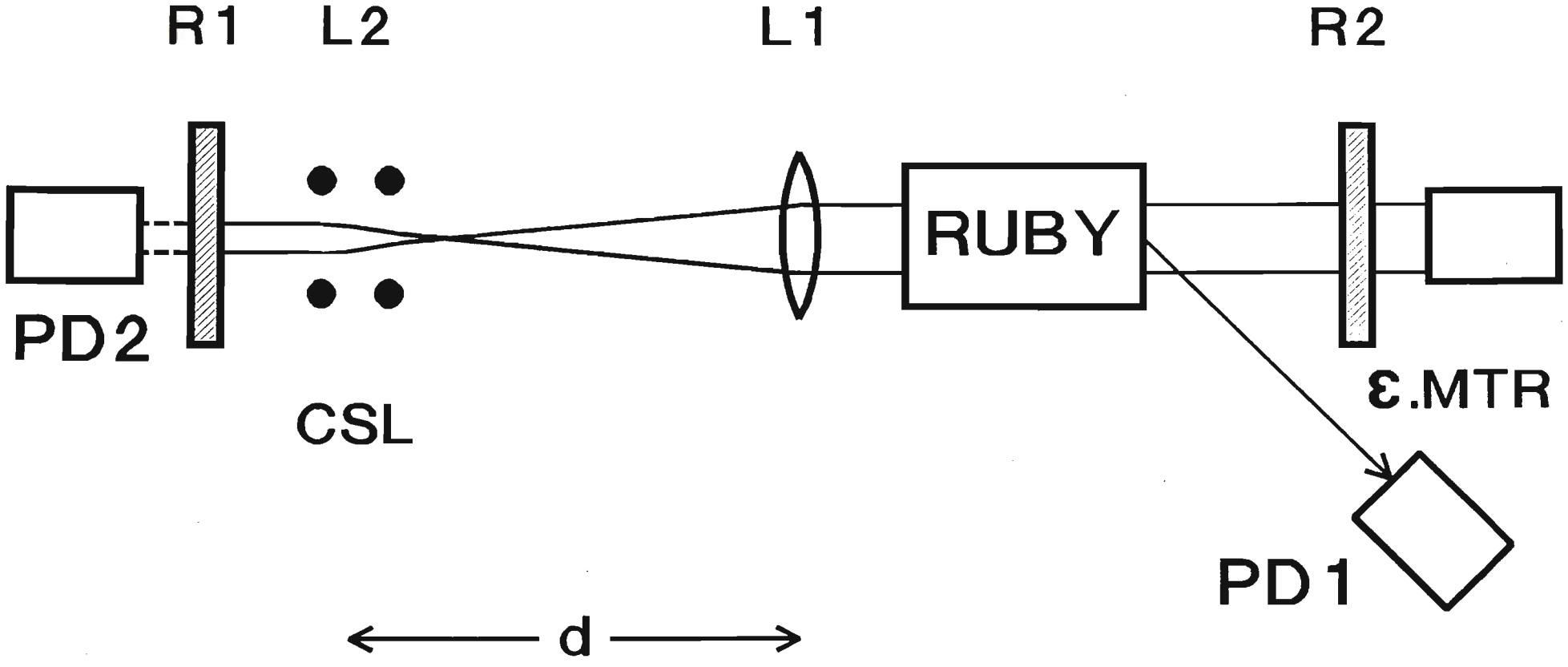

Fig. 2(a)

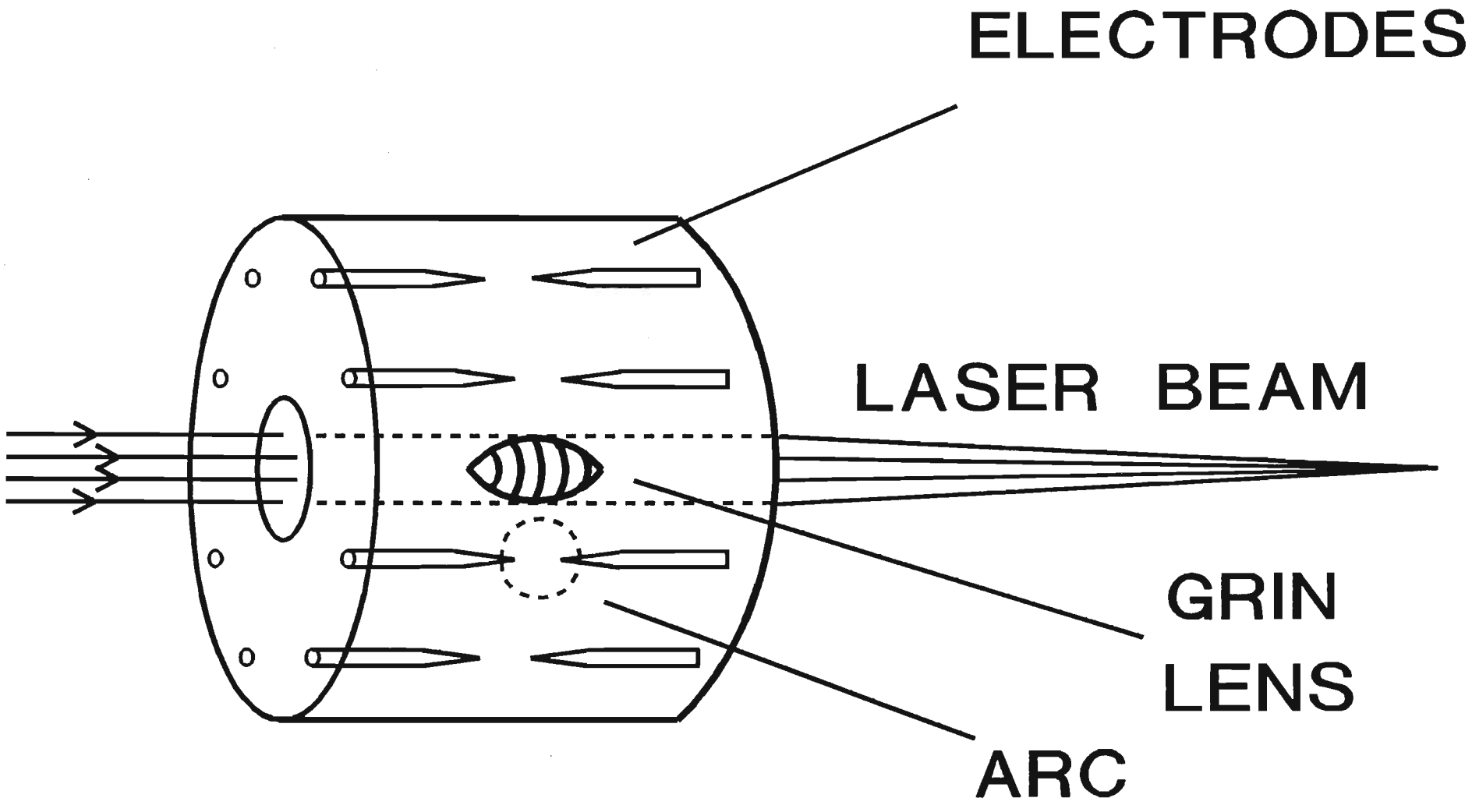

Fig. 2(b)

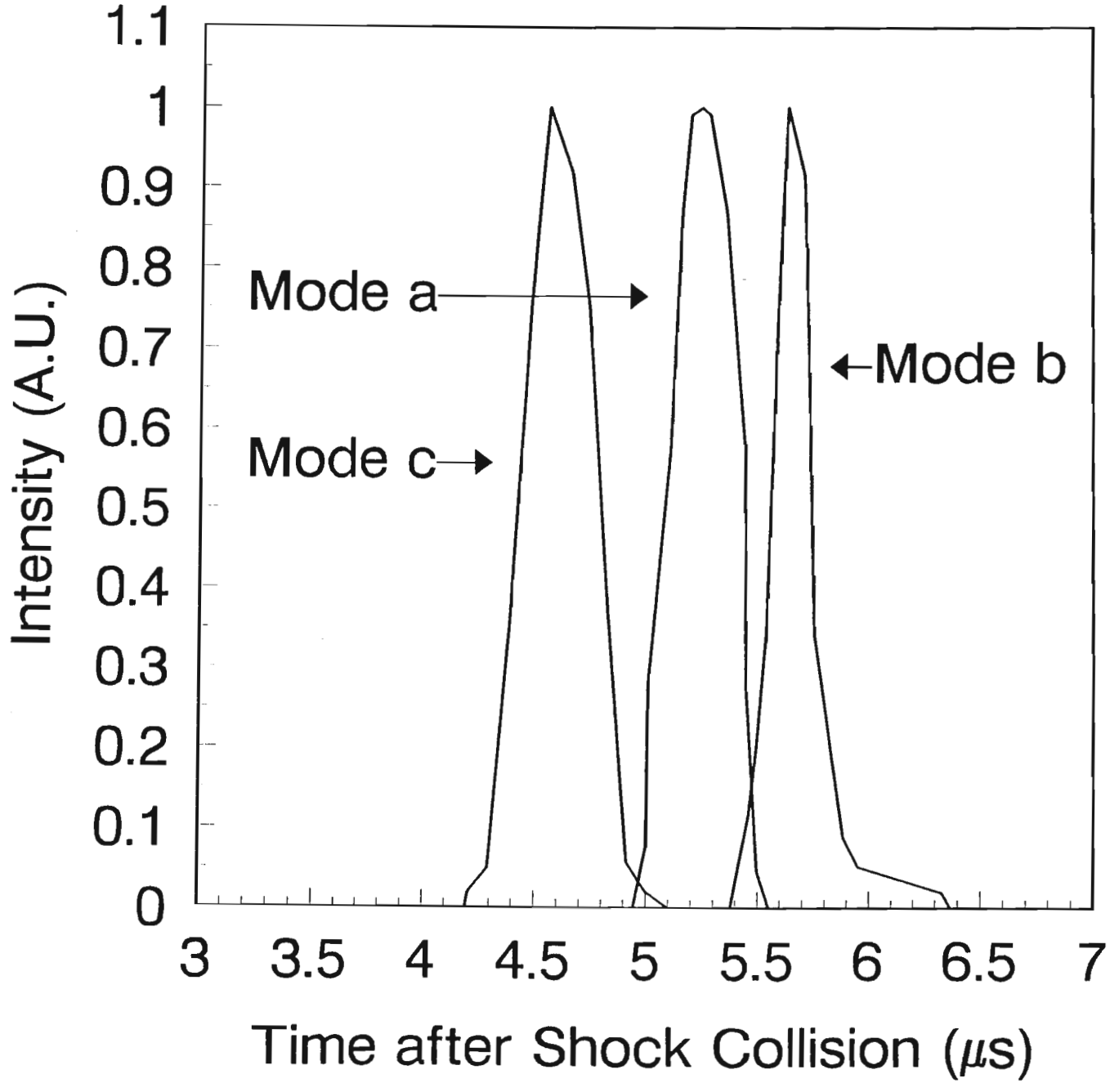
1.1
1
0.9
0.8
0.7
0.6
0.5
0.4
0.3
0.2
0.1
0
Intensity (A.U.)
Mode a
Mode b
Mode c
3
3.5
4
4.5
5
5.5
6
6.5
7
Time after Shock Collision (μs)

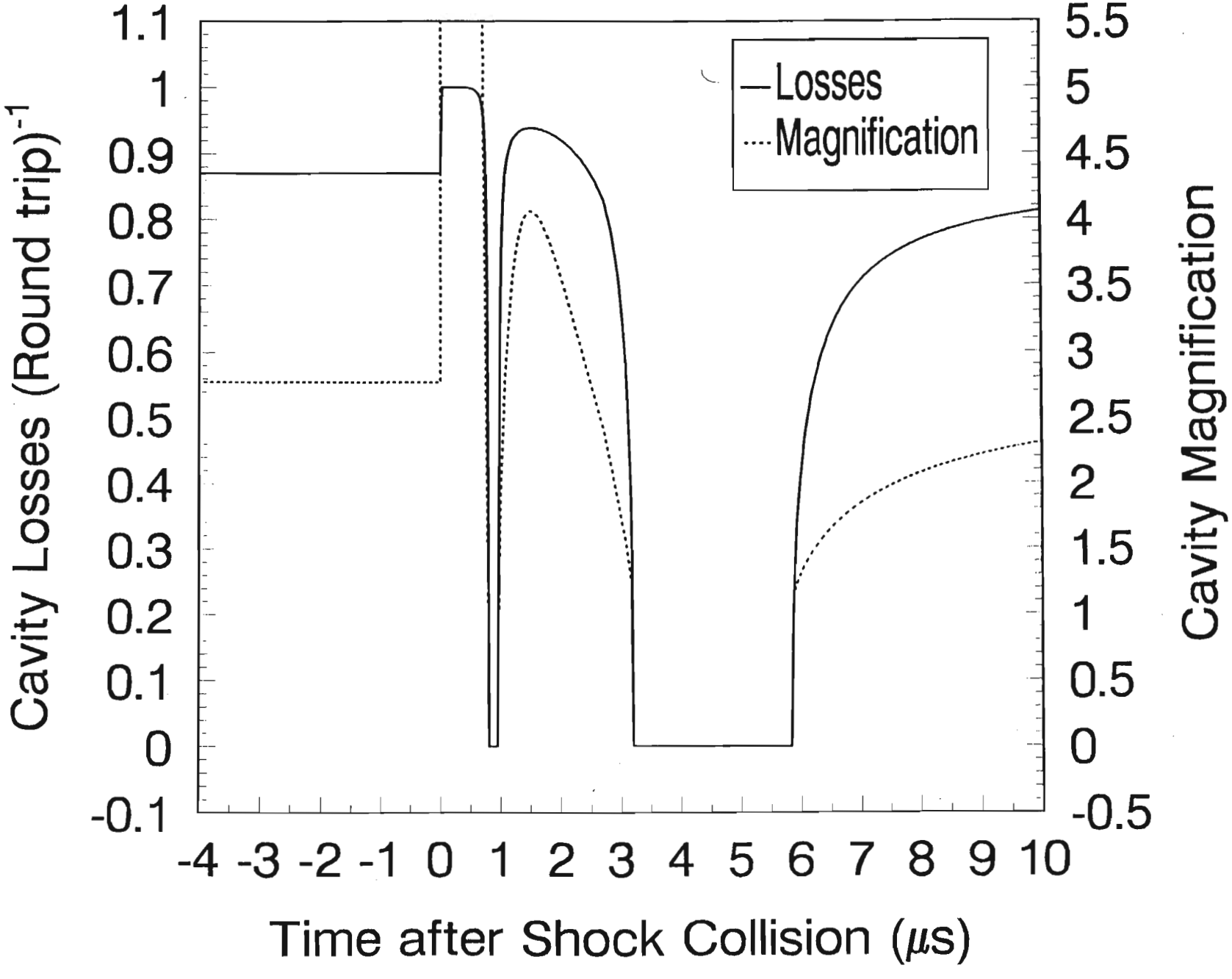
Losses
Magnification
Cavity Losses (Round trip)$^{-1}$
Cavity Magnification
Time after Shock Collision (μs)
1.1
1
0.9
0.8
0.7
0.6
0.5
0.4
0.3
0.2
0.1
0
-0.1
5.5
5
4.5
4
3.5
3
2.5
2
1.5
1
0.5
0
-0.5
-4 -3 -2 -1 0 1 2 3 4 5 6 7 8 9 10

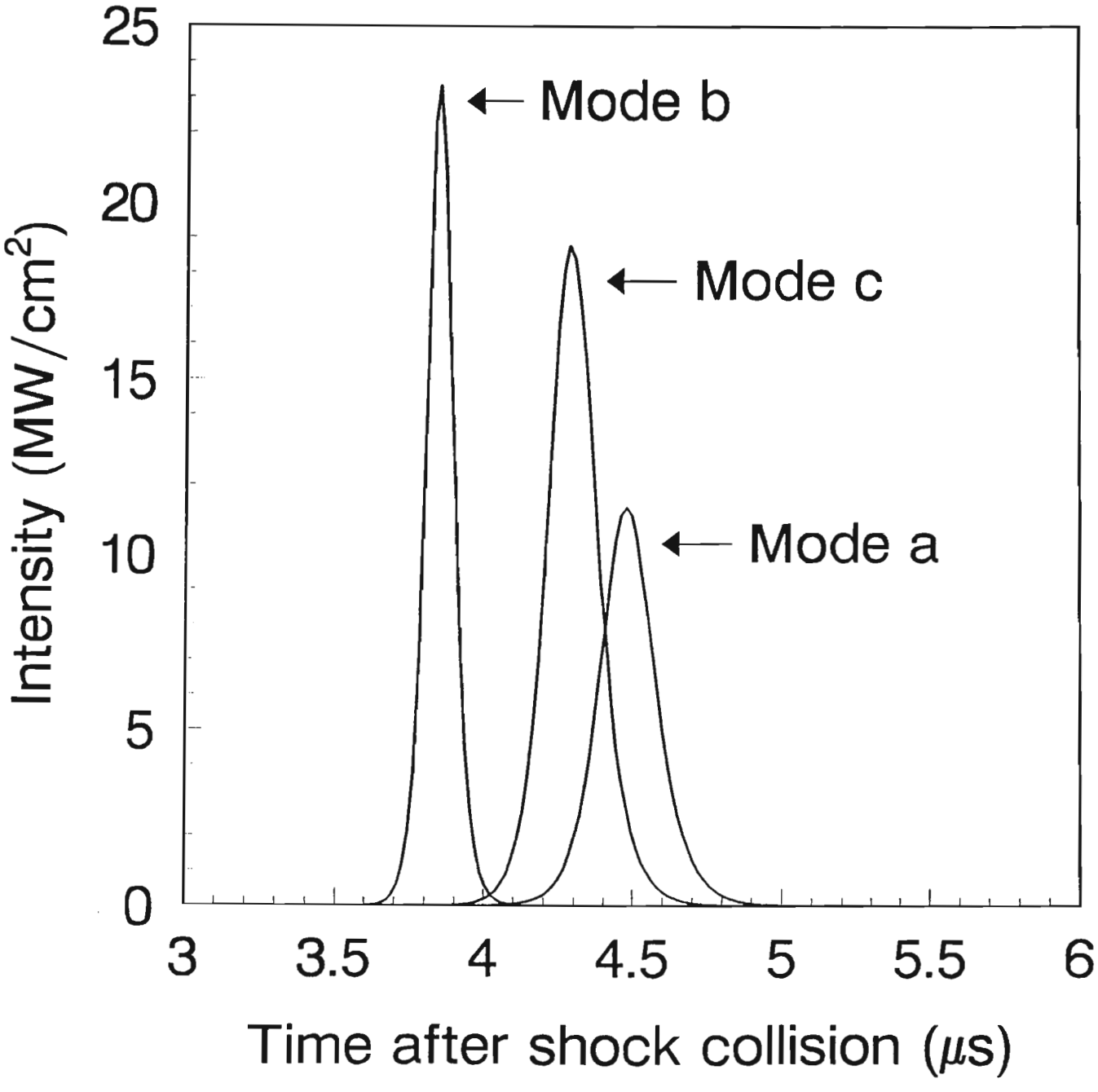
25
20
15
10
5
0
Intensity (MW/cm^2)
Mode b
Mode c
Mode a
3
3.5
4
4.5
5
5.5
6
Time after shock collision (μs)